7-1-2014

STRUCTURAL EVOLUTION OF THE RIO GRANDE RIFT: SYNCHRONOUS EXHUMATION OF RIFT FLANKS FROM 20-10 MA, EMBRYONIC CORE COMPLEXES, AND FLUID-ENHANCED QUATERNARY EXTENSION

Jason Ricketts

Jason William Ricketts
Candidate

Earth and Planetary Sciences
Department

This dissertation is approved, and it is acceptable in quality and form for publication:

Approved by the Dissertation Committee:

Dr. Karl Karlstrom, Chairperson

Dr. Laura Crossey

Dr. Brandon Schmandt

Dr. Gary Axen

Dr. Shari Kelley

STRUCTURAL EVOLUTION OF THE RIO GRANDE RIFT: SYNCHRONOUS EXHUMATION OF RIFT FLANKS FROM 20-10 MA, EMBRYONIC CORE COMPLEXES, AND FLUID-ENHANCED QUATERNARY EXTENSION

by

JASON WILLIAM RICKETTS

B.S., Geological Sciences, San Diego State University, 2008
M.S., Geological Sciences, San Diego State University, 2010

DISSERTATION

Submitted in Partial Fulfillment of the
Requirements for the Degree of

Doctor of Philosophy
Earth and Planetary Sciences

The University of New Mexico
Albuquerque, New Mexico

July 2014

Acknowledgements

The completion of this dissertation would not have been possible without the assistance and guidance of a number of people. First I would like to thank the Department of Earth and Planetary Sciences for financial support, the use of equipment and vehicles, and for giving me the opportunity to study rocks in a place like New Mexico. I would also like to thank the New Mexico Bureau of Geology and Mineral Resources for funding a large portion of my research and for providing me with the opportunity to create geologic maps. I would like to thank my committee members for their guidance and feedback on various aspects of my dissertation. In particular, this dissertation would have not been possible without my main advisor, Karl Karlstrom, who seemed to be always available to discuss ideas, review manuscript drafts, provide funding, and of course do field work. Last, but certainly not least, I would like to thank Sarah de los Santos Upton for her moral support and encouragement, and for patiently listening while I practice giving talks.

STRUCTURAL EVOLUTION OF THE RIO GRANDE RIFT: SYNCHRONOUS EXHUMATION OF RIFT FLANKS FROM 20-10 MA, EMBRYONIC CORE COMPLEXES, AND FLUID-ENHANCED QUATERNARY EXTENSION

By

Jason W. Ricketts

B.S., Geological Sciences, San Diego State University, 2008
M.S., Geological Sciences, San Diego State University, 2010
Ph.D., Earth and Planetary Sciences, University of New Mexico, 2014

ABSTRACT

The Rio Grande rift in Colorado and New Mexico is one of the well-exposed and well-studied continental rifts in the world. Interest in the rift is driven not only by pure scientific intrigue, but also by a desire and a necessity to quantify earthquake hazards in New Mexico as well as to assess various water related issues throughout the state. These motivating topics have thus far led to the publication of two Geological Society of America Special Publication volumes in 1994 and 2013. This dissertation aims at building on the wealth of previous knowledge about the rift, and is composed of three separate chapters that focus on the structural evolution of the Rio Grande rift at several different time and spatial scales.

At the largest scale, apatite (U-Th)/He thermochronologic data suggest synchronous extension along the entire length of the Rio Grande rift in Colorado and New Mexico from 20-10 Ma, which is important for understanding and evaluating possible driving mechanisms which are responsible for the rift. Previous tectonic and

magmatic events in western North America were highly influential in the formation of the Rio Grande rift, and the new thermochronologic data suggest that its formation may have been closely linked to foundering and removal of the underlying Farallon Plate. A fundamental result of rift development at these scales is a concentration of strain is some regions of the rift. In these regions of maximum extension, fault networks display a geometry involving both high- and low-angle fault networks. These geometries are similar to the early stages in the development of metamorphic core complexes, and thus these regions in the rift link incipient extensional environments to highly extended terranes. At shorter time scales, heterogeneous strain accumulation may be governed in part by fluids in fault zones. As an example, along the western edge of the Albuquerque basin, travertine deposits are cut by extensional veins that record anomalously high strain rates during the Quaternary at this location. The fluids that precipitated the travertine and calcite in veins also contain a small component of deeply-derived fluids such that surface extension in this part of the rift is coupled with processes at deeper levels. Together, these studies suggest that removal of the Farallon slab beneath Colorado and New Mexico may have been a primary mechanism establishing extension in the Rio Grande rift, while continued extension is heterogeneous in time and space and provides an important link between surface processes and processes that operate at mid-crustal levels.

TABLE OF CONTENTS

LIST OF FIGURES

CHAPTER 1

CHAPTER 2

CHAPTER 3

LIST OF TABLES

CHAPTER 2

CHAPTER 3

CHAPTER 1: Abrupt opening of the Rio Grande rift due to fragmentation of the Farallon slab: Evidence from apatite (U-Th)/He and fission-track thermochronology

Jason W. Ricketts[1], Shari A. Kelley[2], Karl E. Karlstrom[1], Magdalena S. Donahue[1], Gary J. Axen[2], Brandon Schmandt[1], and Jolante van Wijk[2]

[1]Department of Earth and Planetary Sciences, University of New Mexico, MSC03-2040, 1 University of New Mexico, Albuquerque, NM, 87131

[2]Earth and Environmental Science Department, New Mexico Institute of Mining and Technology, 801 Leroy Place, Socorro, NM. 87801

ABSTRACT

152 new apatite (U-Th)/He (AHe) dates are presented from 34 sample locations along the flanks of the Rio Grande rift in New Mexico and Colorado. These data are combined with apatite fission-track (AFT) analyses of the same rocks and modeled together to create well constrained cooling histories for Rio Grande rift flank uplifts. The data indicate rapid cooling from ~28 Ma to Recent in the Sawatch Range and the Sangre de Cristo Mountains, ~21 to 5 Ma in the Albuquerque basin, and ~17 to 8 Ma in the southern Rio Grande rift in southern New Mexico. Rapid cooling of rift flanks followed the Oligocene ignimbrite flare-up and the northern section of the Rio Grande rift in Colorado exhibits semi-continuous cooling since the Oligocene. Overall, however, rift flank cooling along the length of the rift was out of phase with high volume magmatism and hence is inferred to have been driven mainly by exhumation due to faulting. Although each location preserves a unique cooling history, when combined with existing

AHe data from the Gore Range in northern Colorado and the Sandia Mountains in New Mexico together these data indicate ~synchronous extension and rift flank uplift along >850 km of the length of the Rio Grande rift from ~20-10 Ma.

These time-space constraints provide an important new dataset to develop geodynamic models for initiation and evolution of continental rifting. Models involving northward unzipping and Colorado Plateau rotation are not favored as primary mechanisms driving extension. Instead, a geodynamic model is proposed that involves upper mantle dynamics during multi-stage foundering and rollback of the Farallon plate near the Laramide hinge region that extended between the Wyoming and SE New Mexico high velocity mantle domains. First stage delamination accompanied and followed ~40-20 Ma volcanism in the San Juan and Mogollon-Datil ignimbrite centers. A second stage involved a ~20 Ma "Big Break" of the remaining part of the Farallon slab. This produced renewed uplift of the Alvarado Ridge topographic high, enhanced surface uplift of rift flanks, developed a central graben with increased fault- related high strain rates, and resulted in maximum sediment accumulation in the Rio Grande rift. Our geodynamic model thus involves Oligocene removal of parts of the Farallon slab beneath the ignimbrite centers followed by a major Miocene slab break that instigated the discrete N-S Rio Grande rift, continuing upper mantle convection, and differential uplift of the Rocky Mountain - Rio Grande rift region.

INTRODUCTION

There are still fundamental questions about where and why continental rifts initiate, the evolution of rifting processes and feedbacks among them, and large-scale mantle-to-surface interconnections that accompany rifting. The Rio Grande rift extends

more than 1,000 km from Colorado to northern Mexico, and the narrow portion from central Colorado to central New Mexico is one of the world's best exposed and most thoroughly studied examples of a narrow continental rift system. However, its timing of origin, extensional strain history, and location remain incompletely understood. The northward-tapering geometry of the rift has suggested to some that extension initiated in the south and propagated northwards (e.g. McMillan et al., 2002, Leonard, 2002; Heller et al., 2003). Alternatively, Kelley et al. (1992), Chapin and Cather (1994) and Landman and Flowers (2012) documented near-simultaneous extension along the entire length of the rift. Geodynamic mechanisms posited for rifting include rotation of the Colorado Plateau (Chapin and Cather, 1994; Landman and Flowers, 2012), collapse of overthickened crust at the waning stages of the Laramide orogeny (e.g. Cordell, 1978; Eaton, 1986), whole mantle convection (Moucha et al., 2008), and small-scale convective upwelling near a lithospheric step driven by passive extension (van Wijk et al, 2008).

This paper presents new apatite (U-Th)/He (AHe) data modeled in the context of a synthesis of existing apatite fission-track (AFT) thermochronology to resolve space-time patterns in extensionally driven exhumation and cooling along the length of the Rio Grande rift. When combined, these two thermochronometers provide a powerful and robust means of constructing continuous t-T cooling paths from ~120 to ~30 °C. This temperature range corresponds to depths of 1-4 kilometers such that, in a setting such as the Rio Grande rift, cooling through these temperatures can be used to interpret differential cooling due to erosion and tectonic denudation of rift-flank footwalls. Times of rapid cooling derived from age-elevation transects and modeled cooling histories can also be used to reconstruct times of fault activity or inactivity on rift-bounding faults.

Here we present 152 new single aliquot AHe dates from 34 samples from rift flanks in Colorado and New Mexico and combine these data with existing AFT data when available to explore the range of permissible thermal histories constrained by the data. Together these thermal history models are discussed within the context of published AHe dates from the Gore Range (Landman and Flowers, 2012) and prior efforts to combine both systems in the Sandia Mountains (House et al., 2003). We also compare the thermochronologic data with a recent compilation of timing of magmatism for the rift (Chapin et al. 2004) to discriminate exhumational versus magmatic signals. The resulting synthesis of data presented here encompasses >850 km of the length of the Rio Grande rift and our results provide first-order constraints on the mechanisms that drove continental extension.

REGIONAL TECTONIC SETTING

Cenozoic tectonic and magmatic activity in the Rocky Mountain-Rio Grande rift region involved several episodes of uplift, erosion, and cooling (Cather et al., 2012; Karlstrom et al., 2012). By late Cretaceous time, steep subduction of the Farallon plate beneath North America during the Sevier orogeny created a well-established magmatic arc along the western margin of North America, and the region that is now Colorado and New Mexico was near sea level (e.g. Mitrovica et al., 1989; DeCelles, 2004; Dickinson, 2009). By ~80 Ma, the dip of the Farallon plate had shallowed beneath western North America during the early stages of the Laramide orogeny. During this process arc magmatism along western parts of the continental margin ceased or waned, and tectonic and magmatic activity migrated > 1000 km eastward (e.g. Coney and Reynolds, 1977). Dewatering of the shallowly dipping Farallon plate hydrated the base of the overlying

North American lithosphere, weakening the lithosphere and facilitating uplift and deformation of the western U.S. (Humphreys et al., 2003). In central and northern New Mexico and in Colorado, Laramide reverse faulting created the Rocky Mountains, a several-hundred-km-wide, N-S-trending belt of basement cored uplifts due to NE- to ENE-directed shortening as the Colorado Plateau compressed against cratonic North America (Varga, 1993; Erslev, 2005; Humphreys, 2009).

Flat slab subduction during the Laramide orogeny persisted until at least ~45 Ma, and eventually terminated during slab rollback, delamination, and ultimate foundering of the Farallon slab into the asthenosphere. This foundering exposed the hydrated North American lithospheric mantle to underlying hot asthenosphere, which resulted in vigorous magmatism across western North America (Humphreys et al., 2003) that produced large volumes of silicic and bimodal volcanism during the "ignimbrite flare-up" (Coney and Reynolds, 1977; Lawton and McMillan, 1999; Chapin et al., 2004). The ignimbrite event significantly modified the upper mantle (Farmer et al., 2008; Roy et al., 2009) and may have involved partial delamination of the North American lithosphere and accompanying mantle-driven surface uplift (Cather et al., 2012; Karlstrom et al., 2011). The initiation of extension was broadly coincident with voluminous ignimbrite volcanism, which lasted from ~60-55 Ma in the Great Basin (e.g. Armstrong and Ward, 1991; Christiansen and Yeats, 1992), ~35-18 Ma in the San Juan volcanic field in southern Colorado (Colucci et al., 1991; Lipman, 2007), and from ~40-24 Ma in the Mogollon-Datil volcanic field in southern New Mexico (McIntosh et al., 1992).

The Rio Grande rift is a N-S-trending zone of extension that roughly follows the axis of the Rocky Mountains. The rift is characterized by a series of linked structural

depressions (half-grabens), separated by accommodation (or transfer) zones, that are bounded by rift-flank uplifts. Individual basins are typically asymmetrical such that slip is predominantly concentrated along one of the rift flanks resulting in maximum sediment accumulation and rift flank uplift near the more active rift flank (e.g. Chapin and Cather, 1994). Published AFT data for most rift flanks in Colorado and New Mexico (Fig. 1) indicate that cooling of footwall blocks through ~110 °C occurred at different times in different parts of the rift flanks. Laramide AFT ages (> 45 Ma) are found on the "inactive" or "hinge" side of rift half-grabens that preserve earlier cooling episodes. Rift flanks controlled by master normal fault systems give Late Oligocene – Middle Miocene cooling ages (e.g. Kelley et al., 1992; Kelley and Chapin, 1997) interpreted as cooling due to fault slip and accompanying exhumation of footwall blocks from depths in the crust of ~2.5-4 km, assuming average geothermal gradients of 25-35 °C/km and surface temperatures of 10-25 °C. This is in general agreement with timing of most-rapid rotation and faulting of synrift sediments (e.g. Chapin and Cather, 1994; May and Russell, 1994; Koning et al., 2013).

Eaton (1986; 2008) proposed that a broad wavelength topographic ridge extending from central New Mexico to northern Colorado, known as the Alvarado Ridge, was spatially coincident with and had the Rio Grande rift as a central graben. Initial uplift of the Alvarado Ridge in post-middle Eocene time likely resulted from a combination of heating of the lithosphere, inflation of the crust through intrusion of low-density plutons, and warm, buoyant upper mantle (Eaton, 2008). In addition to the broad wavelength swell that defines the Alvarado Ridge, Roy et al. (1999) also noted short wavelength tilts related to rift flank uplifts and concluded that the Alvarado Ridge pre-dates the Rio

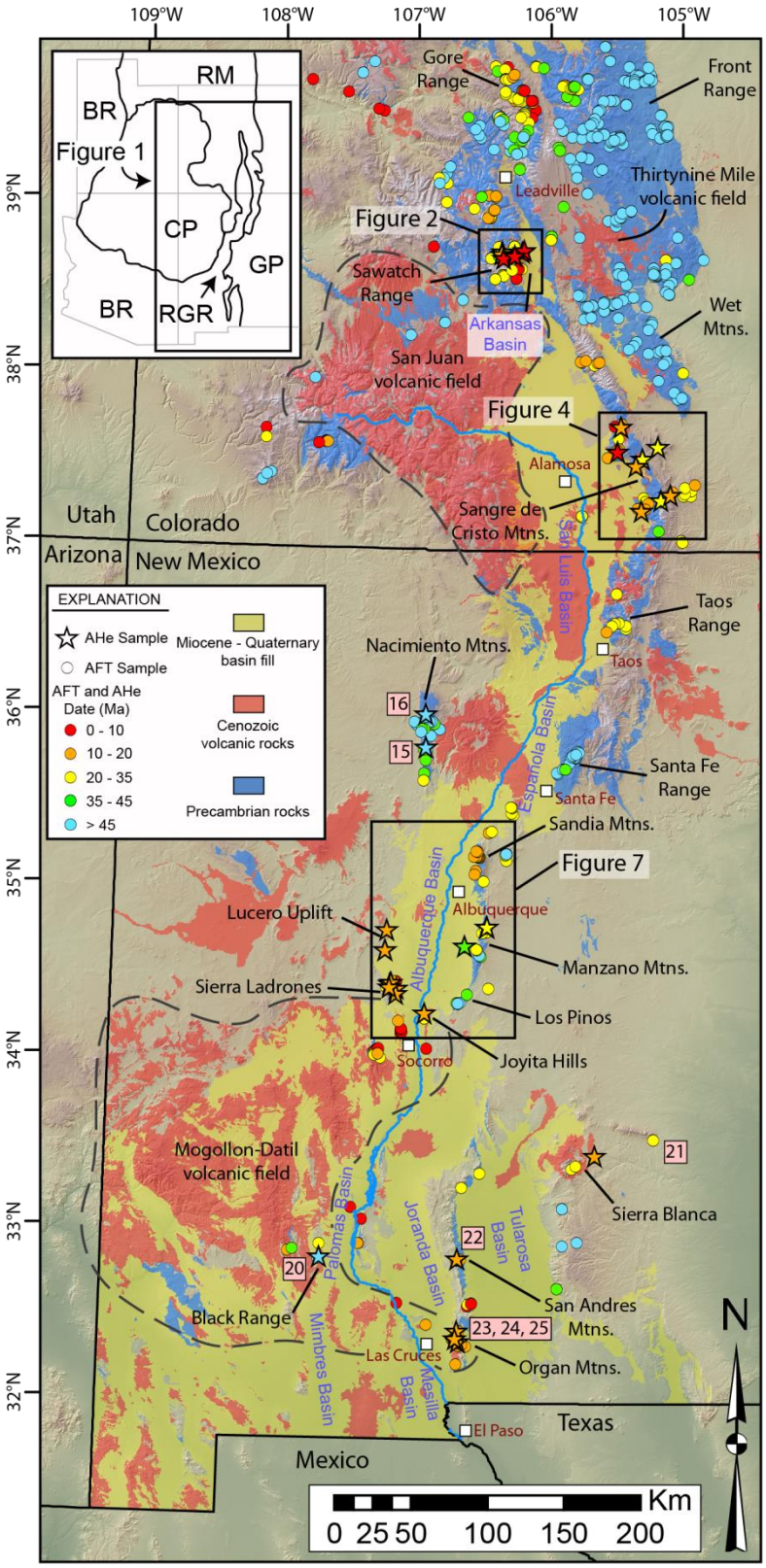
109°W
108°W
107°W
106°W
105°W
39°N
38°N
37°N
36°N
35°N
34°N
33°N
32°N
RM
BR
Figure 1
CP
GP
BR
RGR
Gore Range
Front Range
Leadville
Thirtynine Mile volcanic field
Figure 2
Sawatch Range
Arkansas Basin
Wet Mtns.
San Juan volcanic field
Figure 4
Alamosa
Sangre de Cristo Mtns.
San Luis Basin
Utah
Colorado
Arizona
New Mexico
Taos Range
Taos
Nacimiento Mtns.
16
15
Española Basin
Santa Fe Range
Santa Fe
Sandia Mtns.
Figure 7
Albuquerque
Albuquerque Basin
Lucero Uplift
Manzano Mtns.
Sierra Ladrones
Los Pinos
Socorro
Joyita Hills
Mogollon-Datil volcanic field
21
Sierra Blanca
Palomas Basin
Joranda Basin
Tularosa Basin
22
20
San Andres Mtns.
Black Range
Mimbres Basin
23, 24, 25
Las Cruces
Organ Mtns.
Mesilla Basin
El Paso
Texas
Mexico
N
Km
0 25 50 100 150 200
EXPLANATION
AHe Sample
AFT Sample
AFT and AHe Date (Ma)
0 - 10
10 - 20
20 - 35
35 - 45
> 45
Miocene - Quaternary basin fill
Cenozoic volcanic rocks
Precambrian rocks

Figure 1. Simplified geologic map of the Rio Grande rift system in Colorado and New Mexico. Existing AFT dates, plotted according to their age as circles, are from Abbott et al. (2002), Beaty et al. (1987), Bryant and Naeser (1980), Bryant and Stegen (1990), Bryant et al. (1981), Bookstrom et al. (1987), Church and Bickford (1971), Cunningham et al. (1994), Feldman (2010), Kelley (2002), Kelley and Chapin (1997, 2004), Kelley and Duncan (1986), Kelley et al. (1992), Lindsey et al. (1986), Marvin et al. (1974), McKeon (2009), Miggins et al. (2002), Naeser et al. (1990, 2002), Olson et al (1977), Shannon (1988), Smith (1975), Thompson and Machette (1989), Thompson and Arehart (1990), and Wallace (1995). Previously published AHe dates only exist for the Sandia Mountains (House et al., 2003) and the Gore Range (Landman and Flowers, 2013), and new AHe dates from this study are shown as stars.

Grande rift. Neogene (post- 10 Ma) surface uplift and erosion have also been proposed for the Rocky Mountain- Colorado Plateau region (Karlstrom et al., 2012). AFT and AHe dates of < 10 Ma are found in several places both within and outside the Rio Grande rift (Fig. 1) that have been interpreted to be a signal of young and ongoing mantle-driven surface uplift of the Rocky Mountain region (Karlstrom et al., 2012). Young deformation is also recorded in the rift by localized Quaternary extension (e.g. Machette et al., 1998; Ricketts et al., 2014) and ongoing strain (10's of mm/year) recorded by continuous measurements of GPS sites (Berglund et al., 2012).

GEOLOGY AND GEOPHYSICS OF THE RIO GRANDE RIFT

We use the term "central Rio Grande rift" for the narrow rift segment that extends from Leadville, Colorado to Socorro, New Mexico (Fig. 1). In this segment, the rift is a relatively discrete structural entity several 10's of kilometers wide. North of Leadville, the zone of continental extension is broader and more diffuse, but Miocene grabens that are genetically related to the Rio Grande rift are present in the Gore Range (Naeser et al., 2002; Landman and Flowers, 2012) and Saratoga Valley (Mears, 1998). Similarly, south of the Socorro "constriction" (Kelley, 1952), the Rio Grande rift abruptly widens to merge into the adjacent southern Basin and Range Province (Fig. 1).

Various geophysical investigations in New Mexico and Colorado have been successful in constraining the deep crustal and upper mantle structure associated with the Rio Grande rift and surrounding areas. P- and S-wave tomography of western North America obtained from the Earthscope Transportable Array reveals a highly heterogeneous upper mantle interpreted to reflect Neogene and ongoing shallow convective flow (Schmandt and Humphreys, 2010). At shallow depths (~90 km), the mantle underlying the Rio Grande rift is characterized by anomalously slow velocities, indicative of the presence of partial melt perhaps due to asthenospheric upwelling (van Wijk et al., 2008; Schmandt and Humphreys, 2010). Receiver function analysis from the LA RISTRA passive seismic experiment across the Rio Grande rift in central New Mexico indicates crustal thicknesses of ~45-50 km beneath the Colorado Plateau and Great Plains on either side of the rift, while the crust beneath the axis of the rift has been thinned to ~37 km (Wilson et al., 2005). Similarly, the ~45-65 km lithospheric thickness beneath the rift (West et al., 2004) is dramatically thinner than the ~150-180 km lithospheric thickness beneath the adjacent Great Plains to the east (van der Lee and Nolet, 1997; West et al., 2004; Yuan and Romanowicz, 2010). Absolute S-wave velocities highlight a region of low-velocity mantle centered in central New Mexico, but at depths of >300 km, the seismic velocities beneath the rift resemble those beneath the Colorado Plateau, arguing against deeply sourced upwelling asthenosphere (West et al., 2004).

Integration of seismic images with various geological datasets in Colorado and New Mexico suggests that Oligocene to Recent mantle convection has played a significant role in shaping surface processes (Karlstrom et al., 2012). For example, low

velocity regions in the upper mantle correspond with the locations of large-volume eruptive centers such as the San Juan volcanic field in Colorado, the Colorado Plateau margin in southwestern New Mexico, as well as the NE-trending Jemez lineament in northern New Mexico. Further, highest topography in central Colorado is underlain by thinnest crust (Hansen et al., 2013) and lowest velocity mantle (MacCarthy et al., 2014) indicating the Rocky Mountains are rootless; buoyant mantle and processes involving lithosphere delamination and asthenospheric return flow since the Oligocene supports topography (Karlstrom et al., 2012). It is in the context of these new mantle images that we seek better timing constraints and better geodynamic models for rift formation.

THERMOCHRONOLOGY METHODS

Apatite (U-Th)/He (AHe) and apatite fission-track (AFT) thermochronology are two of the most powerful methods for constraining the low-temperature cooling histories of rocks in tectonically active regions. For example, individual fission-track lengths and angles relative to the crystal's c-axis constrain the sample's time-temperature (tT) history such that long (~15μm) track lengths with a unimodal distribution are indicative of rapid cooling through the AFT partial annealing zone (~60-120 °C), while broad or bimodal track length distributions suggest prolonged residence in this temperature window, or reheating (e.g. Stockli, 2005; Ketchum, 2005; Donelick et al., 2005). Similarly, differential radiation damage in apatite crystals with different U and Th concentrations affects helium diffusion through the crystal lattice such that a positive correlation between AHe dates and effective uranium concentrations (eU) suggests prolonged residence in the AHe partial retention zone (~30-90 °C) (Flowers et al., 2009).

Apatite separates from samples with published AFT data in New Mexico and Colorado (Kelley et al., 1992; Kelley and Chapin, 1997) are housed at the New Mexico Institute of Mining and Technology. From these separates, apatite crystals for AHe dating were selected from samples where prior AFT data included sufficient track length and angle measurements. In addition, several new AHe samples were collected and processed for this study (Table DR1). Individual apatite crystals were selected under a polarizing microscope. Suitable apatite crystals are >70 μm when measured perpendicular to the c-axis, display euhedral crystal shape, and do not have visible inclusions. Crystal lengths and widths were measured in order to apply an age correction (Ft) (Farley et al., 1996). Individual apatite crystals were then packed in platinum tubes, and analyzed at the Arizona Radiogenic Helium Dating Lab at the University of Arizona, and the Colorado Thermochronology Research and Instrumentation Laboratory at the University of Colorado, Boulder. Following the methods of Landman and Flowers (2013), the average sample AHe date and 1σ sample standard deviation is reported for samples with <20% sample standard deviation. For samples with >20% sample standard deviation, the range of AHe dates is listed.

Newly obtained AHe data were coupled with AFT data, when available, and modeled with HeFTy (Ketchum, 2005) to inversely produce continuous time-temperature history paths, where "acceptable" paths have a goodness-of-fit parameter >0.05 and "good" paths have a goodness-of-fit parameter >0.5. Although samples with adequate track length measurements and angles were specifically targeted for AHe analysis, in many cases the track lengths and angles were not compatible with AHe dates and did not produce thermal history solutions in HeFTy. This difficulty in satisfying constraints from

all grains in both AFT and AHe systems is relatively common in combined datasets (e.g. Flowers and Kelley, 2011; Lee et al., 2013) and may reflect incomplete understanding of the kinetics of damage annealing and related complexities in modeling He diffusion in apatite (Fox and Shuster, 2014). In this study, when all constraints from AFT and AHe data did not produce "acceptable" or "good" thermal histories, thermal history models were constructed using the AFT data and as many compatible AHe dates as possible. We assume temperatures due to burial beneath ~3-4 km of Paleozoic and Mesozoic sediments were sufficient to anneal lattice damage from pre-Laramide deposits, especially in the elevated heat flow regime associated with the ignimbrite flare-up (House et al., 2003; Roy et al., 2004) and of the Rio Grande rift (e.g. Reiter et al., 1975), so models begin within a temperature window of 180-200 °C at a time of 90-100 Ma. For samples from intrusions younger than this, thermal models begin at the age of the intrusion. Each model also ends within a temperature range of 5-25 °C, reflecting a range of possible surface temperatures. For all good and acceptable paths computed in HeFTy, the weighted mean path is presented for each sample (which is generally smoother than the calculated "best fit" path). Complete HeFTy modeling results, including input data, number of paths computed, and good and acceptable path envelopes, are presented in the supplementary tables and figures. Results are presented from north to south along the rift.

APATITE (U-TH)/HE RESULTS AND INTERPRETATIONS

Sawatch Range- Mount Princeton Batholith

The Arkansas basin is the northernmost basin of the Rio Grande rift that contains appreciable (km-scale thickness) basin fill. East-dipping normal faults related to the development of the basin exist along the western margin of the basin (Coleman, 1985;

Miller, 1999), although a steep gravity gradient along the eastern edge of the basin suggests significant normal displacement along this margin as well (Case and Sikora, 1984). Constraints on the timing of extension in this part of the rift are poor due to a lack of volcanic rocks in the sedimentary basin, although rift initiation may have begun between ~33 and 24 Ma based on the emplacement of several high-silica plutons along the margins of the Arkansas basin (Chapin and Cather, 1994). The uplifted Sawatch Range, located along the western edge of the Arkansas basin, is composed of Precambrian and Paleozoic rocks which were intruded by the Eocene Mt. Princeton batholith. This range preserves Miocene AFT ages, which show a general increase in AFT age westward from the basin, which has been interpreted to represent westward tilting of this structural block during rifting (Kelley et al., 1992). Geothermal activity has extensively altered the eastern edge of the Mt. Princeton batholith, and is presently manifested by hot springs adjacent to the main faults that bound the Arkansas basin (Fig. 2). Within this region, Sharp (1970) estimated that geothermal activity reached peak temperatures of 195 to 200°C based on secondary mineral assemblages, temperatures that could reset AFT and AHe ages from this location.

Thirty new single-crystal AHe dates from six samples were obtained from the Sawatch Range along the western margin of the Arkansas basin in central Colorado (Table DR1; Figs. 1, 2). These samples are from the Mt. Princeton batholith, which was emplaced between 35.2 and 35.9 Ma based on U/Pb zircon ages (Zimmerer and McIntosh, 2012). For four of the samples, the standard deviation of all five crystals is less than 20%. The two remaining samples each contained one anomalously old AHe date (samples 2 and 3). The old grain from sample 2 contains very low U and Th

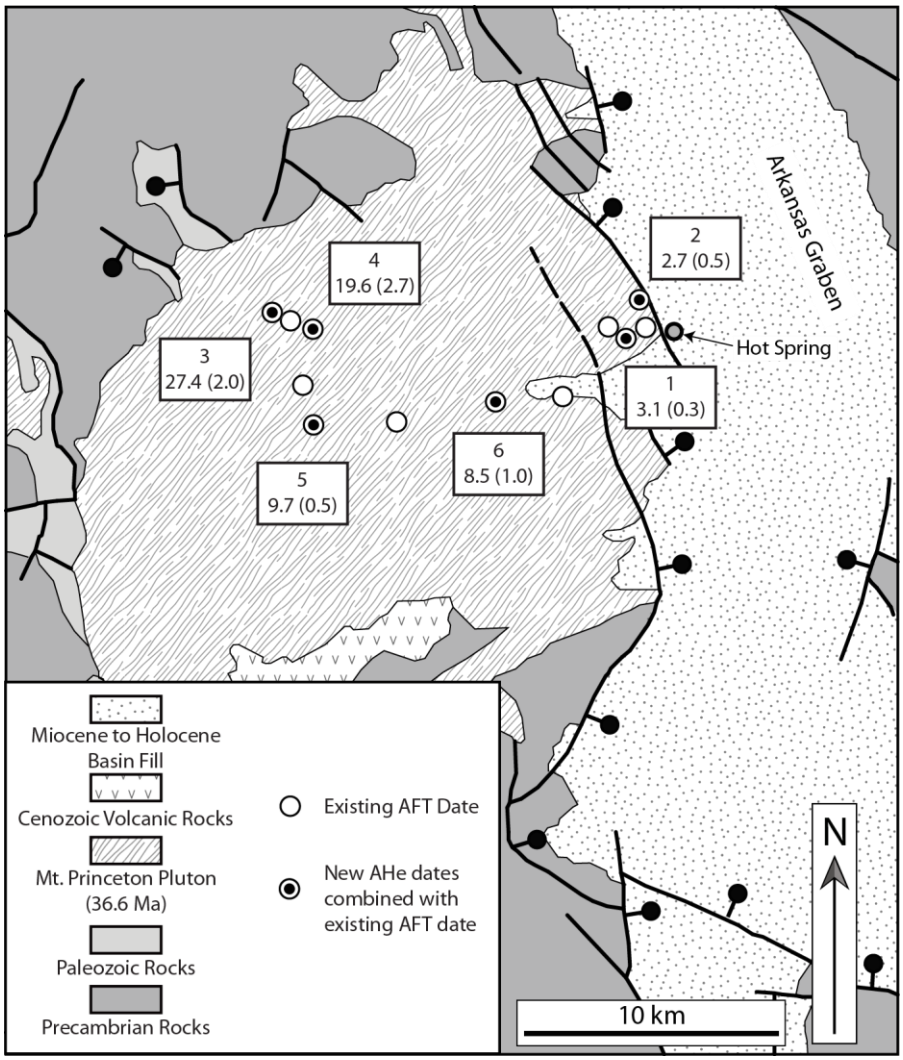

Figure 2. Simplified geologic map of the Mt. Princeton pluton in the Sawatch Range, Colorado. For each sample, sample numbers are shown on top, and the average AHe date (Ma) and 1σ standard deviation (in parentheses) are shown on the bottom.

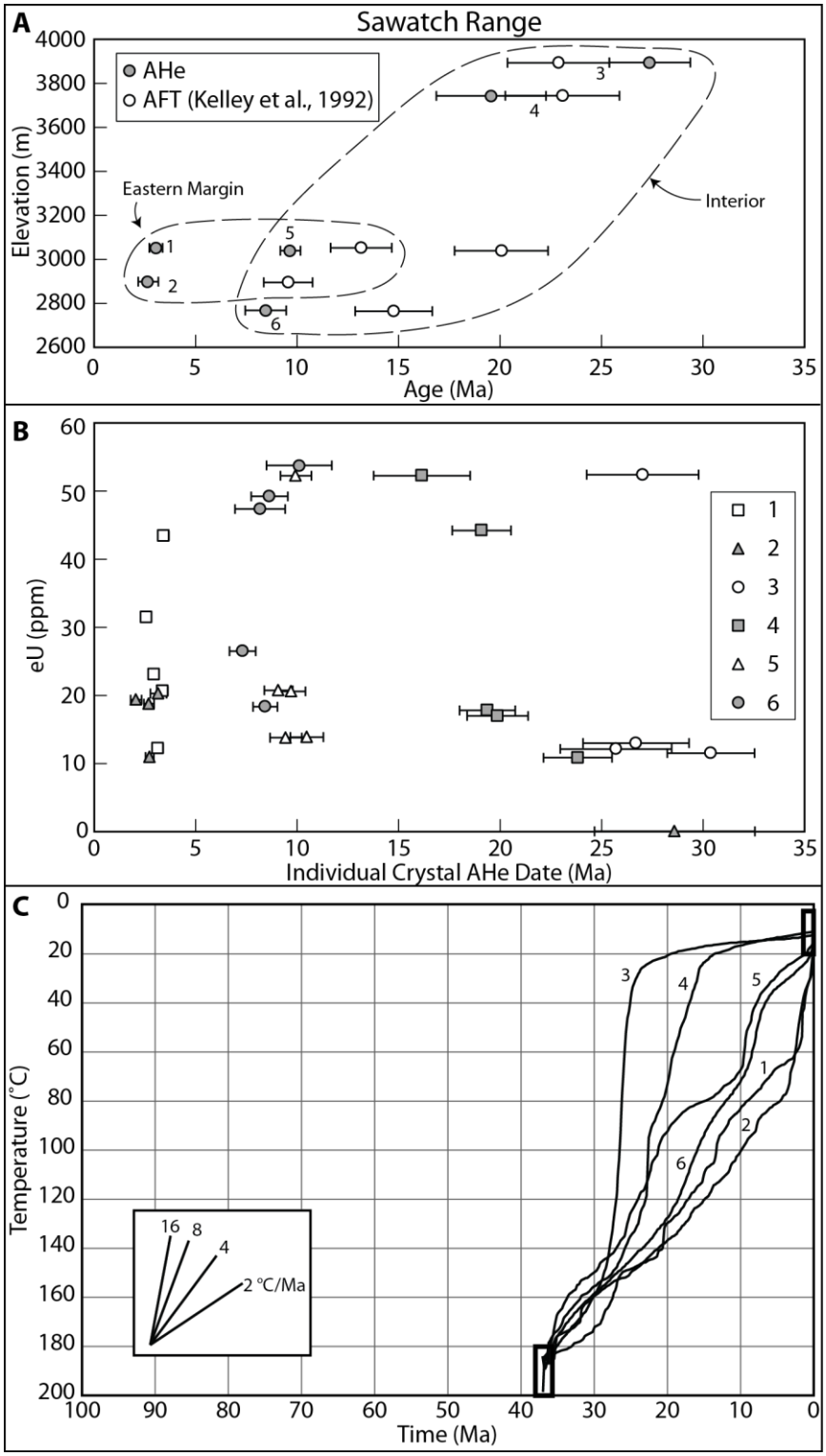

Figure 3. A. Age vs. elevation plot of AFT and AHe data from the Mt. Princeton pluton. **B.** AHe date vs. eU concentration. **C.** Weighted mean time-temperature history paths for samples from the Mt. Princeton pluton.

concentrations, possibly leading to the old age. The 243.5 Ma date and low eU of the anomalously old grain from sample 3 (Table DR1) suggests there might have been an unrecognized inclusion in this grain. For these reasons, these grains have been excluded and sample means and standard deviations are calculated from the remaining four AHe dates. Average sample ages from these six samples range from 2.7 ± 0.5 to 27.4 ± 2.0 Ma (Figs. 2, 3). All of the average AHe dates are younger than or overlap within error of the corresponding AFT ages, which range from 9.6 ± 1.2 to 23.1 ± 2.8 Ma (Kelley et al., 1992) (Fig. 3A). These samples generally have long mean track lengths, which is consistent with the observation that none of the samples show a correlation between individual crystal AHe age and eU concentration (Fig. 3B), suggesting that they cooled relatively rapidly through both the apatite partial annealing zone and the partial retention zone.

The oldest AHe ages from the Sawatch Range (samples 3 and 4) are from the interior of the pluton at high elevations (Figs. 2, 3B). Thermal history models for these two samples, including AFT data, indicate they were rapidly cooled to near-surface temperatures from ~28-16 Ma (Fig. 3C). Two additional samples (samples 5 and 6) are also from the interior of the pluton, but are at lower elevations, and record younger AHe ages of 9.7 ± 0.5 and 8.5 ± 1.0 Ma, respectively. Thermal history modeling of sample 5 suggests it experienced two stages of rapid cooling, from ~26-21 Ma and from ~10-7 Ma, which are separated by a period of slower cooling (Fig. 3C). Sample 6 shows a similar time-temperature history, but cooled at a slightly younger time, possibly because of its slightly lower surface elevation. The youngest AHe ages (samples 1 and 2) obtained in this study are from the eastern margin of the Mt. Princeton batholith in the immediate

footwall of rift-bounding normal faults along the western edge of the Arkansas basin (Fig. 2). When combined with available AFT data, thermal history models suggest that both of these samples experienced relatively slow cooling until ~5 Ma, when they were rapidly cooled to near-surface conditions (Fig. 3C).

All of the AFT and AHe ages are appreciably younger than the age of the Mt. Princeton batholith and cooling is interpreted to be due to tectonic denudation. The thermal history models of samples 3 and 4 at high elevations suggest rapid uplift/exhumation by ~28 Ma in the San Juan and Sawatch region. Although this early cooling is consistent with the rough estimate of 33-24 Ma based on ages of plutonic rocks (Chapin and Cather, 1994), lithospheric delamination and asthenospheric return flow that supported high topography during the late Oligocene may have also contributed to surface denudation recorded by the thermal history models (Karlstrom et al, 2012). The four samples from the pluton interior have AHe and AFT ages that show a good correlation with elevation (Fig. 3A), suggesting that these samples are from a relatively coherent structural block and that cooling occurred during exhumation of this block to shallow levels in the crust. The two-stage cooling history of mid-elevation rocks is best explained by punctuated opening of the Arkansas graben and uplift of the western rift flank in two pulses: A first pulse of uplift ~28-20 Ma may have been more regional, and the second pulse of rapid uplift beginning at ~15 Ma is interpreted to be rift related. The two samples along the eastern pluton margin have anomalously young AHe ages compared to the other four, with accelerated cooling beginning ~5 Ma. Although reheating of samples 1 and 2 due to fluid flux is possible, age-elevation relationships suggest erosional exhumation was responsible for cooling, even for samples potentially

reheated by geothermal activity. This is supported by the similar cooling rates of samples at high elevations from ~28-16 Ma as samples at low elevations from ~5 Ma to Recent (Fig. 3). The interpretation that this young cooling recorded in the AFT and AHe datasets is due to footwall uplift is supported by a series of east-dipping en echelon normal faults along the west side of the Arkansas graben that display Quaternary displacement (Ostenaa et al., 1982). When combined with the other samples, these data together suggest more or less continuous denudation of the Mount Princeton batholith since ~28 Ma. It is difficult to distinguish from this dataset between surface uplift due to regionally buoyant mantle above the San Juan mantle anomaly (Karlstrom et al., 2012) and rift flank uplift due to slip along normal faults, but the two-stage path of some samples (#5) suggests a tectonic lull or transition during the late Oligocene or early Miocene followed by formation of the Arkansas graben.

Sangre de Cristo Mountains

The San Luis basin is primarily an east-tilted half-graben bounded by the west-dipping Sangre de Cristo fault system that forms the basin boundary with the adjacent Sangre de Cristo Mountains footwall in Colorado and northern New Mexico (Figs. 1, 4). This range preserves Laramide-age reverse faults and is cut by numerous rift-related normal faults in the footwall of the main Sangre de Cristo fault zone (Wallace, 2004). Within the San Luis basin, Santa Fe Group rift fill deposits thicken eastward to ~6-7 km along the eastern edge of the basin north of Blanca Peak, and are ~2.5 km thick at the base of the Culebra Range in southern Colorado (Brister and Gries, 1994; Wallace, 2004).

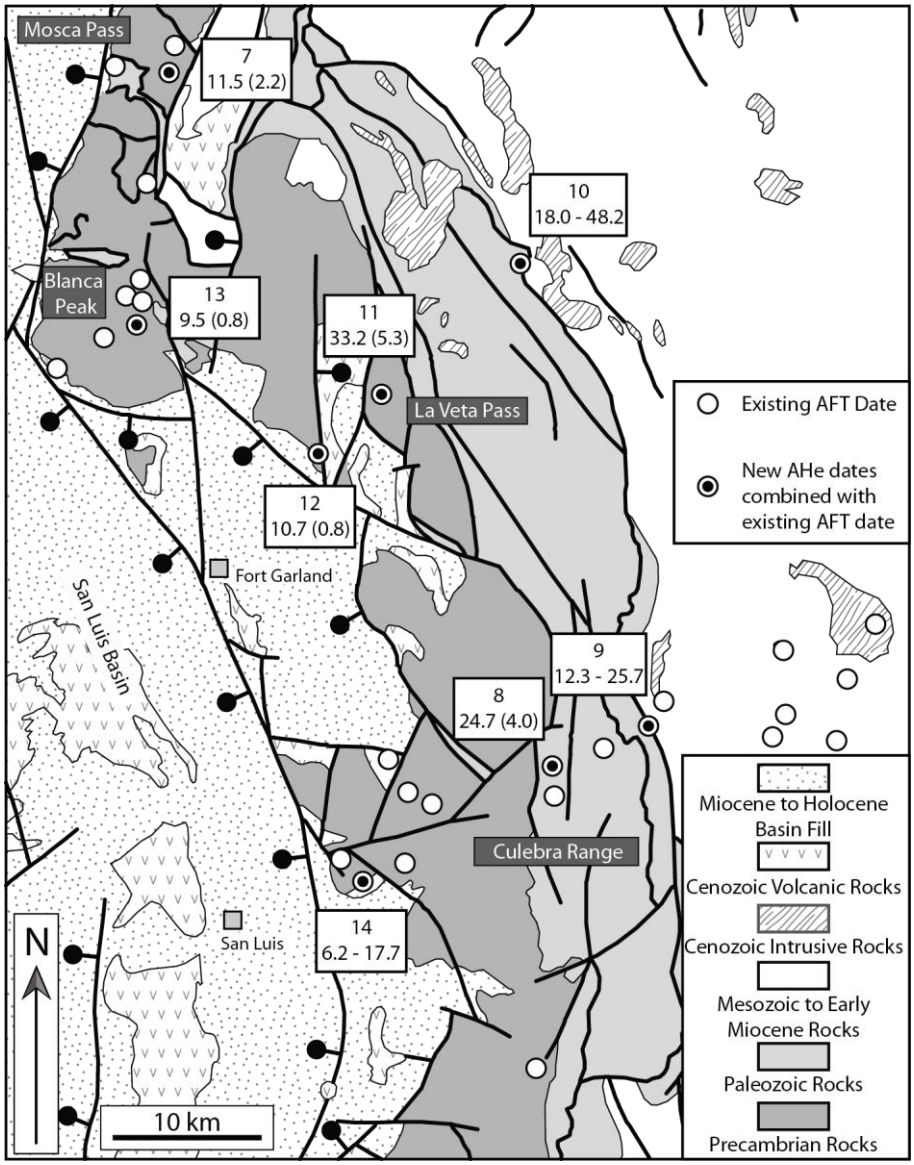

Figure 4. Simplified geologic map of the Sangre de Cristo Mountains along the eastern edge of the San Luis Basin in southern Colorado. For each sample the sample number is on top, average AHe ages (Ma) are shown with 1σ standard deviation (in parentheses) on bottom when single crystal analyses are <20% standard deviation, and the range of dates is given when single crystal dates are >20% standard deviation.

Forty single crystal AHe dates from eight samples were obtained from Mosca Pass, Blanca Peak, La Veta Pass, and the Culebra Range in the Sangre de Cristo Mountains and Culebra Range along the eastern edge of the San Luis basin in southern Colorado (Figs 1, 4). Three samples (11, 12, and 13) have a standard deviation less than 20%. Two samples (7 and 8) each contain one anomalously old AHe date, presumably from unrecognized inclusions, and these two ages have been excluded from average sample age calculations. The three remaining samples (9, 10, and 14) show a slight spread in age which correlates positively with eU (Fig. 5). Average sample AHe ages of these eight samples range from 9.5 ± 0.8 to 33.2 ± 5.3 Ma. Corresponding AFT ages range from 10.4 ± 1.3 to 38.9 ± 4.0 Ma (Kelley et al., 1992) (Fig. 4). At Mosca Pass and Blanca Peak, samples 7 and 13, respectively, both preserve relatively long track lengths, and individual AHe dates cluster within a narrow age range regardless of eU concentration. One sandstone sample from La Veta Pass (sample 11) also preserves long track lengths and doesn't show a correlation between AHe age and eU. Two additional samples from La Veta Pass, sample 10 a sandstone and sample 12 a gneiss, have slightly shortened track lengths (Kelley et al., 1992), but have consistent AHe dates regardless of eU concentration (Fig. 5B). At the southernmost location within the Culebra Range, none of the three samples (samples 8, 9, and 14) shows a spread in age that is related to eU concentration (Fig. 5B). Samples 8 and 14 show slightly shortened track lengths, while sample 9, a sandstone, preserves longer track lengths.

Thermal history models of each of these eight samples suggest variable cooling rates and times (Fig. 5C). AFT and AHe data from the two northernmost samples at Mosca Pass (sample 7) and Blanca Peak (sample 13) yield nearly identical thermal

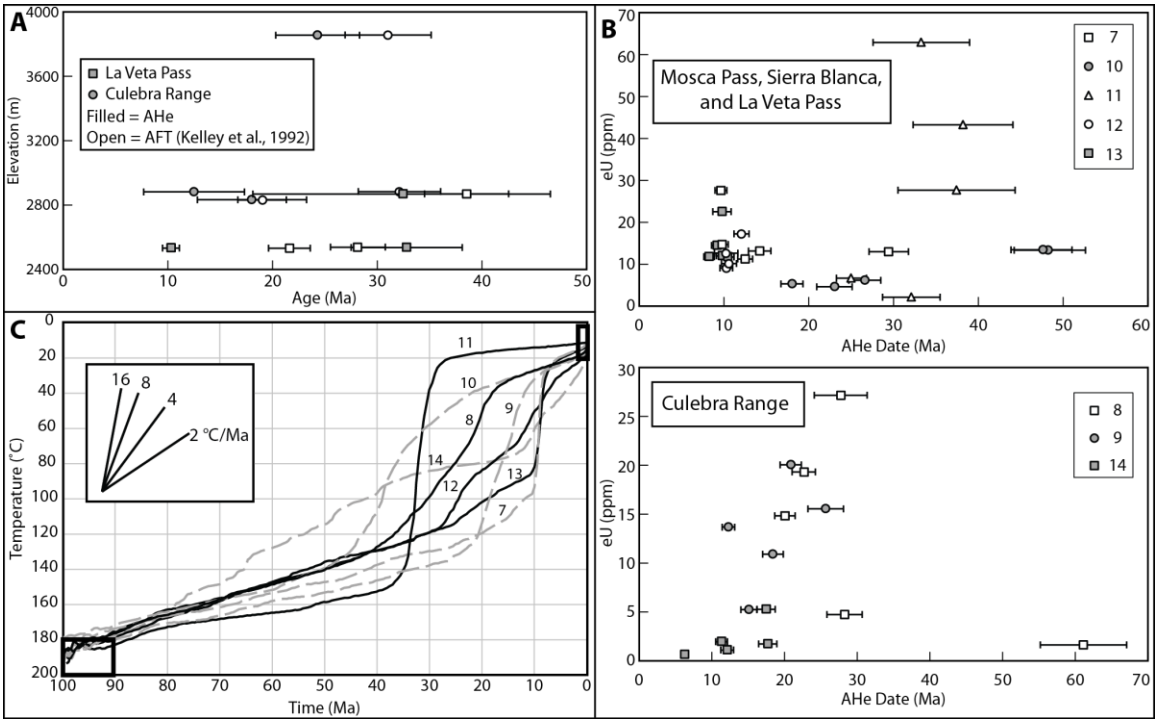

Figure 5. A. Age vs. elevation plot of AFT and AHe data from the southern Sangre de Cristo Mountains in Colorado. **B.** AHe date vs. eU concentration. **C.** Weighted mean time-temperature history paths.

histories, with rapid cooling to near-surface temperatures from ~10-8 Ma at both locations. At La Veta Pass, sample 10 at the highest elevation records a period of cooling from ~45-35 Ma, followed by slower cooling to the surface since 35 Ma. Samples 11 and 12 both lie at low elevations at La Veta Pass, but thermal history models suggest that they were exhumed to the surface at slightly different times. Sample 11 was rapidly cooled from high temperatures to near-surface temperatures from ~35-28 Ma, consistent with the long track lengths and no spread in AHe ages. Alternatively, thermal history modeling of sample 12 indicates two stage rapid cooling from ~26-22 Ma and ~14-7 Ma, separated by a period of slower cooling from ~22-14 Ma (Fig. 5C). At the southernmost location, thermal history modeling again suggests differential cooling of the Culebra Range. At the highest elevation, sample 8 cooled relatively quickly until ~17 Ma, followed by slow cooling to the surface. The two lower samples reside at approximately the same elevation, but on either side of the Culebra Range. On the eastern flank, thermal history modeling of sample 9 indicates that it cooled rapidly from ~23-12 Ma. On the western flank of the Culebra Range, thermal history modeling of sample 14 indicates a more complicated cooling history that includes a period of relative stability at ~80-90 °C from ~35-15 Ma, followed by rapid cooling to near-surface temperatures from ~15-0 Ma (Fig. 5).

Based on an unconformity separating Santa Fe Group sediments from underlying volcanic rocks, Wallace (2004) suggested that sedimentation and rifting in this part of the San Luis basin began ~25 Ma, while rifting in the northern part of the San Luis basin may have begun slightly earlier at ~27 Ma (Brister and Gries, 1994). However, as with the Sawatch Range, these observations are consistent with regional uplift and denudation

associated with the San Juan mantle anomaly and may not directly document fault-related exhumation associated with the rift. Santa Fe Group deposition at the base of the Culebra Range continued until at least 3.7 Ma, and an increasing percentage of Proterozoic clasts in these deposits are inferred to represent Miocene uplift of the basement-cored Culebra block (Wallace, 2004), consistent with ~20-12 Ma AFT cooling ages at Blanca Peak (Kelley et al., 1992). Geochemical and paleocurrent data from volcanic clasts within the Santa Fe Group at the base of the Culebra Range indicate that these sediments were sourced from the Thirtynine Mile volcanic field to the north (Fig. 1), suggesting that when rifting initiated ~25 Ma, the Culebra Range and Sangre de Cristo Mountains had not yet been uplifted as discrete rift flanks (Armstrong et al., 2013). Cooling paths from Mosca Pass, Blanca Peak, and the Culebra Range are consistent with this, and indicate rapid cooling younger than ~25 Ma. Cooling paths for two samples at La Veta Pass preserve times of older cooling, suggesting that at least some topographic relief and resulting denudation was attained in this area prior to the transport of rift sediments from the north and northeast. The young rapid cooling preserved at the base of the Culebra Range (sample 14) also indicates that uplift due to rifting has continued until very recent times, consistent with the Pliocene age of youngest Santa Fe Group deposits in this region. Sample 14 is also the most basinward sample in the Culebra Range in the immediate footwall of the Sangre de Cristo fault and in the hanging wall of other normal faults that cut the Culebra block. This young cooling age may reflect a basinward migration of faulting, which would have unloaded the eastern interior portions of the Culebra Range prior to the western margin that now lies adjacent to the San Luis Valley (Fig. 4). La Veta Pass is the only location where cooling older than ~25 Ma is evident. At

the highest elevation, sample 10 records a period of cooling (~45-35 Ma) that temporally coincides with a regional period of tectonic quiescence, but continued denudation. Rapid cooling of sample 11 prior to the onset of rifting at ~25 Ma was most likely accomplished during the same period of denudation following the Laramide orogeny. Subsequent cooling preserved in sample 12 is interpreted to reflect continued normal faulting, which dropped sample 11 to lower elevations after it had cooled to near-surface conditions. Overall, this dataset is similar to the Arkansas basin, suggesting relatively continuous unroofing from ~25 Ma to Recent. This cooling may also be the result of regional late Oligocene uplift and cooling above the San Juan mantle anomaly (Karlstrom et al., 2012) which transitioned into more punctuated cooling along rift flanks as the San Luis basin opened.

Nacimiento Mountains

The Nacimiento Mountains are a north-trending range cored by Precambrian rocks along the western edge of the Rio Grande rift in northern New Mexico (Fig. 1). The range is bounded along its western edge by the east-dipping Laramide Nacimiento reverse fault zone that was active through the Eocene (e.g. Baltz, 1967; Woodward, 1983, 1987). Based on unconformities within sedimentary rocks shed from the Nacimiento uplift as well as structures within the uplift, Baltz (1967) suggested that vertical displacement along the Nacimiento fault increases from south to north such that the northern part of the uplift may have been exhumed to near-surface levels prior to the southern end. This interpretation is supported by AFT ages of 88 ± 1 to 46 ± 7 Ma for the northern part, compared to AFT ages of 46 ± 5 to 33 ± 4 Ma for the southern part of the uplift (Kelley et al., 1992).

Ten single-crystal AHe dates were obtained from two samples in the Nacimiento Mountains (samples 15 and 16). Five single-crystal AHe ages from a Permian siltstone from the northern Nacimiento Mountains (sample 16) are within 20% standard deviation, and give an average AHe age of 66.5 ± 13.4 Ma, which is very similar to this sample's reported AFT age of 65.9 ± 3.9 Ma (Kelley et al., 1992). This sample shows a positive correlation between AHe age and eU (Fig. 6), and also shows a bimodal distribution in fission-track lengths. Individual AFT grain ages for this sample fail the Chi-square test, indicating that it contains multiple age populations (Kelley et al., 1992). Sample 15 is from a Proterozoic granite from the southern part of the range, and individual grain AHe dates from this sample range from 85.4 to 353.5 Ma (Table DR1, Fig. 6), all of which are significantly older that the sample's AFT age of 39.4 ± 3.0 Ma (Kelley et al., 1992). Individual grains from this sample don't display a large variation in eU, so any possible relationship between AHe age and eU is not observed (Fig. 6), and the sample also preserves relatively long track lengths that show a unimodal distribution (Kelley et al., 1992). Apatites obtained for AHe dating are typically assumed to have a homogenous distribution of U and Th, and this assumption can lead to erroneous AHe dates for grains which are zoned. The discrepancy between AFT and AHe dates for sample 15 may be an effect of eU zonation.

A thermal history model is not presented for sample 15 because neither good nor acceptable paths were obtained from HeFTy using the available AHe and AFT data. This sample passes the Chi-square test and retains long track lengths such that the fission-track data indicate it was completely reset during burial. Because no acceptable paths are found when combining these AFT data with new AHe data, differences in eU or grain size most

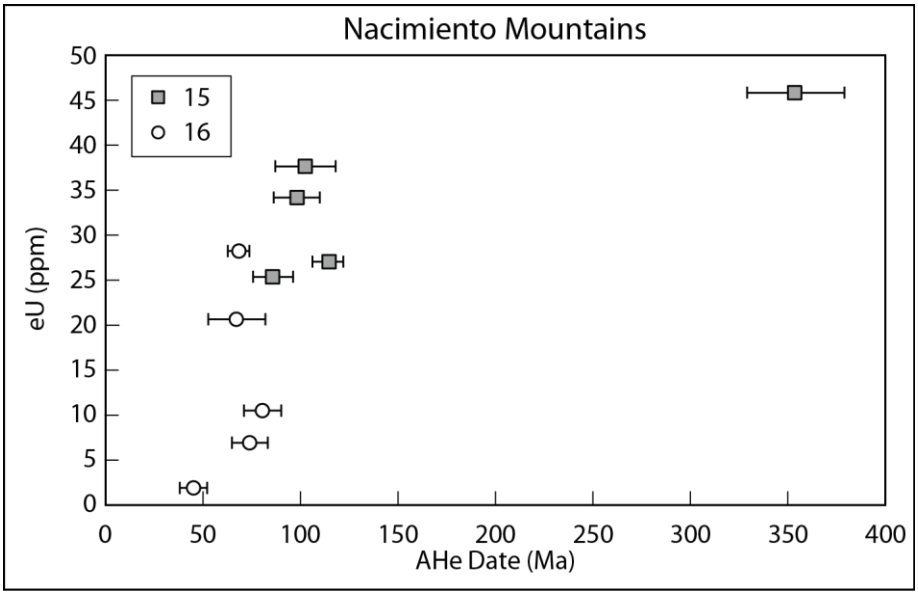

Figure 6. AHe date vs. eU concentration for two samples from the Nacimiento Mountains.

likely do not explain the older AHe dates. Alternatively, as pointed out by Flowers and Kelley (2011), potential causes of such dispersion could be a strong zonation of eU within the grain, He implantation from neighboring grains, or U-Th rich micro-inclusions that were not detected during the picking process. Sample 16 contains multiple AFT age populations and a correlation between AHe age and eU, suggesting that the grains most likely contain inherited damage and were not completely reset during burial. These two samples from the Nacimiento uplift both preserve Laramide-age AFT and AHe dates, suggesting that this range has experienced little or no denudation due to uplift and deformation during development of the Rio Grande rift.

Albuquerque Basin

The Albuquerque basin in central New Mexico is one of the largest basins in the Rio Grande rift. Structurally this basin is bounded on almost all sides by normal faults, and it is composed of multiple sub-basins (Fig. 7). The northern Albuquerque sub-basin is an east-tilted half-graben where Santa Fe Group strata dip towards the master west-dipping normal faults that form the western edge of the Sandia Mountains. The geometry of the southern Belen sub-basin is more complicated, but generally it is a west-dipping half-graben where Santa Fe Group strata dip towards a master east-dipping normal fault system at the base of the Sierra Ladrones uplift (Grauch and Connell, 2013). Russell and Snelson (1994) and Lewis and Baldridge (1994) proposed that a narrow NE-trending accommodation zone separates these two oppositely-dipping half-grabens, but an integration of diverse geophysical datasets suggests that a discrete structure does not extend across the Albuquerque basin (Grauch and Connell, 2013). Instead an oblique anticlinal accommodation zone crosses the basin (Fig. 7) (Faulds and Varga, 1998;

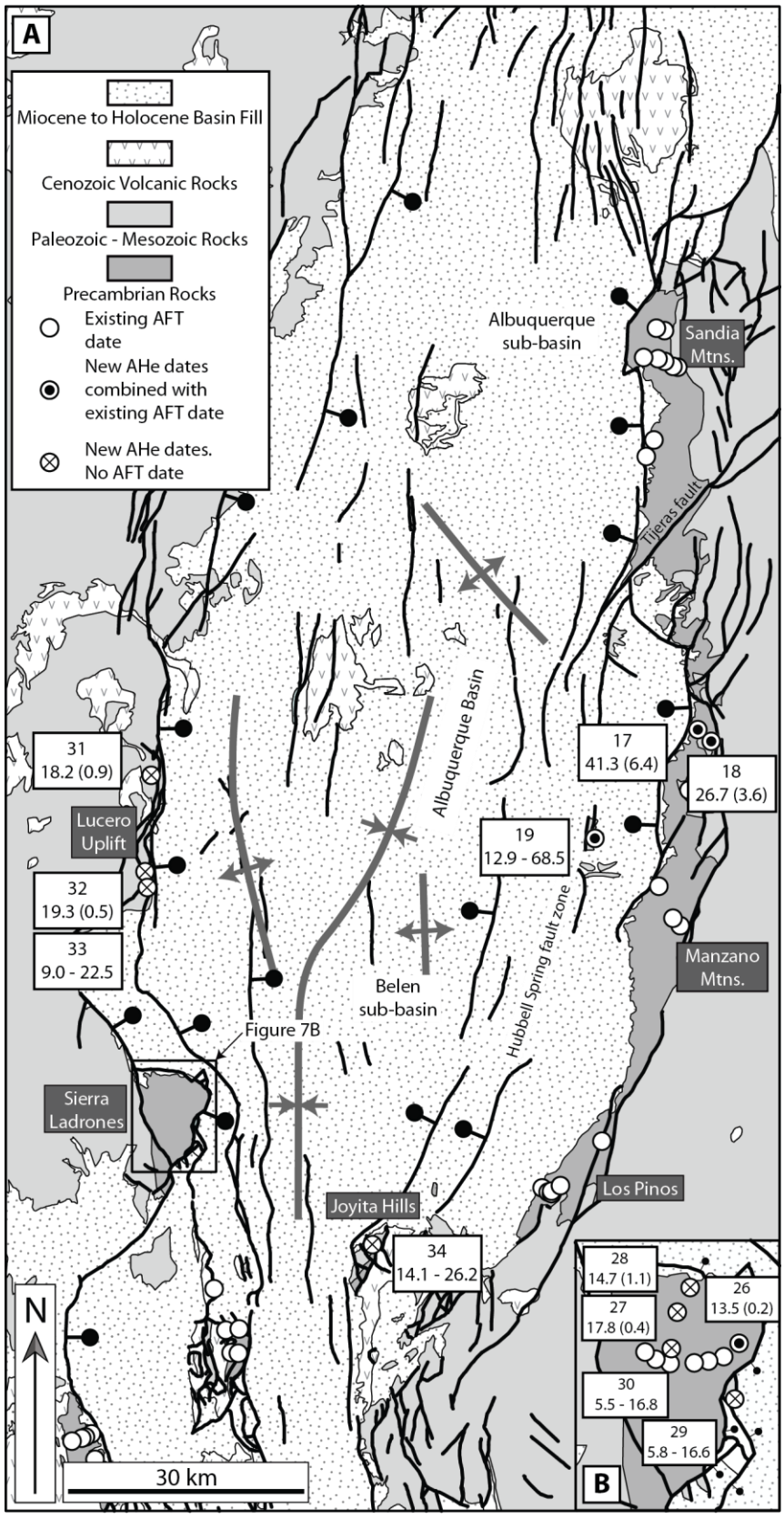
A
Miocene to Holocene Basin Fill
Cenozoic Volcanic Rocks
Paleozoic - Mesozoic Rocks
Precambrian Rocks
Existing AFT date
New AHe dates combined with existing AFT date
New AHe dates. No AFT date
Albuquerque sub-basin
Sandia Mtns.
Tijeras fault
Albuquerque Basin
31
18.2 (0.9)
Lucero Uplift
32
19.3 (0.5)
33
9.0 - 22.5
17
41.3 (6.4)
18
26.7 (3.6)
19
12.9 - 68.5
Hubbell Spring fault zone
Manzano Mtns.
Belen sub-basin
Figure 7B
Sierra Ladrones
Joyita Hills
34
14.1 - 26.2
Los Pinos
N
30 km
28
14.7 (1.1)
26
13.5 (0.2)
27
17.8 (0.4)
30
5.5 - 16.8
29
5.8 - 16.6
B

Figure 7. A. Simplified geologic map of the Albuquerque Basin. For each sample with new AHe dates, the sample number is on top, and average AHe ages (Ma) are shown with 1σ standard deviation (in parentheses) on bottom when single crystal analyses are <20% standard deviation. The range of dates is given when single crystal dates are >20% standard deviation. Anticline and syncline symbols show the structure of Santa Fe Group deposits, from Grauch and Connell (2013). **B.** Close-up of the Sierra Ladrones range and locations of new AHe dates.

Grauch and Connell, 2013). Initial extension in the Albuquerque basin is poorly constrained due to a lack of exposures of lower Santa Fe Group rocks. Ingersoll and Yin (1993) suggested that extension initiated during Miocene time, but a basalt flow at the base of the Santa Fe Group sediments in the northern part of the basin that yields an 40Ar/39Ar age of 25.41 ± 0.32 Ma suggests that extension was beginning by this time (Connell, 2004). Based on sedimentary deposits above and below dated volcanic rocks in the Santa Fe Group, sedimentation rates in the Albuquerque basin dramatically increased after ~16 Ma and continued through the late Miocene (Chapin and Cather, 1994).

The Sandia Mountain block in the Albuquerque basin is one of two locations in the Rio Grande rift for which AHe data have previously been published (House et al., 2003). Reported average AHe ages from the Sandia Mountains range from 12.9 ± 0.9 to 18.5 ± 1.3 Ma, and coupled with additional AFT ages, these data indicate that this rift flank was exhumed to near-surface levels from ~22-13 Ma (House et al., 2003). This period of rapid cooling was most likely associated with rapid slip along main rift-bounding normal faults along the western edge of Sandia uplift.

To complement these results from the Sandia Mountains, 44 individual aliquot AHe ages from 13 samples were obtained from the Manzano Mountains, the Sierra Ladrones, the Lucero Uplift, and the Joyita Hills flanking the Albuquerque basin (Figs. 1,

6). Many of these are single-crystal ages, but several aliquots contained three apatite crystals in a single Pt tube (Table 1).

Manzano Mountains

The Manzano Mountains are part of the same rift flank as the Sandias, but they dominantly record pre-rift cooling episodes. Fifteen single grain AHe dates from three samples were obtained from the Manzano Mountains (Fig. 7). Two of these samples (17 and 18) are from the Manzano uplift, and give average AHe ages of 41.3 ± 6.4 Ma and 26.7 ± 3.6 Ma, respectively (Fig. 7). Neither of these two samples shows a spread in AHe date that correlates with eU (Fig. 8A), and the average AHe dates for each of these samples are very similar to reported AFT ages of 38.8 ± 4.3 Ma and 28.5 ± 2.9 Ma (Kelley et al., 1992), respectively. The third sample (19) is a Permian siltstone from the Hubbell Bench, a shallow structural bench in the Albuquerque basin that was downfaulted from higher levels and subsequently covered with Santa Fe Group rift fill sediments. Individual AHe dates for this sample range from 12.9 - 68.5 Ma (Table DR1; Fig. 8), compared to the sample's reported AFT age of 47.7 ± 5.5 Ma (Kelley et al., 1992). The spread in AHe ages show an inverse relationship with eU concentrations, where the highest eU grains are also the oldest. The two oldest grains, therefore, were not used in thermal history modeling. Track lengths in this sample show a slightly bimodal distribution, with an average length of 13.2 ± 0.5 μm (Kelley et al., 1992).

Thermal history modeling suggests that sample 17 cooled rapidly from ~48-38 Ma, consistent with its Eocene AHe dates and relatively long track lengths. Sample 18, which is at a slightly lower elevation, cooled rapidly from ~33-23 Ma (Fig. 8). Sample 19 within the Hubbell Bench preserves a slightly more complicated cooling history,

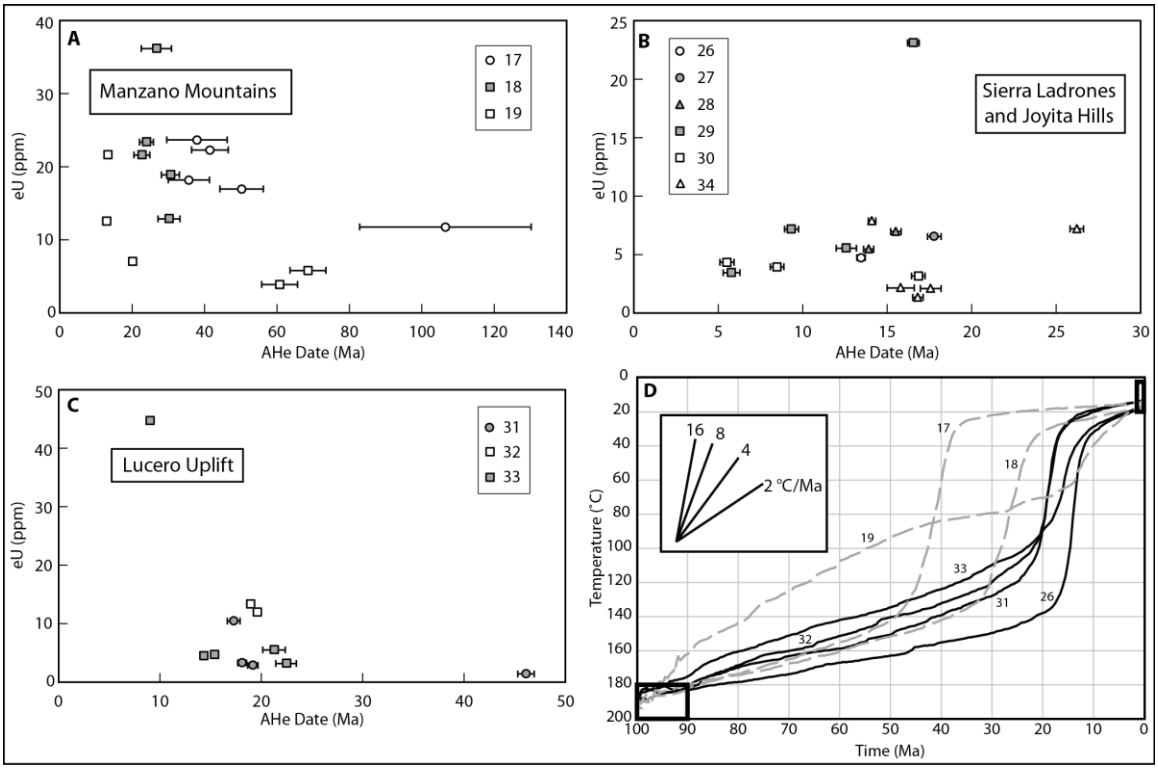

Figure 8. AHe date vs. eU concentration for samples in the **A.** Manzano Mountains, **B.** Sierra Ladones and Joyita Hills, and **C.** Lucero Uplift. **D.** Weighted mean time-temperature history paths from samples in the Albuquerque Basin.

involving slow cooling until ~14 Ma, followed by rapid cooling from ~14-5 Ma to near-surface temperatures (Fig. 8D). These observations are consistent with the spread in AHe dates and the shortened track lengths.

Although normal faults with Quaternary displacement bound the western edge of the Manzano Mountains (Personius et al., 1999), this uplift is typically thought of as residing along the relatively passive margin of the southern Belen sub-basin (Fig. 7). Uplift prior to development of the Albuquerque basin is evident by the west-dipping, Laramide-age Montosa fault, which lies along the eastern edge of the Manzano Mountains and displays reverse-sense movement. AFT data from the Manzano Mountains range from 20.1 ± 4.8 to 47.7 ± 5.5 Ma, and high elevation samples record earlier cooling that is attributed to uplift during the Laramide orogeny followed by slow denudation of the fault block (Kelley et al., 1992). Thermal history modeling of sample 17, the highest elevation of the three investigated in this study, is consistent with denudation following uplift during the waning stages of the Laramide orogeny ~45 Ma in central New Mexico. Sample 18 remained at higher temperatures until ~33 Ma, potentially records a component of Oligocene regional uplift and/or continued denudation, and was largely exhumed to the surface by the time of initial fault-related denudation in the Albuquerque basin at ~25 Ma. Within the Hubbell Bench, sample 19 resided within the AFT partial annealing zone and AHe partial retention zone for prolonged periods of time, before rapid cooling to the surface at ~14 Ma. This slow cooling is most likely indicative of slow erosion and denudation, similar to sample 18. The rapid cooling coincides with development of the Albuquerque basin and extensional faulting, and most likely was accomplished through relatively young normal fault slip

along the Hubbell Spring fault zone after this structural block had been downdropped to lower elevations (Fig. 7A). In this way the structural block may have remained at elevated temperatures until normal faults migrated basinward. This structural narrowing and basinward migration of normal faulting is supported by trenching studies across the Hubbell Springs fault zone which document rupture events as young as ~12 ka (Personius and Mahan, 2003).

Sierra Ladrones and Joyita Hills

Eleven AHe dates from five samples were collected from the Sierra Ladrones Mountains along the southwest edge of the Albuquerque basin (Figs. 7, 8). Four samples were collected from Precambrian granitic rocks located in the footwall of the Jeter fault, the main rift-bounding normal fault in this part of the basin. The fifth sample (sample 29) was collected in the immediate hanging wall of the Jeter fault. Individual aliquot AHe dates for this location range from 5.5 ± 0.4 Ma to 17.8 ± 0.4 Ma (Table 1; Figs. 7, 8B). Only one of these samples (sample 26) has a corresponding published AFT age (14.1 ± 2.0 Ma; Kelley et al., 1992), which is very similar to the sample's AHe date of 13.46 ± 0.2 Ma (Table DR1). Published AFT ages for the Sierra Ladrones range from 9.0 ± 1.5 to 32.2 ± 11.9 Ma and preserve long track lengths that display unimodal histograms (Kelley et al., 1992). Five single crystal AHe dates were obtained from one sample of Triassic sandstone in the Joyita Hills, and individual AHe dates range in age from 14.1 ± 0.2 to 26.2 ± 0.4 Ma (Table 1; Figs. 7, 8). These dates are similar to reported AFT ages from underlying granitic rocks in the Joyita Hills that range from 22.0 ± 3.1 to 26.8 ± 4.7 Ma (Kelley et al., 1992). None of the samples from the Sierra Ladrones or Joyita Hills show a

positive correlation between AHe data and eU, although eU concentrations for each of these samples is relatively low (Fig. 8B).

Thermal history modeling was performed on only one of the samples collected from the Sierra Ladrones (sample 26), and the results indicate that this structural block was rapidly cooled from ~18-10 Ma (Fig. 8D). Although other samples from the Sierra Ladrones weren't modeled, the clustering of AHe dates from ~20-10 Ma is also consistent with rapid cooling through the AHe partial retention zone. Similarly, although AHe dates from the Joyita Hills show a slight spread, when coupled with AFT ages these data suggest rapid cooling to near-surface temperatures ~25-15 Ma (Fig. 8B).

The Sierra Ladrones uplift is bounded on three sides by normal fault systems (Fig. 7B). The most prominent of these faults is the low-angle (~15-25° dipping) Jeter fault along the eastern margin, which separates Precambrian granitic and metamorphic rocks in the footwall from Paleozoic and Mesozoic rocks, as well as Santa Fe Group rift fill in the hanging wall. Oligocene-age volcanic rocks that were derived from the southern Mogollon-Datil volcanic field crop out along the northern and eastern sides of the Sierra Ladrones, indicating that the significant topography that is associated with this range today did not exist during the Oligocene (Kelley et al., 1992). Published Miocene AFT ages that define an age-elevation transect corroborates this interpretation, as does the thermal history model of sample 26. The Joyita Hills preserve a long and complex structural history, including deformation related to the ancestral Rocky Mountains, the Laramide orogeny, and the Rio Grande rift (Beck and Chapin, 1994), but published AFT ages of ~22-27 Ma (Kelley et al., 1992) and new AHe data presented here suggest that this structural block did not reach near-surface conditions until the early Miocene.

The observations presented above support a model where uplift and exposure of the Sierra Ladrones is due to rapid slip along the east-dipping Jeter fault, as proposed by previous authors (e.g. Kelley et al., 1992; Lewis and Baldridge, 1994; May and Russell, 1994; Russell and Snelson, 1994). The thermal history model incorporating AFT and AHe data further constrain this interpretation, and suggest that the Jeter fault rapidly exhumed this structural block from ~18-10 Ma, consistent with rapid sedimentation rates in the basin beginning ~16 Ma (Chapin and Cather, 1994). Although the Joyita Hills lie along the eastern flank of the Albuquerque basin, AHe and AFT ages from this region are more similar to cooling ages in the Sierra Ladrones than to cooling ages in the Manzano Mountains.

Lucero Uplift

The Lucero Uplift is part of the west flank of the Albuquerque basin north of Ladron peak that is west of the antithetic anticlinal accommodation zone of the central Albuquerque basin. The east side of the uplift is delineated by a narrow zone of deformation that separates relatively undeformed rocks of the Colorado Plateau on the west from Santa Fe Group basin fill on the east (Figs 1, 7). The uplift preserves deformation related to multiple geologic events, including Laramide-age reverse faults and folds that have been overprinted by normal faults related to the development of the Rio Grande rift (Callender and Zilinski, 1976; Lewis and Baldridge, 1994). Today the main rift-bounding normal fault is the east-dipping Santa Fe fault, which separates Paleozoic and Mesozoic rocks from Santa Fe Group sediments in the Albuquerque basin. Due to its relatively subdued topography compared to other uplifts in the Albuquerque basin, no thermochronologic data have yet been published from this location.

Eleven individual AHe dates were obtained from three samples of Precambrian granitic and Pennsylvanian sedimentary rocks in the Lucero Uplift along the western margin of the Albuquerque basin (samples 31, 32, and 33; Figs. 7, 8). Excluding one anomalously old grain, AHe dates from the Lucero Uplift cluster within a relatively narrow range from 9.0 ± 0.3 to 22.5 ± 1.0 Ma. A correlation between AHe age and eU concentration is not observed for any of the three samples (Table 1; Fig. 8C). Thermal history models were obtained for each of these three samples using only AHe constraints. As seen in Figure 8D, the results from each of these samples are nearly identical, and suggest that much of the Lucero Uplift was rapidly cooled as it was exhumed to near-surface levels in the crust ~21-15 Ma (Fig. 8D).

The AHe dates and cooling histories of the three samples obtained from the Lucero Uplift are very similar to the cooling history of the Sierra Ladrones to the south (Fig. 8), and suggest that the entire western flank of the Albuquerque basin was constructed during the growth of the Albuquerque basin. These results are similar to the ~22-13 Ma rapid cooling of the Sandia block on the eastern rift flank (House et al., 2003), but strikingly different than results from the Manzano Mountains of the eastern rift flank. These results support the interpretation by Grauch and Connell (2013) that the Tijeras fault is not a major structure that extends across the entire Albuquerque basin, and that the Lucero Uplift was predominantly exhumed to the surface through slip along the Santa Fe fault.

Southern Rio Grande Rift

South of the Albuquerque basin in central New Mexico, the Rio Grande rift widens into a broad zone that is physiographically more similar to the adjacent southern

Basin and Range Province. In this region of southern New Mexico, extension is distributed across multiple basins, including the Palomas, Jornada, Tularosa, Mimbres, and Mesilla basins (Fig. 1). Although physiographically similar to the Basin and Range, a semi-linear southward extension of the Rio Grande rift can still be distinguished by deeper basins, more active Quaternary volcanism and faulting, and higher heat flow relative to other parts of the southern Basin and Range (Seager and Morgan, 1979; Keller et al., 1990; Mack, 2004). To complement the existing AFT data within this region (Kelley and Chapin, 1997), a total of 30 single crystal AHe dates from six samples were obtained in the Black Range, the Organ Mountains, the San Andres Mountains, and Sierra Blanca (Fig. 1).

Black Range

The Black Range is a north-trending range on the southeastern margin of the Eocene-Oligocene Mogollon-Datil volcanic field (Fig. 1). Much of the Black Range consists of the remnants of the Emory caldera, which erupted the voluminous ~35 Ma Kneeling Nun Tuff (McIntosh et al., 1992). Subsequent deformation related to the Rio Grande rift produced east-dipping normal faults that bound the eastern edge of the uplift, which shed alluvial fan deposits into the Palomas basin during evolution of the rift. Although the oldest basin deposits are concealed, younger deposits interbedded with volcanic rocks indicate a major pulse of deformation during the Latest Miocene to Pliocene (Mack, 2004).

Five single crystal AHe dates from one sample (sample 20) were obtained from a dacite that is part of the ~74-75 Ma Copper Flat stratovolcano and associated intrusions (McLemore et al., 2000). The remnants of this stratovolcano are exposed on the Animas

horst along the eastern edge of the Mogollon-Datil volcanic field in southern New Mexico (Fig 1). Excluding one anomalously old grain, the remaining four dates give an average sample AHe date of 48.1 ± 3.3 Ma, and individual AHe dates do not display a spread related to eU concentration (Fig. 9). The sample has an AFT age of 63.7 ± 4.5 Ma, and track lengths display a slightly bimodal distribution (Kelley and Chapin, 1997).

Thermal history modeling of this sample indicates that it underwent a multi-stage cooling history. Initial relatively rapid cooling lasted until ~60 Ma, followed by relative stability from ~60-50 Ma. A final pulse of rapid cooling from ~50-40 Ma brought the sample to near-surface temperatures (Fig. 9).

Cooling of this sample overlaps temporally with Laramide-age compression, suggesting that the multi-stage cooling recorded in the AFT and AHe data is most likely due to differential slip rates along Laramide reverse faults in the region. Even though this sample is from the margin of the 35-25 Ma Mogollon-Datil volcanic field, it records no Oligocene cooling, and was apparently never buried beneath sufficient volcanic cover to reset the AFT or AHe ages.

San Andres and Organ Mountains

The San Andres and Organ Mountains are a north-trending, west-tilted structural block separating the Jornada basin to the west from the Tularosa basin to the east (Fig. 1). This range is bounded on the east by east-dipping normal faults, which down drop the west-tilted Tularosa basin. The San Andres Mountains are composed of Precambrian igneous and metamorphic rocks capped by Paleozoic sedimentary rocks. To the south, the Organ Mountains are primarily made up of silicic plutonic and volcanic rocks that make up the Organ caldera complex (e.g. Zimmerer and McIntosh, 2013), which lies along the

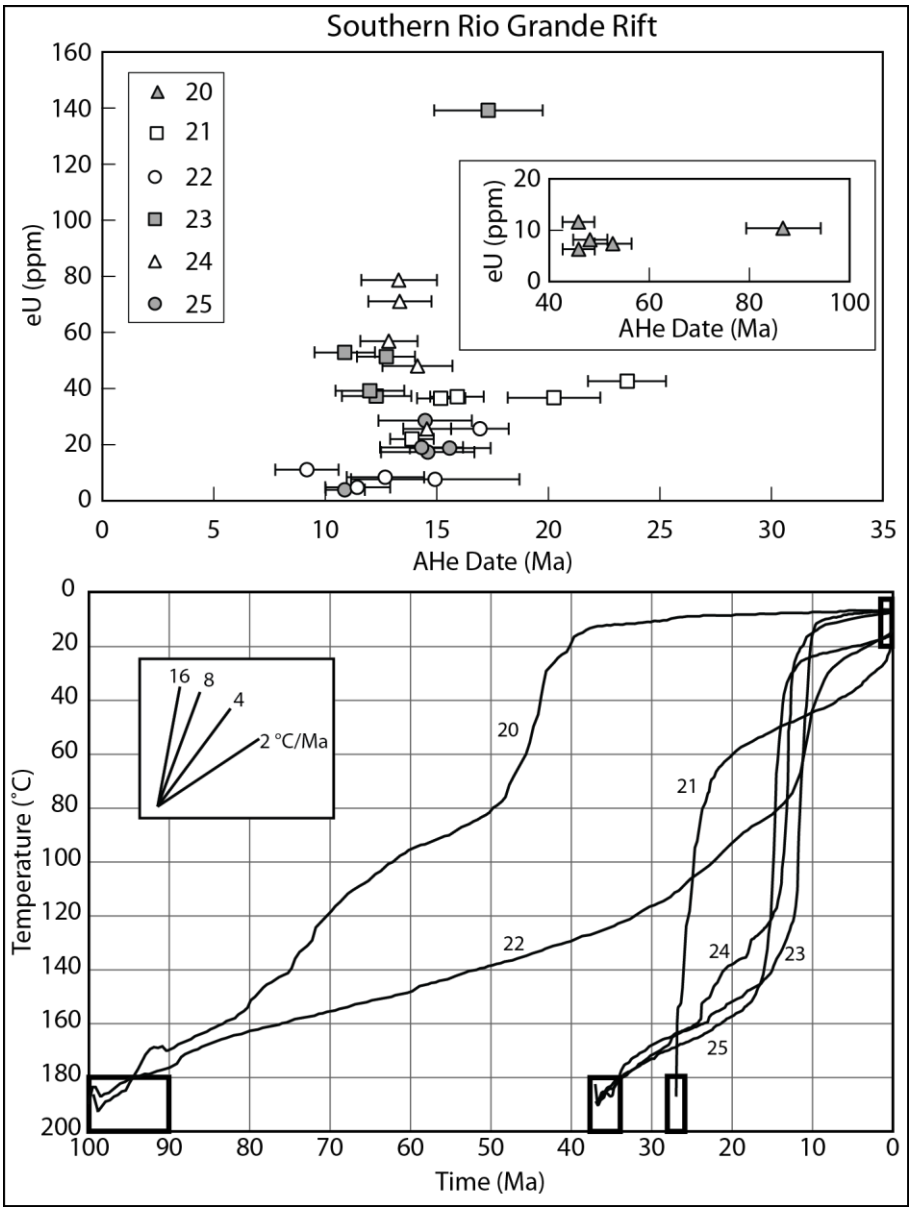

Figure 9. A. AHe date vs. eU concentration from samples in the southern Rio Grande rift. Inset graph is data from the Black Range. **B.** Weighted mean time-temperature history paths from samples in the southern Rio Grande rift.

eastern extent of the Mogollon-Datil volcanic field. The Organ caldera complex erupted three ignimbrite packages between ~36.5 and 36.0 Ma, and postcaldera plutons were emplaced between ~36.0 and 34.3 Ma (Zimmerer and McIntosh, 2013). Combined gravity and well data in the Tularosa basin reveal that maximum sediment thicknesses occur just east of the San Andres and Organ Mountains, and the thick sediment accumulations suggest that this basin has been active at least since the Miocene (Mack, 2004).

Five single crystal AHe dates from one sample (sample 22) were obtained from the San Andres Mountains (Table DR1; Fig. 9). Individual AHe dates range from 9.2 ± 1.4 to 16.9 ± 1.3 Ma, compared to a published AFT age of 21.8 ± 4.5 Ma (Kelley and Chapin, 1997). AHe dates show little correlation with eU concentrations. No fission-track length data are available for this sample. To the south, 15 individual AHe dates were obtained from three samples (samples 23, 24, and 25) in the Organ Mountains (Table DR1; Fig. 9). Average sample AHe dates for each of these three samples are 13.0 ± 2.5 Ma, 13.6 ± 0.7 Ma, and 14.0 ± 1.8 Ma, compared to reported AFT ages of 10.3 ± 1.4 Ma, 13.7 ± 1.4 Ma, and 13.8 ± 1.6 Ma, respectively (Kelley and Chapin, 1997). Individual AHe dates show very little variation, despite an eU span from 3.9 to 139.0 ppm (Table 1; Fig. 9).

Thermal history modeling of sample 22 in the San Andres Mountains suggests that this sample was rapidly cooled from ~15-8 Ma (Fig. 9). Similarly, thermal history modeling of three samples in the Organ Mountains suggests that they all experienced near-identical thermal histories, involving slow cooling that lasted until ~17 Ma,

followed by a period of rapid cooling from ~17-10 Ma, when they were cooled to near-surface temperatures (Fig. 9).

The nearly identical cooling histories from samples in the San Andres and Organ Mountains indicate that these ranges behaved as a relatively coherent structure during cooling. The ~36 Ma Organ Mountains are considered part of the Mogollon-Datil volcanic field (McIntosh et al., 1992); however, the cooling ages in both ranges post-date heating and cooling due to magmatism. For example, the samples collected from Eocene volcanic rocks in the Organ Mountains all display a period of slow cooling after emplacement (Fig. 9). The abrupt shift towards rapid cooling from ~17-10 Ma in the Organ Mountains and ~15-8 Ma in the San Andres Mountains therefore most likely reflects fault-related uplift and exhumation along the east-dipping normal faults that bound the western edge of the Tularosa basin, consistent with this portion of the basin containing the thickest sediment accumulations.

Sierra Blanca

Sierra Blanca represents the northern extent of the north-trending Sacramento Mountains along the eastern edge of the Tularosa basin (Fig. 1). Structurally, this range is bounded along the western edge by the west-dipping Alamogordo fault. While the Sacramento Mountains are an east-tilted block composed of various Precambrian lithologies overlain by Paleozoic strata (Pray, 1961), Sierra Blanca primarily consists of late Eocene-Oligocene plutonic and volcanic rocks that overlie and intrude Paleozoic, Cretaceous and Paleocene sedimentary rocks (Thompson, 1972). Although the Sacramento Mountains preserve AFT ages that range from 35.4 ± 8.3 Ma to 112.7 ± 25.3 Ma (Kelley and Chapin, 1997), analysis of fault scarps along the Alamogordo fault

indicates multiple Quaternary rupture events (Koning and Pazzaglia, 2002). In contrast to the Sacramento Mountains, published AFT ages for the Sierra Blanca igneous complex range from ~24-33 Ma (Kelley and Chapin, 1997).

Five single crystal AHe dates were obtained from the Three Rivers Stock at Sierra Blanca (Fig. 9) (sample 21). 40Ar/39Ar dates of the Three Rivers Stock indicate that it was emplaced ~27 Ma (Goff et al., 2011). Individual AHe dates range from 13.9 ± 1.0 Ma to 23.5 ± 1.8 Ma, compared to the sample's reported AFT age of 23.8 ± 2.6 Ma (Kelley and Chapin, 1997). The observed spread in AHe dates for this sample shows a positive correlation with eU concentrations, which range from ~22-43 ppm (Fig. 9). Average fission-track lengths in this sample are 14.4 ± 2.0 μm (Kelley and Chapin, 1997), suggesting that this sample was cooled quickly through the AFT partial annealing zone.

Thermal history modeling of sample 21 indicates a two-stage cooling history. Following emplacement in the crust this sample was initially cooled quickly to temperatures of ~60 °C at ~23 Ma. Beginning ~23 Ma, the sample cooled relatively slowly to surface temperatures (Fig. 9).

The observation that the intrusion at Sierra Blanca has similar K-Ar and AFT ages suggests that this intrusion was emplaced at shallow levels in the crust at temperatures <~110°C, which is supported by the observation that the Three Rivers stocks intrude lavas from earlier ~34 – 38 Ma eruptions in the Sierra Blanca volcanic field. Further, the long track lengths in the sample indicate that it was emplaced at an ambient crustal temperature below the apatite partial annealing zone (~60-120 °C). In contrast, the slight spread in AHe dates may be a reflection of prolonged residence in the AHe partial

retention zone (~30-90 °C). Based on the cooling history of this sample, it was most likely emplaced at a temperature of ~60 °C (Fig. 9). The period of slow cooling to surface temperatures beginning ~23 Ma may reflect erosional denudation rather than rift-related tectonic uplift and exhumation, consistent with the observation that the main basin-bounding Alamogordo fault lies along the edge of the Sacramento Mountains to the south and appears to die out to the north.

DISCUSSION

AHe data from the rift flanks and Laramide highlands between northern Colorado and southern New Mexico preserve some component of the multi-stage cooling history of the region because of different structural positions and elevations of samples. The emerging dataset is rich enough to evaluate the hypothesis (Cather et al., 2012; Karlstrom et al., 2011) for regional large-scale cooling trends and processes associated with several episodes: 1) Laramide thrust-related exhumation, 2) Oligocene thermal relaxation of isotherms, epeirogenic uplift, and regional denudation, and 3) fault-driven denudation of rift flanks for the Rio Grande rift. Here we focus on the Rio Grande rift episode and describe cooling patterns observed in the AHe data, and their relationship to cooling patterns observed in the available AFT dataset, as well as trends in the production and timing of emplacement of middle Cenozoic igneous rocks in New Mexico. These time-space patterns of magmatism and cooling are then used to evaluate previously proposed models to explain the origin of the Rio Grande rift. Finally, we present a new evolutionary model for the rift that reconciles these data within the context of the multi-stage Cenozoic tectonic and magmatic history of western North America.

Space-Time Patterns in Cooling and Comparison with Igneous Activity

Similarities in space and time between AHe and AFT ages and K-Ar and $^{40}Ar/^{39}Ar$ dates of igneous rocks document changes in the region during the Cenozoic. Figure 10 summarizes all new and published AFT and AHe dates from the Rio Grande rift and compares them to compiled ages of magmatism and volcanism in New Mexico (Chapin et al., 2004). The AFT age-probability curve (644 ages) provides a template for our interpretation of a multicomponent cooling history involving ~80-50 Ma, ~35-25 Ma, and ~25-10 Ma cooling pulses. The AHe age probability plot (250 dates, including 152 new dates reported here) contains few Laramide ages, but the oldest ages are ~45-50 Ma. A more pronounced ~35-25 Ma peak is evident in the AHe data and a corresponding "shoulder" in the AFT age probability plot. A prominent Neogene peak in AHe (~20-9 Ma) is offset from the most prominent peak in the AFT data (~25-10 Ma). Importantly, the main peaks in AFT and AHe data correspond with a lull in the magmatic age-probability plot. Very young (~5-0 Ma) peaks are present in both the AHe and magmatic data documenting both young magmatism and continued post-10 Ma cooling that is affecting at least parts of the region (Karlstrom et al., 2012).

The Laramide orogeny in Colorado and New Mexico is most evident in a probability density curve of AFT dates, which shows a broad ~80-50 Ma peak (Fig. 10A). The second broad ~35-25 Ma peak in the AHe and AFT cooling dates overlap with a peak in the ages of igneous rocks and corresponds well with the timing of the ignimbrite-flare-up; the San Juan volcanic field in Colorado was active from ~35-18 Ma (Colucci et al., 1991; Lipman, 2007), while the Mogollon-Datil volcanic field in New Mexico was active from ~40-24 Ma (McIntosh et al., 1992). These 40-25 Ma cooling

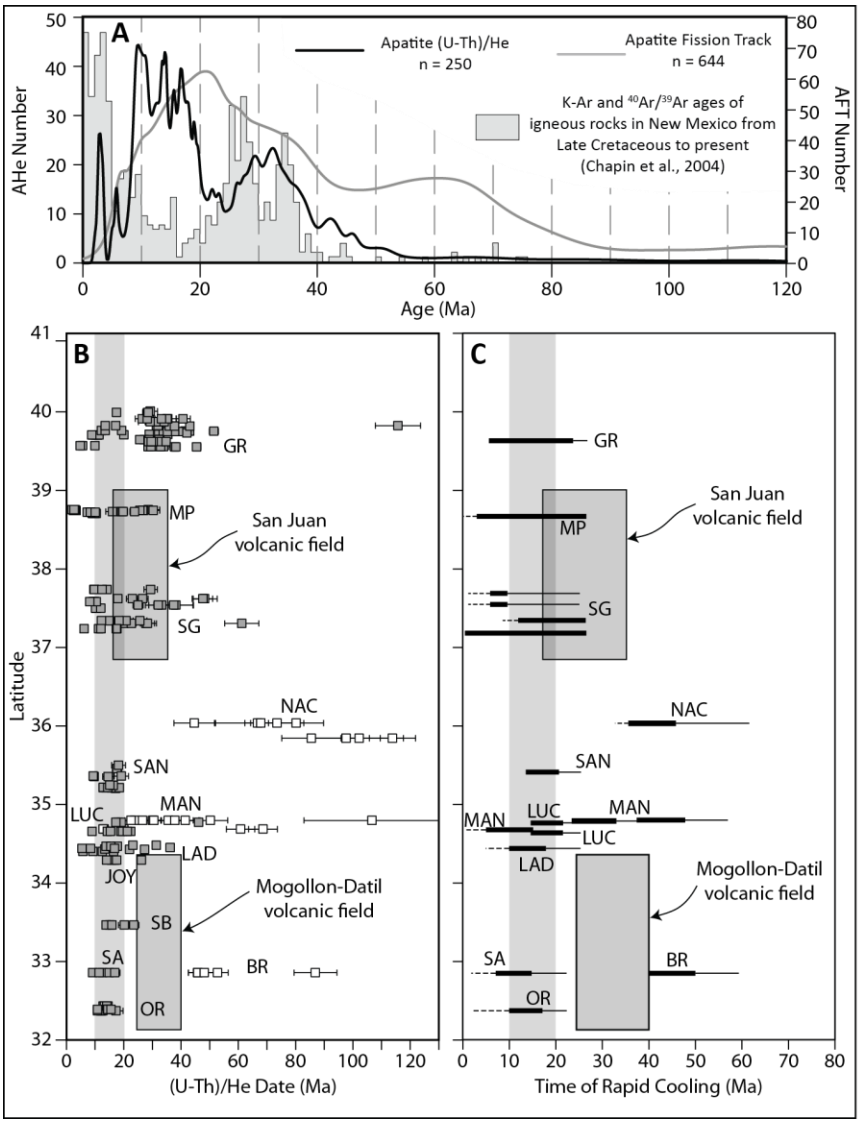

Figure 10. A. Age-probability plot of all new and existing AFT (black line) and AHe (grey line) data from the region in Colorado and New Mexico portrayed in Figure 1. Grey histogram is a compilation of the ages of igneous rocks in New Mexico from Chapin et al. (2004). **B.** Plot of individual AHe date vs. latitude for all new and existing data from the Rio Grande rift. **C.** Plot of times of rapid cooling of rift flanks vs. latitude. The thick part of each line is the time of rapid cooling constrained by the thermal history models. The solid thin line is the time of extension constrained by other geologic data, typically sedimentary fill in the basin. The dashed thin line represents probable continuation of extension not captured in the thermal history models. The vertical gray bands represent the ~20-10 Ma time period of synchronous extension along the length of the rift based on thermal history models.

ages are also distributed across the region in close regional proximity to both older and younger ages. The largest peaks in the probability density curves (~25-10 Ma for AFT and ~20-9 Ma for AHe) overlap with a well-documented magmatic and volcanic lull in New Mexico (Fig. 10A). The majority of these AFT and AHe cooling ages are from the active sides of basins in rift flank uplifts that lie adjacent to master normal faults, and were most likely exhumed to the surface during development of the high elevation rift flanks of the Rio Grande rift. Both the association of these samples with the largest faults and highest elevation rift flanks, and the observation that this main phase of rapid denudation and cooling is out of phase with volcanism and plutonism suggests that the cooling ages in the Rio Grande rift record predominantly exhumation due to slip along normal faults, rather than cooling following intrusion of melts into the crust, or post-Laramide or post-Oligocene slow cooling. Thermal history models produced from each of the rift flanks in Colorado and New Mexico preserve slightly older cooling in the Gore Range, Mount Princeton, and in the Sangre de Cristo Mountains, where rapid cooling began >28 Ma and continued until recent times. In contrast, in central and southern New Mexico, rapid cooling was underway by ~21 Ma and continued until ~5 Ma (Fig. 10C). Thus, although these data cannot detect when extension began or when it ceased in different parts of the rift, they do indicate that cracking of the crust and uplift of active rift flanks occurred simultaneously from 32-41° latitude and the entire Rio Grande rift from southern New Mexico to northern Colorado developed much of its present configuration during the timeframe of ~20-10 Ma.

The youngest igneous rocks in the region (~5-0 Ma) are mostly concentrated along the NE-trending Jemez lineament in northern New Mexico (Chapin et al., 2004). In

contrast, samples within the young peak in the AHe probability density curve (~10-0 Ma) are widely distributed across the region, including in the Sawatch Range, the Gore Range, the Sangre de Cristo Mountains, the Sierra Ladrones Mountains and the Lucero uplift. Some of these may be related to continued faulting along the rift flanks, but the regional distribution of young cooling ages has also been interpreted to be due to more diffuse post-10 Ma exhumation reflecting regional differential uplift driven by mantle reorganization and continued small-scale convection (e.g. Karlstrom et al., 2012; Lazear et al., 2013).

Discussion of Geodynamic and Kinematic Models for Rio Grande Rifting

In spite of decades of geologic studies that are providing increasingly resolved data for the kinematic and temporal evolution of the Rio Grande rift, there is no agreed upon geodynamic model for what caused Rio Grande rifting. The following discussion evaluates possible contributing mechanisms and tries to move beyond the decades-long debate about end member "passive" versus "active" rifting models. The following sections discuss both dynamic (forces/stresses) and kinematic (movements) models for formation and evolution of the Rio Grande rift. The goal is to comment on published models and consider new kinematic/dynamic models for rifting. Ultimately, models need to reconstruct a viable kinematic evolution that leads from Laramide contraction to Neogene extension, and provide a physically plausible geodynamic explanation for uplift and extension. Important constraints that need to be included are the ~1000-km-long discrete N-S location and geometry, new crust/mantle geophysical images (e.g. West et al., 2004; Schmandt and Humphreys, 2010; Hansen et al., 2013, MacCarthy et al., 2014), and new data on timing of exhumational cooling (this paper).

Gravitational Potential Energy Driving Rifting

Crustal compression during the Laramide orogeny thickened the crust in New Mexico and Colorado with estimates that vary from ~ 25% thickening due to middle crustal channel flow (McQuarrie and Chase, 2000) to better accepted estimates of < 5-10% thickening documented by upper crustal shortening across Wyoming (Chapin and Cather, 1981) and the Front Range (Erslev, 2005). Cordell (1978) and Eaton et al. (1986) suggested that after compressional forces ceased, overthickened crust of the Rocky Mountains collapsed gravitationally to form the Rio Grande rift. A future modeling analysis is needed of the relationship between the surface elevation, buoyancy distribution in the crust and mantle, and the geoid anomaly during Cenozoic tectonic evolution of the Rocky Mountain region. This is beyond the scope of this paper, and data probably remain inadequate regarding the evolution of surface elevation (Cather et al., 2012), but our new timing data have implications for evaluating the role of gravitational potential energy, which was likely one of the drivers for rifting.

Total extensional strain in the rift diminishes northward, from 50-100% in the southern Rio Grande rift (Morgan et al., 1986), to 30-33% in the southern Albuquerque basin (Russell and Snelson, 1994; Ricketts et al., 2011), to 17-25% in the northern Albuquerque basin (Russell and Snelson, 1994; Roy et al., 1999), to 8-12% in the San Luis basin (Kluth and Schaftenaar, 1994). This is accompanied by an overall increase in smoothed modern elevation from ~1 km in southern New Mexico to ~3 km in Colorado (Karlstrom et al., 2011). Thus, if end-Laramide starting conditions were broadly similar north-to-south, and if topographic collapse of overthickened crust was a dominant driving force in crustal extension, then high post-Laramide gravitational potential energy in

southern New Mexico may be largely dissipated whereas gravitational potential energy may remain high to the north. Such a scenario might be compatible with the south-to-north decrease in extension, as well as with the new timing data for a near-synchronous ~20-10 Ma pulse of rift flank cooling if extension rates were higher in the south during this timeframe. However, this model is more difficult to reconcile with the location and geometry of the narrow N-S rift valley, and with observed ongoing young denudation that is taking place across the region rather than preferentially localized in regions of highest topography (Fig. 1). These relationships suggest that, while gravitational potential energy likely contributed to overall extension in the Rio Grande rift, other mechanisms are needed to explain the time-space relations of Rio Grande rifting.

Rotation of the Colorado Plateau

Landman and Flowers (2013) revived a kinematic explanation proposed by Chapin and Cather (1994) that middle to late Miocene clockwise rotation of the Colorado Plateau resulted in its separation from the Great Plains Province to form the Rio Grande rift. This type of kinematic model seems required to explain decreasing extension magnitude from south to north in the central rift, and is supported by present-day relative motions between the Colorado Plateau and Rio Grande rift from observed GPS stations, which show a rotation of 0.1 degrees/ Ma and a pole of rotation in Wyoming (Kreemer et al., 2010). However, it does not readily explain contemporaneous extension in the southern Basin and Range as the Colorado Plateau does not extend that far south. This is also more of a kinematic model, and not a geodynamic explanation because the underlying cause(s) of Colorado Plateau rotation remain unspecified. Therefore, this

mechanism does not provide additional insight into why the Rio Grande rift extends north and south of the Colorado Plateau margin or why the Rio Grande rift was formed.

Change in Far Field Stresses

Another possible explanation of the Rio Grande rift involves changes in far-field stresses due to the transition from a convergent to a transform plate margin along the western edge of North America over the last ~30 Ma. From this perspective, the Rio Grande rift is best treated as the easternmost segment of the Basin and Range province, and space-time patterns in extension should mimic the progressive lengthening of the San Andreas fault as it gradually released compressional forces on North America to allow the crust to extend. Extension in the entire Basin and Range province was possibly driven by gravitational collapse of overthickened crust (e.g. Coney and Harms, 1984; Glazner and Bartley, 1985; Wernicke et al. 1987; Axen et al., 1993). This model would therefore predict earliest extension near the latitude where the Pacific Plate first encountered the North American Plate, and extension should sweep both north and south as the San Andreas fault grew. Space-time patterns of extension in the Basin and Range province, however, indicate that earliest extension began in southern Canada during the Eocene and swept south during the Oligocene. In contrast, in northern Mexico, extension initiated during the Oligocene and swept north during the Miocene (Axen et al., 1993; McQuarrie and Wernicke, 2005). These patterns are the exact opposite of what would be expected if plate boundary stresses were a first-order control on extension. In our view, a change from contraction to extension at the 1000-km-distant plate margin during progressive ~ 30 – 0 Ma lengthening of the San Andreas fault would not explain synchronous extension in the rift, or its 1000-km-long narrow geometry in the Rocky Mountain region.

Transmitting stress change more than 1000 km across the relatively unaffected Colorado Plateau would likely be lower magnitude than more local geodynamic forcings in the crust or at the base of the North American plate.

Whole Mantle Flow

Moucha et al. (2008) modeled whole mantle flow beneath the Colorado Plateau and Rio Grande rift, and predicted upwelling asthenosphere that impacted the base of the North America lithosphere obliquely beneath the Rio Grande rift, possibly providing a driving force that results in extension in the upper crust. However, mantle convection in the western U.S. seems to be dominated by large upper-mantle velocity variations that imply shallow convective flow (West et al., 2004; Schmandt and Humphreys, 2010; Levander et al., 2011). As mentioned earlier, seismic velocities beneath the Rio Grande rift at depths >300 km are similar to the velocities in surrounding regions (West et al., 2004). This argues against mantle drag as a major "active" driving force for lithospheric deformation. Whole-mantle driven uplift and related warming of the western North American lithosphere likely have played a role in redistributing heat and buoyancy and may have added to surface elevation, but this geodynamic contribution does not seem to provide a good explanation for the location, geometry, kinematics, or timing of extension in the Rio Grande rift.

Small-Scale Mantle Convection

Seismic velocity variations of the upper mantle beneath the Rio Grande rift and Great Plains are interpreted to reflect differences in composition, temperature, and/or percent melt. To test these interpretations, van Wijk et al. (2008) use a thermal dynamic model to compare the lithospheric thicknesses in the model to the thicknesses imaged

tomographically. The results indicated that, following compression during the Laramide orogeny, a rift could have formed because of a step in thickness from the Colorado Plateau (~120 km thick) to the Great Plains (~150-180 km thick) combined with an imposed increase in westward plate velocity of the Colorado Plateau relative to the Great Plains. In this model, progressive rifting initiates small-scale convection, and upwelling warm asthenosphere accompanies lithospheric thinning. This model of small-scale mantle convection does not test rift location, morphology, or age because these are largely dictated by model starting assumptions, but it produces a physically realistic interaction of mantle flow, crustal extension, and surface uplift of the type that likely accompanies rifting and that is needed to explain the extreme variation in mantle seismic velocity anomalies beneath the Rio Grande rift and Great Plains.

A New Geodynamic Model for Initiation and Evolution of the Rio Grande Rift

Although the Rio Grande rift is one of the best studied continental rifts worldwide, none of the previous models seem adequate to completely explain the rift's location, its ~1000 km N-S extent and narrow geometry, nor the denudation history involving near-simultaneous Miocene rapid cooling of rift flanks along its entire length. Here we present a model in which large-scale lithosphere-asthenosphere interactions immediately beneath the rift provided the dominant driving forces for rift localization and evolution. Below we summarize important constraints and observations regarding western North America, and postulate that final breaking of a large part of the Farallon slab took place beneath the Rio Grande rift at ~20 Ma; the "Big Break" of Sigloch (2011).

As an analogy to Laramide flat-slab subduction in western U.S., flat-slab segments appear to be relatively common in the Andean orogen, where today the subducting slab includes variably-dipping segments (e.g. Coira et al., 1993; Sandeman et al., 1995; Kay et al., 1999; James and Sacks; 1999; Ramos, 2009). In North America, Laramide flat-slab subduction may have been induced by subduction of a conjugate of the Shatsky oceanic plateau (Tarduno et al., 1985; Liu et al., 2010), and this flat-slab segment may have conformed to variations in North American plate thickness. For example, the Archean Wyoming craton is characterized by ~50 km thick crust (Gorman et al., 2002) and 200-300 km thick lithosphere (Gung et al., 2003; Michaut et al., 2007; Yuan and Romanowicz, 2010). Similarly, the Great Plains craton in eastern New Mexico and Colorado is ~150-180 km thick. Each of these thick lithospheric keels is associated with positive P-wave velocity anomalies compared to western North America (Schmandt and Humphreys, 2010, Karlstrom et al., 2011). A similar high velocity anomaly (Western Great Plains anomaly) is located in west Texas and southern New Mexico (Song and Helmberger, 2007; Schmandt and Humphreys, 2010). There is no direct evidence for where the transitions between slab segments were, but it is plausible that one may have been located near the southern boundary of the Archean Wyoming craton and, more speculatively, another may have been near the northern boundary of the Texas high velocity anomaly (Fig. 11). Today the Rio Grande rift resides within this cradle of thicker lithosphere to the north, east, and south (Fig. 11A).

During the waning stages of the Laramide Orogeny, the Farallon plate detached from the base of North America in a complex fashion to produce andesitic and large-volume silicic volcanism. Large-volume magmatism, which is often ascribed to

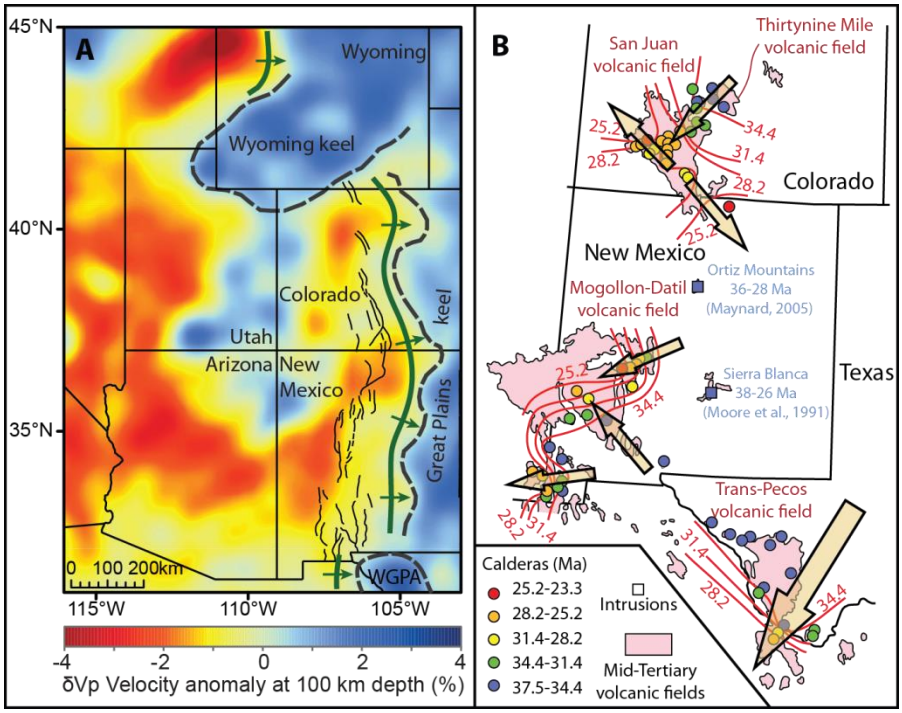

Figure 11. A. Vp velocity anomaly at 100 km depth, modified from Karlstrom et al. (2011). Thick green lines with arrows represent suggested monoclinal hinges in the Farallon slab as it encountered thicker North American lithosphere. Thin black lines represent main faults in the Rio Grande rift. WGPA = western Great Plains anomaly. **B.** Map of large-volume volcanic fields (pink) and distribution of Eocene – Miocene calderas in Colorado, New Mexico, and west Texas, color coded by age of intracaldera fill (Modified from Chapin et al., 2004). Ages are contoured in red, and arrows show interpreted sweep directions of volcanism.

foundering and tearing of the Farallon plate, was happening near-simultaneously in the Great Basin (Armstrong and Ward, 1991; Christensen and Yeats, 1992), and as shown in Figure 11B, also in the San Juan volcanic field in Colorado and the Mogollon-Datil volcanic field in New Mexico (McIntosh et al., 1992; Chapin et al., 2004; Farmer et al., 2008). In the southern Basin and Range, Coney and Reynolds (1977) first proposed that shallowing, then steepening of the Farallon plate resulted in eastward, then westward sweep of volcanism, the latter during the Eocene and Oligocene. This is supported by a westerly sweep in ~38-23 Ma magmatism in the Mogollon-Datil volcanic field, although volcanism is slightly more complicated and also shows a northwestern sweep. In southern Colorado, calderas show a ~38-18 Ma southwest younging trend from the Thirtynine Mile volcanic field to the San Juan volcanic field. Within the San Juan volcanic field, volcanism spreads both northwest and southeast from ~31-23 Ma. Volcanism in the Trans-Pecos volcanic field in western Texas shows a relatively simple progression to the southwest from ~38-25 Ma (Fig. 11B). Similarly, in the Great Basin, the distribution in space and time of volcanic rocks indicates a southward migration in volcanism during the Eocene – Oligocene, while in northern Mexico, Arizona, and eastern California volcanism was sweeping north during the Oligocene - Miocene due to northward migration of the subducted Mendocino fracture zone (Stewart and Carlson; 1976; Glazner and Bartley; 1984; Best et al., 1989; Axen et al., 1993; Humphreys, 1995). Although these directions may be approximate due to incomplete data, together these observations suggest that the Farallon plate was decoupling from the North American plate simultaneously in different locations and directions beneath the western U.S. (Atwater, 1989; Chapin et al., 2004). One important aspect of this model is that large coherent slab

fragments beneath the western U.S were partly decoupled from the older, easterly portions of the slab and stress fields were shifting from contractional to extensional in this timeframe.

Tomographic P-wave models of North American asthenosphere are interpreted to image intact segments of subducted oceanic lithosphere. These images suggest that the Farallon plate remains relatively intact in the mid mantle (800 to at least 1800 km depth) beneath eastern North America (Old Farallon) (Fig. 12), whereas other Farallon slab segments are interpreted at different depths beneath western North America (Sigloch, 2011). In particular, Sigloch (2011) pointed out the presence of a large-scale break in the Farallon plate, a slab window referred to as "The Big Break," which has also been imaged and described in Texas (van der Lee and Nolet, 1997) and in Wyoming (Sigloch et al. 2008). Plate motion studies of North America suggest that the Farallon plate at the location of the "Big Break" was initially subducted beneath North America ~60 Ma (Sigloch, 2011), and that the western edge of the "Big Break" in the Farallon segment was beneath the present-day Rio Grande rift in New Mexico and Colorado at ~20 Ma (Fig. 12).

Our proposed model incorporates these observations, and places the evolution of the Rio Grande rift within this overall tectonic and volcanic setting (Fig. 13). The Wyoming keel and the western Great Plains keel protrude west from the Great Plains craton such that a shallowly subducting Farallon plate may have been forced to change dip or tear laterally during the Laramide Orogeny. The Farallon plate beneath New Mexico remained shallow until it reached the Great Plains keel, where it was forced downward. It may be that the localization of the Laramide shortening in the Rocky

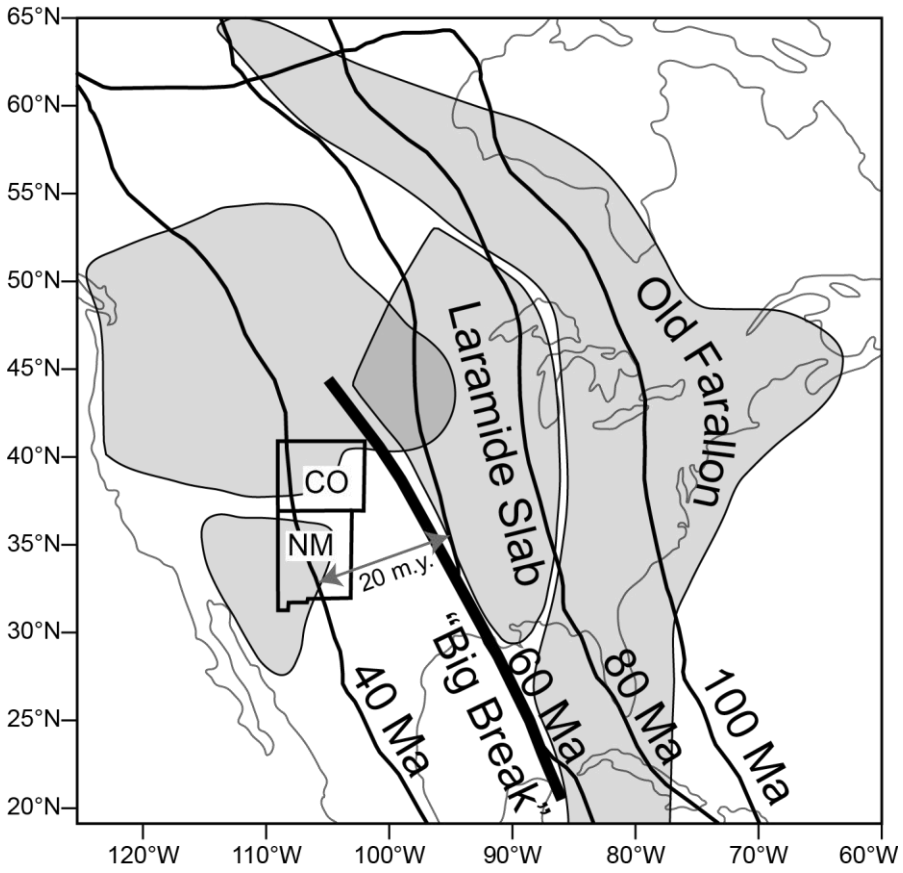

Figure 12. Locations of imaged subducted Farallon segments beneath North America. Thin black lines are times when Farallon slab was subducted at the trench, based on plate motion reconstructions from O'Neill et al. (2005). Thick black line represents the "Big Break" in the Farallon Plate. Figure is modified from Sigloch (2011).

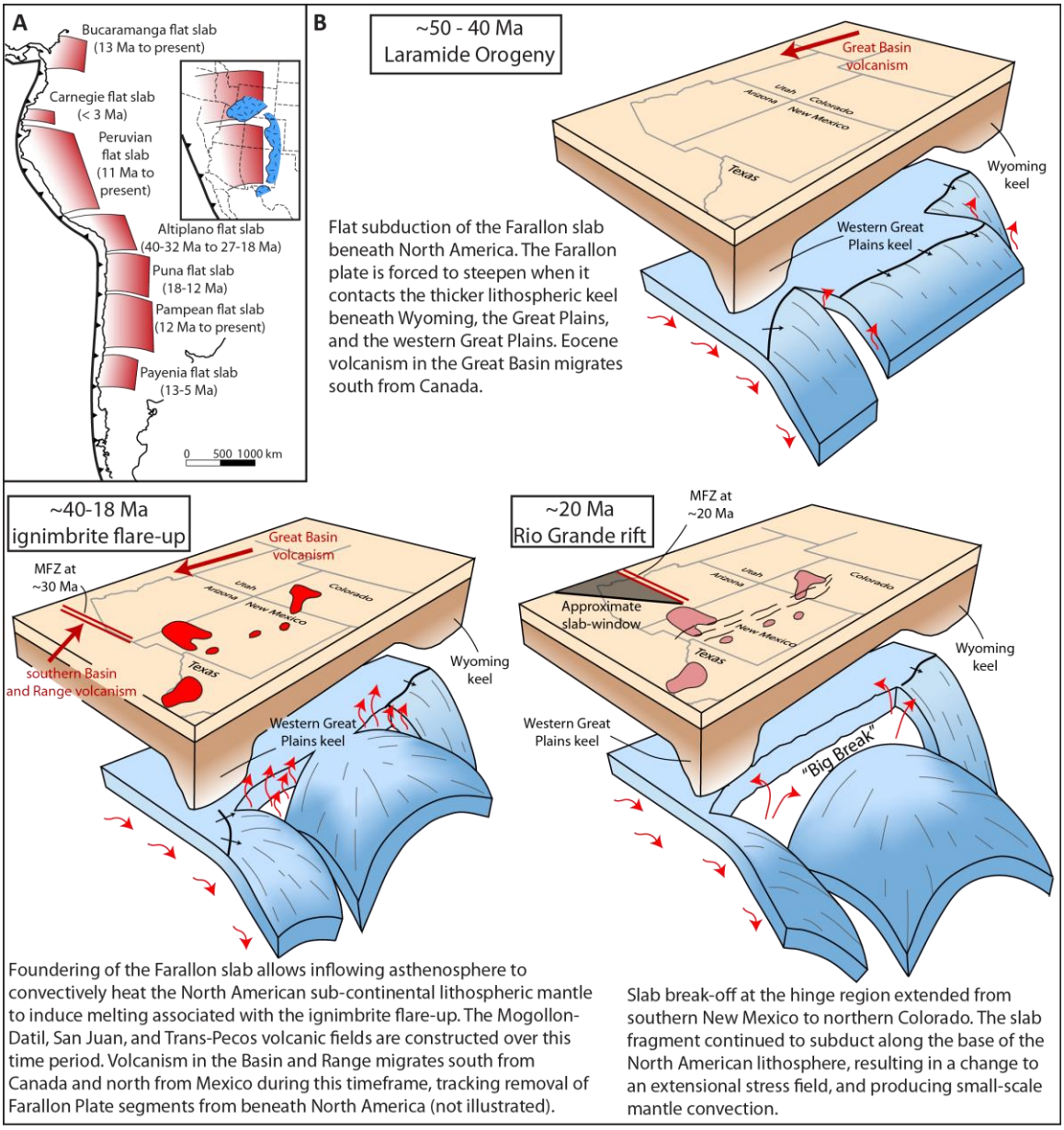

Figure 13. A. Size comparison of the proposed flat slab segment extending from the Wyoming craton to the western Great Plains anomaly (inset) to different flat slab segments in South America. South America segments are modified from Ramos (2009). **B.** Proposed evolution of the Rio Grande rift and relationship to the Laramide Orogeny and ignimbrite flare-up in Colorado, New Mexico, and west Texas. Volcanic trends in the Basin and Range are shown for each time slice, but the changing geometry of the Farallon Plate is only illustrated beneath the Rio Grande rift, and not beneath the Basin and Range. MFZ = Mendocino fracture zone.

Mountains and the subsequent N-S central segment of the Rio Grande rift may both have been influenced by a downward bend in the slab at this location. Beginning ~40 Ma, parts of the Farallon slab began to founder or roll back beneath the volcanic fields, which themselves might have been localized by changes in slab segment dip. This early removal of portions of the Farallon slab allowed asthenosphere to interact with the hydrated base of the North American lithosphere, resulting in vigorous magmatism in the Mogollon-Datil, San Juan, and Trans-Pecos volcanic fields (e.g. Chapin et al., 2004; Farmer et al., 2008). The west and southwest sweep in volcanism in the Mogollon-Datil and San Juan volcanic fields, respectively, indicate that in the region beneath the future Rio Grande rift the Farallon slab was likely beginning to become unstable, but the relatively low volume of Oligocene magmatism in this segment permit the speculation that other parts of this flap had not yet became detached. At around ~20 Ma, near simultaneous tearing of the slab at the remaining hinge line may have linked the previously foundered portions with final slab detachment extending the length from northern Colorado to southern New Mexico. This would have promoted upwelling asthenosphere to thermally weaken the North American lithosphere in the region that is beneath the present-day Rio Grande rift. In this model, rapid uplift and extension in the Rio Grande rift may have been driven by thermal weakening of North American lithosphere and subsequent gravitational collapse of the overthickened Alvarado Ridge, with the timing and spatial distribution of extension being governed by the location and ultimate foundering of a segment of the underlying Farallon Plate. As discussed previously, gravitational potential energy may still be high in Colorado, whereas it has largely dissipated in New Mexico, which is supported by the relative abundance of young AHe dates in the Gore Range, Sawatch

Range, and Sangre de Cristo Mountains (Fig. 10B) which indicate young and ongoing extension in Colorado. Space-time patterns in volcanism and extension in the Great Basin and southern Basin and Range led Axen et al. (1993) to a similar conclusion for this region, where these authors concluded that volcanism and extension are most likely triggered by thermal weakening at the base of the North American lithosphere and subsequent gravitational collapse of thickened crust, rather than by stresses generated at the plate margin.

This type of slab detachment beneath Colorado and New Mexico may have several important implications. First, it may be one possible explanation for the relative paucity of volcanism in the central Rio Grande rift from ~23-10 Ma. Calculations of mantle source volumes needed to fuel volcanism in the San Juan and Mogollon-Datil volcanic fields suggests that the remaining lithospheric mantle beneath the entire Rio Grande rift region may have been relatively infertile when rapid extension began (Farmer et al., 2008). Second, based on numerical models (e.g. Gerya et al., 2004), this type of slab detachment also may have resulted in surface uplift. The Alvarado Ridge in Colorado and New Mexico was most likely initiated in post-middle Eocene time (Eaton, 2008), but renewed surface uplift due to slab detachment may have created a shorter wavelength swell superimposed on the existing Rocky Mountains-Great Plains swell. Uplift caused central grabens to form in the elastic plate, with continued uplift of even shorter wavelength rift flank uplifts driven by fault unloading as well as denudation of rift flanks.

Such a model may help explain the “early rift phase” of rifting (e.g. Chapin and Seager, 1975; Baldridge et al., 1980; Baldridge et al., 1984; Seager et al., 19840) that

overlapped with ignimbrite volcanism, followed by the "Big Break " and rapid cooling of rift flanks due to faulting and denudation. This model plausibly explains the N-S discrete character of the central Rio Grande rift, the change in character to more diffuse extension to the north and south of this central segment, and the compound uplift evidence seen in thermochronology and topographic data.

CONCLUSIONS

152 new AHe dates are presented from 34 samples adjacent to the Rio Grande rift in New Mexico and Colorado. These data, when combined with published AFT and AHe dates, indicate near synchronous, rapid cooling due to denudation of active rift flanks along >850 km of the Rio Grande rift from ~20-10 Ma. This time period coincides with a documented magmatic lull, suggesting that this main phase of extension was accomplished through surface uplift of rift flanks and slip along normal faults, rather than by cooling following emplacement of igneous intrusions into the crust. To explain the near synchronous extension, we rely on important observations and constraints of the tectonic and volcanic history of North America. Our geodynamic model invokes tearing and ultimate foundering of the Farallon slab, which had a segmented dip geometry controlled initially by thick cratonic keels beneath Wyoming, the Great Plains, and western Texas/southeastern New Mexico. A bend formed in the Farallon slab as it was forced to subduct beneath the thick Great Plains keel, and this bend was influential is localizing both the Rocky Mountain-Great Plain transition in the early Cenozoic and subsequent Neogene localization of the central discrete segment of the Rio Grande rift. Slab foundering along this N-S segment ~20 Ma is postulated to have led to the "Big Break" in the modern image of the intact Farallon slab under eastern North America. As

the Farallon continued to founder, small-scale mantle convection thermally weakened the base of the overlying North American lithosphere in the region that is below the present-day Rio Grande rift, and this combined with mantle buoyancy-driven surface uplift ultimately drove extension at the surface possible due to gravitational collapse of overthickened crust. This model attempts to account for near-synchronous extension to produce the Rio Grande rift while placing its evolution within the context of the Cenozoic tectonic and magmatic history of western North America.

ACKNOWLEDGEMENTS

Student funding for AHe analyses comes from the Geological Society of America, New Mexico Geological Society, and the Graduate and Professional Student Association at the University of New Mexico awarded to Jason Ricketts.

REFERENCES

Abbott, J.C., Goodwin, L.B., Kelley, S.A., Maynard, S.R., and McIntosh, W.C., 2004, The anatomy of a long-lived fault system: Structural and thermochronologic evidence for Laramide to Quaternary activity in the Tijeras fault system, New Mexico, *in* Cather, S.M., McIntosh, W.C., and Kelley, S.A., eds., Tectonics, Geochronology, and Volcanism in the Southern Rocky Mountains and Rio Grande Rift: New Mexico Bureau of Geology and Mineral Resources, Bulletin 160, p. 113-138.

Armstrong, R.L., and Ward, P., 1991, Evolving geographic patterns of Cenozoic magmatism in the North American Cordillera: The temporal and spatial association of magmatism and metamorphic fore complexes: Journal of Geophysical Research, v. 96, p. 13,201-13,224.

Armstrong, C., Dutrow, B.L., Henry, D.J., and Thompson, R.A., 2013, Provenance of volcanic clasts from the Santa Fe Group, Culebra graben of the San Luis Basin, Colorado: A guide to tectonic evolution, *in* Hudson, M.R., and Grauch, V.J.S., eds., New Perspectives on Rio Grande Rift Basins: From Tectonics to Groundwater: Geological Society of America Special Paper 494, p. 21-45, doi: 10.11.30/2013.2494(02).

Atwater, T., 1989, Plate tectonic history of the northeast Pacific and western North America: Geological Society of America, The Geology of North America, v. N., p. 21-72.

Axen, G.J., Taylor, W.J., and Bartley, J.M., 1993, Space-time patterns and tectonic controls of Tertiary extension and magmatism in the Great Basin of the western United States: Geological Society of America Bulletin, v. 105, p. 56-76.

Baldridge, W.S., Olsen, K.H., and Callender, J.F., 1984, Rio Grande rift: Problems and Perspectives: New Mexico Geological Society Guidebook, 35th Annual Conference, 46 p.

Baldridge, W.S., Damon, P.E., Shafiqullah, M., and Bridwell, R.J., 1980, Evolution of the central Rio Grande rift, New Mexico: New potassium-argon ages: Earth and Planetary Science Letters, v. 51, p. 309-321.

Baltz, E.H., 1967, Stratigraphy and regional tectonic implications of part of Upper Cretaceous and Tertiary rocks, east-central San Juan Basin, New Mexico: U.S. Geological Survey, Professional Paper 552, 101 p.

Beaty, D.W., Naeser, C.W., and Lynch, W.C., 1987, The origin and significance of the strata-bound, carbonate-hosted gold deposits at Tennessee Pass, Colorado: Economic Geology, v. 82, p. 2158–2178.

Beck, W.C., and Chapin, C.E., 1994, Structural and tectonic evolution of the Joyita Hills, central New Mexico: Implications of basement control on Rio Grande rift, *in* Keller, G.R., and Cather, S.M., eds., Basins of the Rio Grande Rift: Structure, Stratigraphy, and Tectonic Setting: Boulder, Colorado, Geological Society of America Special Paper 291, p. 187-205.

Berglund, H.T., Sheehan, A.F., Murray, M.H., Roy, M., Lowry, A.R., Nerem, R.S., and Blume, F., 2012, Distributed deformation across the Rio Grande Rift, Great Plains, and Colorado Plateau: Geology, v. 40, p. 23-26.

Best, M.G., Christiansen, E.H., Deino, A.L., Gromme, C.S., McKee, E.H., and Noble, D.C., 1989, Eocene through Miocene volcanism in the Great Basin of the western United States, *in* Chapin, C.E., and Zidek, J., eds., Field excursions to volcanic terrains in the western United States, Volume II: Cascades and intermountain west: New Mexico Bureau of Mines and Mineral Resources Memoir 47, p. 91-133.

Bookstrom, A.A., Naeser, C.W., and Shannon, J.R., 1987, Isotopic age determinations, unaltered and hydrothermally altered igneous rocks, north-central Colorado mineral belt: Isochron/West, no. 49, p. 13–20.

Bryant, B., and Naeser, C.W., 1980, The significance of fission-track ages of apatite in relation to the tectonic history of the Front and Sawatch ranges, Colorado: Geological Society of America Bulletin, v. 91, p. 156– 164, doi:10.1130/0016-7606(1980)91<156:TSOFAO >2.0.CO;2.

Bryant, B., Naeser, C.W., and Stegen, R.J., 1990, Reconnaissance fission-track geochronology of the Aspen mining district, central Colorado, *in* Beaty, D.W., Landis, G.P., and Thompson, T.B., eds., Carbonate-hosted sulfide deposits of the central Colorado mineral belt: Economic Geology Monograph No. 7, p. 301–307.

Bryant, B., Marvin, R.F., Naeser, C.W., and Mehnert, H.H., 1981, Ages of igneous rocks in the South Park-Breckenridge region, Colorado, and their relation to the tectonic history of the Front Range uplift: U.S. Geological Survey Professional Paper 1199-C, 35 p.

Brister, B.S., and Gries, R.R., 1994, Tertiary stratigraphy and tectonic development of the Alamosa Basin (northern San Luis Basin), Rio Grande rift, south-central Colorado, *in* Keller, G.R., and Cather, S.M., eds., Basins of the Rio Grande Rift: Structure, Stratigraphy, and Tectonic Setting: Boulder, Colorado, Geological Society of America Special Paper 291, p. 39-58.

Callendar, J.F., and Zilinski, R.E., 1976, Kinematics of Tertiary and Quaternary deformation along the eastern edge of the Lucero uplift, central New Mexico: New Mexico Geological Society Special Publication 6, p. 53-61.

Case, J.E., and Sikora, R.F., 1984, Geologic interpretation of gravity and magnetic data in the Salida region, Colorado: U.S. Geological Survey Open File Report 84–372, 46p.

Cather, S.M., Chapin, C.E., and Kelley, S.A., 2012, Diachronous episodes of Cenozoic erosion in southwestern North America and their relationship to surface uplift, paleoclimate, paleodrainage, and paleoaltimetry: Geosphere, v. 8, p. 1177-1206.

Chapin, C.E., and Seager, W.R., 1975, Evolution of the Rio Grande rift in the Socorro and Las Cruces area: New Mexico Geological Society, Guidebook 26, p. 297-321.

Chapin, C,E, and Cather, S.M., 1981, Eocene tectonics and sedimentation in the Colorado Plateau-Rocky Mountain area, *in* Dickinson, W.R., and Payne, M.D., eds., Relations of tectonics to ore deposits in the southern Cordillera: Arizona Geological Society Digest, v. 14, p. 33-55.

Chapin, C.E., and Cather, S.M., 1994, Tectonic setting of axial basins of the northern and central Rio Grande rift, *in* Keller, G.R., and Cather, S.M., eds., Basins of the Rio Grande Rift: Structure, Stratigraphy, and Tectonic Setting: Boulder, Colorado, Geological Society of America Special Paper 291, p. 5-25.

Chapin, C.E., Wilks, M., and McIntosh, W.C., 2004, Space-time patterns of Late-Cretaceous to present magmatism in New Mexico-comparison with Andean volcanism and potential for future volcanism: New Mexico Bureau of Geology and Mineral Resources Bulletin 160, p. 13-40.

Christiansen, R.L., and Yeats, R.L., 1992, Post-Laramide geology of the U.S. Cordilleran region, *in* Burchfiel, B.C., Lipman, P.W., and Zoback, M.L., eds., The Cordilleran Orogen: Conterminous U.S.: Geological Society of America, Geology of North America, v. G-3, p. 261-406.

Church, S.E., and Bickford, M.E., 1971, Spontaneous fission-track studies of accessory apatite from granitic rocks of the Sawatch Range, Colorado: Geological Society of America Bulletin, v. 82, p. 1727–1734.

Coira, B., Mahlburg Kay, S., and Viramonte, J., 1993, Upper Cenozoic magmatic evolution of the Argentine Puna – A model for changing subduction geometry: International Geology Review, v. 35, 677-720.

Coleman, S.M., 1985, Map showing tectonic features of late Cenozoic origin in Colorado: U.S. Geological Survey Miscellaneous Geological Investigations Map I-1566, scale 1:1 000 000, 1 sheet.

Colucci, M.T., Dungan, M.A., Ferguson, K.M., Lipman, P.W., and Moorbath, S., 1991, Precaldera lavas of the southeast San Juan volcanic field: Parent magmas and crustal interactions: Journal of Geophysical Research, v. 96, p. 13412–13434.

Coney, P.J., and Reynolds, S.J., 1977, Cordilleran Benioff zones: Nature, v. 270, p. 403-406, doi: 10.1038/270403a0.

Coney, P.J., and Harms, T.A., 1984, Cordilleran metamorphic core complexes: Cenozoic extensional relics of Mesozoic compression: Geology, v. 12, p. 550-554.

Connell, S.D., 2004, Geology of the Albuquerque Basin and tectonic development of the Rio Grande rift in north-central New Mexico, *in* Mack, G.H., and Giles, K.A., eds., the Geology of New Mexico, A Geologic History: New Mexico Geological Society Special Publication 11, p. 359-388.

Cordell, L., 1978, Regional geophysical setting of the Rio Grande rift: Geological Society of America Bulletin, v. 89, p. 1073–1090, doi: 10.1130/0016-7606(1978)89<1073:RGSOTR>2.0.CO;2.

Cunningham, C.G., Naeser, C.W., Marvin, R.F., Luedke, R.G., and Wallace, A.R., 1994, Age of selected intrusive rocks and associated ore deposits in the Colorado Mineral Belt: U.S. Geological Survey Bulletin 2109, 31 p.

DeCelles, P.G., 2004, Late Jurassic to Eocene evolution of the Cordilleran thrust belt and foreland basin system, western U.S.A.: American Journal of Science, v. 304, p. 105-168, doi: 10.2475/ajs.304.2.105.

Dickinson, W.R., 2009, Anatomy and global context of the North American cordillera, *in* Kay, S.M., Ramos, V.A., and Dickinson, W.R., eds., Backbone of the Americas: Shallow Subduction, Plateau Uplift, and Ridge and Terrane Collision: Geological Society of America Memoir 204, p. 1-29, doi: 10.1130/2009.1204(01).

Donelick, R.A., O'Sullivan, P.B., and Ketchum, R.A., 2005, Apatite fission-track analysis, *in* Reiners, P.W., and Ehlers, T.A., eds., Low-Temperature Thermochronology: Techniques, Interpretations, and Applications: Reviews in Mineralogy and Geochemistry, v. 58, p. 49-93.

Eaton, G.P., 1986, A tectonic redefinition of the southern Rocky Mountains: Tectonophysics, v. 132, p. 163–193, doi:10.1016/0040-1951(86)90031-4.

Eaton, G.P., 2008, Epeirogeny in the southern Rocky Mountains regions: Evidence and origin: Geosphere, v. 4, p. 764–784; doi: 10.1130/GES00149.1.

Erslev, E.A., 2005, 2D Laramide geometries and kinematics of the Rocky Mountain region, *in* Karlstrom, K.E., and Keller, G.R., eds., The Rocky Mountain Region-An

Evolving Lithosphere: Tectonics, Geochemistry, and Geophysics: Washington D.C., American Geophysical Union, p. 7-20.

Farley, K.A., Wolf, R.A., and Silver, L.T., 1996, The effects of long alpha-stopping distances on (U-Th)/He ages: Geochimica et Cosmochimica Acta, v. 60, p. 4,223-4,229.

Farmer, G.L., Bailley, T., and Elkins-Tanton, L.T., 2008, Mantle source volumes and the origin of the mid-Tertiary ignimbrite flare-up in the southern Rocky Mountains, western U.S.: Lithos, v. 102, p. 279-294.

Faulds, J.E., and Varga, R.J., 1998, The role of accommodation zones and transfer zones in the regional segmentation of extended terranes, *in*, Faulds, J.E., and Stewart, J.H., eds., Accommodation zones and transfer zones: the regional segmentation of the basin and range provinces: Geological Society of America Special Paper, v. 323, p. 1-45.

Feldman, J. D., 2010, The emplacement and exhumation history of the Twin Lakes batholith and implications for the Laramide Orogeny and flat slab subduction [M.S. thesis]: Socorro, New Mexico Institute of Mining and Technology, 174 p.

Flowers, R.M., and Kelley, S.A., 2011, Interpreting data dispersion and "inverted" dates in apatite (U-Th)/He and fission-track datasets: An example from the US midcontinent: Geochimica et Cosmochimica Acta, v. 75, p. 5169-5186.

Flowers, R.M., Ketchum, R.A., Shuster, D.L., and Farley, K.A., 2009, Apatite (U-Th)/He thermochronometry using a radiation damage accumulation and annealing model: Geochimica et Cosmochimica Acta, v. 73, p. 2,347-2,365.

Fox, M. and Shuster, D.L., 2014, The influence of burial heating on the (U-Th)/He system in apatite: Grand Canyon case study: Earth and Planetary Science Letters, v. 397, p. 174-183.

Gerya, T.V., Yuen, D.A., and Maresch, W.V., 2004, Thermomechanical modelling of slab detachment: Earth and Planetary Science Letters, v. 226, p. 101-116, doi: 10.1016/j.epsl.2004.07.022.

Glazner, A.F., and Bartley, J.M., 1984, Timing and tectonic setting of Tertiary low-angle normal faulting and associated magmatism in the southwestern United States: Tectonics, v. 3, p. 385-396.

Glazner, A.F., and Bartley, J.M., 1985, Evolution of lithospheric strength after thrusting: Geology, v. 13, p. 42-45.

Goff, F., Dunbar, N., Kelley, S.A., Peters, L., McIntosh, W., Heizler, L.L., and Goff, C.J., 2011, Three Rivers Stock and Palisades Tuff: Correlating intrusive source with ignimbrite sheet in the tectonically disrupted Sierra Blanca Igneous Complex, New Mexico: Geological Society of America Abstracts with Programs, v. 43, p. 651.

Gorman, A.R., Clowes, R.M., Ellis, R.M., Henstock, T.J., Spence, G.D., Keller, G.R., Levander, A., Snelson, C.M., Burianyk, M.J.A., Kanasewich, E.R., Asudeh, I., Hajnal, Z., and Miller, K.C., 2002, Deep Probe: Imaging the roots of western North

America: Canadian Journal of Earth Sciences, v. 39, p. 375-398, doi: 10.1139/E01-064.

Grauch, V.J.S., and Connell, S.D., 2013, New perspectives on the geometry of the Albuquerque Basin, Rio Grande rift, New Mexico: Insights from geophysical models of rift-fill thickness, *in* Hudson, M.R., and Grauch, V.J.S., eds., New Perspectives on Rio Grande Rift Basins: From Tectonics to Groundwater: Geological Society of America Special Paper 494, p. 427-462, doi: 10.1130/2012.2494(16).

Gung, Y.C., Panning, M., and Romanowicz, B., 2003, Global anisotropy and the thickness of continents: Nature, v. 422, p. 707-711, doi: 10.1038/nature01559.

Hansen, S.M., Dueker, K.G., Stachnik, J.C., Aster, R.C., and Karlstrom, K.E., 2013, A rootless rockies – Support and lithospheric structure of the Colorado Rocky Mountains inferred from CREST and TA seismic data: Geochemistry Geophysics Geosystems, v. 14, p. 2,670-2,695, doi: 10.1002/ggge.20143.

Heller, P.L., Dueker, K., and McMillan, M.E., 2003, Post-Paleozoic alluvial gravel transport as evidence of continental tilting in the U.S. Cordillera: Geological Society of America Bulletin, v. 115, p. 1122–1132, doi:10.1130/B25219.1.

House, M.A., Kelley, S.A., and Roy, M., 2003, Refining the footwall cooling history of a rift flank uplift, Rio Grande rift, New Mexico: Tectonics, v. 22, doi: 10.1029/2002TC001418.

Humphreys, E.D., 1995, Post-Laramide removal of the Farallon slab, western United States: Geology, v. 23, p. 987-990.

Humphreys, E., 2009, Relation of flat slab subduction to magmatism and deformation in the western United States, *in* Kay, S.M., Ramos, V.A., and Dickinson, W.R., eds., Backbone of the Americas: Shallow Subduction, Plateau Uplift, and Ridge and Terrane Collision: Geological Society of America Memoir 204, p. 85-98, doi: 10.1130/2009.1204(04).

Humphreys, E., Hessler, E., Dueker, K., Erslev, E., Farmer, G.L., and Atwater, T., 2003, How Laramide-age hydration of North America by the Farallon slab controlled subsequent activity in the western U.S.: International Geology Review, v. 45, p. 575-595, doi: 10.2747/0020-6814.45.7.575.

Ingersoll, R.V., and Yin, A., 1993, Two stage evolution of the Rio Grande rift, northern New Mexico and southern Colorado: Geological Society of America, Abstracts with Programs, v. 25, p. A-409.

James, D.E., and Sacks, S., 1999, Cenozoic formation of the Central Andes: A geophysical perspective, *in* Skinner, B., ed., Geology and Mineral Deposits of Central Andes: Society of Economic Geology Special Publication 7, p. 1-25.

Karlstrom, K.E., Coblentz, D., Dueker, K., Ouimet, W., Kirby, E., Van Wijk, J., Schmandt, B., Kelley, S., Lazear, G., Crossey, L.J., Crow, R., Aslan, A., Darling, A., Aster, R., MacCarthy, J., Hansen, S.M., Stachnik, J., Stockli, D.F., Garcia, R.V., Hoffman, M., McKeon, R., Feldman, J., Heizler, M., Donahue, M.S., and the CREST

Working Group, 2011, Mantle-driven dynamic uplift of the Rocky Mountains and Colorado Plateau and its surface response: Toward a unified hypothesis: Lithosphere, v. 4, p. 3-22, doi: 10.1130/L150.1.

Kay, S.M., Mpodozis, C., and Coira, B., 1999, Neogene magmatism, tectonism, and mineral deposits of the Central Andes (22°S to 33°S), *in* Skinner, B., ed., Geology and Mineral Deposits of Central Andes: Society of Economic Geology Special Publication 7, p. 27-59.

Keller, G.R., Morgan, P., and Seager, W.R., 1990, Crustal structure, gravity anomalies and heat flow in the southern Rio Grande rift and their relationship to extensional tectonics: Tectonophysics, v. 174, p. 21-37, doi: 10.1016/0040-1951(90)90382-I.

Kelley, V.C., 1952, Tectonics of the Rio Grande depression of central New Mexico: New Mexico Geological Society Guidebook 3, p. 92-105.

Kelley, S.A., 2002, Unroofing of the southern Front Range, Colorado: A view from the Denver Basin: Rocky Mountain Geology, v. 37, no. 2, p. 189-200.

Kelley, S.A. and Duncan, I.J., 1986, Late Cretaceous to Middle Tertiary tectonic history of the northern Rio Grande rift, New Mexico: Journal of Geophysical Research, v. 91, p.6246-6262.

Kelley, S.A., and Chapin, C.E., 1997, Cooling histories of mountain ranges in the southern Rio Grande rift based on apatite fission-track analysis – a reconnaissance survey: New Mexico Geology, v. 9, p. 1-14.

Kelley, S.A., and Chapin, C.E., 2004, Denudation history and internal structure of the Front Range and Wet Mountains, Colorado, based on apatite fission-track thermochronology, in Cather, S.M., McIntosh, W.A., and Kelley, S.A., eds., Tectonics, geochronology, and volcanism in the southern Rocky Mountains and the Rio Grande rift: New Mexico Bureau of Geology and Mineral Resources Bulletin 160, p. 41-77.

Kelley, S.A., Chapin, C.E., and Corrigan, J., 1992, Late Mesozoic to Cenozoic cooling histories of the flanks of the northern and central Rio Grande rift, Colorado and New Mexico: New Mexico Bureau of Mines and Mineral Resources Bulletin 145, 39 p.

Ketchum, R.A., 2005, Forward and inverse modeling of low-temperature thermochonometry data, *in* Reiners, P.W., and Ehlers, T.A., eds., Low-Temperature Thermochronology: Techniques, Interpretations, and Applications: Reviews in Mineralogy and Geochemistry, v. 58, p. 275-311.

Kluth, C.F., and Schaftenaar, C.H., 1994, Depth and geometry of the northern Rio Grande rift in the San Luis Basin, south-central Colorado, in Keller, G.R., and Cather, S.M., eds., Basins of the Rio Grande Rift: Structure, Stratigraphy, and Tectonic Setting: Geological Society of America Special Paper 291, p. 27–38, doi:10.1130/SPE291-p27.

Koning, D.J., and Pazzaglia, F.J., 2002, Paleoseismicity of the Alamogordo fault along the Sacramento Mountains, southern Rio Grande rift, New Mexico, *in* Lueth, V.,

Giles, K.A., Lucas, S.G., Kues, B.S., Myers, R.G., and Ulmer-Scholle, D., eds., Geology of White Sands: New Mexico Geological Society, Guidebook 53, p. 107-119.

Koning, D.J., Grauch, V.J.S., Connell, S.D., Ferguson, J.,McIntosh, W., Slate, J.L., Wan, E., and Baldridge, W.S., 2013, Structure and tectonic evolution of the eastern Espanola Basin, Rio Grande rift, north-central New Mexico, *in* Hudson, M.R., and Grauch, V.J.S., eds., New Perspectives on Rio Grande Rift Basins: From Tectonics to Groundwater: Geological Society of America Special Paper 494, p. 185-219, doi: 10.11.30/2013.2494(08).

Kreemer, C., Blewitt, G., and Bennett, R.A., 2010, Present-day motion and deformation of the Colorado Plateau: Geophysical Research Letters, v. 37, L10311, doi:10.1029/2010GL043374.

Landman, R.L., and Flowers, R.M., 2012, (U-Th)/He thermochronologic constraints on the evolution of the northern Rio Grande rift, Gore Range, Colorado and implications for rift propagation models: Geosphere, v. 9, p. 170-187, doi: 10.1130/GES00826.1.

Lawton, T.F., and McMillan, N.J., 1999, Arc abandonment as a cause for passive continental rifting: Comparison of the Jurassic Mexican Borderland Rift and the Cenozoic Rio Grande Rift: Geology, v. 27, p. 779-782.

Lazear, G., Karlstrom, K.E., Aslan, A., and Kelley, S., 2013, Denudation and flexural isostatic response of the Colorado Plateau and southern Rocky Mountain region since 10 Ma: Geosphere, v.9, p. 792-814, doi:10.1130/GEO00836.1.

Lee, J.P., Stockli, D.F., Kelley, S.A., Pederson, J.L., Karlstrom, K.E., and Ehlers, T.A., 2013, New thermochronometric constraints on the Tertiary landscape evolution of the central and eastern Grand Canyon, Arizona: Geosphere, v. 9, p. 1-13, doi: 10.1130/GES00842.1.

Leonard, E.M., 2002, Geomorphic and tectonic forcing of late Cenozoic warping of the Colorado piedmont: Geology, v. 30, p. 595-598, doi:10.1130/00917613(2002)030<0595:GATFOL>2.0.CO;2.

Levander, A., Schmandt, B., Miller, M.S., Liu, K., Karlstrom, K.E., Crow, R.S., Lee, C.-T.A., and Humphreys, E.D., 2011, Continuing Colorado plateau uplift by delamination-style convective lithospheric downwelling: Nature, v. 472, p. 461-466, doi: 10.1038/nature10001.

Lewis, C.J., and Baldridge, W.S., 1994, Crustal extension in the Rio Grande rift, New Mexico: Half-grabens, accommodation zones, and shoulder uplifts in the Ladron Peak–Sierra Lucero area, *in* Keller, G.R., and Cather, S.M., eds., Basins of the Rio Grande Rift: Structure, Stratigraphy, and Tectonic Setting: Geological Society of America Special Paper 291, p. 135–156, doi:10.1130/SPE291-p135.

Lindsey, D.A., Andriessen, P.A.M., and Wardlaw, B.R., 1986, Heating, cooling, and uplift during Tertiary time, northern Sangre de Cristo Range, Colorado: Geological Society of America Bulletin, v. 97, p. 1133–1143.

Lipman, P.W., 2007, Incremental assembly and prolonged consolidation of Cordilleran magma chambers: Evidence from the southern Rocky Mountain volcanic field: Geosphere, v. 3, p. 42-70, doi: 10.1130/GES00061.1.

Liu, L., Gurnis, M., Seton, M., Saleeby, J., Muller, R.D., and Jackson, J.M., 2010, The role of oceanic plateau subduction in the Laramide orogeny: Nature Geoscience, v. 3, p. 353–357, doi: 10.1038/ngeo829.

MacCarthy, J.K., Aster, R.C., Dueker, K., Hansen, S., Borchers, B., Karlstrom, K.E., 2014, Seismic Tomography of the Colorado Rocky Mountains Upper Mantle from CREST: Lithosphere-Asthenosphere Interactions and Mantle Support of Topography: Earth and Planetary Science Letters EPSL-D-13-00517.

Machette, M.N., Personius, S.F., Kelson, K.I., Haller, K.M., and Dart, R.L., 1998, Map and data for Quaternary faults and folds in New Mexico: U.S. Geological Survey, Open-file Report 98-521, 443 p.

Mack, G.H., 2004, Middle and late Cenozoic crustal extension, sedimentation, and volcanism in the southern Rio Grande rift, Basin and Range, and southern transition zone of southwestern New Mexico, *in* Mack, G.H., and Giles, K.A., eds., The Geology of New Mexico, A Geologic History: New Mexico Geological Society Special Publication 11, p. 389-406.

Marvin, R.F., Young, E.J., Mehnert, H.H., and Naeser, C.W., 1974, Summary of radiometric age determinations on Mesozoic and Cenozoic igneous rocks and uranium and base metal deposits in Colorado: Isochron/West, no. 11, p. 1–41.

May, S.J., and Russell, L.R., 1994, Thickness of the syn-rift Santa Fe Group in the Albuquerque Basin and its relation to structural style, *in* Keller, G.R., and Cather, S.M., eds., Basins of the Rio Grande Rift: Structure, Stratigraphy, and Tectonic Setting: Boulder, Colorado, Geological Society of America Special Paper 291.

McIntosh, W.C., Chapin, C.E., Ratte, J.C., and Sutter, J.F., 1992, Time- stratigraphic framework for the Eocene–Oligocene Mogollon-Datil volcanic field, southwest New-Mexico: Geological Society of America Bulletin, v. 104, p. 851–871.

McKeon, Ryan E., 2009, The interaction between tectonics, topography and climate in the San Juan Mountains, southwestern Colorado [M.S. thesis]: Bozeman, Montana State University, 86 p.

McLemore, V.T., Munroe, E.A., Heizler, M.T., and McKee, C., 1999, Geochemistry of the Copper Flat porphyry and associated deposits in the Hillsboro mining district, Sierra County, New Mexico, USA: Journal of Geochemical Exploration, v. 66, p. 167-189.

McMillan, M.E., Angevine, C.L., and Heller, P.L., 2002, Postdepositional tilt of the Miocene-Pliocene Ogallala Group on the western Great Plains: evidence of late Cenozoic uplift of the Rocky Mountains: Geology, v. 30, p. 63-66, doi: 10.1130/0091-7613(2002)030<0063:PTOTMP>2.0.CO;2.

McQuarrie, N., and Chase, C.G., 2000, Raising the Colorado Plateau: Geology, v. 28, p. 91-94.

McQuarrie, N., and Wernicke, B.P., 2005, An animated tectonic reconstruction of southwestern North America since 36 Ma: Geosphere, v. 1, p. 147-172, doi: 10.1130/GES00016.1.

Mears, B., Jr., 1998, Neogene normal faulting superposed on a Laramide uplift: Medicine Bow Mountains, Sierra Madre, and intervening Saratoga Valley, Wyoming and Colorado: Contributions to Geology, v. 32, p. 181-185.

Michaut, C., Jaupart, C., and Bell, D.R., 2007, Transient geotherms in Archean continental lithosphere: New constraints on thickness and heat production of the subcontinental lithospheric mantle: Journal of Geophysical Research, v. 112, 17 p. doi: 10.1029/2006JB004464.

Miggins, D.P., Thompson, R.A., Pillmore, C.L., Snee, L.W., and Stern, C.R., 2002, Extension and uplift of the northern Rio Grande Rift—Evidence from $^{40}Ar/^{39}Ar$ geochronology from the Sangre de Cristo Mountains, south-central Colorado and northern New Mexico, *in* Menzies, M.A., Klemperer, S.L., Ebinger, C.J., and Baker, J., eds., Volcanic rifted margins: Geological Society of America Special Paper 362, p. 47–64.

Miller, M.G., 1999, Active breaching of a geometric segment boundary in the Sawatch Range normal fault, Colorado, USA: Journal of Structural Geology, v.21, p. 769–776.

Mitrovica, J.X., Beaumont, C., and Jarvis, G.T., 1989, Tilting of continental interiors by the dynamic effects of subduction: Tectonics, v. 8, p. 1079-1094, doi: 10.1029/TC008i005p01079.

Morgan, P., Seager, W.R., and Golombek, M.P., 1986, Cenozoic thermal, mechanical and tectonic evolution of the Rio Grande rift: journal of Geophysical Research, v. 91, p. 6263-6276.

Moucha, R., Forte, A.M., Rowley, D.B., Mitrovica, J.X., Simmons, N.A., and Grand, S.P., 2008, Mantle convection and recent evolution of the Colorado Plateau and the Rio Grande Rift valley: Geology, v. 36, p. 439-442, doi: 10.1130/G24577a.1.

Naeser, C.W., Cunningham, C.G., and Beaty, D.W., 1990, Part III. Fission-track and fluid inclusion studies, *in* Beaty, D.W., ed., Origin of the ore deposits at Gilman, Colorado: Economic Geology Monograph 7, p. 219–228.

Naeser, C.W., Bryant, B., Kunk, M.J., Kellogg, K., Donelick, R.A., and Perry, W.J., 2002, Tertiary cooling and tectonic history of the White River uplift, Gore Range, and western Front Range, central Colorado: Evidence from fission-track and 39Ar/40Ar ages, *in* Kirkham, R.M., et al., eds., Late Cenozoic Evaporite Tectonism and Volcanism in West-central Colorado: Geological Society of America Special Paper 355, p. 31-53, doi: 10.1130/0-8137-2366-3.31.

Olson, J.C., Marvin, R.F., Parker, R.L., and Mehnert, H.H., 1977, Age and tectonic setting of lower Paleozoic alkalic and mafic rocks, carbonatites, and thorium veins in

south-central Colorado: U.S. Geological Survey Journal of Research, v. 5, p. 673–687.

O'Neill, C.D., Muller, D., and Steinberger, B., 2005, On the uncertainties in hot spot reconstructions and the significance of moving hot spot reference frames: Geochemistry, Geophysics, Geosystems: v. 6, Q04003, doi: 10.1029/2004GC000784.

Ostenna, D.A., Losh, S.L., and Nelson, A.E., 1982, Upper Arkansas valley seismic hazards evaluation: Unpublished report on file at U.S. Bureau of Reclamation, Denver, Colorado.

Personius, S.F., and Mahan, S.A., 2003, Paleoearthquakes and eolian-dominated fault sedimentation along the Hubbell Spring fault zone near Albuquerque, New Mexico: Bulletin of the Seismological Society of America, v. 93, p. 1355-1369.

Personius, S.F., Machette, M.N., and Kelson, K.I., 1999, Quaternary faults in the Albuquerque area-An update, *in* Pazzaglia, F.J., and Lucas, S.G., eds., Albuquerque Geology: New Mexico Geological Society Guidebook, v. 50, p. 189-200.

Pray, L.C., 1961, Geology of the Sacramento Mountains escarpment, Otero County, New Mexico: New Mexico Bureau of Mines and Mineral Resources, Bulletin 35, 144 p.

Ramos, V.A., 2009, Anatomy and global context of the Andes: Main geologic features and the Andean orogenic cycle, *in* Kay, S.M., Ramos, V.A., and Dickinson, W.R., eds., Backbone of the Americas: Shallow Subduction, Plateau Uplift, and Ridge and Terrane Collision: Geological Society of America Memoir 204, p. 31-65, doi: 10.1130/2009.1204(02).

Reiter, M., Edwards, C.L., Hartman, H., and Weidman, C., 1975, Terrestrial heat flow along the Rio Grande rift, New Mexico and southern Colorado: Geological Society of America Bulletin, v. 86, p. 811-818.

Ricketts, J.W., Karlstrom, K.E., Kelley, S.A., and Read, A.S., 2011, Cross-section restoration from Ladron Peak to the Joyita Hills and investigations of the timing and mechanism of low-angle normal faulting in the Rio Grande rift: New Mexico Geological Society Spring Meeting, Abstracts, p. 56.

Ricketts, J.W., Karlstrom, K.E., Priewisch, A., Crossey, L.J., Polyak, V.J., and Asmerom, Y., 2014, Quaternary extension in the Rio Grande rift at elevated strain rates recorded in travertine deposits, central New Mexico: Lithosphere, v. 6, p. 3-16, doi: 10.1130/L278.1.

Roy, M., Karlstrom, K.E., Kelley, S.A., Pazzaglia, F.J., and Cather, S.A., 1999, Topographic setting of the Rio Grande rift, New Mexico: Assessing the role of "rift-flank uplift" in the Sandia Mountains, in Pazzaglia, F.J., and Luca, S.G., eds., Albuquerque Geology: New Mexico Geological Society 50th Annual Field Conference Guidebook, p. 167-174.

Roy, M., Kelley, S., Pazzaglia, F., Cather, S., and House, M., 2004, Middle Tertiary buoyancy modification and its relationship to rock exhumation, cooling, and

subsequent extension at the eastern margin of the Colorado Plateau: Geology, v. 32, p. 925-928, doi: 10.1130/G20561.1.

Roy, M, Jordan, T.H., and Pederson, J., 2009, Colorado Plateau magmatism and uplift by warming of heterogeneous lithosphere: Nature, v. 459, p. 978-982, doi: 10.1038/nature08052.

Russell, L.R., and Snelson, S., 1994, Structure and tectonics of the Albuquerque Basin segment of the Rio Grande rift: Insights from reflection seismic data, *in* Keller, G.R., and Cather, S.M., eds., Basins of the Rio Grande Rift: Structure, Stratigraphy, and Tectonic Setting: Boulder, Colorado, Geological Society of America Special Paper 291.

Sandeman, H.A., Clark, A.H., and Farrar, E., 1995, An integrated tectono-magmatic model for the evolution of the Southern Peruvian Andes (13°-20°S) since 55 Ma: International Geology Review, v. 37, p. 1,039-1,073.

Schmandt, B., and Humphreys, E., 2010, Complex subduction and small-scale convection revealed by body-wave tomography of the western United States upper mantle: Earth and Planetary Science Letters, v. 297, p. 435-445, doi:10.1016/j.epsl.2010.06.047.

Seager, W.R., and Morgan, P., 1979, Rio Grande rift in southern New Mexico, west Texas, and northern Chihuahua, *in* Riecker, R.E., ed., Rio Grande Rift: Tectonics and Magmatism: Washington, D.C., American Geophysical Union, p. 87-106.

Seager, W.R., Shafiqullah, M., Hawley, J.W., and Marvin, R.F., 1984, New K-Ar dates from basalts and the evolution of the southern Rio Grande rift: Geological Society of America Bulletin, v. 95, p. 87-99.

Shannon, J.R., 1988, Geology of the Mount Aetna cauldron complex, Sawatch Range, Colorado [Ph.D. thesis]: Golden, Colorado School of Mines, 434 p.

Sharp, W.N., 1970, Extensive zeolitization associate with hot springs in central Colorado: U.S. Geological Survey, Professional Paper 700-Bp. 14-20.

Sigloch, K., 2011, Mantle provinces under North America from multifrequency P wave tomography: Geochemistry Geophysics Geosystems, v. 12, p. 1-27, doi: 10.1029/2010GC003421.

Sigloch, K., McQuarrie, N., and Nolet, G., 2008, Two-stage subduction history under North America inferred from multiple-frequency tomography: Nature Geoscience, v. 1, p. 458-462, doi: 10.1038/ngeo231.

Smith, R.P., 1975, Structure and petrology of Spanish Peaks dikes, south central Colorado [Ph.D. thesis]: Boulder, University of Colorado, 270 p.

Song, T.-R.A., and Helmberger, D.V., 2007, A depleted, destabilized continental lithosphere near the Rio Grande rift: Earth and Planetary Science Letters, v. 262, p. 175-184, doi: 10.1016/l.epsl.2007.07.052.

Stewart, J.H., and Carslon, J.E., 1976, Cenozoic rocks of Nevada: Nevada Bureau of Mines and Geology Map 52.

Stockli, D.F., 2005, Application of low-temperature thermochronometry to extensional settings, *in* Reiners, P.W., and Ehlers, T.A., eds., Low-Temperature Thermochronology: Techniques, Interpretations, and Applications: Reviews in Mineralogy and Geochemistry, v. 58, p. 449-466.

Tarduno, J.A., McWilliams, M., Debiche, M.G., Sliter, W.V., and Blake, M.C. Jr, 1985, Franciscan Complex Calera limestones: Accreted remnants of Farallon Plate oceanic plateaus: Nature, v. 317, p. 345-347.

Thompson, R.A., and Machette, M.N., 1989, Geologic map of the San Luis Hills area, Conejos and Costilla counties, Colorado: U.S. Geological Survey Miscellaneous Investigations Series Map I–1906, scale 1:50,000.

Thompson, T.B., 1972, Sierra Blanca igneous complex, New Mexico: Geological Society of America Bulletin, v. 83, p. 2,341-2,356.

Thompson, T.B., and Arehart, G.B., 1990, Geology and the origin of ore deposits in the Leadville district, Colorado—Part I. Geologic studies of orebodies and wall rocks, *in* Beaty, D.W., Landis, G.P., and Thompson, T.B., eds., Carbonate-hosted sulfide deposits of the central Colorado mineral belt: Economic Geology Monograph no. 7, p. 130-155.

van der Lee, S., and Nolet, G., 1997, Upper mantle S velocity structure of North America: Journal of Geophysical Research, v. 102, p. 22,815–22,838, doi: 10.1029/97JB01168.

van Wijk, J., van Hunen, J., and Goes, S., 2008, Small-scale convection during continental rifting: Evidence from the Rio Grande rift: Geology, v. 36, p. 575–578; doi: 10.1130/G24691A.1.

Varga, R.J., 1993, Rocky Mountain foreland uplifts: Products of a rotating stress field or strain partitioning?: Geology, v. 21, p. 1115-1118, doi: 10.1130/0091-7613(1993)021<1115:RMFUPO>2.3.CO;2.

Wallace, A.R., 1995, Isotopic geochronology of the Leadville 1° x 2° quadrangle, west-central Colorado−Summary and discussion: U.S. Geological Survey Bulletin 2104, 51p.

Wallace, A.R., 2004, Evolution of the southeastern San Luis basin margin and the Culebra embayment, Rio Grande rift, southern Colorado, *in* Brister, B., Bauer, P.W., Reed, A.S., and Lueth, V.W., eds., Geology of the Taos Region: New Mexico Geological society Guidebook 55, p. 181-192.

Wernicke, B.P., Christiansen, R.L., England, P.C., and Sonder, L.J., 1987, Tectonomagmatic evolution of Cenozoic extension in the North America Cordillera, *in* Coward, M.P., Dewey, J.F., and Hancock, P.L., eds., Continental extensional tectonics: Geological Society Special Publication 28, p. 203-221.

West, M., Ni, J., Baldridge, W.S., Wilson, D., Aster, R., Gao, W., and Grand, S., 2004, Crust and upper mantle shear wave structure of the southwest United States:

Implications for rifting and support for high elevation: Journal of Geophysical Research, v. 109, B03309, doi: 10.1029/2003JB002575.

Wilson, D., Aster, R., West, M., Ni, J., Grand, S., Gao, W., Baldridge, W.S., Semken, S., and Patel, P., 2005, Lithospheric structure of the Rio Grande rift: Nature, v. 433, p. 851-855, doi: 10.1038/nature03297.

Woodward, L.A., 1983, Potential oil and gas traps along the overhang of the Nacimiento uplift, northwestern New Mexico, *in* Lowell, J.D., and Gries, R., eds., Rocky Mountain Foreland Basins and Uplifts: Rocky Mountain Association of Geologists, Guidebook, p. 213-218.

Woodward, L.A., 1987, Geology and mineral resources of Sierra Nacimiento and vicinity, New Mexico: New Mexico Bureau of Mines and Mineral Resources, Memoir 42, 84 p.

Yuan, H., and Romanowicz, B., 2010, Lithospheric layering in the North American craton: Nature, v. 466, p. 1063-1068, doi:10.1038/nature09332.

Zimmerer, M.J., and McIntosh, W.C., 2012, An investigation of caldera-forming magma chambers using the timing of ignimbrite eruptions and pluton emplacement at the Mt. Aetna caldera complex: Journal of Volcanology and Geothermal Research, v. 245-246, p. 128-148, doi: 10.1016/j.jvolgeores.2012.08.007.

Zimmerer, M.J., and McIntosh, W.C., 2013, Geochronologic evidence of upper-crustal in situ differentiation" Silicic magmatism at the Organ caldera complex, New Mexico: Geosphere, v. 9, p. 155-169.

CHAPTER 2: Embryonic core complexes in narrow continental rifts: The importance of low-angle normal faults in the Rio Grande rift of central New Mexico

Jason W. Ricketts[1], Karl E. Karlstrom[1], Gary A. Axen[2], and Shari A. Kelley[2]

[1]Department of Earth and Planetary Sciences, University of New Mexico, MSC03-2040, 1 University of New Mexico, Albuquerque, NM, 87131

[2]Earth and Environmental Sciences Department, New Mexico Institute of Mining and Technology, 801 Leroy Place, Socorro, NM. 87801

ABSTRACT

The Rio Grande rift in central New Mexico provides an excellent location to study early stages in the development of low-angle (15-35°) normal faults (LANF's). Here we document two brittle LANF systems on salients in adjacent opposite-polarity half-grabens. These fault systems were both active ~20-10 Ma, and are locations of maximum fault slip as indicated by thickness of sedimentary fill in adjacent sub-basins and highest elevation rift flanks. Average fault dip increases basinward, and outbound faults were abandoned while intrabasinal faults cut Quaternary units, supporting an evolutionary model where master normal faults initiated at a higher dip, were shallowed by isostatic footwall uplift in regions of highest slip, and became inactive while younger normal faults emerged basinward. This mechanism has been widely applied to core complexes in highly-extended terranes (e.g. Basin and Range), regions of orogenic collapse, and mid-ocean ridges, and is shown here to be applicable to narrow continental rifts of modest (~ 35%) extension. Similarities to core complexes include a physiographic

expression of domal uplifts, evolution of a master detachment horizon that initiated as a breakaway, and isostatically-rotated low-angle normal faults, although the degree of extension was too low to juxtapose ductile footwall rocks against brittle hanging wall rocks. The Rio Grande rift, therefore, provides a snapshot of the embryonic stages of core complex formation, bridging the gap between mature core complexes and incipient extensional environments.

INTRODUCTION

The Rio Grande rift, extending more than 1,000 km from Colorado to Mexico, is one of the world's premier and best studied continental rift systems. Although research on understanding the geology of the rift has been ongoing for decades, many questions still remain regarding the timing and style of its structural development. Continued interest in the rift is driven not only by the need to understand continental extensional processes, but also because of a need to understand and characterize potential seismic hazards (e.g. Wong et al., 2004), the valuable water resources of the basin fill aquifers in Colorado and New Mexico (e.g. Bartolino and Cole, 2002; Plummer et al., 2004; Johnson et al., 2013), and potential oil and gas production (Black, 2013). These issues are especially important in the Albuquerque metropolitan area, the fastest growing region in New Mexico. To address important earthquake, oil and gas, and water-related issues in New Mexico, it is necessary to have a firm understanding of young deformation (e.g. Berglund et al., 2012; Ricketts et al., 2014) as well as the longer term evolutionary history of rift faults and basin geometry. Continuing efforts to understand these issues related to the Rio Grande rift have led to the development of two Geological Society of

America (GSA) Special Papers: GSA Special Paper 291, edited by Keller and Cather (1994), and GSA Special Paper 494, edited by Hudson and Grauch (2013).

The goal of this paper is to evaluate two conflicting models for rift geometry and evolution of the Albuquerque basin of central New Mexico, one of the largest basins in the Rio Grande rift. Russell and Snelson (1994) used seismic reflection and borehole data to develop one of the most widely cited models of the subsurface geometry of the Albuquerque basin, which suggested that the Albuquerque basin is composed of two individual half-grabens which alternate polarity. In their subsurface interpretations, surface faults are listric and sole into low angle faults at shallow (5-10 km) crustal depths. Alternatively, Grauch and Connell (2013) utilized diverse geophysical datasets from the Albuquerque basin to construct a model of the subsurface that indicates a predominance of extension along high angle faults and a more complex anticlinal accommodation zone between opposite polarity basin segments. The differences in interpretations are depicted in Figure 1 that shows ~EW cross-sections constructed across the northern Albuquerque basin by Russell and Snelson (1994) and Grauch and Connell (2013) that highlight their different interpretations of basin depth and fault geometry. The most prominent difference between these two interpretations is the importance of low-angle normal faults (LANF's) in the Russell-Snelson model, and the lack of such features in the Grauch-Connell model. Assuming no movement in or out of the sections and rigid body rotations and translations, palinspastic reconstructions of these two cross-sections along the Great Unconformity at the top of Precambrian rocks suggests that LANF's in the subsurface provide a better way to balance upper crustal brittle extension with middle crust ductile extension across shear zones (Fig. 1), an observation that has been supported by

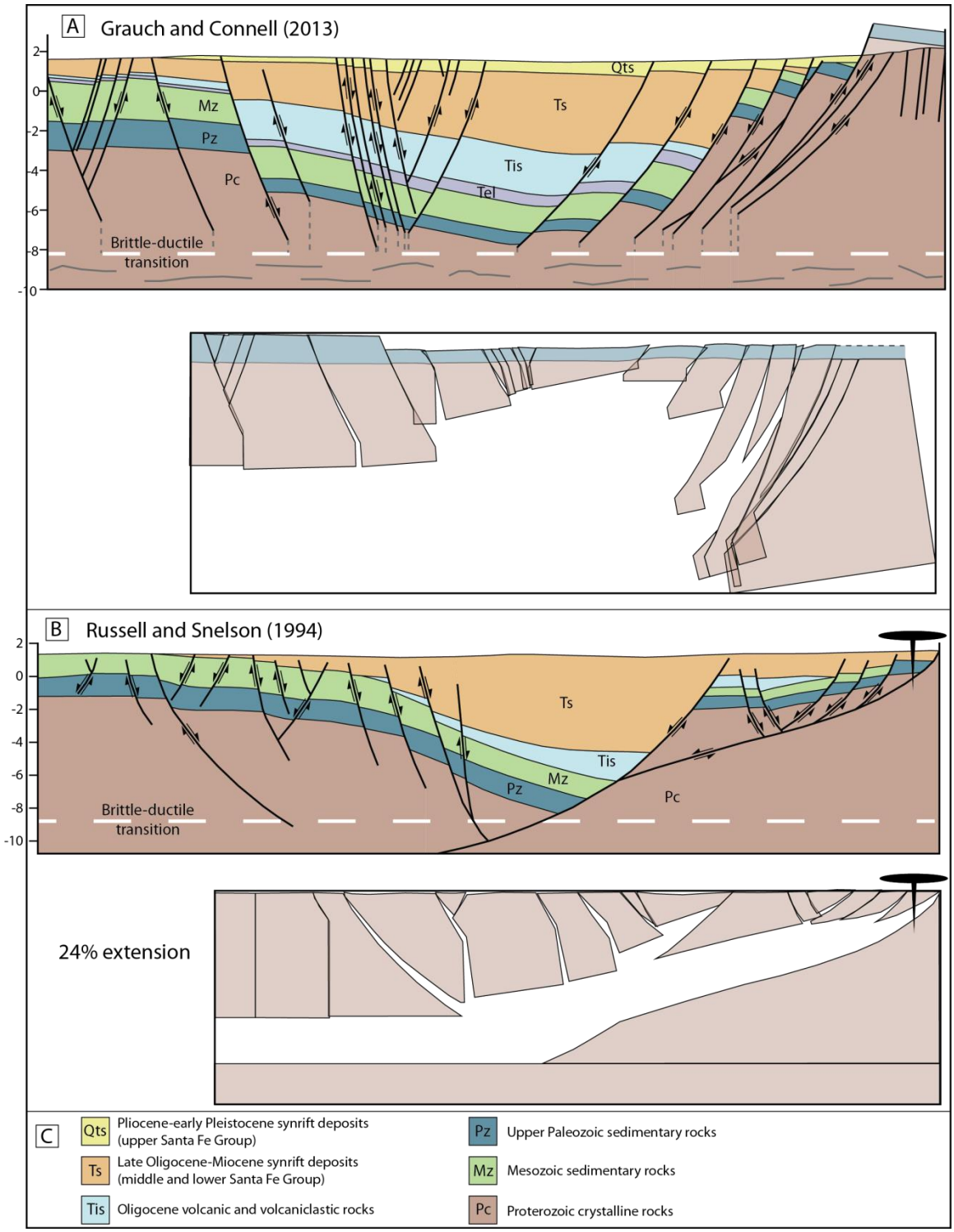

Figure 1. A. EW cross-section across the northern Albuquerque basin (Grauch and Connell, 2013), and our palinspastic reconstruction at the top of the Precambrian rocks. **B**. EW cross-section across the northern Albuquerque basin (Russell and Snelson, 1994) and a modified version of their palinspastic reconstruction. **C.** Explanation of units.

numerous authors (e.g. McKenzie, 1978; Wernicke, 1985). Alternatively, the Grauch and Connell (2013) cross section does not explicitly address strain compatibility issues, but presumably would rely on pervasive pure shear-dominated middle crustal flow (McKenzie, 1978).

This paper examines and evaluates the importance of exposed LANF's in the Rio Grande rift to help answer the question of their overall importance in the modest-extension (~17-35%; Russell and Snelson, 1994) Albuquerque basin of the Rio Grande rift, central New Mexico. We apply a combination of physiographic observations, fault orientations, kinematic studies, and low-temperature thermal history modeling to understand the evolution of some long-recognized (Black, 1964), but poorly-understood (e.g. Baldridge et al., 1984), LANF segments. We examine whether these LANF's initiated and moved at low or high angle, and what can be learned in this moderate extension, narrow, continental rift system to inform models for rift basin segmentation, rift geometry, and early stages of core complex development in extensional domains. On a scale of the Rio Grande rift, we explore the importance of fault rotation and LANF's, as opposed to models involving only high-angle faults (e.g. Grauch and Connell, 2013), to explain rift flank geometries and strain compatibility between upper crustal and deeper crustal extension. Within this context, and with the ultimate goal of producing a robust fault evolutionary model for the Albuquerque basin, below we summarize observations and constraints on fault geometry and fault age in the Albuquerque basin, central New Mexico.

BACKGROUND ON EXTENSIONAL FAULT GEOMETRIES

The expression of extension in both oceanic and continental settings appears to be strongly dependent on the geotherm, and the ability of the deep crust to flow (Block and Royden, 1990; Brun and van den Driessche, 1994; Lavier et al., 2000; Rey et al., 2009a, 2009b; Whitney et al., 2013). Heat flow dictates, to a large extent, the degree to which the brittle upper crust and lower ductile crust are mechanically coupled. In regions of cold to average continental heat flow, there is a strong mechanical coupling between the brittle upper crust and the lower ductile crust, and two-dimensional models predict that the lower ductile crust will thin homogeneously without responding to gravitational stresses (Whitney et al., 2013). As the lower crust thins, numerous normal faults develop in the brittle upper crust to produce graben and half-graben geometry, as well as domino-style block rotation (Fig. 2A). In relatively hot crust, the brittle upper crust is mechanically decoupled from the lower ductile crust (e.g. Brun et al., 1994; Whitney et al., 2013). Under these conditions, strain becomes localized along a single, large-offset normal fault system, which often initiates at a high angle and rotates to shallower dips due to isostatic rebound (Spencer, 1984; Buck, 1988; Wernicke and Axen, 1988; Wdowinski and Axen, 1992; Axen and Bartley, 1997). New high-angle faults then emerge basinward, and if this process continues, eventually lower crustal ductilely-deformed rocks can be exhumed to the surface in the footwall of the LANF to form a core complex (Fig. 2B). In this model, normal faults young towards the axis of the basin.

LANF's are observed in sandbox experiments, are predicted in numerical models, and are a near-ubiquitous feature of extensional domains. However, LANF's in modest-extension, narrow (< 100 km wide), upper-crustal continental rifts are not as well

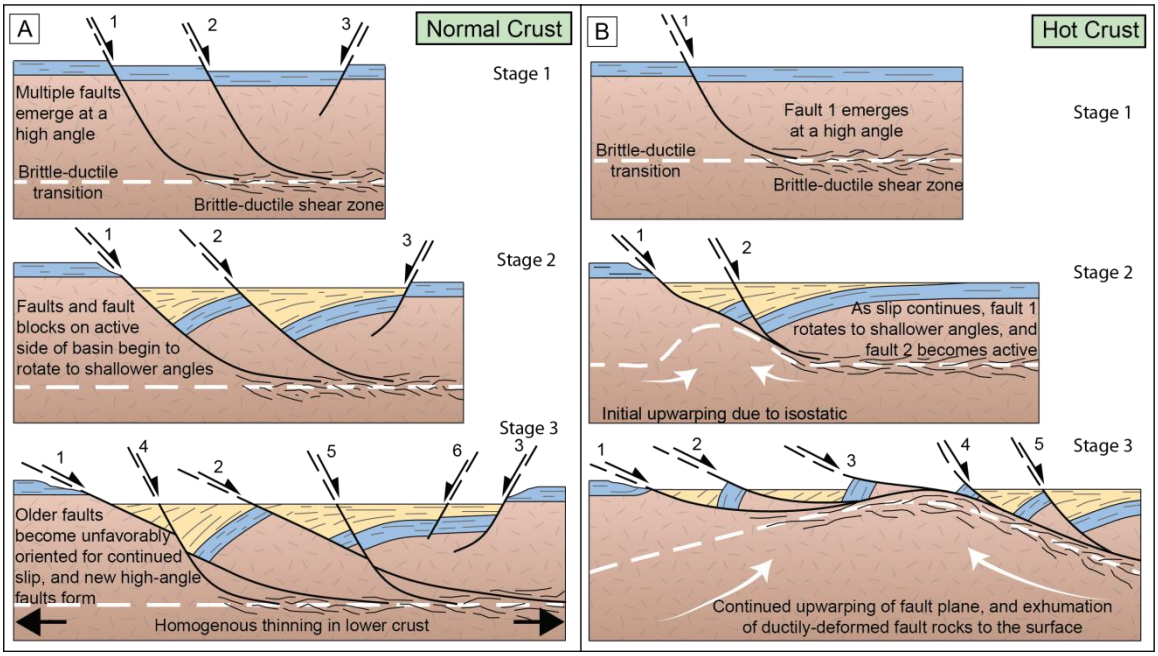

Figure 2. Schematic evolution of low-angle normal faults under **A**. normal and **B.** hot crustal conditions.

documented. This paper takes the view that understanding faults in these settings may provide clues about the early development of LANF's and core complexes in general.

GEOLOGIC SETTING OF THE ALBUQUERQUE BASIN

The north-south trending Rio Grande rift is a classic, well-exposed, and well-studied example of a narrow and still-active (e.g. Berglund et al., 2012; Ricketts et al., 2014) continental rift system. Early extension began ~36-37 Ma (Kelley and Chamberlain, 2012), and resulted in modest magnitude extension that likely began the process of separating the relatively undeformed Colorado Plateau to the west from the Great Plain province to the east. However, the modern physiography and N-S extent of the rift is the result of mainly Miocene extension, which was the time of accumulation of most of the E-W extensional strain. Normal fault geometries were influenced to some degree by reactivated earlier faults of Precambrian, Ancestral Rockies, and Laramide age (e.g. Karlstrom et al., 1999; Marshak et al., 2000).

The rift is composed of a series of NS-trending basins that form an array of *en echelon* grabens and half-grabens that alternate polarity and are linked by NE-trending accommodation zones (e.g. Chapin and Cather, 1994) that serve to transfer the maximum displacement from one rift margin to the other (e.g. Faulds and Varga, 1998; Russell and Snelson, 1994; Minor et al., 2013). Within the Rio Grande rift, isolated exposures of LANF's have been known for decades (e.g. Baldridge et al., 1984), although they exist within a predominantly high-angle normal fault environment, and models for their formation are largely lacking. Recent models and maps for the Rio Grande rift (Connell, 2008; Grauch and Connell, 2013) emphasize steep faults in accommodating crustal

extension and apparently do not consider LANF's to be an important component of the overall rift geometry and kinematic evolution.

The Albuquerque basin, located in central New Mexico, is one of the largest basins of the Rio Grande rift. Structurally it is bounded on all sides by normal fault systems, and growth of the basin has resulted in the development of multiple sub-basins that are filled with the syn-extensional sedimentary basin fill of the Santa Fe Group (Fig. 3). The northern (Albuquerque) sub-basin is an east-tilted half-graben, where Santa Fe Group sediments dip towards west-dipping normal fault systems along the Sandia uplift (> 3 km elevation; Fig. 3). The southern (Belen) sub-basin encompasses multiple half-grabens that are filled with gently-dipping Santa Fe Group sediments. Steeper southwest-dipping beds of the Santa Fe Group are restricted to the southwestern part of the basin (Grauch and Connell, 2013), and dip into an east-dipping normal fault system (Jeter fault) that bounds the Ladron rift-flank (2.7 km elevation; Fig. 3).

Southern Albuquerque Basin and the Ladron Uplift

The Ladron uplift is a high elevation promontory that protrudes east along the southwestern edge of the Albuquerque basin, at the junction between a relatively narrow Rio Grande rift to the north and more distributed extension to the south that is similar in style to the Basin and Range province. This uplift is bounded on its western edge by the Ladron fault, which separates Precambrian granitic and metamorphic rocks in the footwall from Paleozoic sediments in the hanging wall. The rift-bounding structure along the eastern margin of the Ladron uplift is the Jeter fault, the best-known and most well-studied LANF in the Albuquerque basin (Black, 1964; Lewis and Baldridge, 1994; Read

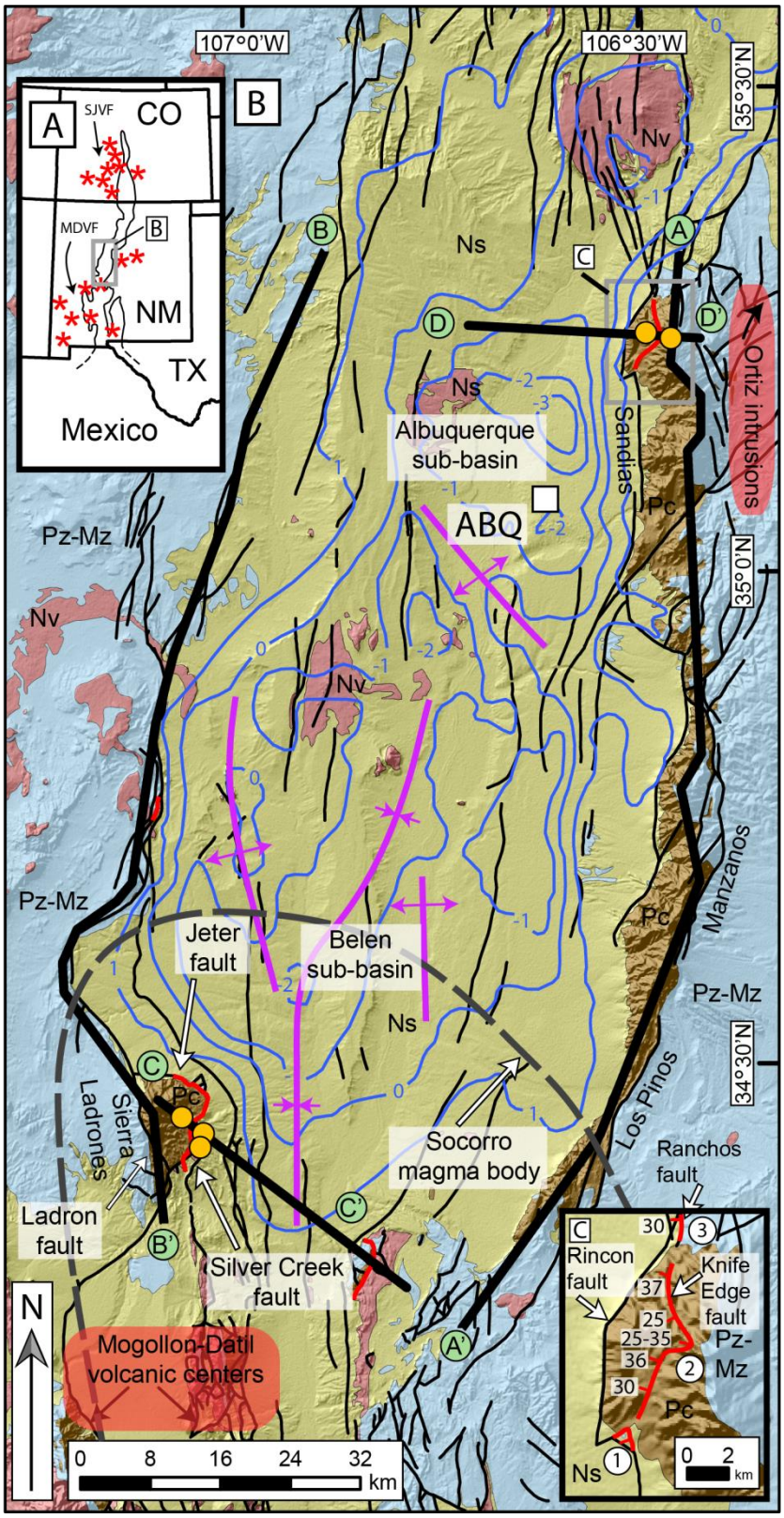
107°0'W
106°30'W
35°30'N
35°0'N
34°30'N
A
B
SJVF
CO
MDVF
NM
TX
Mexico
Nv
Ns
C
D
D'
Ortiz intrusions
Sandias
Pc
Albuquerque sub-basin
ABQ
Pz-Mz
Manzanos
Belen sub-basin
Jeter fault
Socorro magma body
Los Pinos
Ranchos fault
Sierra Ladrones
Ladron fault
Silver Creek fault
Mogollon-Datil volcanic centers
N
0 8 16 24 32 km
Rincon fault
Knife Edge fault
0 2 km

Figure 3. A. General outline of the Rio Grande rift and study area in New Mexico. Red stars are locations of Oligocene – early Miocene calderas or igneous intrusions. SJVF = San Juan volcanic field; MDVF = Mogollon-Datil volcanic field **B.** Simplified geologic map of the Albuquerque basin in central New Mexico. Thick black lines are topographic profiles depicted in Figure 2. Red lines are locations of LANF's in the Albuquerque basin. Structural elevation of the base of the Santa Fe Group shown as blue lines in kilometers above sea level and green fold axes are from Grauch and Connell (2013). Orange circles are sample locations for joint apatite fission-track and apatite (U-Th)/He thermal history models. Ns = Neogene sedimentary basin fill deposits; Nv = Neogene volcanic rocks; Pz-Mz = Paleozoic and Mesozoic strata; Pc = Precambrian granitic and metamorphic rocks; ABQ = Albuquerque. **C.** Close-up of low-angle normal faults in the Sandia Mountains shown as red lines. Fault dips indicated where measured. Numbered locations are referred to in the text.

et al., 2007). This structure dips ~15-25° east and contains Precambrian granitic and metamorphic rocks in the footwall (Fig. 4). The hanging wall adjacent to the Jeter fault is an intensely brecciated zone containing slivers of Paleozoic and Mesozoic rocks, Neogene volcanic and volcaniclastic rocks, and Santa Fe Group rift fill. Santa Fe Group sediments dip ~25-35° west towards the fault plane (Read et al. 2007). Fault plane and slickenline orientations along the Jeter fault define a shallowly-dipping normal fault system with SE-directed slip that we interpret to be the movement direction for rifting in this part of the rift (Fig. 4). In the hanging wall of the Jeter fault, the Silver Creek fault dips ~25-35° east, and is inferred to sole into the Jeter master detachment at depth. The Silver Creak fault largely separates Paleozoic and Mesozoic rocks in the footwall from Santa Fe Group rift fill sediments in the hanging wall (Read et al., 2007).

Northern Albuquerque Basin and the Sandia Uplift

The Sandia uplift is the highest elevation part of the eastern rift flanks and is located along the northeastern edge of the Albuquerque basin. It is composed of Precambrian granitic and metamorphic rocks capped by east-dipping Paleozoic sedimentary rocks (Fig. 3C). The rift-bounding structures on the west side of the Sandia uplift include the high-angle Rincon fault and disconnected LANF's at three separate

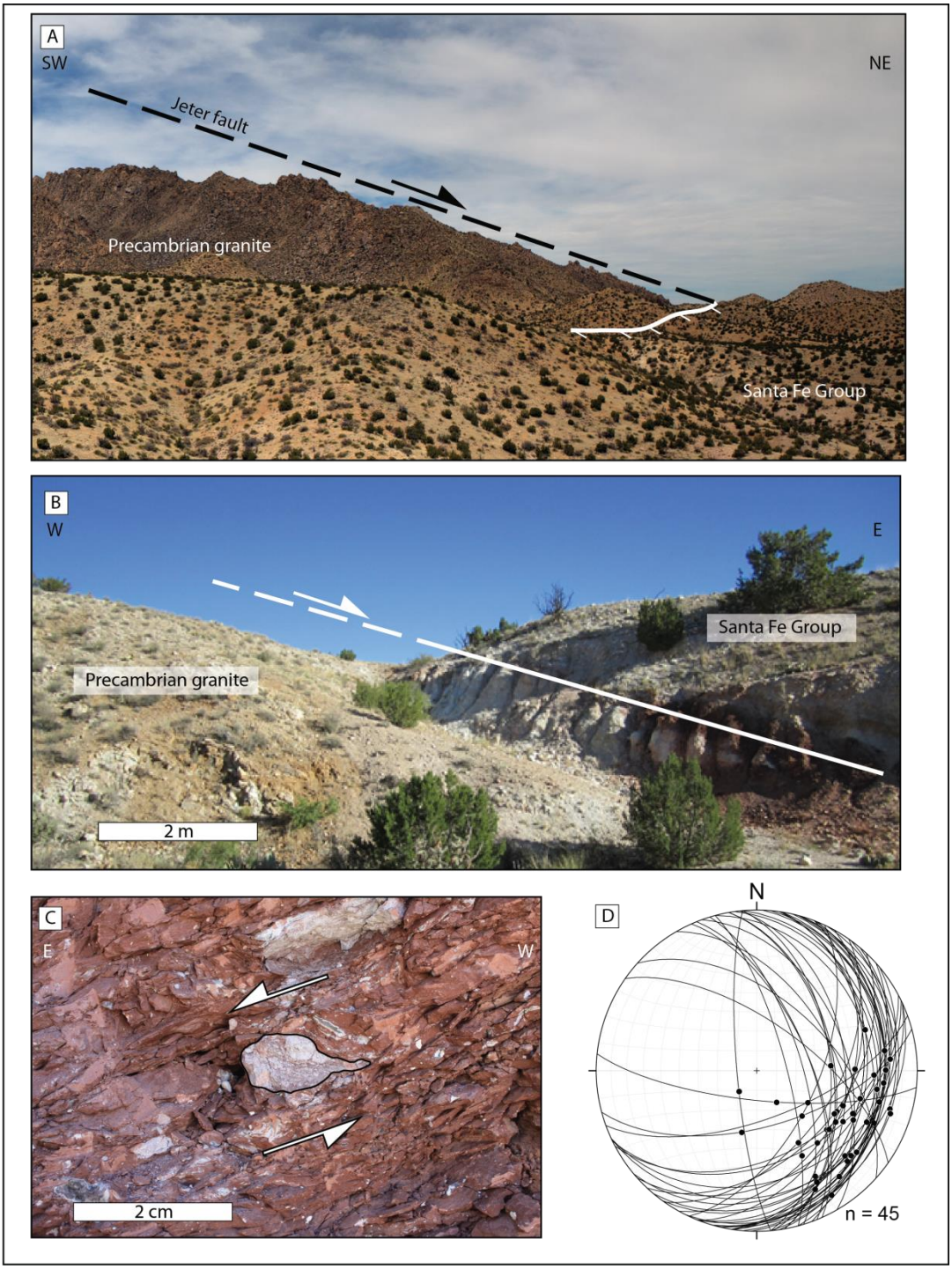

Figure 4. A. View looking northwest of the Ladron uplift, bounded by the low-angle Jeter fault. **B.** Jeter fault separating Precambrian granite in the footwall from Santa Fe Group rift-fill in the hanging wall. **C.** Close-up view looking south of reddish-purple foliated fault gouge that makes up the core of the Jeter fault. Gouge contains pulverized fragments of granite, with well-developed shear bands and sigma clasts (outlined), indicating normal-sense movement. **D.** Lower hemisphere equal-area stereographic projections of fault planes (plotted as planes) and slickenlines (plotted as lines) for the Jeter fault.

locations (1, 2, and 3 in Fig. 3C). Location 1, at the base of the Sandia uplift in the Juan Tabo area, preserves a small klippe of ~30° east-dipping Mesozoic rocks that are underlain by Precambrian granite (Fig. 5). Although the fault is mostly concealed, magnetic surveys plus the geometry of the contact suggests this is a low-angle fault contact (Van Hart, 1999). We refer to this low-angle fault as the Juan Tabo fault. At location 2, Read et al. (1999) mapped a low-angle fault zone that cuts Precambrian granitic rocks. They refer to this structure as the Knife Edge fault. New mapping, along with fault plane and slickenline measurements along this zone, suggest it dips ~25°-35° west with top-to-the-west slip (Fig. 5). This fault is aligned with the ridge of the bedrock facet above called the Shield, suggesting that the "Knife Edge of the Shield" is an exhumed upward continuation of this fault zone as shown in Figure 5A. Riedel shears and slickenlines indicate normal-sense movement with top-to-the-west movement direction (Fig. 5B). Farther north, the Ranchos fault (location 3 in Fig. 3C) separates 15° east dipping Santa Fe Group sediments from Mesozoic footwall rocks along a normal fault dipping ~30° (Fig. 5D; Kelley, 1975; May et al., 1994). Truncation of hanging wall strata and a ~6 cm thick gouge zone show this is not an unconformable contact. At all locations, deformation associated with these structures is entirely brittle.

Central Albuquerque Basin Accommodation Zone

Accommodation zones in the Rio Grande rift vary in width from >10 km to narrower transfer zones that are < 3 km wide. They variably consist of single faults, multiple fault zones, single folds, multiple folds, or any combination of these (Faulds and Varga, 1998; Smith et al, 2001; Goteti et al., 2013; Koning et al., 2013). The observation of opposing polarities of half-grabens between the northern and southern parts of the

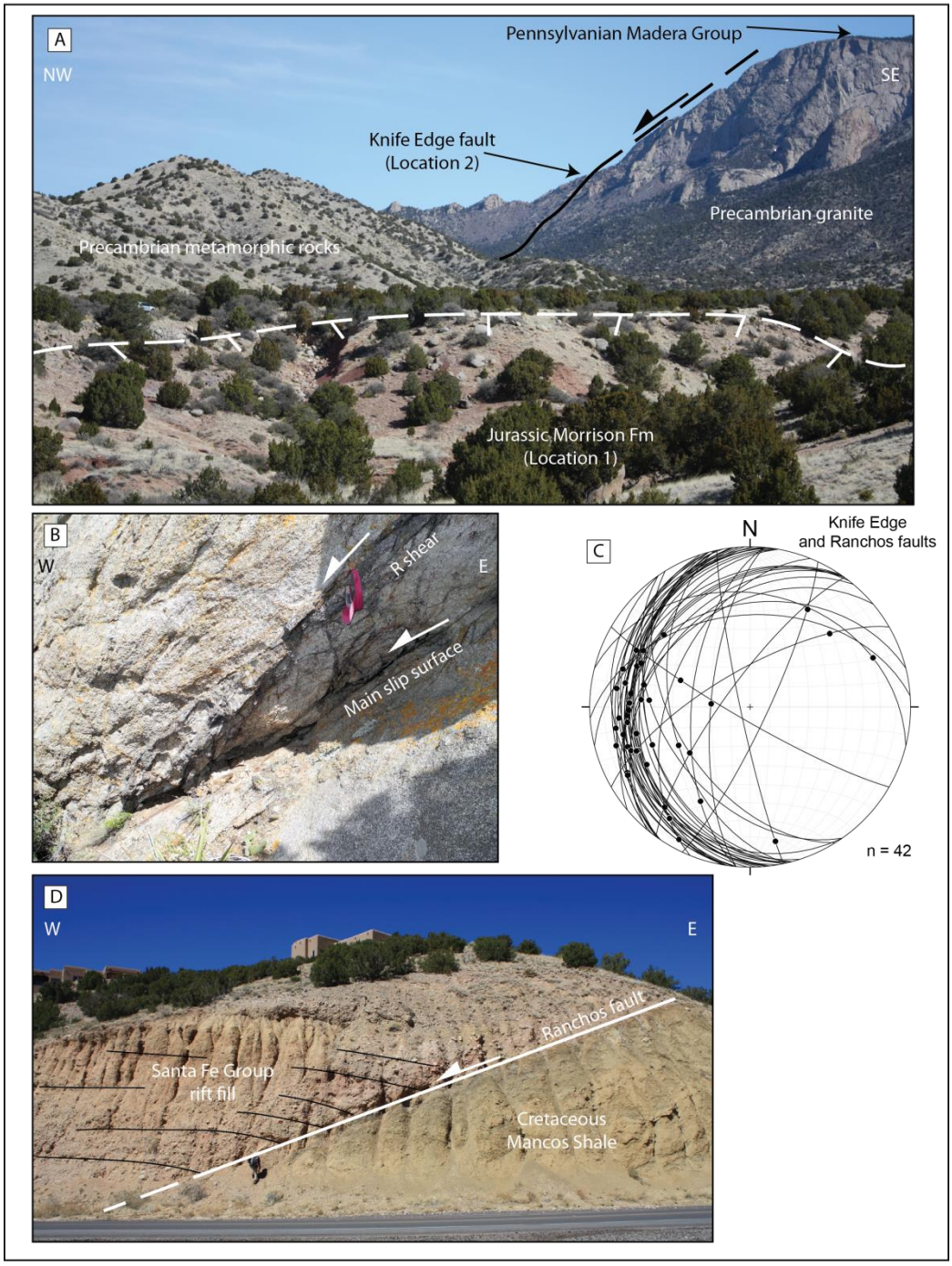

Figure 5. A. View looking N-NE towards the Sandia uplift, where the Knife Edge fault cuts Precambrian granite in the background. In the foreground, a low-angle fault at Juan Tabo separates Mesozoic rocks from Precambrian rocks. **B.** Close-up of the Knife Edge fault looking north. Synthetic R shears form at angles of ~15° from the main shear surface. **C.** Lower hemisphere equal-area stereographic projections of fault planes (plotted as planes) and slickenlines (plotted as lines) for the Knife Edge and Ranchos faults. **D.** View looking north of the Ranchos fault, separating Mesozoic rocks in the footwall from Santa Fe Group rift fill in the hanging wall.

Albuquerque basin necessitates the presence of an accommodation zone in the central Albuquerque basin, but its geometry has been controversial. Originally, this structure was hypothesized to be a narrow fault zone that was a continuation of the Tijeras fault at the southern end of the Sandia uplift (Cather, 1992; Russell and Snelson, 1994; May et al., 1994; Lewis and Baldridge, 1994). However, aeromagnetic surveys of the Albuquerque basin did not directly image such a structure (Grauch, 2001), calling into question its existence. More recently, utilizing diverse geophysical datasets, Grauch and Connell (2013) suggested that this accommodation zone instead consists of a series of NW-trending anticlinal structures, and referred to it as an oblique anticlinal accommodation zone, after Faulds and Varga (1998).

METHODS OF STUDY

The goals of this study are to construct evolutionary models of the northern and southern parts of the Albuquerque basin that explain the observed high- and low-angle normal fault networks. Here we synthesize relationships between basin geometry and fault networks, as well as timing of faulting for producing evolutionary (kinematic) models. We constructed longitudinal topographic profiles along the rift flanks from 10m digital elevation models to observe variation in rift flank elevation from north to south on each rift flank. These were compared to longitudinal profiles that were created along the base of the Santa Fe Group rift fill near the eastern and western edges of the rift based on structure contour maps of the base of the Santa Fe Group that have recently been constrained at a high resolution utilizing multiple geophysical methods (Grauch and Connell, 2013).

Fault geometries and ages were also investigated along transverse cross-section lines C-C' and D-D' (Fig. 3) through the Ladron and Sandia uplifts. These cross-sections are parallel to the extension direction as inferred from slickenlines on fault planes. Fault dips were compiled, and geologic cross-sections were constructed from published geologic maps in the northern (Connell, 2008), and southern (Machette, 1978; DeMoor et al., 2005; Connell and McGraw, 2007; Read et al., 2007) parts of the Albuquerque basin, as well as new mapping of faults.

We also report new data on timing constraints on fault activity in the Sandia and Ladron uplifts inferred from apatite fission-track (AFT) and apatite (U-Th)/He (AHe) cooling ages. We build on existing data that includes AFT ages for the Ladron uplift (Kelley et al., 1992), and AFT and AHe data for the Sandia uplift (House et al., 2003). To expand upon this dataset, additional AFT and AHe data were collected from the Ladron uplift. For intrabasinal faults, times of most recent activity are from the U.S. Geological Survey and New Mexico Bureau of Geology and Mineral Resources (2006).

MORPHOMETRIC ANALYSIS OF THE ALBUQUERQUE BASIN

Basin Geometry and Rift Flank Topography

Facing rift flanks on opposite sides of the Albuquerque basin (Fig. 6A) show roughly a mirror image of the other, with the Sandia (3.2 km) and Ladron (2.7 km) uplifts forming the highest rift flanks in the northern and southern Albuquerque basin, respectively. Geophysical data indicate these uplifts are adjacent to the deepest depocenters located in the northeastern and southwestern portions of the basin. The northern Albuquerque sub-basin depocenter reaches minimum elevations of < -3 km, while the southern Belen sub-basin depocenter extends to < -2 km elevation. Using the

elevation difference between rift flanks and base of the Santa Fe Group as a first-order proxy for total throw along rift-bounding normal faults, we identify a close spatial association between regions of maximum fault throw, highest rift-flanks, and localities of LANF's, as it is in these two locations that LANF's are best developed (Fig. 6A).

Fault Geometry

In both the northern and southern parts of the Albuquerque basin adjacent to the Ladron and Sandia uplifts, average fault dip increases from the rift flank towards the axis of the basin (Figs. 6B, 7). In the northern Albuquerque basin, low-angle normal faults (faults at locations 1, 2, and 3 in Figure 3) are restricted to the Sandia Mountain front. Based on total offset and relation to the high-angle faults nearby, the Ranchos and Juan Tabo faults are nearly coplanar and may have once been part of the same fault system, but now exist as isolated remnants that were cut by the high-angle Rincon fault (Fig. 3C). The Knife Edge fault is most likely a separate structure from the other two because it separates Precambrian from Precambrian rocks without significant offset of the Great Unconformity. This is supported by indistinguishable AFT cooling ages on either side of the fault (House et al., 2003). All other faults along the cross-section line dip >50°. In addition, both synthetic and antithetic faults contribute to the total extension observed (Figs. 6B, 7).

In the southern parts of the basin, faults have somewhat different geometries. LANF segments are restricted to the Ladron uplift, and there is a progression from low- to high-angle towards the center of the basin. For example, the Jeter fault dips ~15°-25°. In the hanging wall of the Jeter fault, the Silver Creek fault has multiple strands, with recorded fault plane dip measurements of 24° and 48° in the direction towards the axis of

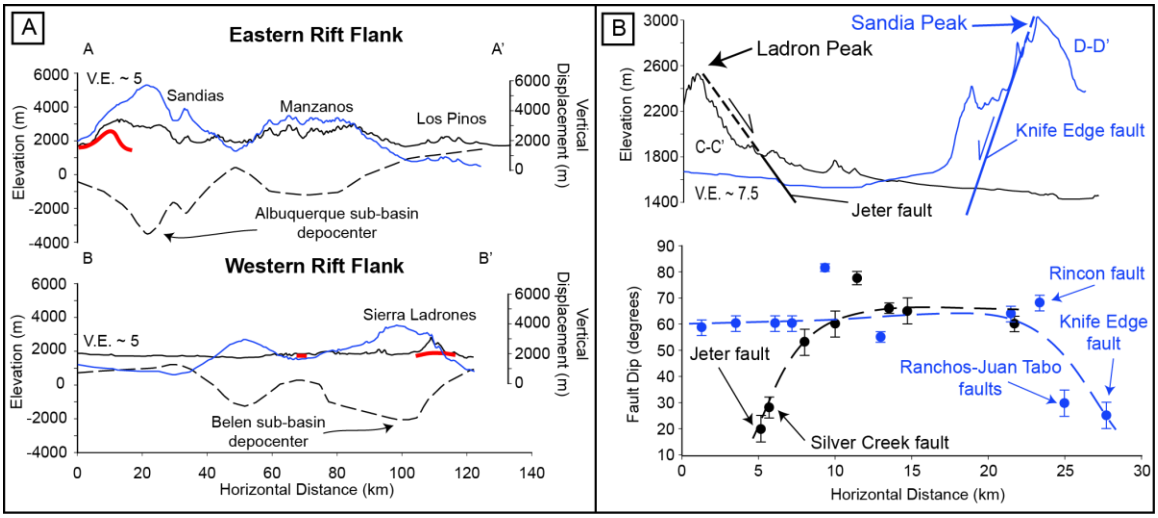

Figure 6. A. North-south topographic profiles (solid black lines) along the uplifted shoulders of rift margins. Black dashed line is base of the Santa Fe Group. LANF's are shown as thick gray lines along each topographic profile. Variations in vertical displacement along rift-bounding faults (gray lines) are estimated by subtracting the base of Santa Fe Group from topographic profiles. Locations of topographic profiles shown in Figure 2. **B.** Plots of horizontal distance vs. elevation (top), and fault dip (bottom), along C-C' (in black) and D-D' (in gray).

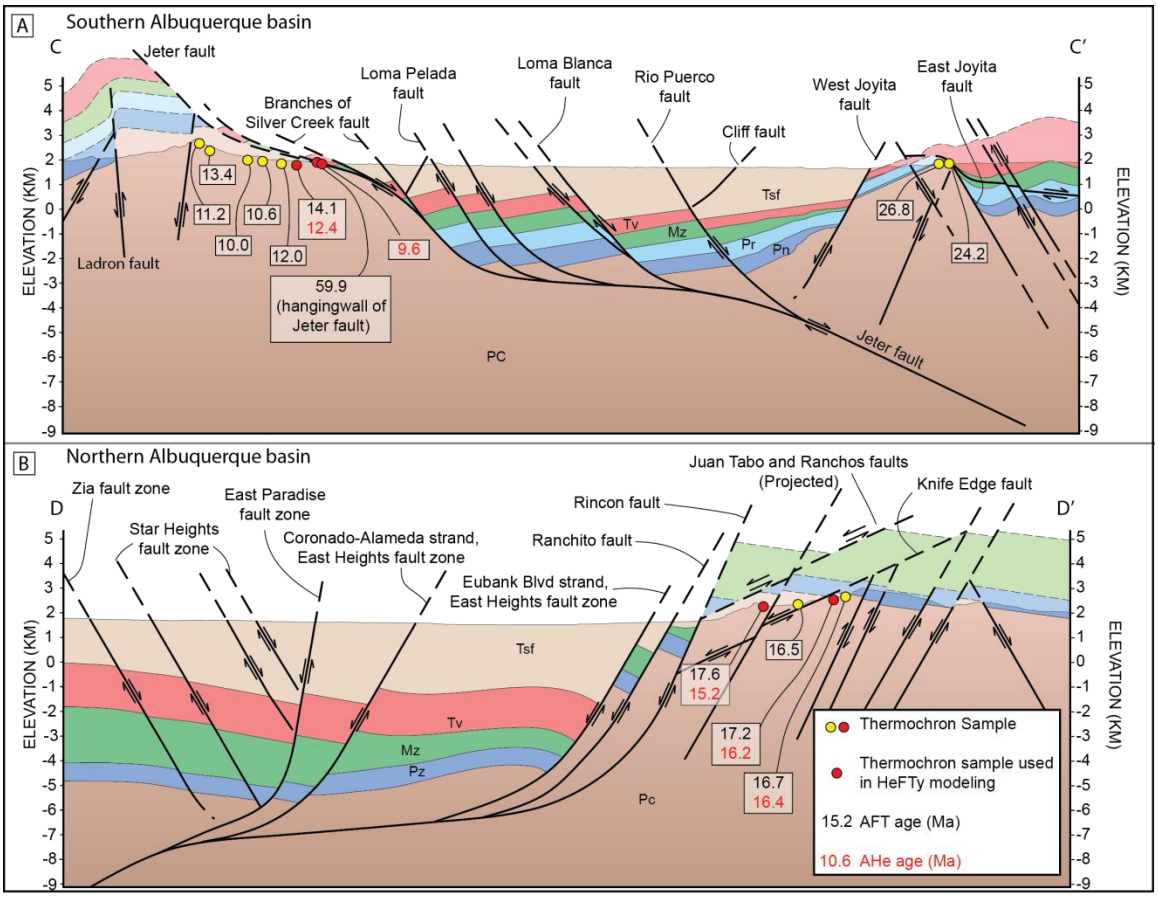

Figure 7. Cross-sections depicting fault geometries in the **A.** southern and **B.** northern parts of the Albuquerque basin. Cross-sections are drawn along lines C-C' and D-D' in Figure 2. Numbers are AFT ages in Ma. Numbers in parentheses are AHe ages in Ma. Red circles are samples used in thermal history modeling. Pc = Precambrian; Pz = Paleozoic; Pn = Pennsylvanian; Pr = Permian; Mz = Mesozoic; Tv = Tertiary volcanic and volcaniclastic; Tsf = Tertiary Santa Fe Group.

the basin (Figs. 6B, 7; Read et al., 2007). All other intrabasinal faults in this region dip >50°, and extension is primarily accomplished through slip along faults that are synthetic with the Jeter fault (Fig. 7).

Thermochronometric Constraints on Timing of Fault Slip

Constraints on the timing of main fault activity associated with the Sandia and Ladron uplifts is important for producing evolutionary models for these fault systems. New and published AFT and AHe data were used for the purpose of producing continuous thermal history models from ~120 °C to surface temperatures. The power of using both apatite fission-track (AFT) and apatite (U-Th)/He (AHe) on the same sample is that the temperature sensitivities of AFT (120° - 60°C) overlap with those of AHe (90° - 30°C), providing the ability to jointly invert AFT and AHe datasets to constrain the sample's continuous cooling path through the temperature range ~120 to ~30 °C (e.g. Donelick et al., 2005; Ketchum, 2005; Flowers et al., 2009). Regions with data include the footwall of the Jeter fault and the fault sliver bounded by the Jeter and Silver Creek faults in the southwestern part of the basins, and the footwall and hanging wall of the Knife Edge fault in the northeastern part of the basin.

AFT ages from both locations show a roughly linear relationship with elevation (Fig. 8A). In the Ladron uplift, AFT data and track length measurements from the footwall of the Jeter fault suggest rapid exhumation from ~18-10 Ma. Long track lengths with unimodal histograms suggest that these rocks cooled rapidly at rates of ~12-20 °C/Ma during this time (Kelley et al., 1992). Similarly, AFT and AHe data in the footwall and hanging wall of the Knife Edge fault in the Sandia uplift suggest rapid cooling to near-surface temperatures between ~22-14 Ma (House et al., 2003). Track length and age

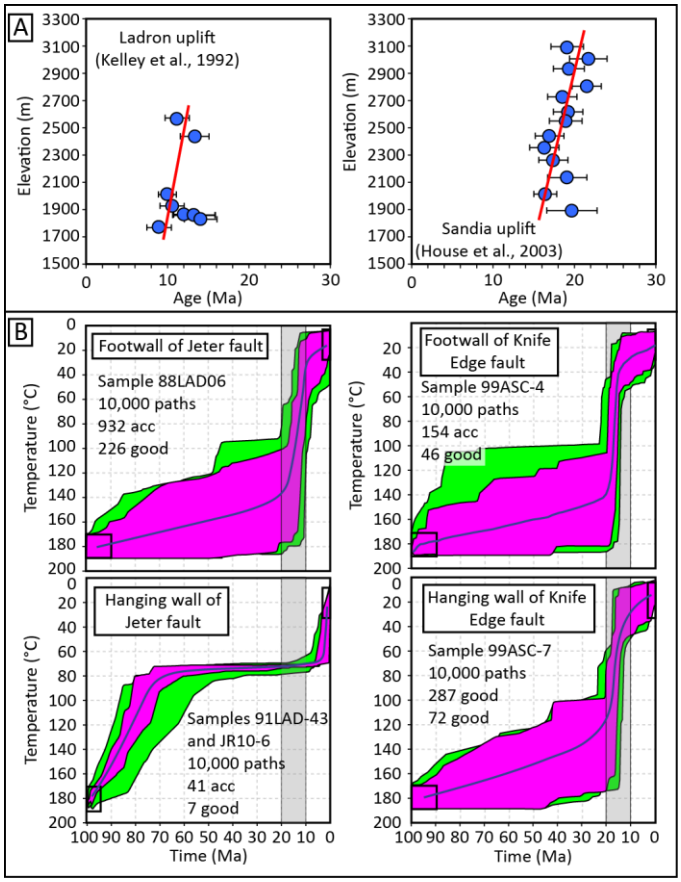

Figure 8. A. Apatite fission-track age-elevation plots. **B.** Apatite fission-track and apatite (U-Th)/He joint inversion thermal history models of samples within the Ladron and Sandia rift flank uplifts. Black boxes are initial time-temperature constraints, blue line is the central time-temperature path, and gray bands highlight the time interval from 20-10 Ma.

data indicate that this structural block cooled at rates of ~7-12°C/Ma during the early Miocene (Kelley et al., 1992). To add to this dataset in the Ladron uplift, apatite grains were picked from sample 88LAD06 in the footwall of the Jeter fault for AHe analysis. Two additional samples were collected from the hanging wall of the Jeter fault (footwall of the Silver Creek fault). 91LAD-43 provided an AFT age, while JR10-6 yielded sufficient apatite grains for AHe analysis (Tables 1, 2, 3).

In all, five samples were targeted to produce new joint AFT and AHe thermal history models from four fault blocks with the purpose of identifying times of rapid exhumation associated with slip along rift-bounding normal faults (Fig. 8B). Thermal history models were produced utilizing HeFTy v. 1.7.5 (Ketchum, 2005), which incorporates RDAAM (Flowers et al., 2009). In each simulation, 10,000 random paths were generated. Pink envelopes encompass all "good" fit paths (goodness of fit >0.5), and green envelopes encompass all "acceptable" fit paths (goodness of fit >0.05) (Fig. 8B).

Joint AFT and AHe thermal history models for the footwall of the Jeter fault suggest that it was rapidly exhumed to near-surface temperatures during a major pulse ~18-10 Ma (Fig. 8B). In contrast, the fault sliver that is bounded by the Jeter and Silver Creek faults (hanging wall of Jeter fault) records two separate pulses of exhumation. Initial ~80-60 Ma exhumation of this fault block was followed by relative stability at ~80°C for ~50 Ma. A second period of uplift ~10-5 Ma brought this block to near-surface temperatures (Fig. 8B).

The Ladron fault along the western flank of the Ladron uplift shows reverse-sense movement (Fig. 7), and although Lewis and Baldridge (1994) suggest that this structure

Table 1. AFT and AHe sample locations

Location	Sample	Rock Type	Data Used	Latitude	Longitude	Elevation (m)	Reference
Footwall of Jeter fault	88LAD-6	Granite	AFT and AHe	34°25.65'	107°01.73'	1829	Kelley et al. (1992) This study
Hanging wall of Jeter fault	JR10-6	Sandstone	AHe	34°23.84'	107°01.78'	1750	This study
Hanging wall of Jeter fault	91LAD-43	Sandstone	AFT	34°23.88'	107°2.12'	1756	This study
Footwall of Knife Edge fault	99ASC-4	Granite	AFT and AHe	35°14.54'	106°28.00'	2633	House et al. (2003)
Hanging wall of Knife Edge fault	99ASC-7	Granite	AFT and AHe	35°14.64'	106°28.45'	2499	House et al. (2003)

Table 2. Apatite fission track data

Sample	Grains counted	$\rho_s \times 10^5$ t/cm^2	$\rho_i \times 10^5$ t/cm^2	$\rho_d \times 10^6$ t/cm^2	Central Age, Ma (±1 SE)	Uranium content (ppm)	Mean Track Length, µm (±1 SE)
91LAD-43	9	0.79 (28)	0.88 (156)	1.91 (4600)	59.9 ± 12.4	7	11.2 ± 0.8 (21)

ρ_s = spontaneous track density, ρ_i = induced track density, ρd = track density in muscovite detector. Numbers in parenthesis are total number of tracks counted. Zeta value for is 351 ± 40 based on CN5 glass.

Table 3. Apatite (U-Th)/He data

	Radius (μm)	Mass U (ng)	Mass Th (ng)	Mass Sm (ng)	U (ppm)	Th (ppm)	Sm (ppm)	eU (ppm)	4He (nmol)/g	Ft	Raw Age ±1σ (Ma)	Corrected Age ±1σ (Ma)	Mean Age ±1σ (Ma)
88LAD-6													12.4 ± 0.3
a1	62	0.0393	0.0506	0.2665	4	5	27	5	0.267	0.77	9.5 ± 0.2	12.4 ± 0.3	
JR10-6													9.6 ± 0.8
a1	62	0.0432	0.0323	0.2160	13	10	67	15	0.733	0.77	8.6 ± 0.4	11.2 ± 0.5	
a2	46	0.1323	0.2151	0.3715	100	163	281	138	7.131	0.68	9.5 ± 0.2	13.9 ± 0.3	
a3	57	0.0234	0.0730	0.1710	9	29	69	16	0.543	0.74	6.1 ± 0.3	8.3 ± 0.4	
a4	49	0.0097	0.0250	0.0527	6	15	33	10	0.179	0.70	3.4 ± 0.3	4.9 ± 0.4	

could have formed during extension of the Rio Grande rift, a long belt of contractional faults along the western length of the Albuquerque basin (e.g. Callender and Zilinski, 1976; Lewis and Baldridge, 1994) suggests to us that the Ladron fault was most likely developed during the Laramide Orogeny. If so, then the ~80-60 Ma period of cooling preserved in the hanging wall of the Jeter fault may have been accomplished through compressional deformation along the Ladron fault. The ~18-10 Ma period of cooling preserved in the footwall of the Jeter fault most likely represents erosional exhumation during a time of rapid slip along the Jeter fault. Finally, the most recent ~10-5 Ma cooling in the hanging wall of the Jeter fault occurred after main slip along the Jeter fault, and is interpreted to record normal-sense slip along the Silver Creek fault to further exhume this fault sliver to the surface.

In the northern Albuquerque basin, thermal history models of the footwall and hanging wall of the Knife Edge fault both record similar cooling histories, where both fault blocks were exhumed to the near surface ~20-12 Ma (Fig. 8). This suggests that movement along the Knife Edge fault is relatively minor and that unroofing may have taken place on the larger-displacement Juan Tabo-Ranchos LANF during this time. The Juan Tabo fault, which juxtaposes Triassic and Jurassic rocks against Precambrian granite, has accumulated more than 3 km of stratigraphic displacement (Van Hart, 1999). Low-temperature thermochronometers used in this study do not detect any Laramide-age cooling in the Sandia uplift, but previous work suggests that the Sandia uplift was affected by Laramide compression (Karlstrom et al., 1999), such that Precambrian granitic rocks were most likely not exhumed to shallow enough levels in the crust to have cooled through ~110°C in the Laramide.

Spatial Progression of Fault Slip

Figure 9 shows a plot of horizontal distance along cross-section lines C-C' and D-D' vs. fault age. Although adequately constraining the times when faults became active and inactive is challenging, here we use available constraints on faults in the Albuquerque Basin from thermal history models of different fault blocks as well as latest movements reported for Quaternary faults in the Albuquerque basin. In both the northern and southern Albuquerque basin, intrabasinal faults typically record Quaternary displacements (U.S. Geological Survey and New Mexico Bureau of Geology and Mineral Resources, 2006), including the Rincon fault, with a probable latest rupture event younger than ~5 ka (Connell, 1995). Combining available age constraints on different faults, the early-formed faults seem restricted to the Sandia and Ladron uplifts. These faults were subsequently abandoned, and intrabasinal faults typically cut Quaternary units (Fig. 9). This observation is supported by the presence of long, narrow structural benches preserved along the flanks of the basin (Chapin and Cather, 1994). An important difference, however, is that in the Sandia region young faults tend to cut earlier-formed LANF's, whereas in the southern part of the basin there is a more systematic progression of younger synthetic faults forming basinward through time.

DISCUSSION

Kinematic Evolution of Rift Flank Uplifts in the Albuquerque Basin

Synthesizing observations on topography, basin depth, fault geometry, and fault ages, we propose a model for LANF's in the Albuquerque basin that applies previous models developed for highly-extended terranes, where isostatic uplift is a main driving force that rotates high-angle faults to shallower angles (Spencer, 1984; Buck, 1988;

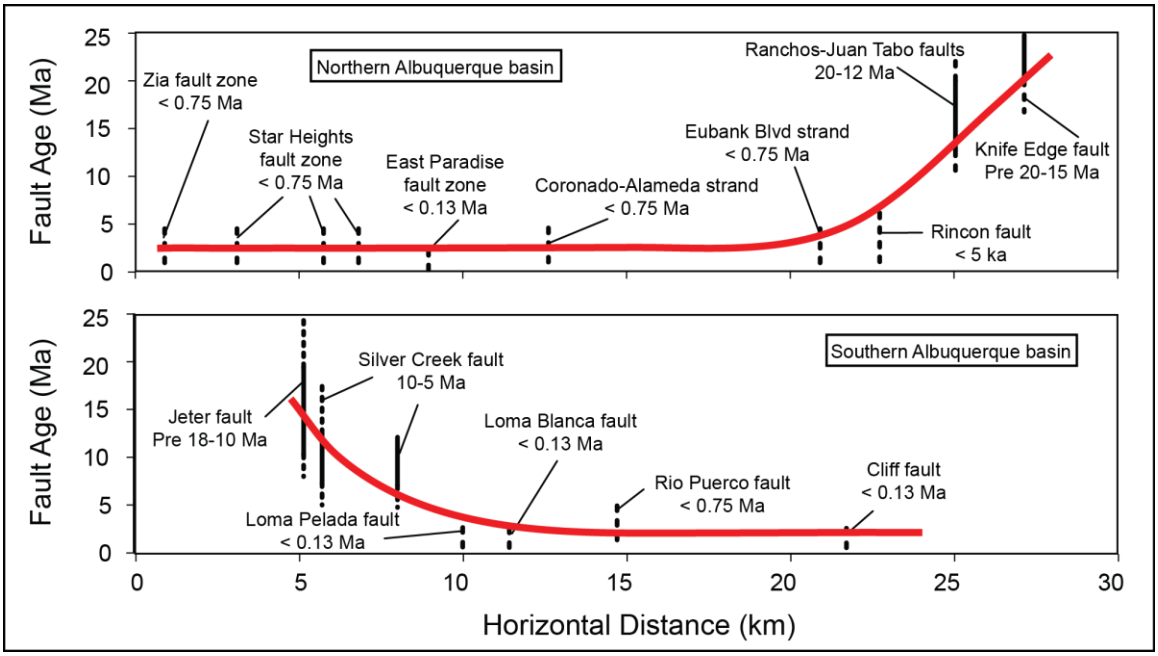

Figure 9. Plots of horizontal distance vs. fault age along C-C' and D-D' for the northern and southern Albuquerque basin. Dotted lines indicate possible continuation of faulting. Quaternary fault dip measurements and youngest slip events are from U.S. Geological Survey and New Mexico Bureau of Geology and Mineral Resources (2006).

Wernicke and Axen, 1988; Wdowinski and Axen, 1992; Axen and Bartley, 1997). In the Albuquerque basin, isostatic uplift of footwall blocks has been proposed for the Sandia uplift (May et al. 1994; Roy et al., 1999) and the Ladron uplift (Wernicke and Axen, 1988; Lewis and Baldridge, 1994). Our model expands on these previous studies, and expands on the recent synthesis by Grauch and Connell (2013) by attempting to integrate the observed high-and low-angle faults, geophysical data, and thermochronometric data into a robust kinematic model for the central Rio Grande rift.

Southern Albuquerque Basin

Following initial uplift ~80-60 Ma during the Laramide Orogeny, initial extension in the Albuquerque basin began during the Oligocene (Chapin and Cather, 1994). Continued, rapid exhumation captured by AFT and AHe techniques began prior to 18 Ma, with major slip concentrated along the Jeter fault. This main period of extension is supported by thermal history models, as well as by thick syntectonic rift fill sections; Grauch and Connell (2013) estimate that more than half the thickness of Santa Fe Group rift fill was deposited from ~ 16-8 Ma. Thermal history models suggest that the hanging wall of the Jeter fault, which preserves Laramide-age exhumation, was further exhumed to the surface ~10-5 Ma, which we interpret to reflect a main period of slip along the Silver Creek fault.

A several meter thick belt of mylonitic rocks is preserved in the Precambrian granitic rocks immediately adjacent to the Jeter fault (Read et al., 2007) suggesting possible ductile deformation associated with the Jeter fault. However, microtextural analysis of rocks collected from this zone suggests that movement along this shear zone was reverse-sense (Fig. 10). The Jeter fault, therefore, is most likely a brittle fault that

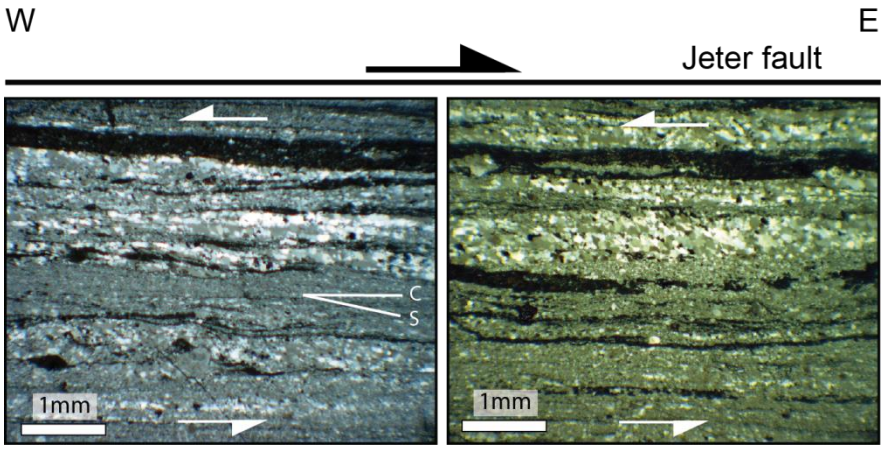

Figure 10. Microphotographs of Precambrian mylonitic rocks from the footwall of the Jeter fault. The left photograph displays S-C fabrics, and the right photograph displays grain shape preferred orientation, both of which indicate reverse shear sense.

offsets rocks that have undergone an older (Precambrian?) ductile strain. In addition, Lewis and Baldridge (1994) suggested that the Jeter fault had an original dip of ~48° based on the cutoff angle between the Jeter fault and Paleozoic beds along the western edge of the Ladron uplift.

In our model, the basin-bounding Jeter fault (pre ~18 Ma) initiated as moderately high-angle (~48°) structure that inherited an earlier fabric (Fig. 11). Continued extension caused the Jeter fault to rebound isostatically due to the lateral removal of hanging wall material. As discussed previously, the low-angle Jeter fault lies along the southern flank of the basin depocenter. We interpret this to be a potential consequence of isostatic footwall uplift, as this would elevate portions of the deep basin to shallower levels in regions where extension is greatest. After ~10 Ma, the Jeter fault is interpreted to have become inactive because it was unfavorably oriented for continued slip, and the new high-angle Silver Creek fault formed basinward to facilitate continued extension. The upwarping of the abandoned low-angle Jeter fault during progressive slip exposed the Precambrian-cored Ladron uplift as a rift salient, and continued slip began to rotate strands of the Silver Creek fault to lower angle as younger intrabasinal faults emerged.

Northern Albuquerque Basin

Thermal history models generated for the Sandia uplift, along with current fault geometry, differs slightly from the Ladron block to the south. In the Sandia uplift, both the hanging wall and footwall of the Knife Edge fault were exhumed at about the same time, ~20-12 Ma (Fig. 8). This suggests no significant offset along that structure after this time (House et al., 2003), and that another major fault was responsible for the exhumation of the Sandia block towards the surface. We suggest that main exhumation

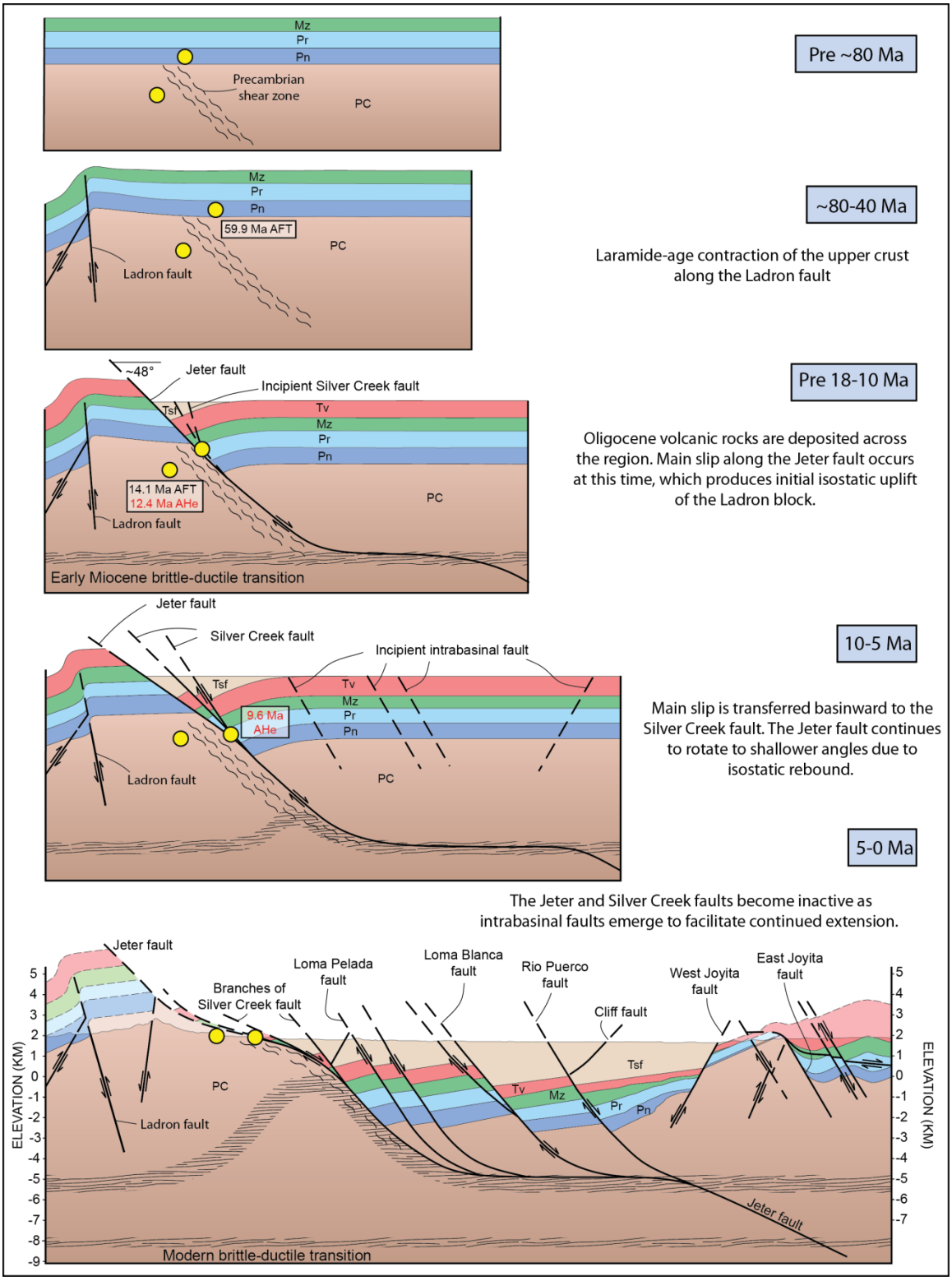

Figure 11. Kinematic evolution of the southern Albuquerque basin.

was related to the Ranchos-Juan Tabo system. In addition, published cross-sections of the northern Albuquerque basin display steeper faults offsetting older, shallower normal faults (e.g. Connell et al., 2008). A new aspect of our model is that the Sandia block preserves at least three now-separate LANF segments, with segments of the once-continuous LANF system preserved between younger high-angle normal faults.

These observations lead to a kinematic model for the northern Albuquerque basin in which early-formed normal faults most likely emerged as relatively high-angle (~50°-70°) structures. Instead of being concentrated within a single narrow zone, the strain was instead partitioned among several different structures. As extension continued, faults began to rotate to shallower angles. Fault rotation in this region was likely predominantly due to isostatic rebound of the footwall block. Flexural modeling using finite-element code involving joint-inversion of topography and gravity suggests that ~18% extension of the northern Albuquerque basin near the Sandia Mountains would result in isostatic uplift that is sufficient to produce the modern rift flank geometry and the observed ~15° east dip of Paleozoic sediments on the eastern side of the Sandias (Roy et al., 1999). In addition, LANF segments are found above the northern flank of the deepest depocenter in the Albuquerque basin (Fig. 6), similar to relationships in the southern parts of the basin. We again suggest this may be a potential consequence of isostatic basin uplift in a region of maximum extension, which would uplift the basin depocenter to shallower levels as it rotated early-formed normal faults to shallow levels. As the early-formed Ranchos, Knife Edge, and Juan Tabo faults rotated to shallower angles, and slip along them diminished,

new intrabasinal faults facilitated continued extension in the northern Albuquerque basin (Fig. 12), including the Rincon fault, which dissected the Ranchos-Juan Tabo fault system.

The klippe of Mesozoic rocks (location 1 in Figure 3C) has long been a conundrum in the evolutionary history of the Sandia Mountains (e.g. Read et al., 1944; Kelley and Northrup, 1975, Van Hart, 1999). The proposed evolutionary history outlined here provides a viable explanation of its development. Initially, the Mesozoic klippe formed the hanging wall of a relatively high-angle normal fault that accumulated enough displacement to place it against Precambrian granitic rocks. As slip progressed along this fault as well as others, the fault plane rotated, and was eventually dissected by younger faults. The preserved structures thus require an interaction of both high- and low-angle fault segments.

Elevated Heat Flow

Our preferred evolutionary model for the central Rio Grande rift recognizes synchronous slip on opposite mirrored active rift flanks, and development of a broad accommodation zone beginning ~20 Ma. In addition, we perceive a link between LANF development and morphometry of both rift flanks and basin depth. This section seeks to understand the evolution of LANF systems in the southern and northern parts of the Albuquerque basin in terms of elevated heat flow that existed at the end of the Oligocene.

Widespread intermediate to silicic composition eruptions affected much of the western U.S. and Mexico during the Eocene-Oligocene (e.g. Elston, 1984, Lipman, 1992, Farmer et al., 2008). In Colorado and New Mexico, volcanic and magmatic activity was mainly centered in two major centers, the San Juan volcanic field in southwestern

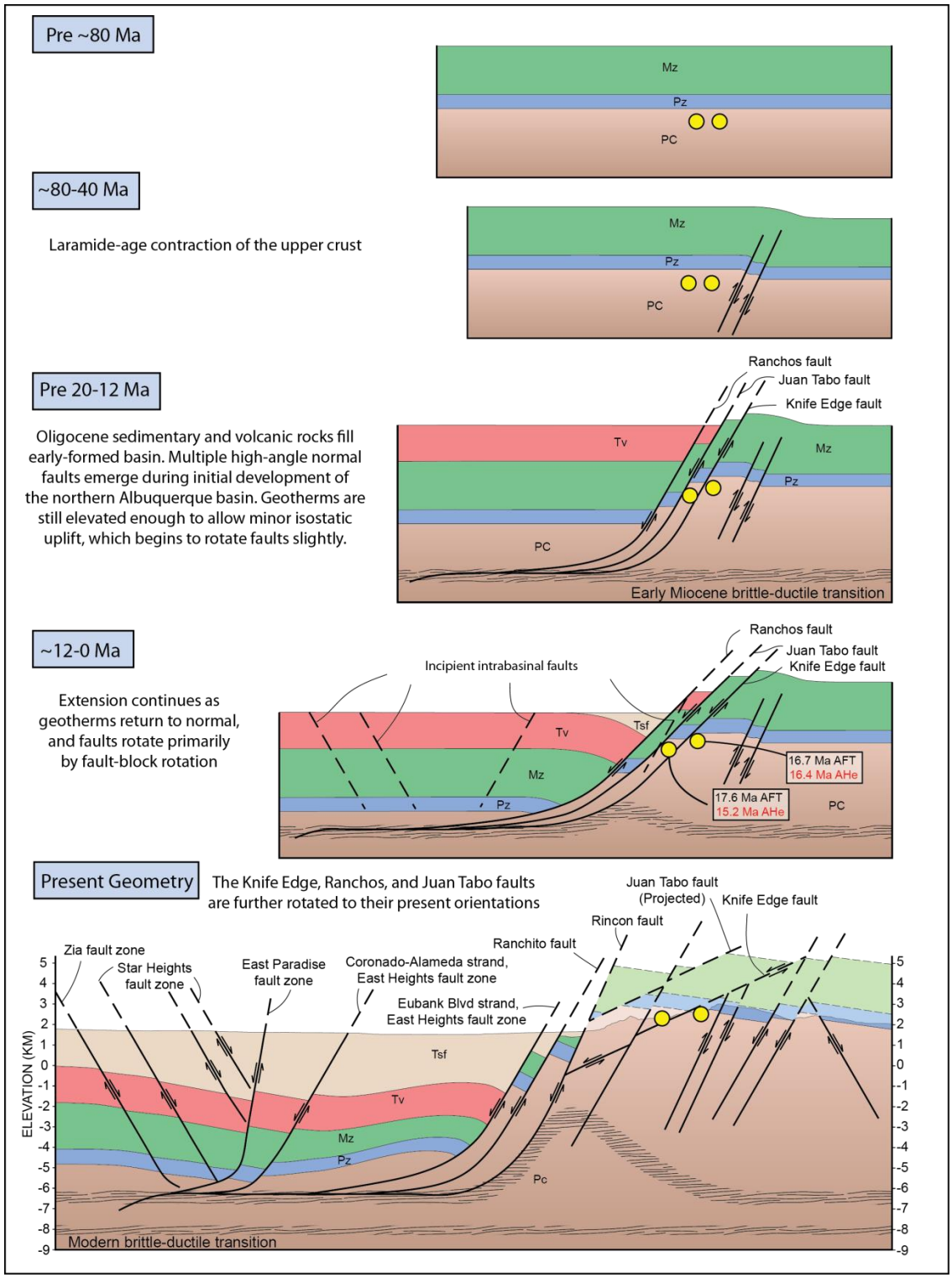

Figure 12. Kinematic evolution of the nothern Albuquerque basin.

Colorado and the Mogollon-Datil volcanic field in southwestern New Mexico. The Mogollon-Datil volcanic field, active from ~40-21 Ma, covers ~40,000 km^2, produced more than ten calderas in southwestern New Mexico, and is surrounded by a large apron of ignimbrites and lavas (Chapin et al., 2004). Volcanic and magmatic rocks in the Mogollon-Datil volcanic field are thought to have been derived from lithospheric sources, although the ultimate cause of melting may have been the foundering of the underlying Farallon slab, which caused asthenospheric circulation (McMillan et al., 2000). Additional minor magmatic centers are found east of the Sandia Mountains (Fig. 3), including the Ortiz belt, active from ~36-27 Ma, which consists of at least 12 individual laccoliths (Maynard, 2005).

By ~21 Ma, regional volcanism and magmatism had elevated the heat flow in much of New Mexico and southern Colorado (Kelley, 2002). These magmatic centers also likely heated the crust for several million years after their emplacement. Continued Neogene heat flow is exemplified by modern-day heat flow measurements above the Socorro magma body (Fig. 3), which are higher than the heat flow estimated from a basaltic melt of its size (Reiter et al., 2010). These calculations suggest that the measured heat flow is residual from now-solidified magmatic intrusions that were emplaced ~1-3 Ma. Similarly, magmatic and volcanic centers in southwestern New Mexico ended ~21 Ma, yet residual heat flow likely elevated temperatures in the crust for several million years after. Based on thermal history models of the Sandia and Ladron uplifts, rapid extension along early-formed faults began prior to ~20 Ma in the north and prior to ~18 Ma in the south. These times of rapid extension coincide with times of elevated heat flow in much of New Mexico. In the Sandia region, House et al. (2003) use AFT data, unit

thicknesses, and thermal conductivity values for different rock types to estimate geothermal gradients. Their calculations indicate that at the end of Oligocene magmatic and volcanic activity, heat flow in this region was ~105 mW/m^2, corresponding to a geothermal gradient in the upper crust of ~38°C/km, compared to a calculated modern-day heat flow of ~80 mW/m^2, corresponding to a modern geothermal gradient of ~29°C/km (House et al., 2003). Due to its close proximity to the Mogollon-Datil volcanic field, it is possible that heat flow in the southern Rio Grande rift may have even been higher than in the Sandia uplift.

In the Ladron uplift, our model is that rapid slip along the Jeter fault led to isostatic uplift, rotation of early-formed faults to shallower angle, and the emergence of new intrabasinal faults at a high angle. Similar mechanisms of formation for LANF's have been widely applied to explain the formation of core complexes in regions of large magnitude (> 100%) extension, such as the Basin and Range Province (e.g. Spencer, 1984), along mid-ocean ridges (e.g. Smith et al., 2012), as well as in regions undergoing orogenic collapse such as Tibet (Kapp et al., 2008). As discussed previously, the development of core complexes such as these requires hot crustal conditions to expose ductiley-deformed rocks at the Earth's surface. Deformation along the Jeter fault is entirely brittle, although fault ages and geometries are consistent with early stages of a core-complex evolutionary model. The high elevation footwall, rift promontory aspect and domal character of a footwall core are all similar to core complex geometries seen in high extension regions (e.g. Spencer, 1984). Thus we propose that the Ladron uplift is an example of an embryonic core complex, and that a combination of insufficient

extensional strain and heat flow following late Oligocene magmatic and volcanic activity inhibited the development of a mature core complex exposing ductiley-deformed rocks.

In the Sandia uplift, the style of extension is very similar to that observed in the southern Albuquerque basin, where older faults are rotated to shallow angles as extension progresses. The Knife Edge fault accumulated relatively minor amounts of slip, and unroofing of the Sandia block was most likely accomplished via slip along the Juan Tabo-Ranchos fault system. In this part of the basin, it is clear that younger faults (i.e. Rincon fault) cross-cut older LANF's, suggesting that perhaps fault rotation may have been due to a combination of fault block rotation coupled with minor isostatic uplift.

CONCLUSIONS

Our work sheds light on early stages in the development of LANF systems in regions of elevated heat flow and leads to the following general conclusions. 1) The Albuquerque basin evolved into a narrow, low-extension (~17-35%) setting characterized by an abandonment of faults within rift flanks, 10-km scale salients cored by basement uplifts that form the highest parts of the rift flanks, broad accommodation zones separating deep sub-basins, and, at least in this case, simultaneous slip on opposite sides of the rift. 2) We support previous work suggesting that core complexes typically form in regions of hot crust where decoupling between the upper brittle crust and lower ductile crust localizes strain. 3) In the southern Albuquerque basin, elevated heat flow and extension magnitude were insufficient to lead to a mature core complex where ductilely-deformed rocks are preserved in the footwalls of large-offset LANF's. 4) LANF's in the northern Albuquerque basin may have formed dominantly through isostatic footwall uplift. Thus, we show that fundamental processes that are required to produce core

complexes (both oceanic and continental) operated to moderate degrees within the Rio Grande rift from ~25-10 Ma. These regions, therefore, where LANF's make up a small percentage of the total exposed fault population, are important and under-utilized natural laboratories for documenting the sequential stages in development of highly-extended core complexes and provide a new perspective on the importance of LANF's in narrow continental rifts.

ACKNOWLEDGEMENTS

Partial funding came from the New Mexico Geological Society, New Mexico Statemap program, the Alfred P. Sloan Foundation, and the University of New Mexico for JWR, and EAR- 0607808, 0838575, and 1119629 for KEK. We thank Dirk Van Hart, Peter Reiners, and Tien Grauch for fruitful discussions that improved the paper, and Adam Read who collected samples used for microstructural analysis of the Jeter fault.

REFERENCES

Axen, G.J., and Bartley, J.M., 1997, Field tests of rolling hinges: Existence, mechanical types, and implications for extensional tectonics: Journal of Geophysical Research, v. 102, p. 20,515-20,537.

Baldridge, W.S., Olsen, K.H., and Callender, J.F., 1984, Rio Grande rift: Problems and Perspectives, *in* New Mexico Geological Society Guidebook, 35th Annual Conference, 47 p.

Bartolino, J.R., and Cole, J.C., 2002, Ground-Water Resources of the Middle Rio Grande Basin, New Mexico: U.S. Geological Survey Circular 1222, 132 p.

Berglund, H.T., Sheehan, A.F., Murray, H., Roy, M., Lowry, A.R., Nerem, R.S., and Blume, F., 2012, Distributed deformation across the Rio Grande rift, Great Plains, and Colorado Plateau: Geology, v. 40, p. 23-26.

Black, B.A., 1964, The geology of the northern and northeastern parts of the Ladron Mountains, Socorro County, New Mexico [M.S. thesis]: Albuquerque, University of New Mexico, 117 p.

Black, B.A., 2013, "Elephant tracks"…In search of a possible "giant": Geological Society if America Abstracts with Programs, v. 45, p. 443.

Block, L., and Royden, L.H., 1990, Core complex geometries and regional scale flow in the lower crust: Tectonics, v. 9, p. 557–567, doi:10.1029/TC009i004p00557.

Brun, J.P., and Van Den Driessche, J., 1994, Extensional gneiss domes and detachment faults-structure and kinematics: Bulletin de la Societe Geologique de France, v. 165, p. 519-530.

Brun, J.-P., Sokoutis, D., and van den Driessche, J., 1994, Analogue modeling of detachment fault systems and core complex: Geology, v. 22, p. 319–322, doi:10.1130/0091-7613(1994)022<0319:AMODFS>2.3.CO;2.

Buck, W.R., 1988, Flexural rotation of normal faults: Tectonics, v. 7, p. 959-973.

Callender, J.F., and Zilinski, R.E., 1976, Kinematics of Tertiary and Quaternary deformation along the eastern edge of the Lucero uplift, central New Mexico, in Woodward, L.A., and Northrop, S.A., eds., Tectonics and Mineral Resources of Southwestern North America: New Mexico Geological Society Special Publication 6, p. 53–61.

Cather, S.M., 1992, Suggested revisions to the Tertiary tectonic history of north-central New Mexico, *in* Lucas, S.G., Kues, B.S., Williamson, T.F., and Hunt, A.P., eds., San Juan Basin IV: New Mexico Geological Society Guidebook 43, p. 109-122.

Chamberlin, R.M., 1983, Cenozoic domino-style crustal extension in the Lemitar Mountains, New Mexico: A summary, *in* Chapin, C.E., and Callender, J.F., eds., Guidebook, 34th Field Conference, Socorro Region II, v. 34: Socorro, New Mexico, New Mexico Geological Society, p. 111-118.

Chapin, C.E., and Cather, S.M., 1994, Tectonic setting of the axial basins of the northern and central Rio Grande rift, *in* Keller, G.R., and Cather, S.M., eds., Basins of the Rio Grande Rift: Structure, Stratigraphy, and Tectonic Setting: Boulder, Colorado, Geological Society of America Special Paper 291.

Chapin, C.E., McIntosh, W.C., and Chamberlin, R.M., 2004, The late Eocene-Oligocene peak of Cenozoic volcanism in southwestern New Mexico, , *in,* Mack, G.H., and Giles, K.A., eds, The Geology of New Mexico: A Geologic History: New Mexico Geological Society Special Publication 11, p. 271-293.

Connell, S.D., 1995, Quaternary geology and geomorphology of the Sandia Mountains piedmont, Bernalillo and Sandoval Counties, central New Mexico [M.S. thesis]: Riverside, University of California, 414 p.

Connell, S.D., 2008, Geologic map of the Albuquerque-Rio Rancho metropolitan area and vicinity, Bernalillo and Sandoval counties: New Mexico Bureau of Geology and Mineral Resources Geologic Map 78, scale 1:50,000, 2 sheets.

Connell, S.D., and McCraw, D.J., 2007, Preliminary geologic map of the La Joya NW quadrangle, Socorro County, New Mexico: New Mexico Bureau of Geology and Mineral Resources Open File Geologic Map 140, scale 1:24,000, 1 sheet.

DeMoor, M., Zinsser, A., Karlstrom, K., Chamberlain, R., Connell, S., and Read, A., 2005, Preliminary geologic map of the La Joya 7.5-minute quadrangle, New Mexico Bureau of Geology and Mineral Resources Open File Geologic Map 102, scale 1:24,000, 1 sheet.

Donelick, R.A., O'Sullivan, P.B., and Ketcham, R.A., 2005, Apatite fission-track analysis, *in* Reiners, P.W., and Ehlers, T.A., eds., Low-Temperature Thermochronology: Techniques, Interpretations, and Applications: Reviews in Mineralogy and Geochemistry, v. 58, p. 49-94.

Elston, W.E., 1984, Mid-Tertiary ash flow tuff cauldrons, southwestern New Mexico: Journal of Geophysical Research, v. 89, p. 8,733-8,750.

Farmer, G.L., Bailley, T., and Elkins-Tanton, L.T., 2008, Mantle source volumes and the origin of the mid-Tertiary ignimbrite flare-up in the southern Rocky Mountains, western U.S., Lithos, v. 102, p. 279-294.

Faulds, J.E., and Varga, R.J., 1998, The role of accommodation zones and transfer zones in the regional segmentation of extended terranes, *in*, Faulds, J.E., and Stewart, J.H., eds., Accommodation zones and transfer zones: the regional segmentation of the basin and range provinces: Geological Society of America Special Paper, v. 323, p. 1-45.

Flowers, R.M., Ketchum, R.A., Shuster, D.L., and Farley, K.A., 2009, Apatite (U-Th)/He thermochronometry using a radiation damage accumulation and annealing model: Geochimica et Cosmochimica Acta, v. 73, p. 2,347-2,365.

Goteti, R., Mitra, G., Becene, A., Sussman, A., and Lewis, C., 2013, Three-dimensional finite-element modeling of fault interactions in rift-scale normal fault systems: Implications for the late Cenozoic Rio Grande rift of north-central New Mexico: Geological Society of America, Special Paper 494, p. 157-184.

Grauch, V.J.S., 2001, High-resolution aeromagnetic data, a new tool for mapping intrabasinal faults: Example from the Albuquerque basin, New Mexico: Geology, v. 29, p. 367-370.

Grauch, V.J.S., and Connell, S.D., 2013, New perspectives on the geometry of the Albuquerque Basin, Rio Grande rift, New Mexico: Insights from geophysical models of rift-fill thickness, *in* Hudson, M.R., and Grauch, V.J.S., eds., New Perspectives on Rio Grande Rift Basins: From Tectonics to Groundwater: Geological Society of America Special Paper 494, p. 427-462, doi: 10.1130/2012.2494(16).

House, M.A., Kelley, S.A., and Roy, M., 2003, Refining the footwall cooling history of a rift flank uplift, Rio Grande rift, New Mexico: Tectonics, v. 22, doi: 10.1029/2002TC001418.

Hudson, M.R., and Grauch, V.J.S., eds, 2013, New Perspectives on Rio Grande Rift Basins: From Tectonics to Groundwater: Geological Society of America Special Paper 494, 500 p.

Johnson, P.S., Koning, D.J., and Partey, F.K., 2013, Shallow groundwater geochemistry in the Española Basin, Rio Grande rift, New Mexico: Evidence for structural control of a deep thermal source, *in* Hudson, M.R., and Grauch, V.J.S., eds., New Perspectives on Rio Grande Rift Basins: From Tectonics to Groundwater: Geological Society of America Special Paper 494, p. 261-301, doi: 10.1130/2013.2494(11).

Kapp, P., Taylor, M., Stockli, D., and Ding, L., 2008, Development of active low-angle normal fault systems during orogenic collapse: Insight from Tibet: Geology, v. 36, no.1, p. 7-10, doi: 10.1130/G24054A.1.

Karlstrom, K.E., Cather, S.M., Kelley, S.A., Heizler, M.T., Pazzaglia, F.J., and Roy, M., 1999, Sandia Mountains and Rio Grande rift: Ancestry of structures and history of deformation: New Mexico Geological Society Guidebook, 50th Field Conference, Albuquerque Geology, p. 155-165.

Keller, G.R, and Cather, S.M., eds., 1994, Basins of the Rio Grande Rift: Structure, Stratigraphy, and Tectonic Setting: Geological Society of America Special Paper 291, 304 p.

Kelley, V.C., 1975, Geology of Albuquerque basin, New Mexico: New Mexico Bureau of Mines and Mineral Resources, Memoir 33.

Kelley, V.C., and Northrup, S.A., 1975, Geology of Sandia Mountains and vicinity, New Mexico: New Mexico Bureau of Mines and Mineral Resources, Memoir 29, 135 p.

Kelley, S.A., 2002, Evidence for elevated regional heat flow during Late Oligocene time on the Southern High Plains, Geol. Soc. Am. Abstr. Programs, v. 34, p. 322.

Kelley, S.A., Chapin, C.E., and Corrigan, J., 1992, Late Mesozoic to Cenozoic cooling histories of the flanks of the northern and central Rio Grande rift, Colorado and New Mexico: New Mexico Bureau of Mines and Mineral Resources Bulletin 145, 39 p.

Kelley, S.A. and Chamberlin, R.C., 2012, Our growing understanding of the Rio Grande rift: New Mexico Earth Matters, v. 12, no.2, p. 1-4.

Ketchum, R.A., 2005, Forward and inverse modeling of low-temperature thermochronometry data: Reviews in Mineralogy and Geochemistry, v. 58, p. 275-314.

Koning, D.J., Grauch, V.J.S., Connell, S.D., Ferguson, J., McIntosh, W., Slate, J.L., Wan, E., and Baldridge, W.S., 2013, Structure and tectonic evolution of the eastern Española Basin, Rio Grande rift, north-central New Mexico: Geological Society of America, Special Paper 494, p. 185-219.

Lavier, L.L., Buck, W.R., and Poliakov, A.N.B., 2000, Factors controlling normal fault offset in an ideal brittle layer: Journal of Geophysical Research, v. 105, p. 23,431–23,442, doi:10.1029/2000JB900108.

Lewis, C.J., and Baldridge, W.S., 1994, Crustal extension in the Rio Grande rift, New Mexico: Half-grabens, accommodation zones, and shoulder uplifts in the Ladron Peak-Sierra Lucero area, *in* Keller, G.R., and Cather, S.M., eds., Basins of the Rio Grande Rift: Structure, Stratigraphy, and Tectonic Setting: Boulder, Colorado, Geological Society of America Special Paper 291.

Lipman, P.W., 1992, Magmatism in the Cordilleran United States; progress and problems, *in* Burchfiel, B.C., Lipman, P.W., and Zoback, M.L., eds., The Cordilleran Orogeny: Conterminous U.S. The Geology of North America: Boulder, Colorado, Geological Society of America, p. 481-514.

Machette, M.N., 1978, Geologic map of the San Acacia quadrangle, Socorro County, New Mexico: U.S. Geological Survey Geologic Quadrangle Map GC-1415, scale 1:24,000.

Marshak, S., Karlstrom, K., and Timmons, J.M., 2000, Inversion of Proterozoic extensional faults: An explanation for the pattern of Laramide and Ancestral Rockies intracratonic deformation, United States: Geology, v. 28, p. 735-738.

May, S.J., Kelley, S.A., and Russell, L.R., 1994, Footwall unloading and rift shoulder uplifts in the Albuquerque Basin: Their relation to syn-rift fanglomerates and apatite fission-track ages, *in* Keller, G.R., and Cather, S.M., eds., Basins of the Rio Grande Rift: Structure, Stratigraphy, and Tectonic Setting: Boulder, Colorado, Geological Society of America Special Paper 291.

Maynard, S.R., 2005, Laccoliths of the Ortiz porphyry belt, Santa Fe County, New Mexico: New Mexico Geology, v. 27, p. 3-21.

McKenzie, D., 1978, Some remarks on the development of sedimentary basins: Earth and Planetary Science Letters, v. 40, p. 25-32.

McMillan, N.J., Dickin, A.P., and Haag, D., 2000, Evolution of magma source regions in the Rio Grande rift, southern New Mexico: Geological Society of America Bulletin, V. 112, p. 1,582-1,593.

Minor, S.A., Hudson, M.R., Saul Caine, J., and Thompson, R.A., 2013, Oblique transfer of extensional strain between basins of the middle Rio Grande rift, New Mexico: Fault kinematic and paleostress constraints, *in* Hudson, M.R., and Grauch, V.J.S., eds., New Perspectives on Rio Grande Rift Basins: From Tectonics to Groundwater: Geological Society of America Special Paper 494, p. 345-382, doi: 10.1130/2013.2494(14).

Plummer, L.N., Bexfield, L.M., Anderholm, S.K., Sanford, W.E., and Busenberg, E., 2004, Geochemical Characterization of Ground-Water Flow in the Santa Fe Group Aquifer System, Middle Rio Grande Basin, New Mexico: U.S. Geological Survey Water-Resources Investigations Report 03-4131, 395 p.

Read, C.B., Wilpol, R.H., Andrews, D.A., Summerson, C.H., and Wood, G.H., 1944, Geologic map and stratigraphic sections of Permian and Pennsylvanian rocks of parts of San Miguel, Santa Fe, Sandoval, Bernalillo, Torrance, and Valencia Counties, north-central New Mexico: U.S., Geological Survey, Oil and Gas Investigations, Preliminary Map 21.

Read, A.S., Karlstrom, K.E., Connell, S., Kirby, E., Ferguson, C.A., Ilg, B., Osburn, G.R., Van Hart, D., and Pazzaglia, F.J., 1999, Open-file geologic map - 6: Geology of Sandia Crest quadrangle, Bernalillo and Sandoval Counties, New Mexico, scale 1:24,000 http://geoinfo.nmt.edu/publications/maps/geologic/ofgm/details.cfml?Volume=6.

Read, A.S., Cather, S.M., Chamberlin, R.M., Connell, S.D., and Karlstrom, K.E., 2007, Preliminary geologic map of the Ladron Peak Quadrangle, Socorro County, New

Mexico, New Mexico Bureau of Geology and Mineral Resources Open File Geologic Map 142, scale 1:24,000, 1 sheet.
Reiter, M.R., Chamberlain, R.M., and Love, D.L., 2010, New data refl ect on the thermal antiquity of the Socorro magma body locale, Rio Grande rift, New Mexico: Lithosphere, v. 2, no. 6, p. 447–453, doi:10.1130/L115.1
Rey, P., Teyssier, C., and Whitney, D.L., 2009a, Crustal melting and core complex dynamics: Geology, v. 37, p. 391–394, doi:10.1130/G25460A.1.
Rey, P., Teyssier, C., and Whitney, D.L., 2009b, The role of partial melting and extensional strain rates in the de- velopment of metamorphic core complexes (McMCC): Tectonophysics, v. 477, p. 135–144, doi:10.1016 /j.tecto.2009.03.010.
Ricketts, J.W., Karlstrom, K.E., Priewisch, A., Crossey, L.J., Polyak, V.J., and Asmerom, Y., 2014, Quaternary extension in the Rio Grande rift at elevated strain rates recorded in travertine deposits, central New Mexico: Lithosphere, v. 6, p. 3-16, doi: 10.1130/L278.1.
Roy, M., Karlstrom, K., Kelley, S., Pazzaglia, F.J., and Cather, S., 1999, Topographic setting of the Rio Grande rift, New Mexico: Assessing the role of flexural "rift-flank uplift" in the Sandia Mountains: New Mexico Geological Society Guidebook, 50th Field Conference, Albuquerque Geology, p. 167-174.
Russell, L.R., and Snelson, S., 1994, Structure and tectonics of the Albuquerque Basin segment of the Rio Grande rift: Insights from reflection seismic data, *in* Keller, G.R., and Cather, S.M., eds., Basins of the Rio Grande Rift: Structure, Stratigraphy, and Tectonic Setting: Boulder, Colorado, Geological Society of America Special Paper 291.
Smith, D.K., Escartín, J., Schouten, H., and Cann, J.R., 2012, Active long-lived faults emerging along slow-spreading mid-ocean ridges: Oceanography, v. 25, p. 94-99.
Smith, G.A., McIntosh, W., and Kuhle, A.J., 2001, Sedimentologic and geomorphic evidence for seesaw subsidence of the Santo Domingo accommodation-zone basin, Rio Grande rift, New Mexico: Geological Society of America Bulletin, v. 113, p. 561-574.
Spencer, J.E., 1984, Role of tectonic denudation in warping and uplift of low-angle normal faults: Geology, v. 12, p. 95-98.
U.S. Geological Survey and New Mexico Bureau of Geology and Mineral Resources, 2006, Quaternary fault and fold database for the United States, accessed Aug 22, 2013, from USGS web site: http//earthquake.usgs.gov/regional/qfaults/.
Van Hart, D., 1999, Geology of Mesozoic sedimentary rocks in the Juan Tabó area, northwest Sandia Mountains, Bernalillo County, New Mexico: New Mexico Geology, v. 21, p. 104-111.
Wdowinski, S., and Axen, G.J., 1992, Isostatic rebound due to tectonic denudation: A viscous flow model of a layered lithosphere: Tectonics, v. 11, p. 303-315.

Wernicke, B., 1985, Uniform-sense normal simple shear of the continental lithosphere: Canadian Journal of Earth Sciences, v. 22, p. 108-125.

Wernicke, B., and Axen, G.J., 1988, On the role of isostasy in the evolution of low-angle normal fault systems: Geology, v. 16, p. 848-851.

Whitney, D.L., Teyssier, C., Rey, P., and Buck, W.R., 2013, Continental and oceanic core complexes: Geological Society of America Bulletin, v. 125, p. 273-298, doi: 10.1130/B30754.1.

Wong, I., Olig, S., Dober, M., Silva, W., Wright, D., Thomas, P., Gregor, N., Sanford, A., Lin, K., and Love, D., 2004, Earthquake scenario and probabilistic ground-shaking hazard maps for the Albuquerque-Belen-Santa Fe, New Mexico, corridor: New Mexico Geology, v. 26, p. 3-33.

CHAPTER 3: Quaternary extension in the Rio Grande rift at elevated strain rates recorded in travertine deposits, central New Mexico

Jason W. Ricketts[1], Alexandra Priewisch[1], Karl E. Karlstrom[1], Laura J. Crossey[1], Victor J. Polyak[1], and Yemane Asmerom[1]

[1]Department of Earth and Planetary Sciences, University of New Mexico, MSC03-2040, 1 University of New Mexico, Albuquerque, NM, 87131-0001

ABSTRACT

Calcite-filled extension veins and shear fractures are preserved in numerous travertine deposits along the western margin of the Albuquerque basin of the Rio Grande rift. Calcite veins are banded and show geometries suggesting incremental cracking and calcite precipitation. U-series and ^{234}U model ages from calcite infillings indicate that vein formation was active in the Quaternary, from ~250 ka to ~ 2 Ma. Vein orientations are systematic within each deposit, and record a dominant extension direction that was horizontal and varied from EW to NW-SE, consistent with both the regional finite extensional strain in the rift and with the GPS-constrained deformation field. Three sites contain three orthogonal vein sets that cross-cut one another non-systematically suggesting alternating times of: 1) regional E-W horizontal extension (dominant), 2) alternating N-S and E-W vertical veins that suggest vertical σ_1 and $\sigma_2 \sim \sigma_3$, and 3) horizontal veins that are interpreted to reflect times of highest pore fluid pressures and subequal principle stresses. One site contains conjugate normal faults that also record the dominant E-W extensional tectonic stress. Quaternary extensional strain rates calculated

from vein opening for three locations range from $3.2 \times 10^{-16} \pm 1.4 \times 10^{-16}$ s^{-1} to $3.2 \times 10^{-15} \pm 2.7 \times 10^{-16}$ s^{-1}, which is up to ~40 times higher than the long term (Oligocene - Recent) finite strain rates calculated for different basins of the Rio Grande rift (8.5×10^{-17} to 4.5×10^{-16} s^{-1}), and up to ~100 times higher than modern strain rates measured by Global Positioning System data ($3.9 \times 10^{-17} \pm 6.3 \times 10^{-18}$ to $4.4 \times 10^{-17} \pm 6.3 \times 10^{-18}$ s^{-1}). These high Quaternary rates are comparable to modern strain rates measured in the Basin and Range province and East African rift. Thus, this paper documents persistent E-W regional extension through the Quaternary in the Rio Grande rift that bridges geologic, paleoseismic, and GPS rates. Anomalously-high strain rates in the Quaternary were facilitated by ascent of travertine-depositing CO_2-rich waters along rift-bounding normal faults leading to very local high stain accumulations. These sites also provide examples of natural leakage of deeply sourced CO_2 that is interacting with regional tectonism, and emphasize that rift maturation is a highly dynamic process spatially and temporally.

INTRODUCTION

The N-S-trending Rio Grande rift, extending from Colorado to Mexico, provides an exceptional natural laboratory for understanding early stages and processes of continental rifting. Rifting began ~ 36-37 Ma (Kelley and Chamberlain, 2012), underwent maximum extensional activity in the Miocene based on ages of thickest Santa Fe Group rift fill (Chapin and Cather, 1994) and thermochronologic ages (Kelley et al., 1992), and is still active. Here we address the processes that localize strain accumulation by documenting changes in strain rate through time. We also explore how temporal and spatial variations in extensional strain accumulation contribute to the heterogeneity of strain accumulation evident in continental rifts.

A persistent challenge for rift studies has been to bridge time scales in order to link rift evolution to rift processes. At the geologic timescale (10's of millions of years) required to accumulate the total extensional strain restored cross-sections can be drawn from geologic and seismic data and these suggest extension magnitude varied from 30-33 % in the southern Albuquerque basin (Russell and Snelson, 1994; Ricketts et al., 2011), to 17-25% in the northern Albuquerque basin (Russell and Snelson, 1994; Roy et al., 1999), to 8-12% in the San Luis basin (Kluth and Schaftenaar, 1994). At the thousand(s) of year time scale, paleoseismic studies are sometimes available by trenching across Quaternary faults to constrain slip history and recurrence intervals. For example, in the Rio Grande rift, recurrence intervals of ~20-40 k.y. and slip rates of ~0.027 – 1 mm/yr have been estimated for the late Quaternary (McCalpin, 2005; McCalpin et al., 2011; Olig et al., 2011). At the decade scale, data from continuous recording of global positioning system (GPS) has been successful at modeling the present-day strain directions and rates which show the rift is currently extending at rates of ~0.12 mm/yr (Berglund et al., 2012).

This paper examines several questions regarding the history and processes of strain accumulation in the Rio Grande rift: (1) Is the Rio Grande rift still extending in the Quaternary? (2) If so, were the paleostrain and paleostress directions consistent with the generally EW extension inferred at longer and shorter timescale studies? (3) What were Quaternary strain rates? (4) What role do fluids play in the extensional process and what are their sources (endogenic vs. epigenic or meteoric fluids)? Here we show that rift maturation is a highly dynamic process spatially and temporally. Further, the rifting process can be highly influenced by fluid flux through fault systems which can create

elevated pore fluid pressures, modify the local stress field by reducing the effective normal stress and hence can facilitate fault slip and strain accumulation rates (e.g. Hubbert and Rubey, 1959; Malagnini et al., 2012).

GEOLOGIC SETTING

The Rio Grande rift is a NS-trending continental rift that separates the Colorado Plateau to the west from the Great Plains physiographic province to the east. The rift is a narrow structure tens of km wide and is composed of individual half-grabens that alternate polarity from north to south. In northern New Mexico, the rift crosses the Jemez lineament, and continues south where it widens south of Socorro, NM into a broad zone where strain is distributed among multiple adjacent graben and half-graben systems of the Basin and Range Province (Fig. 1) (e.g. Seager et al., 1984). This transition between the narrow Rio Grande rift and the highly-extended Basin and Range Province is also the location of the Socorro magma body, a thin mid-crustal magma sheet located 19 km deep having horizontal dimensions of 50-70 km (Sanford et al., 1973; Reinhart and Sanford, 1981; Balch et al., 1997). Associated with the Socorro magma body is a region of anomalously high seismicity; the Socorro Seismic Anomaly covers ~2% of the state of New Mexico, yet produces ~45% of its seismic events above magnitude 2.5 (Balch et al., 1997). In addition, vertical uplift directly over the Socorro magma body has been persistent at ~2-5 mm/yr for over a century, with uplift diminishing to zero radially outward (Larsen and Reilinger, 1983; Larsen et al., 1986; Fialko and Simons, 2001). These data suggest that the region is still magmatically and seismically active.

Our study site is located along the western margin of the Albuquerque basin of the Rio Grande rift in central New Mexico just north of the Socorro magma body and seismic

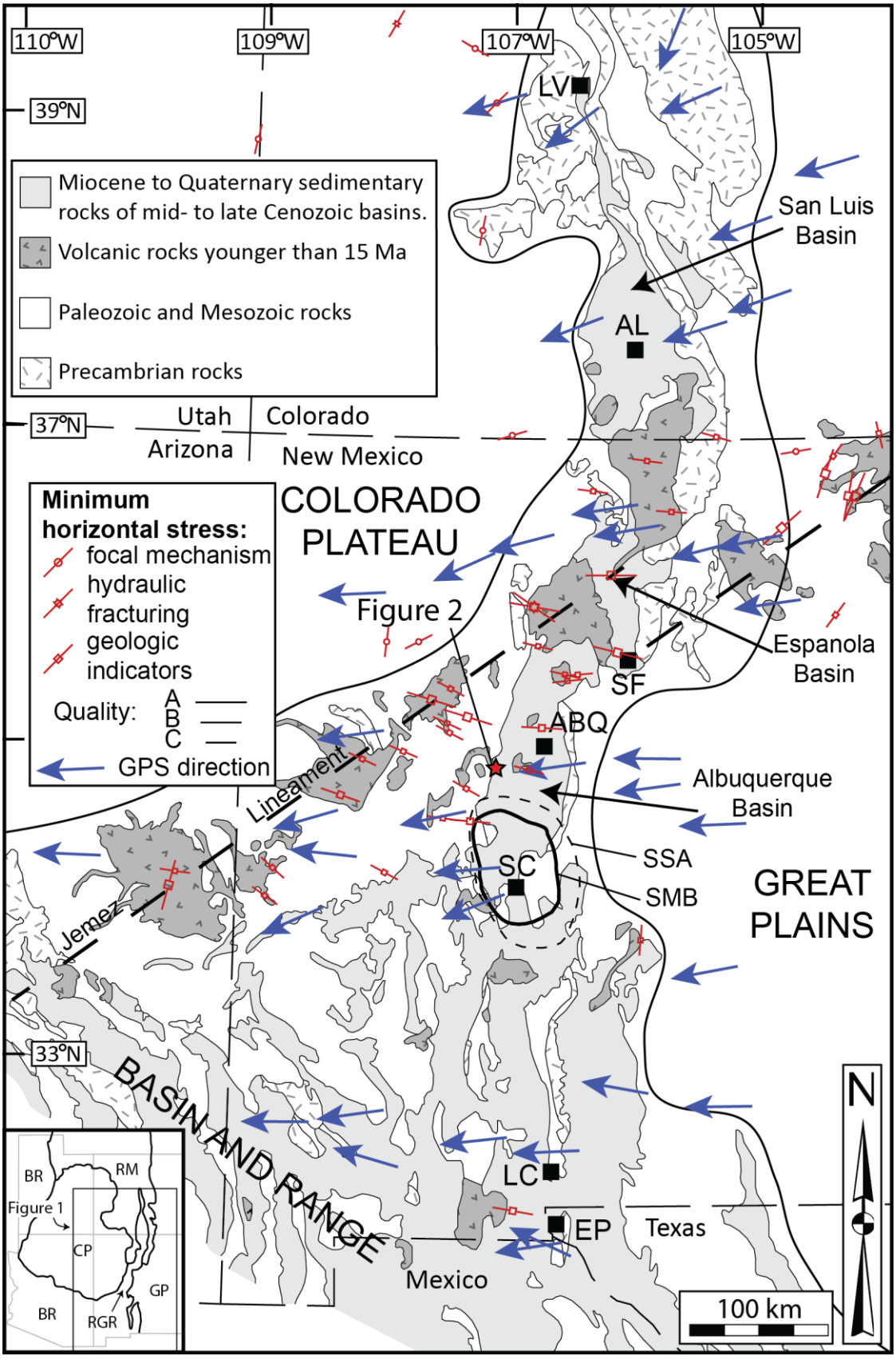
110°W
109°W
107°W
105°W
39°N
37°N
33°N
Miocene to Quaternary sedimentary rocks of mid- to late Cenozoic basins.
Volcanic rocks younger than 15 Ma
Paleozoic and Mesozoic rocks
Precambrian rocks
Utah
Colorado
Arizona
New Mexico
Minimum horizontal stress:
focal mechanism
hydraulic fracturing
geologic indicators
Quality: A B C
GPS direction
COLORADO PLATEAU
Figure 2
LV
AL
SF
ABQ
SC
LC
EP
San Luis Basin
Espanola Basin
Albuquerque Basin
SSA
SMB
GREAT PLAINS
Lineament
Jemez
BASIN AND RANGE
Mexico
Texas
N
100 km
BR
RM
Figure 1
CP
GP
BR
RGR

Figure 1. State of stress and strain in the Rio Grande rift region shown on a regional geologic map. Study area is shown by star on the western margin of Albuquerque Basin. Precambrian rocks (hachured pattern) and Miocene to Quaternary sedimentary rocks (light gray) define the N-S– trending Rio Grande rift. In red are modern and young stress orientations from the World Stress Map, which show the minimum horizontal stress direction (extensional direction of strain). Geologic indicators used in the World Stress Map are generally Quaternary in age (Heidbach et al., 2008). Blue arrows are extension directions measured from global positioning system (GPS; Berglund et al., 2012). Map is modified from Baldridge et al. (1984). LV—Leadville; AL—Alamosa; SF—Santa Fe; ABQ—Albuquerque; SC—Socorro; LC—Las Cruces; EP—El Paso; SMB—Socorro magma body; SSA—Socorro seismic anomaly. Inset shows the Rio Grande rift (RGR) in relation to the Basin and Range Province (BR), Colorado Plateau, (CP), Rocky Mountains (RM), and Great Plains (GP).

anomaly (Figs. 1, 2). This is an important region for neotectonic studies because the rift flank here is characterized by a relatively narrow (< 1 km) zone of several well-exposed faults that are bounded to the west by the Colorado Plateau and to the east by Santa Fe Group basin fill sediments; Pliocene basalts and Quaternary travertines straddle the rift flank here and provide age control on faulting history. Within this zone, EW compression during the Laramide Orogeny produced a set of NS-trending folds and reverse faults, the most prominent of which is the Comanche fault, a west-dipping high-angle structure separating Permian Madera Group from Pennsylvanian Abo and Yeso Formations (Fig. 2) (Callender and Zilinski, 1976). Most of these early-formed reverse faults, including the Comanche fault, were subsequently reactivated or overprinted during extensional deformation related to Neogene development of the Rio Grande rift (Lewis and Baldridge, 1994). Today the main rift-bounding normal fault in the study area is the ~ 55° east-dipping Santa Fe fault, which separates Santa Fe Group syn-rift deposits to the east from Paleozoic and Mesozoic strata of the Colorado Plateau to the west (Fig. 2) (May and Russell, 1994). In some areas the Santa Fe fault offsets Pliocene-early Pleistocene Santa Fe Group rift-fill deposits (Lozinsky and Tedford, 1991). In contrast, a 3.7 ± 0.4 Ma basalt flow (Bachman and Mehnert, 1978) overlies fault strands of the Comanche fault

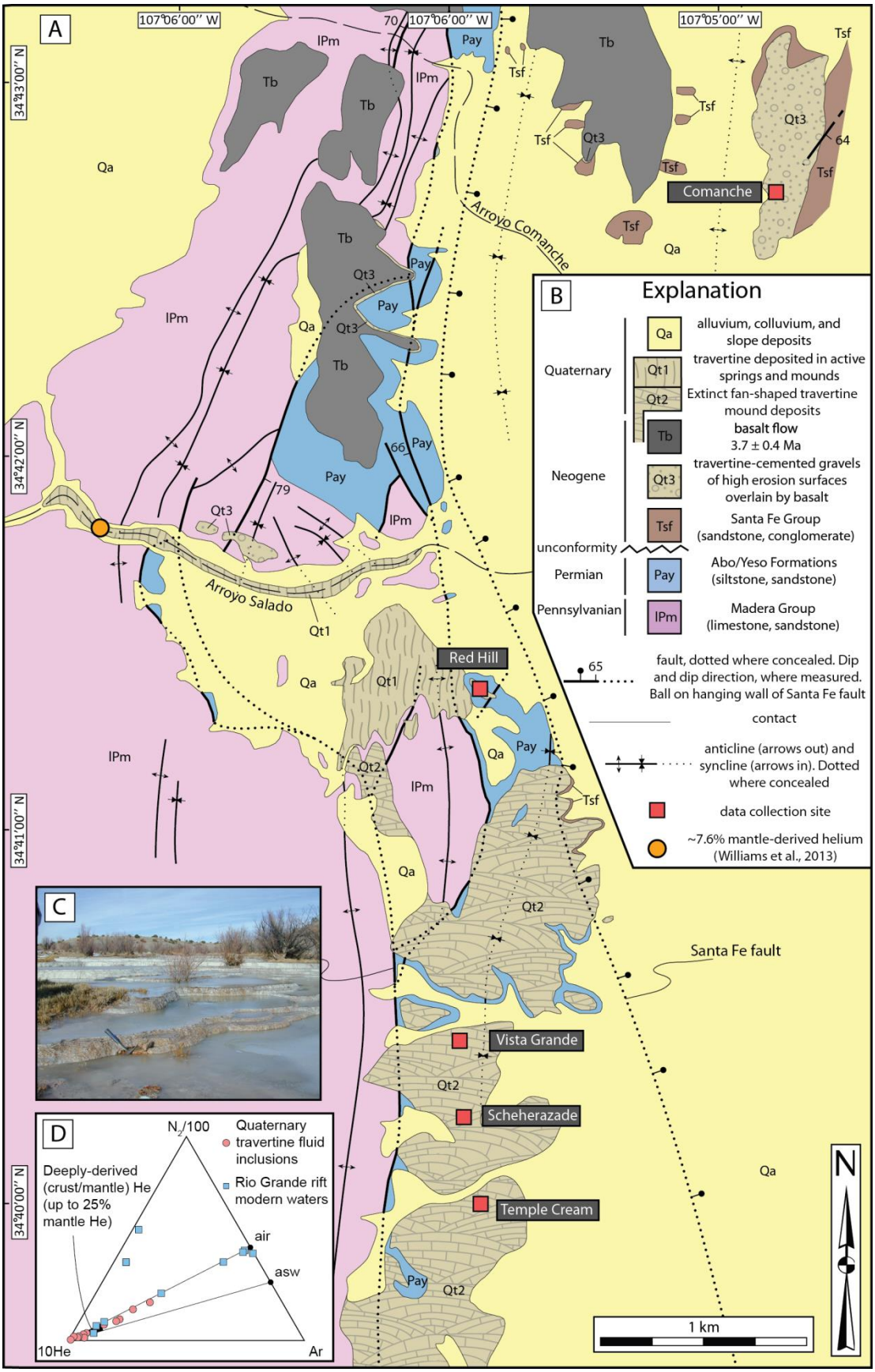
A
107°06'00" W
107°05'00" W
34°43'00" N
34°42'00" N
34°41'00" N
34°40'00" N
Tb
Qa
IPm
Pay
Tsf
Qt3
Qt1
Qt2
Arroyo Comanche
Arroyo Salado
Comanche
Red Hill
Vista Grande
Scheherazade
Temple Cream
Santa Fe fault
B
Explanation
Quaternary
Neogene
unconformity
Permian
Pennsylvanian
alluvium, colluvium, and slope deposits
travertine deposited in active springs and mounds
Extinct fan-shaped travertine mound deposits
basalt flow
3.7 ± 0.4 Ma
travertine-cemented gravels of high erosion surfaces overlain by basalt
Santa Fe Group (sandstone, conglomerate)
Abo/Yeso Formations (siltstone, sandstone)
Madera Group (limestone, sandstone)
fault, dotted where concealed. Dip and dip direction, where measured. Ball on hanging wall of Santa Fe fault
contact
anticline (arrows out) and syncline (arrows in). Dotted where concealed
data collection site
~7.6% mantle-derived helium (Williams et al., 2013)
C
D
N2/100
Quaternary travertine fluid inclusions
Rio Grande rift modern waters
Deeply-derived (crust/mantle) He (up to 25% mantle He)
air
asw
10He
Ar
N
1 km

Figure 2. A. Geologic map of study area. Basalt K-Ar age is from Bachman and Mehnert (1978). **B.** Map explanation. **C.** Actively precipitating travertine in Arroyo Salado. **D.** He-Ar-N_2 plot (after Giggenbach, 1992) for travertine-spring gases from various locations in the Rio Grande rift (from Newell et al., 2005) and from gas analysis of fluid inclusions in vein calcite at quarry site Scheherazade (from Gundimeda, 1995). Fields for crust/mantle-derived gases, air, and air-saturated groundwater (asw) are from Giggenbach (1992).

zone and is not offset by these structures, indicating that Quaternary movement was concentrated along the Santa Fe fault zone (Fig. 2).

Travertine mounds and active springs precipitating travertine are preserved along much of the western margin of the Albuquerque basin. They straddle the rift-bounding faults and blanket much of the older strata and structure, especially in the southern parts of the study area. They are fan- shaped deposits in map view with uphill apex (likely now-extinct spring vents) located along the Comanche fault, but without any observable offset related to growth of the Santa Fe or Comanche fault systems. The close association of these travertine deposits with rift-related structures, and the existence of nearby active travertine-depositing springs within arroyos along multiple fault strands suggests that these platforms were deposited from spring waters emanating from the Comanche-Santa Fe fault system (Fig. 2) (Callender and Zilinski, 1976). Springs that formed these deposits are no longer flowing, and fan apexes are situated above the modern valley floor (Qa to the west of travertine deposits in Figure 2), a result of recent and ongoing denudation of the Albuquerque basin which accelerated between 1.2 and 0.7 Ma and was likely facilitated by climatic changes related to the onset of glaciations in the headwaters of the Rio Grande (Connell, 2004). Additional topographically high erosion surfaces present within the study area are composed of probable Quaternary-aged sandstone and

conglomerate beds containing locally-derived clasts that are cemented with travertine, and as a result, also exist as terraces preserved above the modern valley floor.

The large volume travertine deposits of this study are presently inactive (dry), but smaller volume actively-precipitating travertine deposits are found nearby at low elevation along active springs within Arroyo Salado and Arroyo Comanche to the north (Fig. 2). These springs are also aligned on the same faults and provide an analogy for the types of springs that deposit travertine. They have similar dams, coatings on vegetation, drapes, and travertine facies that are also preserved in the older mound and platform deposits. The main difference in morphology between these and the extinct travertine fans discussed previously is that they occur where faults intersect arroyo bottoms rather than closely spaced and strung out along a short fault segment. This likely reflects the ongoing stream incision into the rift flank in the last 1-2 Ma and relatively dry paleohydrology conditions (hence low head) in the Holocene.

Recent work on similar travertine deposits and modern travertine depositing carbonic springs in the southwest U.S. indicate that source fluids are a mixture of both meteoric (epigenic) and deeply-sourced (endogenic) fluids (Crossey et al., 2006; Crossey et al., 2009; Williams et al., 2013), and that the endogenic fluids are conveyed to the surface along basement-penetrating faults (Crossey et al., 2006). Endogenic fluids that deposit travertine are typically slightly warm (~22-31°C), are rich in dissolved CO_2 (P_{CO2} values as great as $10^{0.1}$), and contain mantle ^3He as part of the trace gases (Crossey et al., 2006). In central New Mexico, the high CO_2 and accompanying trace gases in endogenic waters in active springs are interpreted to be a result of mantle degassing, and are brought to the near-surface through shallow microseismic events associated with the Socorro

magma body and Socorro seismic anomaly (Newell et al 2005; Williams et al., 2013). Within the study area, ^{3}He values of Arroyo Salado waters indicate ~7.6% mantle-derived helium (Williams et al., 2013), and gas abundances from fluid inclusions in travertine at Scheherazade plot within the field of crust/mantle input (Gundimeda, 1995), and overlap with gas abundances measured in modern travertine-depositing springs with a known endogenic component (Fig. 2) (Newell et al., 2005).

STUDY SITES

Some of the largest inactive travertine mounds that were previously discussed are currently being quarried by New Mexico Travertine Inc., providing a spectacular display of the internal geometries at several locations (Fig. 3). Three of these quarry sites (Temple Cream, Scheherazade, and Vista Grande) as well as two additional travertine-cemented terraces north of the quarry sites (Red Hill and Comanche) were chosen as study sites. All of these study sites are currently inactive in terms of travertine deposition. The location of these travertine deposits along rift–flanking faults, and their datable record of progressive vein development offer an exceptional field laboratory to test models for fault-connections between deeply-sourced CO_2 magmatic fluids, fault conduits, carbonic springs, and large volume travertine deposition (Crossey et al., 2009; 2011; Williams et al., 2013; Priewisch et al., 2012). They also offer an opportunity to estimate accumulated strains associated with Quaternary extension in the Rio Grande rift at this location.

At three quarry sites, Temple Cream, Scheherazade, and Vista Grande, abundant veins of different orientations cut the horizontal sedimentary layering of the travertine platforms. The majority of these veins range from ~1 mm to 10-20 cm in width

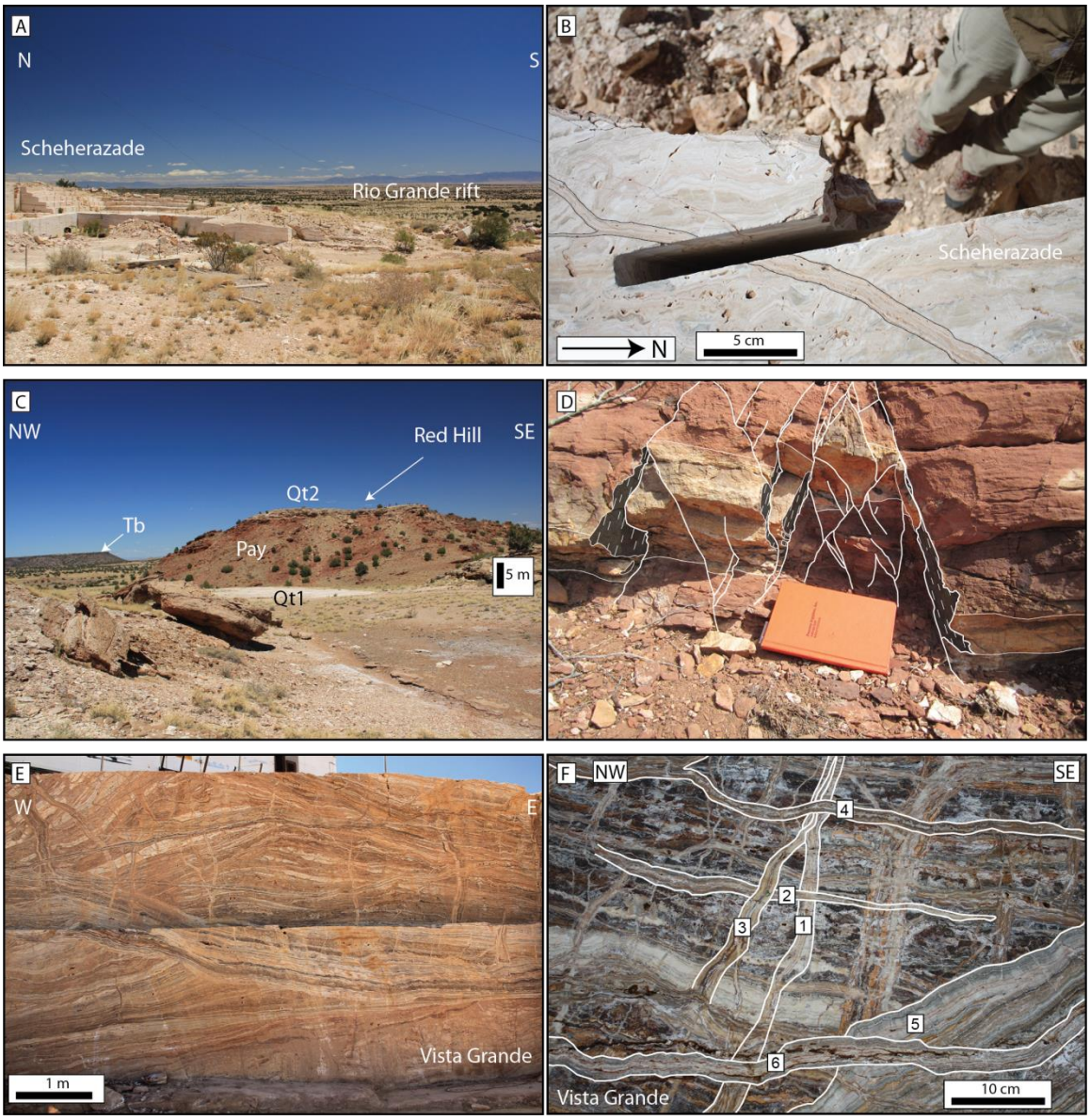

Figure 3. Field photos of study sites. **A.** Looking east into the Rio Grande rift with quarry site Scheherazade in the foreground. **B.** Close-up of Scheherazade. **C.** Looking northeast towards Red Hill and 3.7 Ma basalt in the background. **D.** Small-offset conjugate normal faults cutting Permian Yeso Formation at Red Hill. **E.** View of the northern quarry wall at Vista Grande. **F.** Close-up of quarry wall at Vista Grande highlighting the multiple fracture sets, which cross-cut one another.

perpendicular to the vein wall, and are almost completely filled with sparry calcite, with little to no detrital material. Bedding layers along either side of the veins are offset perpendicular to the walls of the veins, with little shear offset, suggesting that most veins are purely extensional (e.g. Fossen, 2010). Multiple generations of cross-cutting extensional veins are preserved at these three sites (Fig. 3E, F), each with a significant accumulation of vein fill and well developed calcite banding that records multiple deformation events. In thin section, extensional veins from the quarry sites display both syntaxial and antitaxial growth (Ramsay and Huber, 1983). Syntaxial veins display a well-developed median line and elongate calcite fibers grow from the vein wall inward. In contrast, antitaxial vein growth is suggested by radiating calcite fibers that grow from the center of the vein towards the vein wall (Fig. 4). Both suggest incremental deformation and subsequent sealing of cracks by precipitation.

An important morphologically and lithologically different site is Red Hill, whose flanks are composed of reddish-purple brown fine sandstones and siltstones of the Permian Yeso Formation. These Permian rocks are capped by travertine deposits ~2-3 m in thickness that overlie older/elevated terrace gravels from the nearby arroyo that stand ~20 m above Arroyo Salado (Figs. 2, 3). Abundant calcite-filled extensional veins ~ 1 mm to 10 cm in thickness cut both the Yeso Formation and the overlying travertine deposit indicating their Quaternary age. Some small-offset (<1 m shear displacement) faults are observed within the Yeso Formation, but do not offset the overlying travertine. These faults form conjugate pairs, as evidenced by oppositely dipping faults that cross-cut one another. They display normal-sense displacement, and preserve well-defined slickensided surfaces (Fig. 3D). In addition to < 1 m of shear offset, many of the faults

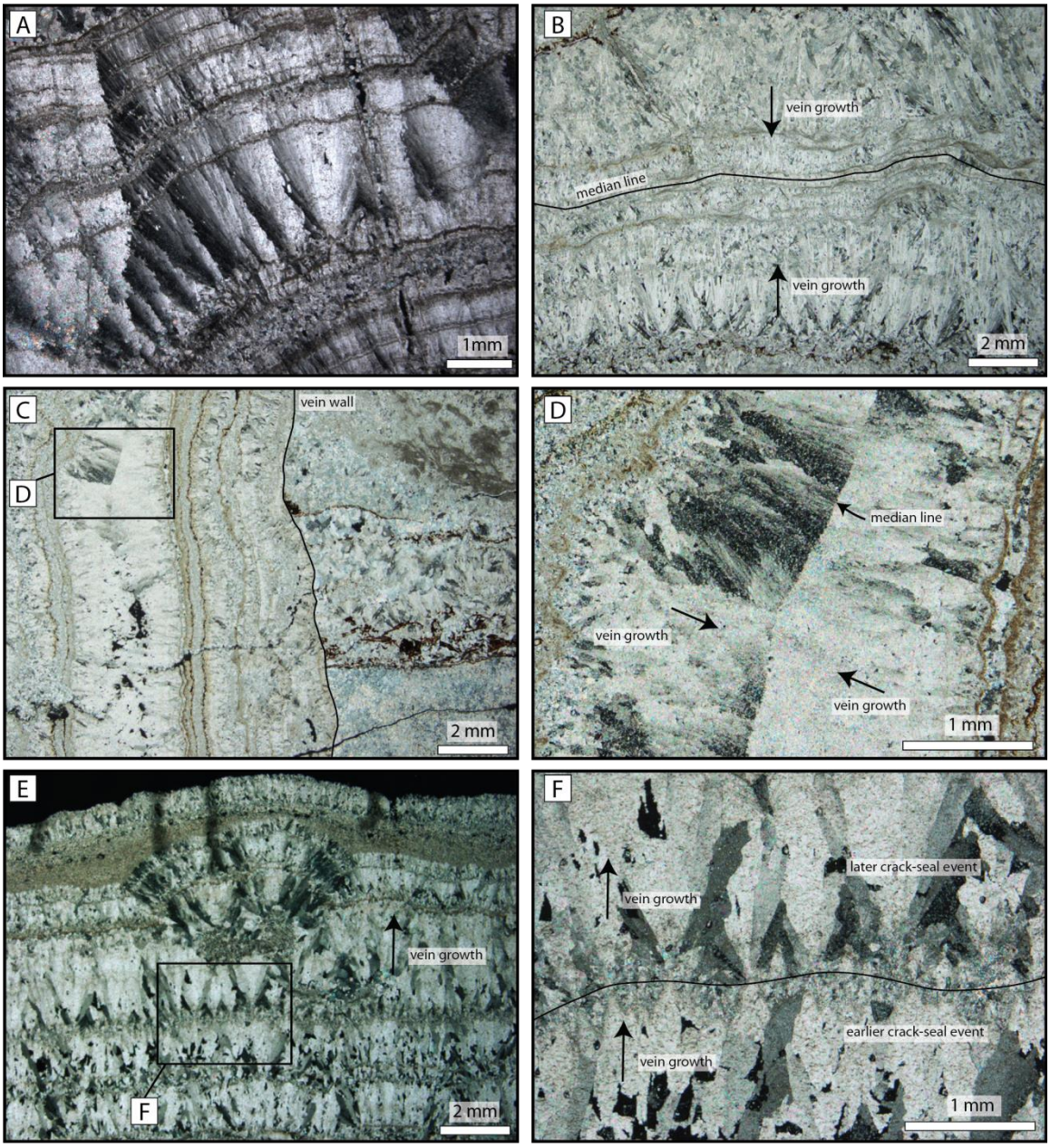

Figure 4. Photomicrographs of calcite-filled extensional veins. **A. and B.** Syntaxial vein growth is indicated at Vista Grande by the radiating geometry of elongate calcite fibers growing towards a central median line. **C.** Perpendicular, cross-cutting veins at Vista Grande. **D.** Well-developed median line suggesting syntaxial vein growth. **E. and F.** Calcite-filled vein at Red Hill. The top of the photomicrograph is the edge of vein, and the fanning geometry of calcite fibers indicates antitaxial growth (from the center of the vein towards the vein wall). Multiple sets of radiating calcite fibers are visible, suggesting multiple episodes of fracture widening and subsequent calcite precipitation.

observed also display a component of extension perpendicular to the walls of the fracture, as evidenced by ~1-4 cm of calcite that has precipitated along the slip surface. The final location, Comanche platform, is a resistant cap consisting of well-cemented sandstone, pebble to cobble conglomerate containing clasts of local Paleozoic rocks, and travertine. Travertine deposits at this location are mostly in the form of infillings which cement the siliciclastic material, but there are also abundant extensional veins which are orthogonal to sedimentary bedding as defined by sandy beds. Veins range from ~2 cm to 20 cm in thickness and are filled predominantly with calcite, and little to no detrital material.

We use the travertine deposits at these five locations, coupled with their associations with the Comanche and Santa Fe fault systems to explore the significance of fractures and veins in the travertine. Given that the 3.7 ± 0.4 Ma basalts in the study area locally overlie fault strands of the Comanche fault zone (Fig. 2) (Callender and Zilinski, 1976), and that timing and amount of Quaternary slip is only poorly documented on the Santa Fe fault, the fractures and veins in travertine provide a record of previously undocumented and quantifiable young tectonism in the zone between the Santa Fe and Comanche faults along the western margin of the Albuquerque basin of the Rio Grande rift.

METHODS

Systematic extensional vein orientation measurements and observations were made at five locations. Sites were chosen to cover a range of different locations along curvilinear faults to test possible stress rotations due to fault orientation, to cover a range of slope aspects to test possible stress contributions from topographically-driven

gravitational stresses, and to include sites dominated by extensional veins as well as conjugate faults to utilize different methods for estimating paleostress.

At Red Hill, slip magnitudes are generally less than ~1 m, so the movement direction was constrained by matching offset bedding layers. Poles to extensional veins from Temple Cream, Scheherazade, Vista Grande, Red Hill, and Comanche were plotted on lower hemisphere equal area stereographic projections using Stereonet software. Similarly, faults at Red Hill were plotted as planes using FaultKin software (Marrett and Allmendinger, 1990; Allmendinger et al., 2012). Statistical analysis of normal faults and extensional veins are computed by means of a Bingham axial distribution (Mardia, 1972). The eigenvalues are a measure of the relative concentrations of measured veins and faults and indicate significant extensional directions. Thus the eigenvalues can be used to quantify the extension directions that are most significant given the population of extensional veins at each study site, and of normal faults at Red Hill. These directions can then be compared to the regional extension direction in the rift.

To evaluate the timing of fracturing and associated calcite precipitation within fractures, samples of fine-grained spar calcite within veins were collected from all three orthogonal extensional vein sets for dating using the uranium-thorium disequilibria method. Vein samples were collected from Temple Cream, Scheherazade, Vista Grande, and Red Hill, and material from the veins was drilled out and analyzed at the Radiogenic Isotope Laboratory at the University of New Mexico following methods described in Asmerom et al. (2010). Samples were collected from the veins because of the observation that most veins contained very little or no detrital material, which reduces the possible contamination of external ^{230}Th.

Extensional displacements from individual veins at each of the three quarry sites were measured with the ultimate goal of calculating strain rates. At each quarry, the extensional displacements of vertical veins were measured along a horizontal line in vertical quarry faces. The initial length along this line was then estimated by subtracting the extensional displacements of all veins from the final length of the line. These values were used to calculate extension at the three quarry sites (Fig. 5), and strains were combined with the available U-series and model ages from vein infillings to calculate strain rates.

RESULTS

Extensional Veins and Faults

Below we discuss the results of extensional veins and normal faults at each of the five study sites and their inferred constraints on principle stress directions. The orientations of extensional veins and normal faults at each location are summarized on lower hemisphere equal area stereographic projections (Fig. 6). Normal faults at Red Hill are plotted as planes, and each associated slickenline is plotted as an arrow that points in the movement direction of the hanging wall. Statistics computed from a Bingham axial distribution analysis from extensional veins are reported in Table 1.

Temple Cream, Scheherazade, and Vista Grande Quarry Sites

Temple Cream quarry displays three orthogonal vein sets corresponding to three orthogonal extension directions. A linked Bingham analysis combining all extensional veins suggests a dominant extension direction that is essentially E-W and horizontal (plunges 00.5° towards 090.6°; $\lambda = 0.6778$; Table 1; Fig. 6). The quarry site Scheherazade, to the north of Temple Cream, contains three similarly-oriented orthogonal

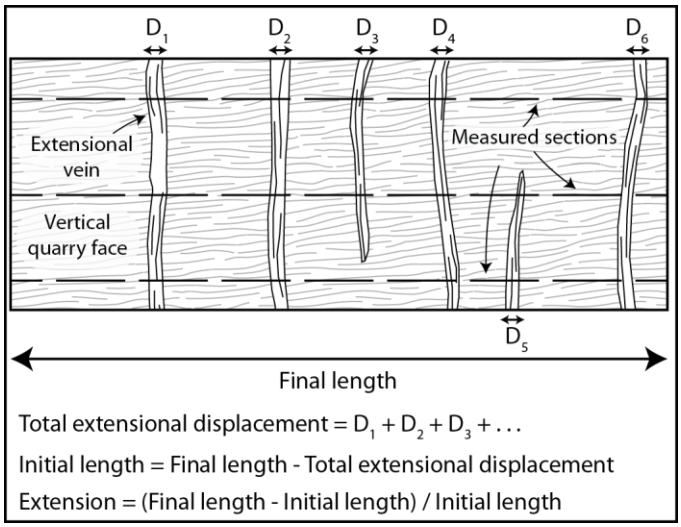

Figure 5. Schematic cross-sectional diagram illustrating the vein measurement and strain calculation process at the three quarry sites.

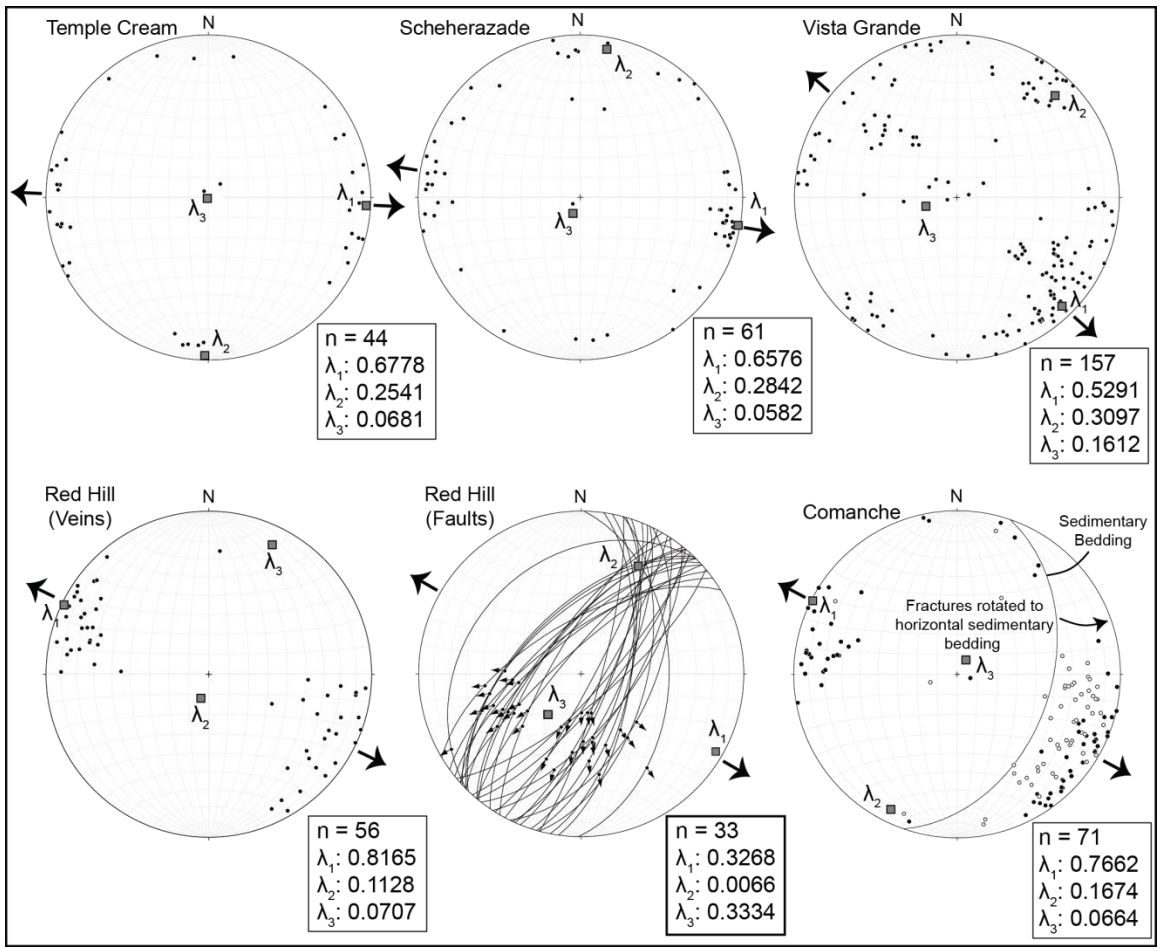

Figure 6. Lower hemisphere, equal area stereographic projections of extensional veins at each location and normal faults at Red Hill. Extensional veins are plotted as poles to planes. Faults at Red Hill are plotted as planes, and arrows on each fault plane are orientations of slickenlines, which indicate the direction of hanging wall motion. The grey squares are the eigenvalue orientations calculated using a linked Bingham axial distribution. Hollow circles at Comanche are measured vein orientations before sedimentary beds are rotated back to horizontal. Plots and Bingham axial distributions are from Stereonet and FaultKin software.

Table 1. Statistics computed from Bingham axial distribution

Study Site	Number of Fractures	Eigenvalue (λ)	Orientation	
			Trend (°)	Plunge (°)
Temple Cream (Extensional Veins)	44	0.6778	090.6	00.5
		0.2541	180.6	01.7
		0.0681	344.0	88.2
Scheherazade (Extensional Veins)	61	0.6576	100.6	01.4
		0.2842	010.4	05.9
		0.0582	204.2	84.0
Vista Grande (Extensional Veins)	157	0.5291	135.9	08.1
		0.3097	043.9	13.9
		0.1612	255.2	73.8
Red Hill (Extensional Veins)	56	0.8165	295.6	01.4
		0.1128	199.3	77.6
		0.0707	025.9	12.3
Red Hill (Faults)	33	0.3268	119.9	05.4
		0.0066	027.2	27.0
		0.3334	220.3	62.3
Comanche (Extensional Veins)	71	0.7662	296.4	00.4
		0.1674	206.3	08.7
		0.0664	029.3	81.3

vein sets. As seen in Figure 6, these veins indicate a dominant near horizontal extension direction that plunges 01.4° towards 100.6° (λ = 0.6576). Vista Grande quarry site contains the highest vein density of any of the study locations (Fig. 3), and is similar to the previous two locations in that it is cut orthogonal subvertical vein sets as well as a system of horizontal veins. Bingham analysis of these veins suggests that the dominant extension direction plunges 08.1° towards 135.9° (λ = 0.5291) (Fig. 6). At each of the three quarry sites, orthogonal vein sets cross-cut one another allowing relative ages to be determined at a given vein intersection, but cross-cutting is nonsystematic such that all three orthogonal vein sets formed contemporaneously.

Red Hill

In contrast to the three previously discussed locations, extensional veins that cut Permian Yeso Formation and overlying travertine deposit at Red Hill are relatively consistent, displaying a dominant extension direction that plunges 01.4° towards 295.6° (λ = 0.8156). Red Hill is also unique because it is the only location of the five dominated by small-offset normal faults rather than extensional veins. In all cases observed, normal faults are cross-cut by extensional veins, indicating they formed first. Even so, the system of conjugate normal faults indicates a dominant extension direction that plunges 05.4° towards 119.9° (λ = 0.3268) (Fig. 6), essentially identical to that of extensional veins, suggesting the two formed in the same stress field.

Comanche

The final location, Comanche, is similar to Red Hill in that sedimentary deposits are only cut by one system of extensional veins. The calcite-filled veins cut sedimentary beds of the Santa Fe Group that have been tilted away from horizontal (present

orientation is approximately 020, 40 SE). This tilting is most likely due to continued movement along the Santa Fe fault which folded the Santa Fe Group into a series of fault-parallel synclines and anticlines (Fig. 2). In most cases, veins are oriented perpendicular and parallel to bedding, and on the eastern edge of the Comanche site, the bedding returns to horizontal and veins are vertical and horizontal, suggesting that extensional fracturing and calcite precipitation at this location occurred prior to tilting of the beds. Thus, to estimate the dominant extension direction during formation of extensional veins, sedimentary beds were restored back to horizontal. Figure 6 shows the vein measurements before and after rotation back to their inferred primary orientation, and indicates a primary extension direction that plunges 00.4° towards 296.4° ($\lambda = 0.7662$), similar to results obtained from Red Hill.

Uranium Series Dating and Model Ages

U-series dating has an upper age limit of ~500,000 – 700,000 years (depending on uranium content) where samples that are older than this return to a state of secular equilibrium with respect to the ^{238}U-^{230}Th radiogenic system, and cannot be precisely or accurately dated with this method (Bourdon et al., 2003). Nevertheless their geochemistry can be used to place important, although less precise, constraints on when they formed. For samples that are outside of this age range, U-series model ages can be calculated for samples if the ^{238}U-^{234}U radiogenic system is not yet in a state of secular equilibrium (younger than ~1.5 Ma). Therefore, samples which are not yet in secular equilibrium with respect to this system cannot be older than ~1.5 Ma (hence 0.5 to 1.5 Ma) , while samples that are in secular equilibrium with respect to both systems must be older than ~1.5 Ma.

A total of 14 samples of calcite in extensional veins were collected from the study sites for U-series dating. Four samples yielded U-series ages that range from ~250 to ~700 ka, six samples were outside of the U-series limit, but not in secular equilibrium with respect to the ^{238}U-^{234}U system (indicating they are older than ~500,000 years and younger than 1.5 Ma), and two samples were in secular equilibrium with respect to the ^{238}U-^{234}U system (i.e. older than ~1.5 Ma). Two samples (JR-BQ-1 and JR-BQ-3) have negative measured $\delta^{234}U$ values, possibly suggesting uranium loss, and so ages are not presented for these samples (Table 2). To further constrain the ages of the six samples that are not in secular equilibrium with respect to the ^{238}U-^{234}U system, U-series model ages were calculated for each of these samples. Model ages are less precise than U-series ages because the initial $\delta^{234}U$ is unknown, and must be estimated. To estimate initial $\delta^{234}U$ values for samples that are outside of U-series range, we use the range of initial $\delta^{234}U$ values obtained from the four successful analyses in this study, and combined them with successful analyses from other travertine deposits in nearby areas at Mesa del Oro and Riley South Mesa (Priewisch et al., 2012). Successful U-series analyses indicate that initial $\delta^{234}U$ values range from 41-849 (Table 2). We choose to disregard the 849 value because of the very large errors associated with it, and instead use a preferred range of 41-525, or initial $\delta^{234}U = 283 \pm 242$. Model ages are calculated using the equation

$$^{234}U\ model\ age = \frac{ln\left[\frac{\left(\delta^{234}U\right)_m - 1}{\left(\delta^{234}U\right)_i - 1}\right]}{-\lambda_{234}} \quad (1)$$

Where $\left(\delta^{234}U\right)_m$ is the measured $\delta^{234}U$ value, $\left(\delta^{234}U\right)_i$ is the initial $\delta^{234}U$ value, and λ_{234} is the decay constant of ^{234}U, which has a value of 245,250 ± 490 years (Cheng et al., 2000). Calculated model ages have large 2σ errors, reflecting the uncertainty in the initial

Table 2. U-series geochemistry, ages, and model ages

Sample number	Location	UTM (E)	UTM (N)	U (ppm)	Th (ppm)	$\delta^{234}U_m$* (± 2σ)	$\delta^{234}U_i$†	($^{230}Th/^{234}U$)§ (± 2σ)	($^{230}Th/^{238}U$)§ (± 2σ)	U-series age (ka)	± 2σ	Calculated Model age (Ma)	Best-fit model age constraints (Ma)
Succesful U-Series Ages From Quarry Sites													
LC02-BQTC-a	Temple Cream	3E+05	4E+06	0.53	0.02	28.2 (1.0)	58	0.9115 (0.0021)	0.9373 (0.0020)	253.6	2.7	--	--
KLC11-SH10c	Scheherazade	3E+05	4E+06	0.5	0	114.6 (1.1)	849	1.0427 (0.0024)	1.1621 (0.0024)	709.4	193.0	--	--
KLC11-SH2b	Scheherazade	3E+05	4E+06	0.45	0	6.3 (1.0)	41	1.0004 (0.0023)	1.0066 (0.0021)	662.7	252.1	--	--
KLC11-VG1a	Vista Grande	3E+05	4E+06	0.550	0	42.6 (1.0)	145	1.0002 (0.0039)	1.0447 (0.0040)	434.6	14.4	--	--
Successful U-Series Ages From Nearby Localities#													
AP10-MDO4a	Mesa del Oro	3E+05	4E+06	0.54	0.01	95.2 (1.6)	195	0.9234 (0.0052)	1.0113 (0.0055)	252.8	5.3	--	--
AP10-MDO13	Mesa del Oro	3E+05	4E+06	0.21	0.04	156.3 (0.6)	410	0.9999 (0.0039)	1.1562 (0.0044)	337.2	8.0	--	--
AP10-MDO30	Mesa del Oro	3E+05	4E+06	0.93	0.370	78.6 (1.1)	399	1.0249 (0.0041)	1.1055 (0.0042)	565.7	68.5	--	--
AP10-MDO53B-a	Mesa del Oro	3E+05	4E+06	0.17	0	105.5 (2.3)	293	0.9954 (0.0049)	1.1004 (0.0049)	360.6	13.2	--	--
LC03-RS10	Riley South Mesa	3E+05	4E+06	2.68	0.03	280.1 (1.1)	525	0.9180 (0.0080)	1.1751 (0.0102)	221.9	5.5	--	--
LC03-RS2	Riley South Mesa	3E+05	4E+06	0.46	0.03	335.4 (0.5)	498	0.7538 (0.0029)	1.0066 (0.0039)	138.2	1.2	--	--
U-Series Model Ages													
KLC11-TC2	Temple Cream	3E+05	4E+06	0.61	0.03	0.9 (1.0)	--	1.0077 (0.0023)	1.0086 (0.0021)	--	--	>1.50**	>1.50**
KLC11-TC20a	Temple Cream	3E+05	4E+06	0.87	0.03	2.7 (1.0)	--	1.0473 (0.0042)	1.0558 (0.0040)	--	--	1.12 - 2.03	1.12 - 1.50

JR-BQ-1	Temple Cream	3E+05	4E+06	1.68	0	-1.6 (1.0)	--	1.0014 (0.0015)	0.9998 (0.0015)	--	--	--	--
JR-BQ-3	Temple Cream	3E+05	4E+06	1.79	0	-2.1 (1.0)	--	1.0018 (0.0023)	0.9997 (0.0021)	--	--	--	--
JR-BQ-4	Temple Cream	3E+05	4E+06	0.87	0.01	53.3 (1.1)	--	1.0545 (0.0016)	1.1107 (0.0013)	--	--	-0.10 - 0.82	0.60 - 0.82
JR-BQ-5	Scheherazade	3E+05	4E+06	1.16	0.01	0.7 (1.0)	--	0.9996 (0.0023)	1.0003 (0.0020)	--	--	>1.50**	>1.50**
JR-BQ-7	Scheherazade	3E+05	4E+06	0.69	0.01	4.5 (1.0)	--	0.9963 (0.0023)	1.0008 (0.0021)	--	--	0.86 - 1.77	0.86 - 1.50
KLC11-VG4a	Vista Grande	3E+05	4E+06	0.88	0.010	21.4 (1.0)	--	1.0274 (0.0041)	1.0532 (0.0040)	--	--	0.24 - 1.15	0.60 - 1.15
JR-BQ-8	Vista Grande	3E+05	4E+06	0.57	0	7.2 (1.0)	--	1.0015 (0.0023)	1.0087 (0.0021)	--	--	0.66 - 1.57	0.66 - 1.50
RedHill-1	Red Hill	3E+05	4E+06	--	--	--	--	1.0532 (0.0044)	1.0212 (0.0042)	--	--	0.62 - 1.53	0.62 - 1.50

*Measured $\delta^{234}U$ values.

†Initial $\delta^{234}U$ values.

[§]Values reported as activity ratios.

[#]Nearby locality samples are from Priewisch et al. (2012).

**Sample is in secular equilibrium with respect to the ^{234}U - ^{238}U system.

$\delta^{234}U$ values used in the calculation. For some model age calculations, this wide range of initial $\delta^{234}U$ values resulted in model ages that are younger than 0.5 Ma or older than 1.5 Ma, even though the sample was in secular equilibrium with respect to the ^{238}U-^{230}Th system, but not in secular equilibrium with respect to the ^{238}U-^{234}U system. These additional constraints can therefore be used to further refine the initial model age calculations that incorporate a generous, but self-consistent, range of initial $\delta^{234}U$ values. Best-estimate model ages for six samples are provided in Table 2. Two samples are in secular equilibrium with respect to the ^{238}U-^{234}U system and hence are older than ~1.5 Ma.

Thus our dating results from calculated model ages and successful U-series ages range from ~250 ka to 1.5 Ma, and two samples are older than 1.5 Ma. All are from calcite sampled from both vertical and horizontal veins in travertine. The important conclusion of the present dating is that fracture formation in travertine mounds was episodically active for over 1.5 Ma and hence measured strains can be considered to be representative of long term (several million year timescale) strain magnitudes, directions, and rates for most or all of the Quaternary (last 2.6 Ma).

Strain Rates

The precipitation kinetics of calcite nucleation and growth control the time and fluid required for a certain volume of calcite to grow in extensional veins (Morse and MacKenzie, 1993). These two variables are often poorly constrained because the fluids themselves are not preserved, but models which precipitate calcite in controlled laboratory environments predict that typical fluid/calcite volume ratios for the formation of thin short veins is 10^5-10^6 (Lee and Morse, 1999). Their model also indicates that the

time necessary to precipitate calcite in nature is highly variable, ranging from thousands to perhaps millions of years for meter-scale veins. In a natural example, high-precision U-series dating of an extensional vein system in Turkey suggested that a 29 mm-thick vein formed through multiple opening events and subsequent calcite precipitation over a time period of ~12 ka (~2.5 mm/ka average rate; Uysal et al., 2011). A nearby study at Soda Dam, New Mexico farther north along the western flank of the Rio Grande rift shows that a ~15 cm calcite vein was developed over a ~100 ka time period (~0.15 mm/ka average rate; Tafoya, 2012). If vein formation occurred on timescales comparable to these empirical results, our veins, which are typically < 5 cm thick, likely developed on timescales of 10's of thousands of years rather than millions of years. Thus an important assumption of this study is that long-term (million year timescale) strain rates can be calculated incorporating measurements of multiple extensional veins across a site that each record 10-100 ka strain accumulation.

Strain rates at each quarry site were calculated parallel to the dominant extension directions illustrated in Figure 6. Strain calculations were made at the three quarry sites by comparing the extensional displacement of all fractures with the total length measured (Fig. 5). We use the parameter longitudinal extension (e) where e = final length - original length/ original length. Although it is difficult to constrain exactly when extensional fractures began to form, several authors have suggested that the travertine platforms found along the western edge of the Albuquerque basin are Pleistocene and younger (Kelley, 1977) and that the waters moving through these fault zones have been active for the last ~2 Ma (Callender and Zilinski, 1976). The U-series and model ages in this study are consistent with this, where the majority of extensional fractures are younger than ~1.5

Ma (Table 2). Therefore, to convert these extensional strain calculations to strain rates, we use a strain accumulation time of 2 Ma to estimate maximum duration for the observed finite extensions of all veins at the quarry sites and hence to produce estimates of Quaternary strain rates (Table 3). To compare our calculations to published data in the Rio Grande rift, all values of published extension in the literature were converted into cumulative strain rates (in units of s^{-1}) for different basins. These rates are listed in Table 4, along with the strain rates calculated in this study and current strain rates calculated across the rift and other regions using GPS.

The strain rates calculated in this study vary from $3.2 \times 10^{-16} \pm 1.4 \times 10^{-16}$ s^{-1} at Temple Cream to $6.9 \times 10^{-16} \pm 3.1 \times 10^{-16}$ s^{-1} at Scheherazade to $3.2 \times 10^{-15} \pm 2.7 \times 10^{-16}$ s^{-1} at Vista Grande. The 10^{-16} s^{-1} strain rates at Temple Cream and Scheherazade are comparable to the long-term strain rates reported for the central Rio Grande rift which are estimated by restored cross-sections (Table 4), but the 10^{-15} s^{-1} calculated strain rates at Vista Grande are an order of magnitude faster. The strain rates from the quarry sites are also significantly faster than the current strain rates for the Rio Grande rift of 10^{-17} s^{-1} measured by GPS. The Basin and Range province, which interfingers with the Rio Grande rift south of the study region, has reported current strain rates of 10^{-16} to 10^{-15} s^{-1} that are comparable to the Quaternary rates calculated in this study (Bennett et al., 2003). Quaternary strain rates calculated in the Rio Grande rift were also compared to the GPS-measured rates in the East African rift. Although the driving mechanisms of extension may differ between the Rio Grande and East African rifts, a simple comparison of strain rates is presented because these two locations are among the most well-studied and definitive examples of continental rifts worldwide. Measured GPS-constrained strain

Table 3. **Calculated strain rates at quarry sites**

Study site	Final length (Lf) (cm)	# of veins measured	Total extensional displacement (cm)	Initial length (Li) (cm)	Extension	Accumulation time (m.y.)	Strain rate (s^{-1})	Average strain rate (st dev) (s-1)
Temple Cream								
Transect 1	876.3	18	22.0	854.3	0.026	2	4.08×10^{-16}	3.19×10^{-16} (1.43×10^{-16})
Transect 2	551.0	8	13.4	537.6	0.025	2	3.95×10^{-16}	
Transect 3	860.0	14	8.3	851.7	0.010	2	1.54×10^{-16}	
Scheherazade								
Transect 1	3086.1	58	141.0	2945.1	0.048	2	7.59×10^{-16}	6.85×10^{-16} (3.05×10^{-16})
Transect 2	2198.0	33	58.7	2139.3	0.027	2	4.35×10^{-16}	
Transect 3	2198.0	41	62.0	2136.0	0.029	2	4.60×10^{-16}	
Transect 4	833.0	20	53.4	779.6	0.068	2	1.09×10^{-15}	
Vista Grande								
Transect 1	1280.2	68	221.5	1058.7	0.209	2	3.32×10^{-15}	3.23×10^{-15} (2.71×10^{-16})
Transect 2	2808.0	115	437.9	2370.1	0.185	2	2.93×10^{-15}	
Transect 3	1500.0	126	268.2	1231.8	0.218	2	3.45×10^{-15}	

Note: Extension = (Lf - Li)/Li; strain rate = extension/second (s^{-1}).

Table 4. Summary of long-term and active strain rates in extensional environments.

Location	Total Extension*	Time Period	Strain Rate (s^{-1})†	Reference
Long-Term Strain Rates of the Rio Grande Rift				
San Luis Basin	0.08 - 0.12	~30-27 Ma to Holocene	8.45×10^{-17} to 1.41×10^{-16}	Kluth and Schaftenaar (1994)
Espanola Basin	0.10	~26 Ma to Holocene	1.22×10^{-16}	Golombek et al. (1983)
Northern Albuquerque Basin	0.17	~28-21 Ma to Holocene	1.92×10^{-16} to 2.57×10^{-16}	Russell and Snelson (1994)
Southern Albuquerque Basin	0.28 - 0.30	~28-21 Ma to Holocene	3.17×10^{-16} to 4.53×10^{-16}	Russell and Snelson (1994)
Current GPS Strain Rates of the Rio Grande Rift				
San Luis Basin	--	2008 - 2012	$4.41 \times 10^{-17} \pm 6.34 \times 10^{-18}$	Berglund et al. (2012)
Espanola Basin	--	2008 - 2012	$3.90 \times 10^{-17} \pm 6.34 \times 10^{-18}$	Berglund et al. (2012)
Southern Albuquerque Basin	--	2008 - 2012	$3.96 \times 10^{-17} \pm 6.34 \times 10^{-18}$	Berglund et al. (2012)
Quaternary Strain Rates of the Western Albuquerque Basin				
Temple Cream	0.02	2 Ma to Recent	$3.19 \times 10^{-16} \pm 1.43 \times 10^{-16}$	This Study
Scheherazade	0.04	2 Ma to Recent	$6.85 \times 10^{-16} \pm 3.05 \times 10^{-16}$	This Study
Vista Grande	0.20	2 Ma to Recent	$3.23 \times 10^{-15} \pm 2.71 \times 10^{-16}$	This Study
Current GPS Strain Rates of the East African Rift				
Afar Triple Junction	--	1992 - 2010	6.34×10^{-17} to 6.02×10^{-15}	Kogan et al. (2012)
Central Main Ethiopian Rift	--	1992 - 2010	6.34×10^{-17} to 4.85×10^{-14}	Kogan et al. (2012)
Southern Main Ethiopian Rift	--	1992 - 2010	9.51×10^{-17} to 7.26×10^{-15}	Kogan et al. (2012)
Current GPS Strain Rates of the Basin and Range				
Western Great Basin	--	1991 - 1999	$7.92 \times 10^{-16} \pm 1.58 \times 10^{-16}$ to $1.81 \times 10^{-15} \pm 2.85 \times 10^{-16}$	Bennett et al. (2003)
Northern Basin and Range	--	1991 - 1999	$3.17 \times 10^{-16} \pm 3.17 \times 10^{-17}$	Bennett et al. (2003)

*Extension = $(l_f - l_i)/l_i$.

†Strain rate = Extension/second (s^{-1}).

§GPS—global positioning system.

rates in the East African rift vary by several orders of magnitude. At the slow end, 10^{-17} s^{-1} rates are comparable to the current rates measured in the Rio Grande rift (Berglund et al., 2012), and are slower than calculated rates in this study. The fastest extensional strain rates were measured within the central Main Ethiopian Rift, where rates are as high as 4.9 x 10^{-14} s^{-1} (Kogan et al., 2012). The Afar Triple Junction (6.3 x 10^{-17} to 6.0 x 10^{-15} s^{-1}) and the southern Main Ethiopian Rift (9.5 x 10^{-17} to 7.3 x 10^{-15} s^{-1}) have fastest strain rates that are comparable to the 10^{-15} s^{-1} rates calculated at quarry site Vista Grande.

DISCUSSION

This section discusses several important implications of our calcite vein and strain rate data, beginning with the possible causes of stress which could result in the extensional vein and fault orientations. Then we discuss the role of high fluid pressures on the fracture process and calculated strain rates, and finally we include a discussion of the possible sources of fluid available for travertine deposition. Figure 8 is a summary diagram that helps bring these concepts together.

Origin and Nature of Stresses

Stress fields in tectonically active regions deviate from lithostatic conditions where stresses are equal in all directions and reflect an instantaneous resolution of combined gravitational and tectonic driving forces. Fluids that precipitated calcite within veins was most likely coupled with near-surface hydrologic processes and could for example, have filled cracks formed from gravitationally induced near-surface downslope movement. If downslope movement was important, vein arrays would be expected to fan around sloping mound deposits and otherwise be perpendicular to topographic slopes.

Instead, the uniformity of vein orientations at study sites with different slope aspects suggests that topography did not control vein orientation.

Rather than surface gravitational stresses controlling the orientations of extensional veins, extension directions are parallel to the regional E-W finite extension direction and GPS-recorded velocity vectors, suggesting that veins are most likely products of a local tectonic stress field. This is supported by the compiled "young" stress indicators from the World Stress Map (Heidbach et al., 2008) that indicate EW to NW-SE directed extension in the rift throughout much of New Mexico (Fig. 1), including the alignment of Quaternary cinder cones at two separate locations in the central Albuquerque Basin near the study site (Kelley and Kudo; 1978; Aldrich and Laughlin; 1984). The parallelism of extension directions indicated by extensional veins and conjugate normal faults at Red Hill also supports the interpretation of a tectonic origin for the stresses. The broad sweep of extension orientations from E-W to NW-SE follows the orientation of rift-bounding structures arguing that fault anisotropy may have resulted in small-scale stress reorientations (e.g. Faulkner et al., 2006). We therefore consider the veins and normal faults at these study sites as records of tectonic strain accumulation at the 1-2 Ma time scale.

Effect of Elevated Fluid Pressure

The travertines at each of the five study sites record a large flux of fluids through the upper crust at the time the fractures developed. Almost all fractures are completely filled with calcite with very little detrital material, suggesting migration of CO_2-rich fluids which healed the fracture. Elevated fluid pressures alter the regional stress field by reducing the normal stress (Hubbert and Rubey, 1959), which amplifies the development

of fractures that are favorably oriented with respect to the regional stress field. In the low-differential stress environment at each of the study sites, these high fluid pressures resulted primarily in the development of extensional veins. Thus the anomalously-high strain rates calculated at these sites, which are 1-2 orders of magnitude larger than the present day strain rates, may have been facilitated by high fluid pressures at these locations in the rift during the Quaternary.

Although study sites Red Hill and Comanche only contain veins that suggest NW-SE directed horizontal extension, quarry sites Temple Cream, Scheherazade, and Vista Grande contain three orthogonal vein patterns. Veins repeatedly offset one another to produce a mesh-like grid, indicating that all three vein sets formed contemporaneously (Fig. 3). At each location, however, the highest fracture density is ~EW to NW-SE (Fig. 6), parallel to the regional extension direction in the rift. To explain the orthogonal vein sets at the three quarry sites, we invoke a model where during certain time periods high pore fluid pressures create near axial stress conditions with σ_1 vertical and $\sigma_2 \sim \sigma_3$. Under these conditions of very localized high pore fluid pressure, as extensional fractures develop perpendicular to σ_3, stress is relieved in the σ_3 direction, and σ_2 and σ_3 become sub-equal. During these times extensional fractures can develop perpendicular to σ_2 and σ_3 (Caputo, 1995). Although these two steeply-dipping extensional veins sets cross-cut bedding, the layered heterogeneity in the travertine deposit also most likely controlled vein orientation as evidenced by the horizontal vein sets that parallel bedding. In this model, sub-equal principle stresses due to elevated pore fluid pressures combined with heterogeneities in the travertine deposit produced the interweaving pattern of veins most elegantly displayed at Vista Grande (Fig. 3).

Possible Sources of Fluid for Travertine Deposition

Spring discharge and hence accumulation of travertine at each of the five study sites has been shown using U-series dating to be episodic at 100 ka timescales in several locations in the Southwest: at Soda Dam, New Mexico (Tafoya, 2012); San Ysidro, New Mexico (Cron, 2011); La Madera, New Mexico (Crossey et al., 2011); Springerville, Arizona (Embid, 2009); Grand Canyon, Arizona (Szabo, 1990); and the Salt Wash Graben, Utah (Kampman et al., 2012). This episodicity likely reflects both paleoclimate and paleotectonic influences as deposition of travertine requires both ample spring discharge and CO_2 saturation. Well recognized wet/dry periods in the U.S. Southwest (e.g. Polyak and Asmerom, 2001) likely caused fluctuations in head at spring discharge points with higher heads resulting in larger-volume travertine deposition. Fracture age constraints provided in this study are not of high enough resolution to resolve this episodicity, but instead integrate vein growth over the 1-2 Ma timescale and thereby average out the paleoclimate and paleotectonic oscillations.

As discussed previously, in the Albuquerque basin of the Rio Grande rift geochemical tracers of spring waters indicate a mix between endogenic fluids and volumetrically-dominant meteoric and river water (Newell et al, 2005; Williams et al., 2013). Along the western margin of the Albuquerque basin, meteoric groundwater flows east into the basin from the Paleozoic and Mesozoic rocks within the Colorado Plateau, and mixes with local arroyo discharge. Active springs within the study area contribute up to 16% of the total water in this region (Plummer et al., 2004), and contain ^{3}He values which indicate ~7.6% mantle-derived helium (Fig. 2) (Williams et al., 2013), while the He abundances measured in fluid inclusions from travertine at Scheherazade suggest

these deposits were precipitated from geochemically similar fluids as the modern springs (Fig. 2). Faults within the study region, such as the Comanche fault, penetrate into the Precambrian basement rocks (Callender and Zilinski, 1976) and can potentially act as fluid pathways to the surface. Thus these datasets suggest that in this region the fluids available for travertine precipitation are a mixture of predominantly epigenic waters that have been mixed with volumetrically-minor endogenic fluids.

The close spatial association between the study site and the underlying Socorro magma body suggests a possible connection between magmatism, fluid migration through the upper crust, travertine precipitation, and continued rift development. Although the Socorro magma body is thought to only be several hundred years old based on cooling models of a basaltic melt of its size (Fialko and Simons, 2001; Turcotte and Schubert, 2002), observed heat flow data at the surface suggests that the modern Socorro magma body is only the most recent expression of a longer-lived magmatic system in this area (Reiter et al., 2010). Their calculations indicate intra-rift magmatism in this region for at least the past 1 Ma, and possibly longer, which overlaps with the timing of extensional veins in travertine deposits. The longevity of magma emplacement within the crust beneath the study region suggests that the seismic activity recorded today may also have been active throughout the Quaternary.

We prefer a model where epigenic fluids near the surface mix with volumetrically-minor endogenic fluids that are derived from magma melts in the middle crust beneath the study area (Fig. 7). At depth, warm endogenic fluids may be aseismically transported to the surface along basement-penetrating faults either by thermally or chemically driven buoyancy, where thermal buoyancy is governed by the

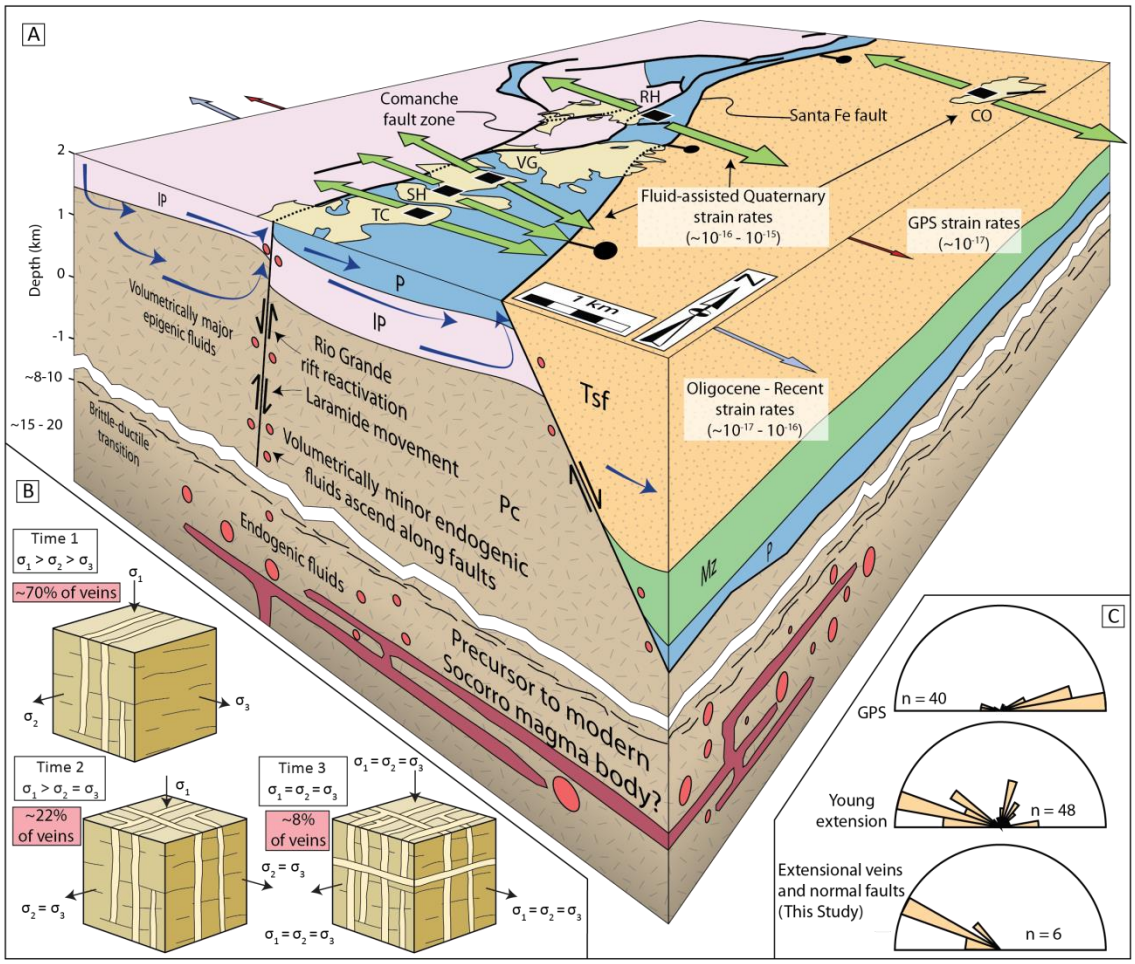

Figure 7. A. Block diagram of the study region highlighting possible fluid sources to precipitate travertine and facilitate the development of tectonic extensional fractures at high strain rates. Pc = Precambrian; IP = Pennsylvanian; P = Permian; Mz = Mesozoic; Tsf = Santa Fe Group; TC = Temple Cream; SH = Scheherazade; VG = Vista Grande; RH = Red Hill; CO = Comanche. **B.** Close-up of stress conditions required to produce orthogonal vein sets at Temple Cream, Scheherazade, and Vista Grande. Extensional veins form perpendicular to σ3, and orthogonal fracture sets only form during times of high pore fluid pressure. **C.** Rose diagrams show sub parallelism of current extension directions from GPS and young extension directions (from Figure 1), and extension directions in this study.

geothermal gradient and chemical buoyancy is driven by differences in salinity (e.g. Schoofs et al., 1999). Alternatively, endogenic fluids may be transported to the surface by "fault valve" processes (e.g. Sibson, 1992), in which case the fluid pressures at depth fluctuate due to seismic cycles. Syntaxial growth of calcite fibers, well-developed median lines, and multiple generations of calcite fiber growth suggest that veins formed and developed episodically and widened incrementally through individual cracking events. The presence of the nearby Socorro Seismic Anomaly permits the possibility that fluid movement at depth may be controlled by seismic as well as aseismic processes, and that the veins and fractures in travertine deposits may record an important surface-to-mantle connection which facilitates the continued development of the Rio Grande rift.

CONCLUSIONS

Calcite-filled extensional veins in travertine deposits at five study sites along the western margin of the Albuquerque basin are inferred to record local Quaternary extensional in the Rio Grande rift. U-series ages and model ages of calcite within veins range from ~250 ka to >1.5 Ma. The veins are dominantly extensional, and formed through multiple cracking events and calcite precipitation. Veins at each site indicate EW to NW-SE oriented extension, which is consistent with the regional extension in the Rio Grande rift, although minor stress reorientations may be due to local stress perturbations within the Comanche-Santa Fe fault system. Three of the five study sites were subjected to high enough pore fluid pressures and were shallow enough to create near axial stress conditions, which results in the development of three orthogonal vein sets during times of sub-equal stress magnitudes. Strain rates observed at the quarry sites range from $3.2 \times 10^{-16} \pm 1.4 \times 10^{-16}$ s^{-1} to $3.2 \times 10^{-15} \pm 2.7 \times 10^{-16}$ s^{-1}, which is higher than both the current

observed rates in the rift, as well as the long term strain rates calculated for different basins of the Rio Grande rift. Thus, although anomalously high strain rates are variable over very short spatial scales, they can persist for millions of years, and these rates instead are comparable to current strain rates within the Basin and Range province and East African rift. Fluids that precipitated travertine are a mixture of meteoric water and volumetrically-minor endogenic fluids which ascend to the surface along basement-penetrating faults through aseismic processes and possibly seismic events.

These data and this model have important implications for understanding early stages of continental rifting. (1) Not only is the Rio Grande rift still extending based on GPS studies, but this study shows anomalously-high, fluid-assisted strain rates in the Quaternary, suggesting that rift maturation is a highly dynamic process spatially and temporally. (2) The observed consistency of EW extension for paleostrain and paleostress directions across different time scales (30 Ma to Recent) points toward persistent tectonic forcings, although strain rates may be highly influenced by fluid flux through fault systems at local scales.

ACKNOWLEDGEMENTS

Field studies and geologic mapping completed during this project were supported by the Educational Component of the National Cooperative Geologic Mapping Program (EDMAP) award number G11AC20152 to Karl E. Karlstrom, and New Mexico STATEMAP funding to Jason Ricketts and Karl Karlstrom. U-series dating of travertine samples was supported by National Science Foundation grant 0838575 awarded to Laura Crossey and Karl Karlstrom and was completed at the Radiogenic Isotope Laboratory at the University of New Mexico. We thank Miela Kolomaznik for laboratory assistance,

and Jim Lardner, who owns and operates New Mexico Travertine, Inc., for providing access to the quarry sites. Grants from the Sloan Foundation, Geological Society of America, and the New Mexico Geological Society to Jason Ricketts are also appreciated. Constructive reviews by Christie Rowe and two anonymous reviewers led to improvements of this manuscript.

REFERENCES

Aldrich Jr, M.J., and Laughlin, A.W., 1984, A model for the tectonic development of the southeastern Colorado Plateau boundary: Journal of Geophysical Research, v. 89, no. B12, p. 10,207-10,218.

Allmendinger, R.W., Cardozo, N., and Fisher, D., 2012, Structural geology algorithms: Vectors and tensors in structural geology: Cambridge University Press.

Asmerom, Y., Polyak, V.J., and Burns, S.J., 2010, Variable winter moisture in the southwestern United States linked to rapid glacial climate shifts: Nature Geoscience, v. 3, p. 114–117, doi: 10.1038/ngeo754.

Bachman, G.O., and Mehnert, H.H., 1978, New K-Ar dates and the late Pliocene to Holocene geomorphic history of the central Rio Grande region, New Mexico: Geological Society of America Bulletin, v. 89, p. 283-292.

Balch, R.S., Hartse, H.E., Sanford, A.R., and Lin, K.W., 1997, A new map of the geographical extent of the Socorro mid-crustal magma body: Bulletin of the Seismological Society of America, v. 87, p. 174-182.

Baldridge, W.S., Olsen, K.H., and Callender, J.F., 1984, Rio Grande rift: Problems and Perspectives: New Mexico Geological Society Guidebook, 35th Annual Conference, 46 p.

Bennett, R.A., Wernicke, B.P., Niemi, N.A., Friedrich, A.M., and Davis, J.L., 2003, Contemporary strain rates in the northern Basin and Range province from GPS data: Tectonics, v. 22, doi: 10.1029/2001TC001355.

Berglund, H.T., Sheehan, A.F., Murray, M.H., Roy, M., Lowry, A.R., Nerem, R.S., and Blume, F., 2012, Distributed deformation across the Rio Grande Rift, Great Plains, and Colorado Plateau: Geology, v. 40, p. 23-26.

Bourdon, B., Turner, S., Henderson, G.M., and Lundstrom, C.C., 2003, Introduction to U-series Geochemistry: Reviews in Mineralogy and Geochemistry, v. 52, no. 1, p. 1–21.

Callendar, J.F., and Zilinski, R.E., 1976, Kinematics of Tertiary and Quaternary deformation along the eastern edge of the Lucero uplift, central New Mexico: New Mexico Geological Society Special Publication 6, p. 53-61.

Caputo, R., 1995, Evolution of orthogonal sets of coeval extension joints: Terra Nova, v. 7, p. 479-490.

Chapin, C.E., and Cather, S.M., 1994, Tectonic setting of the axial basins of the northern and central Rio Grande rift *in* Keller, G.R., and Cather, S.M., eds., Basins of the Rio Grande Rift: Structure, Stratigraphy, and Tectonic Setting: Boulder, Colorado, Geological Society of America Special Paper 291.

Cheng, H., Edwards, R.L., Hoff, J., Gallup, C.D., Richards, D.A., and Asmerom, Y., 2000, The half-lives of uranium-234 and thorium-230: Chemical Geology, v. 169, p. 17-33.

Connell, S.D., 2004, Geology of the Albuquerque Basin and tectonic development of the Rio Grande rift in north-central New Mexico, *in* Mack, G.H., and Giles, K.A., eds., The Geology of New Mexico-A Geologic History: New Mexico Geological Society Special Publication 11, p. 359-388.

Cron, B., 2011, Geochemical characteristics and microbial diversity of CO_2-rich mound springs of the Tierra Amarilla anticline, New Mexico [M.S. thesis]: University of New Mexico, 110 p.

Crossey, L.J., Fischer, T.P., Patchett, P.J., Karlstrom, K.E., Hilton, D.R., Newell, D.L., Huntoon, P., Reynolds, A.C., and de Leeuw, G.A.M., 2006, Dissected hydrologic system at the Grand Canyon: Interaction between deeply derived fluids and plateau aquifer waters in modern springs and travertine: Geology, v. 34, p. 25-28, doi: 10/1130/G22057.1.

Crossey, L.J., Karlstrom, K.E., Springer, A., Newell, D., Hilton, D.R., and Fischer, T., 2009, Degassing of mantle-derived CO_2 and He from springs in the southern Colorado Plateau region-Neotectonic connections and implications for groundwater systems: Geological Society of America Bulletin, v. 121, p. 1,034-1,053.

Crossey, L.J., Karlstrom, K.E., Newell, D.L., Kooser, A., and Tafoya, A., 2011, The La Madera travertines, Rio Ojo Caliente, northern New Mexico: investigating the linked system of CO_2-rich springs and travertines as neotectonic and paleoclimate indicators, *in* Koning, D.J., Karlstrom, K.E., Kelley, S.A., Lueth, V.W., and Aby, S.B., eds., Geology of the Tusas Mountains and Ojo Caliente Area, New Mexico Geological Society, Guidebook 62, p. 301-316.

Embid, E.H., 2009, U-series dating, geochemistry, and geomorphic studies of travertines and springs of the Springerville area, east-central Arizona, and tectonic implications [M.S. thesis]: University of New Mexico, 116 p.

Faulkner, D.R., Mitchell, T.M., Healy, D., and Heap, M.J., 2006, Slip on 'weak' faults by the rotation of regional stress in the fracture damage zone: Nature, v. 444, p. 922-925.

Fialko, Y., and Simons, M., 2001, Evidence for on-going inflation of the Socorro magma body, New Mexico, from interferometric aperture radar imaging: Geophysical Research Letters, v. 28, p. 3,549-3,552, doi: 10.1029/2001GL013318.

Fossen, 2010, Structural Geology: Cambridge, Cambridge University Press, 463 p.

Giggenbach, W.F., 1992, The composition of gases in geothermal and volcanic systems as a function of tectonic setting, *in* Kharaka, Y.K., and Maest, K., eds., Proceedings of the 7th International Symposium on Water-Rock Interaction: Rotterdam, A.A. Balkema, p. 873-878.

Golombek, M.P., McGill, G.E., and Brown, L., 1983, Tectonic and geologic evolution of the Española basin, Rio Grande rift: Structure, rate of extension, and relation to the state of stress in the western United States: Tectonophysics, v. 94, p. 483-507.

Gundimeda, M., 1995, Environmental gas analysis of fluid inclusions in calcium carbonates from New Mexico including vein calcites from Los Alamos National Laboratory, using quadropole mass spectrometer [M.S. thesis]: New Mexico Institute of Mining and Technology, 154 p.

Heidbach, O., Tingay, M., Barth, A., Reinecker, J., Kurfeβ, D., and Müller, B., 2008, The World Stress Map database release 2008, doi: 10.1594/GFZ.WSM.Rel2008

Hubbert, M.K., and Rubey, W.W., 1959, Role of pore fluid pressure in mechanics of overthrust faulting. Part I: Geological Society of America Bulletin, v. 70, p. 115-166.

Kampman, N., Burnside, N.M., Shipton, Z.K., Chapman, H.J., Nicholl, J. a., Ellam, R.M., and Bickle, M.J., 2012, Pulses of carbon dioxide emissions from intracrustal faults following climatic warming: Nature Geoscience, v. 5, p. 352–358, doi: 10.1038/ngeo1451.

Kelley, V.C., 1977, Geology of the Albuquerque basin, New Mexico: New Mexico Bureau of Mines and Mineral Resources, Memoir 33.

Kelley, V.C., and Kudo, A.M., 1978, Volcanoes and related basalts of the Albuquerque Basin, New Mexico: New Mexico Bureau of Mines and Mineral Resources Circular 156, 30 p.

Kelley, S.A., Chapin, C.E., and Corrigan, J., 1992, Late Mesozoic to Cenozoic cooling histories of the flanks of the northern and central Rio Grande rift, Colorado and New Mexico: New Mexico Bureau of Geology and Mineral Resources, Bulletin 145, 39 p.

Kelley, S.A. and Chamberlin, R.C., 2012, Our growing understanding of the Rio Grande rift: New Mexico Earth Matters, v. 12, no.2, p. 1-4.

Kluth, C.F., and Schafenaar, C.H., 1994, Depth and geometry of the northern Rio Grande rift in the San Luis basin, south-central Colorado: Geological Society of America, Special Paper 291, p. 27-37.

Kogan, L., Fisseha, S., Bendick, R., Reilinger, R., McClusky, S., King, R., and Solomon, T., 2012, Lithospheric strength and strain localization in continental extension from observations of the East African Rift: Journal of Geophysical Research, v. 117, B03402, doi: 10.1029/2011JB008516.

Larsen, S., and Reilinger, R., 1983, Recent measurements of crustal deformation related to the Socorro magma body, New Mexico, *in* Chapin, C.E., ed., New Mexico Geological Society Thirty Fourth Annual Conference, Socorro Region II, p. 191-121.

Larsen, S., Reilinger, R., and Brown, L.D., 1986, Evidence of ongoing crustal deformation related to magmatic activity near Socorro, New Mexico: Journal of Geophysical Research, v. 91, p. 6,283-6,292.

Lee, Y., and Morse, J.W., 1999, Calcite precipitation in synthetic veins: implications for the time and fluid necessary for vein filling: Chemical Geology, v. 156, p. 151-170.

Lewis, C.J., and Baldridge, W.S., 1994, Crustal extension in the Rio Grande rift, New Mexico: Half-grabens, accommodation zones, and shoulder uplifts in the Ladron Peak-Sierra Lucero area, *in* Keller, G.R., and Cather, S.M., eds., Basins of the Rio Grande Rift: Structure, Stratigraphy, and Tectonic Setting: Boulder, Colorado, Geological Society of America Special Paper 291.

Lozinski, R.P., and Tedford, R.H., 1991, Geology and paleontology of the Santa Fe Group, southwestern Albuquerque Basin, Valencia County, New Mexico: New Mexico Bureau of Mines and Mineral Resources, Bulletin 132, 35 p.

Malagnini, L., Lucente, F.P., De Gori, P., Akinci, A., and Munafo, I., 2012, Control of pore fluid pressure diffusion on fault failure mode: Insights from the 2009 L'Aquila seismic sequence: Journal of Geophysical Research, v. 117, B05302, doi: 10.1029/2011JB008911.

Mardia, K.V., 1972, Statistics of Directional Data: London, Academic Press.

Marrett, R.A. and Allmendinger, R.W., 1990, Kinematic analysis of fault-slip data: Journal of Structural Geology, v. 12, p. 973-986.

May, S.J., and Russell, L.R., 1994, Thickness of syn-rift Santa Fe Group in the Albuquerque Basin and its relation to structural style, *in* Keller, G.R., and Cather, S.M., eds., Basins of the Rio Grande rift: Structure, Stratigraphy, and Tectonic Setting: Boulder, Colorado, Geological Society of America Special Paper 291.

McCalpin, J.P., 2005, Late Quaternary activity of the Pajarito fault, Rio Grande rift of northern New Mexico, USA: Tectonophysics, v. 408, p. 213-236.

McCalpin, J.P., Harrison, J.B.J., Berger, G.W., and Tobin, H.C., 2011, Paleoseismicity of a low-slip-rate normal fault in the Rio Grande rift, USA: The Calabacillas fault, Albuquerque , New Mexico *in* Audemard, M., F.A., Michetti, F.A., and McCalpin, J.P., eds., Geologic Criteria for Evaluating Seismicity Revisited: Forty Years of Paleoseismic Investigations and the Natural Record of Past Earthquakes: Geological Society of America Special Paper 479, p. 23-46, doi: 10.1130/2011.2479(01).

Morse, J.W., and Mackenzie, F.T., 1993, Geochemical constraints on $CaCO_3$ transport in the subsurface: Chemical Geology, v. 105, p. 181-196.

Newell, D.L., Crossey, L.J., Karlstrom, K.E., and Fischer, T.P., 2005, Continental-scale links between the mantle and groundwater systems of the western United States: Evidence from travertine springs and regional He isotope data: GSA Today, v. 15, p. 4-10.

Olig, S.S., Eppes, M.C., Forman, S.L., Love, D.W., and Allen, B.D., 2011, Late Quaternary earthquakes on the Hubbell Spring fault system, New Mexico, USA:

Evidence for noncharacteristic ruptures of intrabasinal faults in the Rio Grande rift, *in* Audemard, M., F.A., Michetti, F.A., and McCalpin, J.P., eds., Geologic Criteria for Evaluating Seismicity Revisited: Forty Years of Paleoseismic Investigations and the Natural Record of Past Earthquakes: Geological Society of America Special Paper 479, p. 47-77, doi: 10.1130/2011.2479(02).

Polyak, V.J., and Asmerom, Y., 2001, Late Holocene climate and cultural changes in the Southwestern United States: Science, v. 294, p. 148-151.

Plummer, L.N., Bexfield, L.M., Anderholm, S.K., Sanford, W.E., and Busenberg, E., 2004, Hydrochemical tracers in the middle Rio Grande Basin, USA: 1. Conceptualization of groundwater flow: Hydrogeology Journal, v. 12, p. 359-388.

Priewisch, A., Crossey, L.J., Embid, E., Karlstrom, K.E., Polyak, V., Asmerom, Y., Ricketts, J.W., and Nereson, A., 2012, Large-volume Quaternary travertine deposits in the Rio Grande rift and Jemez lineament, New Mexico and Arizona: implications for paleoclimate, landscape evolution, and neotectonics: Geological Society of America Abstracts with Programs, v. 44, no. 6, p. 33.

Ramsay, J.G., and Huber, M.I., 1983, The Techniques of Modern Structural Geology, Volume 1: Strain Analysis: Academic Press, London.

Reinhart, E.J., and Sanford, A.R., 1981, Upper crustal structure of the Rio Grande Rift near Socorro, New Mexico, from inversion of micro earthquake S-wave reflections: Seismological Society of America Bulletin, v. 71, p. 437-450.

Reiter, M.R., Chamberlain, R.M., and Love, D.L., 2010. New data reflect on the thermal antiquity of the Socorro magma body locale, Rio Grande rift, New Mexico. Lithosphere, v. 2, no. 6, p. 447-453.

Ricketts, J.W., Karlstrom, K.E., Kelley, S.A., and Read, A.S., 2011, Cross-section restoration from Ladron Peak to the Joyita Hills and investigations of the timing and mechanism of low-angle normal faulting in the Rio Grande rift: New Mexico Geological Society Spring Meeting, p. 56.

Roy, M., Karlstrom, K.E., Kelley, S.A., Pazzaglia, F.J., and Cather, S.A., 1999, Topographic setting of the Rio Grande rift, New Mexico: Assessing the role of "rift-flank uplift" in the Sandia Mountains: New Mexico Geological Society, 50th Field Conference, Guidebook, p. 167-174.

Russell, L.R., and Snelson, S., 1994, Structure and tectonics of the Albuquerque Basin segment of the Rio Grande rift: Insights from reflection seismic data, *in* Keller, G.R., and Cather, S.M., eds., Basins of the Rio Grande Rift: Structure, Stratigraphy, and Tectonic Setting: Boulder, Colorado, Geological Society of America Special Paper 291.

Sanford, A.R., Alptekin, O.S., and Toppozada, T.R., 1973, Use of reflection phases on microearthquake seismograms to map an unusual discontinuity beneath the Rio Grande rift: Bulletin of the Seismological Society of America, v. 63, p. 2021-2034.

Schoofs, S., Spera, F.J., and Hansen, U., 1999, Chaotic thermohaline convection in low-porosity hydrothermal systems: Earth and Planetary Science Letters, v. 174, p. 213-229.

Seager, W.R., Shafiqullah, M., Hawley, J.W., and Marvin, R.F., 1984, New K-Ar dates from basalts and the evolution of the southern Rio Grande rift: Geological Society of America Bulletin, v. 95, p. 87-99.

Sibson, R.H., 1992, Implications of fault-valve behavior for rupture nucleation and recurrence: Tectonophysics, v. 211, p. 283-293.

Szabo, B.J., 1990, Ages of travertine deposits in eastern Grand Canyon National Park, Arizona: Quaternary Research, v. 34, p. 24-32.

Tafoya, A.J., 2012, Uranium-series geochronology and stable isotope analysis of travertine from Soda Dam, New Mexico: A Quaternary record of episodic spring discharge and river incision in the Jemez Mountains hydrothermal system [M.S. thesis]: University of New Mexico, 104 p.

Turcotte, D.L., and Schubert, G., 2002, Geodynamics: Cambridge UK, Cambridge University Press, 456 p.

Uysal, I.T., Feng, Y., Zhao, J., Bolhar, R., Isik, V., Baublys, K.A., Yago, A., and Golding, S.D., 2011, Seismic cycles recorded in late Quaternary calcite veins: Geochronological, geochemical and microstructural evidence: Earth and Planetary Science Letters, v. 303, p. 84-96.

Williams, A.J., Crossey, L.J., Karlstrom, K.E., Newell, D., Person, M., and Woolsey, E., 2013, Hydrogeochemistry of the Middle Rio Grande aquifer system – Fluid mixing and salinization of the Rio Grande due to fault inputs: Chemical Geology, v. 351, p. 281-298.

APPENDICES

Appendix 1: Apatite (U-Th)/He Data for New Mexico and Colorado

Appendix 2: Apatite Fission Track Data Used in HeFTy Modeling

Appendix 3: HeFTy Output Models

Appendix 1: Apatite (U-Th)/He Data for New Mexico and Colorado

Sample Number	Sample Name	Mass (μg)	Radius (μm)	Length (μm)	Width (μm)	Ft	U (ppm)	Th (ppm)	Sm (ppm)	^{4}He (nmol/g)	eU	Raw Date (Ma)	Corrected Date (Ma)	1σ error (Ma)
Data from the Colorado Thermochronology Research and Instrumentation Laboratory (University of Colorado, Boulder)														
Sawatch Range														
1	84MP03 - 36.6 Ma Granite (Shannon, 1988). 13.2 ± 1.5 Ma AFT age (Kelley et al., 1992).													
	a1	6.11	68.80	217.5	116.2	0.762	20.65	97.31	28.21	0.615	43.5	2.60	3.41	0.26
	a2	3.62	56.34	206.4	91.8	0.696	11.00	51.54	27.10	0.258	23.1	2.04	2.93	0.22
	a3	2.10	48.46	147.1	82.8	0.653	14.98	70.46	14.73	0.287	31.5	1.67	2.56	0.22
	a4	3.20	53.38	209.5	85.7	0.682	6.50	24.36	11.13	0.142	12.2	2.14	3.13	0.25
	a5	5.16	66.52	177.6	118.2	0.760	10.71	42.46	13.12	0.287	20.7	2.55	3.36	0.25
2	84MP05 - 36.6 Ma Granite (Shannon, 1988). 9.6 ± 1.2 Ma AFT age (Kelley et al., 1992).													
	a1	2.09	48.79	140.5	84.6	0.684	12.16	28.39	10.16	0.188	18.8	1.84	2.69	0.25
	a2	1.70	44.30	152.4	73.3	0.632	13.51	29.01	12.21	0.220	20.3	1.99	3.15	0.40
	a3*	2.53	52.37	142.5	92.5	0.824	0.00	0.17	1.78	0.007	0.0	23.56	28.57	3.95
	a4	1.63	43.50	152.7	71.6	0.648	14.58	20.61	6.76	0.140	19.4	1.33	2.05	0.27
	a5	3.04	53.79	185.2	88.9	0.701	5.80	22.04	15.89	0.115	11.0	1.91	2.73	0.21
3	84MP06 - 36.6 Ma Granite (Shannon, 1988). 22.9 ± 2.5 Ma AFT age (Kelley et al., 1992).													
	a1	2.66	49.19	212.5	77.6	0.654	23.70	122.64	47.36	5.065	52.5	17.65	26.99	2.76
	a2	1.92	46.66	149.0	78.6	0.668	8.40	19.66	15.80	1.267	13.0	17.80	26.66	2.61
	a3*	1.83	44.98	162.5	73.6	0.651	2.95	8.61	11.29	4.384	5.0	158.48	243.49	28.67
	a4	2.41	47.98	200.0	76.2	0.662	5.63	27.77	15.45	1.132	12.2	16.99	25.68	2.75
	a5	8.93	77.53	256.5	129.5	0.791	7.31	18.04	11.91	1.513	11.5	23.99	30.35	2.15
4	84MP08 - 36.6 Ma Granite (Shannon, 1988). 23.1 ± 2.8 Ma AFT age (Kelley et al., 1992).													
	a1	1.86	43.30	195.1	67.8	0.612	23.13	124.54	48.74	2.824	52.4	9.87	16.12	2.38
	a2	4.64	60.15	241.4	96.2	0.712	20.12	103.00	27.62	3.277	44.3	13.57	19.06	1.45
	a3	4.14	59.05	213.9	96.5	0.724	9.30	36.33	21.29	1.368	17.8	14.02	19.35	1.37
	a4	7.76	75.39	220.0	130.3	0.791	8.38	10.60	3.66	1.110	10.9	18.83	23.80	1.68
	a5	8.68	78.00	232.9	133.9	0.775	7.98	38.44	18.72	1.432	17.0	15.38	19.84	1.50
5	84MP10 - 36.6 Ma Granite (Shannon, 1988). 20.1 ± 2.3 Ma AFT age (Kelley et al., 1992).													
	a1	2.97	52.93	189.8	86.7	0.683	12.68	34.56	8.98	0.699	20.8	6.19	9.06	0.70
	a2	4.68	55.63	319.6	83.9	0.693	7.88	25.26	7.51	0.491	13.8	6.53	9.43	0.78

	a3	6.23	64.98	288.3	102.0	0.734	11.13	40.48	9.79	0.798	20.6	7.11	9.69	0.69
	a4	3.49	54.40	224.0	86.5	0.702	8.03	25.03	7.03	0.556	13.9	7.35	10.47	0.81
	a5	3.74	56.86	210.2	92.5	0.711	22.74	126.16	34.50	2.015	52.4	7.06	9.92	0.76
6	84MP12 - 36.6 Ma Granite (Shannon, 1988). 14.8 ± 1.9 Ma AFT age (Kelley et al., 1992).													
	a1	1.78	45.58	144.9	76.9	0.662	33.38	67.96	15.94	1.526	49.3	5.70	8.62	0.90
	a2	1.47	41.49	157.4	67.1	0.622	25.97	91.50	32.08	1.311	47.5	5.07	8.16	1.23
	a3	3.89	53.56	279.3	81.9	0.691	13.19	56.89	12.46	0.728	26.6	5.04	7.30	0.65
	a4	3.07	55.42	159.5	96.2	0.716	10.66	32.83	8.32	0.601	18.4	6.02	8.41	0.59
	a5	2.24	43.63	248.7	65.9	0.642	44.30	40.46	11.65	1.885	53.8	6.48	10.10	1.60
Sangre de Cristo Range														
7	88SG03 - Proterozoic Granite. 10.4 ± 1.3 Ma AFT age (Kelley et al., 1992).													
	a1	4.93	58.60	291.1	90.2	0.728	23.36	18.20	11.86	1.049	27.6	7.01	9.63	0.69
	a2	5.86	67.08	227.2	111.4	0.766	12.51	9.47	11.56	0.600	14.7	7.50	9.78	0.69
	a3	1.79	46.26	133.9	80.1	0.676	11.19	8.43	9.96	0.687	13.2	9.61	14.21	1.32
	a4	9.59	82.72	195.1	153.8	0.816	9.80	5.96	4.76	0.618	11.2	10.19	12.48	0.88
	a5*	1.85	47.48	121.0	85.7	0.688	10.96	8.67	13.95	1.433	13.0	20.23	29.41	2.32
8	88SG07 - Pennsylvanian Sandstone. 31.4 ± 4.1 Ma AFT age (Kelley et al., 1992).													
	a1	1.65	43.38	158.4	70.8	0.639	15.74	48.54	25.74	2.628	27.2	17.73	27.77	3.64
	a2	3.53	58.96	148.3	107.0	0.741	11.22	15.25	22.20	1.204	14.8	14.86	20.05	1.41
	a3	3.20	55.18	180.5	92.4	0.722	16.87	10.37	16.42	1.719	19.3	16.37	22.67	1.60
	a4	2.12	48.61	148.1	83.0	0.676	2.37	9.67	44.25	0.518	4.6	19.09	28.26	2.42
	a5*	1.87	46.57	143.6	79.2	0.661	0.72	3.31	21.68	0.367	1.5	40.41	61.11	5.94
9	88SG09 - Pennsylvanian - Permian Siltstone. 19.4 ± 2.3 Ma AFT age (Kelley et al., 1992).													
	a1	2.75	54.26	137.2	98.3	0.721	15.12	21.07	33.07	1.652	20.1	15.02	20.85	1.47
	a2	3.20	55.64	171.9	94.6	0.720	3.78	5.89	13.88	0.310	5.2	10.86	15.07	1.07
	a3	3.49	58.60	151.1	105.4	0.745	12.84	3.55	4.73	0.676	13.7	9.13	12.26	0.87
	a4	2.72	51.98	174.9	86.4	0.684	8.08	11.85	15.86	0.747	10.9	12.57	18.38	1.42
	a5	1.32	42.75	100.5	79.6	0.662	13.72	7.77	16.26	1.437	15.5	16.98	25.65	2.43
10	88SG10 - Pennsylvanian - Permian Arkose. 38.9 ± 4.0 Ma AFT age (Kelley et al., 1992)													
	a1	4.68	61.42	224.0	100.2	0.741	3.92	6.21	6.07	0.391	5.4	13.34	18.00	1.28
	a2	4.57	59.24	250.3	93.8	0.722	5.36	3.80	3.89	0.651	6.2	19.20	26.60	1.87
	a3	2.21	48.55	163.0	80.8	0.668	11.30	8.97	20.72	2.366	13.4	32.21	48.21	4.38
	a4	9.21	81.22	203.4	147.6	0.811	11.88	6.78	6.62	2.827	13.5	38.63	47.60	3.39
	a5	1.93	47.25	141.0	81.1	0.658	3.67	4.29	18.26	0.395	4.7	15.16	23.02	2.08
11	88SG11 - Pennsylvanian Sandstone. 28.5 ± 2.6 Ma AFT age (Kelley et al., 1992).													
	a1	3.08	54.56	177.0	91.6	0.703	5.85	3.43	9.24	0.639	6.7	17.58	25.01	1.76

	a2	1.08	38.91	118.0	66.5	0.621	36.96	27.11	8.21	5.561	43.3	23.71	38.17	5.89
	a3	1.07	37.71	134.7	61.8	0.587	24.60	13.16	24.22	3.312	27.7	21.98	37.42	6.89
	a4	1.01	37.74	118.9	63.8	0.588	54.79	34.88	16.13	6.659	63.0	19.53	33.23	5.68
	a5	1.71	45.33	137.3	77.5	0.664	1.55	2.30	3.01	0.244	2.1	21.33	32.09	3.40
12	88SG12 - Proterozoic Gneiss. 22.0 ± 2.0 Ma AFT age (Kelley et al., 1992).													
	a1	3.53	57.11	184.8	95.9	0.735	8.93	0.31	1.97	0.367	9.0	7.55	10.27	0.73
	a2	3.06	55.93	148.7	99.5	0.735	8.93	0.52	2.11	0.369	9.1	7.55	10.27	0.74
	a3	2.44	50.11	169.3	83.2	0.683	9.94	0.60	2.80	0.393	10.1	7.22	10.57	0.90
	a4	1.92	44.44	185.8	70.5	0.646	12.45	0.64	3.29	0.450	12.6	6.61	10.24	1.36
	a5	3.24	55.42	180.1	93.0	0.727	17.01	0.89	2.83	0.815	17.2	8.78	12.07	0.86
13	88SG13 - Proterozoic Gabbro. 18.0 ± 2.0 Ma AFT age (Kelley et al., 1992).													
	a1	2.53	52.48	139.2	93.5	0.713	12.12	10.50	10.57	0.519	14.6	6.55	9.18	0.65
	a2	3.70	57.49	196.0	95.3	0.730	9.99	8.94	10.63	0.470	12.1	7.15	9.81	0.69
	a3	2.34	47.57	197.4	75.6	0.657	17.43	21.76	11.34	0.784	22.5	6.41	9.76	1.07
	a4	6.94	68.72	277.2	109.8	0.766	9.25	11.41	11.54	0.520	11.9	8.00	10.45	0.74
	a5	3.13	56.08	155.5	98.5	0.727	9.13	11.84	10.54	0.387	11.9	5.97	8.22	0.58
14	89SG23 - Proterozoic Granitic Gneiss. 32.5 ± 3.9 Ma AFT age (Kelley et al., 1992).													
	a1	6.07	66.48	252.6	107.5	0.750	1.42	1.06	4.86	0.123	1.7	13.26	17.68	1.27
	a2	18.07	96.96	342.3	159.4	0.826	0.49	0.26	1.21	0.015	0.5	5.14	6.22	0.49
	a3	10.45	82.66	253.6	140.8	0.812	1.77	0.50	2.08	0.094	1.9	9.19	11.31	0.80
	a4	7.14	71.00	253.8	116.4	0.780	4.94	1.19	2.61	0.385	5.2	13.61	17.45	1.23
	a5	20.49	103.8 7	310.2	178.3	0.849	0.96	0.30	1.12	0.058	1.0	10.27	12.09	0.85
Nacimiento Mountains														
15	88NAC02 - Proterozoic Granite. 39.4 ± 3.0 Ma AFT age (Kelley et al., 1992).													
	a1	4.21	60.33	199.4	100.8	0.743	22.99	16.71	12.80	12.385	26.9	84.40	113.59	8.03
	a2	1.37	42.20	125.1	72.6	0.646	27.71	27.18	15.60	11.686	34.1	62.96	97.42	11.90
	a3	2.04	45.67	185.0	72.9	0.662	20.23	21.19	17.45	7.760	25.2	56.47	85.36	10.31
	a4	1.61	42.11	171.9	67.1	0.639	32.26	22.74	16.24	13.326	37.6	65.12	101.98	15.39
	a5	3.98	58.91	201.0	97.6	0.735	37.13	37.03	14.29	65.790	45.8	259.84	353.51	25.03
16	88NAC15 - Permian Siltstone. 65.9 ± 3.9 Ma AFT age (Kelley et al., 1992).													
	a1	1.42	43.39	112.2	78.0	0.651	4.10	11.05	7.46	1.752	6.7	47.81	73.43	9.25
	a2	1.26	37.30	182.7	57.6	0.595	18.23	9.55	13.08	4.419	20.5	39.69	66.66	14.68
	a3	1.48	43.37	126.5	75.0	0.635	8.79	6.37	20.38	2.876	10.3	50.81	80.02	9.55
	a4	2.10	49.31	131.1	87.7	0.702	27.45	2.74	6.89	7.244	28.1	47.57	67.75	5.56
	a5	2.12	48.98	141.3	85.0	0.672	1.36	1.08	4.16	0.267	1.6	29.95	44.57	7.05

Manzano Mountains														
17	88MAN03 - Proterozoic Granite. 38.8 ± 4.3 Ma AFT age (Kelley et al., 1992).													
	a1	1.16	39.44	127.0	66.3	0.618	13.21	20.83	59.73	2.211	18.1	21.97	35.56	5.65
	a2	1.98	45.96	171.5	74.6	0.650	13.99	12.30	59.79	3.066	16.9	32.63	50.20	5.98
	a3	1.54	43.49	137.0	73.6	0.652	17.30	20.97	63.15	3.325	22.2	27.02	41.43	5.09
	a4*	0.94	35.62	138.3	57.3	0.584	10.30	5.74	50.72	4.071	11.7	62.24	106.49	23.76
	a5	0.89	35.34	127.6	57.8	0.560	19.41	17.92	78.44	2.777	23.6	21.18	37.81	8.31
18	88MAN04 - Proterozoic Granite. 28.5 ± 2.9 Ma AFT age (Kelley et al., 1992).													
	a1	3.98	56.46	240.3	89.3	0.719	18.57	20.29	45.58	2.201	23.3	17.17	23.87	1.85
	a2	1.65	45.22	126.6	79.1	0.674	11.77	4.28	34.94	1.428	12.8	20.25	30.06	3.11
	a3	2.35	49.29	170.3	81.4	0.688	17.68	16.43	50.58	1.842	21.5	15.52	22.55	2.18
	a4	0.91	37.34	98.2	66.7	0.612	30.60	23.66	69.77	3.232	36.2	16.29	26.61	4.21
	a5	2.30	50.05	150.2	85.8	0.697	15.73	13.19	48.10	2.206	18.8	21.24	30.47	2.45
19	88MAN13 - Permian Siltstone. 47.7 ± 5.5 Ma AFT age (Kelley et al., 1992).													
	a1	2.52	51.74	153.2	89.0	0.688	6.00	4.07	3.47	0.519	7.0	13.77	20.00	1.46
	a2	2.11	48.84	142.7	84.4	0.658	1.98	7.59	5.33	0.824	3.8	39.93	60.69	4.94
	a3	1.84	45.50	155.9	75.3	0.648	18.26	13.95	10.00	1.000	21.5	8.56	13.21	1.46
	a4	2.41	51.23	145.4	89.3	0.707	5.06	2.70	2.91	1.498	5.7	48.42	68.50	4.99
	a5	2.02	47.64	150.1	80.6	0.686	11.82	2.73	13.40	0.598	12.5	8.83	12.87	1.18
Black Range														
20	90BR05 - Cretaceous(?) Dacite. 63.7 ± 4.5 Ma AFT age (Kelley and Chapin, 1997).													
	a1	5.96	64.83	271.2	102.8	0.753	9.10	10.74	26.77	2.207	11.6	34.43	45.73	3.21
	a2	6.08	68.23	224.9	114.1	0.763	4.57	12.25	14.00	1.651	7.5	40.22	52.68	3.71
	a3	4.54	61.92	203.4	103.6	0.728	4.25	9.24	13.99	1.180	6.4	33.33	45.80	3.22
	a4*	1.98	47.76	139.8	82.5	0.678	7.04	14.57	23.70	3.403	10.5	58.83	86.75	7.46
	a5	3.50	57.02	183.0	96.0	0.706	5.28	12.57	16.72	1.539	8.2	33.94	48.08	3.37
Sierra Blanca														
21	90SB02 - 26.6 ± 1.4 Ma Syenite (Moore et al., 1991). 23.8 ± 2.6 Ma AFT age (Kelley and Chapin, 1997).													
	a1	4.41	61.73	194.6	104.4	0.744	25.35	46.71	23.54	2.232	36.3	11.30	15.19	1.09
	a2	6.61	68.67	255.7	111.5	0.760	11.95	42.81	21.77	1.269	22.0	10.56	13.89	0.98
	a3	4.63	61.30	222.1	100.2	0.737	26.04	70.40	25.29	4.017	42.6	17.34	23.54	1.75
	a4	6.75	72.41	201.7	126.9	0.777	18.73	78.13	19.63	2.495	37.1	12.36	15.91	1.21
	a5	2.06	47.04	165.6	77.4	0.667	23.72	55.13	30.41	2.701	36.7	13.52	20.25	2.07
San Andres Mountains														
22	90SA08 - Proterozoic Granite. 21.8 ± 4.5 Ma AFT age (Kelley and Chapin, 1997).													
	a1	1.30	41.61	120.3	72.1	0.638	5.87	10.33	37.33	0.377	8.3	8.10	12.69	1.73

	a2	1.18	35.46	196.4	53.8	0.561	4.74	12.43	37.97	0.361	7.7	8.37	14.92	3.77
	a3	2.31	50.76	137.9	89.7	0.694	14.56	47.31	63.45	1.667	25.7	11.75	16.94	1.29
	a4	1.20	40.21	121.8	68.7	0.621	6.88	17.91	52.42	0.356	11.1	5.71	9.19	1.41
	a5	1.89	45.92	157.3	76.0	0.667	3.82	4.20	23.23	0.206	4.8	7.64	11.45	1.45
Organ Mountains														
23	81OR07 - 35.7-36.2 Ma Quartz Monzonite (McIntosh et al., 1992). 10.3 ± 1.4 Ma AFT age (Kelley and Chapin, 1997).													
	a1	1.63	43.65	150.9	72.1	0.629	26.94	44.71	26.43	1.576	37.4	7.74	12.30	1.56
	a2	2.00	47.01	156.2	78.4	0.673	37.93	56.67	35.43	2.384	51.2	8.56	12.73	1.30
	a3	1.61	42.83	160.5	69.5	0.623	101.38	160.10	23.73	8.112	139.0	10.78	17.31	2.43
	a4	1.33	41.75	124.4	71.7	0.637	27.04	51.81	29.27	1.631	39.2	7.65	12.00	1.55
	a5	2.01	45.53	182.7	72.8	0.656	36.91	67.73	35.58	2.050	52.8	7.14	10.88	1.36
24	81OR08 - 35.7-36.2 Ma Quartz Monzonite (McIntosh et al., 1992). 13.7 ± 1.4 Ma AFT age (Kelley and Chapin, 1997).													
	a1	2.85	49.60	229.7	77.3	0.668	53.49	74.61	29.40	3.437	71.0	8.93	13.35	1.41
	a2	2.68	49.72	207.3	78.9	0.668	40.62	69.18	27.37	2.652	56.9	8.59	12.86	1.27
	a3	4.10	60.06	194.0	100.9	0.739	19.64	25.45	14.30	1.497	25.6	10.77	14.56	1.07
	a4	1.25	41.25	115.3	72.2	0.639	60.94	75.09	28.98	3.625	78.6	8.51	13.31	1.69
	a5	1.54	43.94	128.7	75.9	0.656	35.47	53.76	25.13	2.421	48.1	9.27	14.14	1.57
25	81OR15 - 35.7-36.2 Ma Quartz Monzonite (McIntosh et al., 1992). 13.8 ± 1.6 Ma AFT age (Kelley and Chapin, 1997).													
	a1	1.14	40.01	111.3	70.2	0.627	12.43	21.07	7.10	0.863	17.4	9.16	14.61	2.08
	a2	1.91	45.08	174.0	72.7	0.641	14.52	19.37	9.31	0.950	19.1	9.18	14.33	1.85
	a3	0.87	37.26	87.2	69.5	0.612	21.21	31.39	34.53	1.382	28.6	8.86	14.48	2.10
	a4	1.85	45.49	158.2	75.0	0.650	8.55	43.43	54.60	1.055	18.8	10.13	15.60	1.82
	a5	6.13	67.78	236.3	111.7	0.762	2.59	5.73	3.46	0.178	3.9	8.30	10.89	0.88

Data from the Arizona Radiogenic Helium Dating Lab (University of Arizona)									ncc ^{4}He				
Sierra Ladrones													
26	88LAD06 (3 grains per aliquot). Precambrian Granite. 14.1 ± 2.0 AFT age (Kelley et al., 1992).												
	a1	2.10	49.21	134.9	86.7	0.702	3.64	4.68	24.63	0.059	4.7	9.45	13.46	0.2
27	91LAD16 (3 grains per aliquot). Precambrian Granite.													
	a1	1.57	45.04	114.9	81.3	0.684	6.03	1.92	120.72	0.066	6.5	12.16	17.78	0.4
28	91LAD18 (3 grains per aliquot). Precambrian Granite.													
	a1	1.33	41.63	128.5	70.8	0.656	4.46	4.03	100.70	0.045	5.4	9.12	13.90	0.3
	a2	1.30	42.60	100.4	79.2	0.662	5.51	5.73	112.49	0.044	6.9	10.27	15.51	0.3

									pmol ^{4}He				
29	JR-10-6 - Permian Sandstone												

	a1	2.11	47.98	158.1	80.2	0.698	4.71	3.52	23.51	0.0024	5.5	8.79	12.58	0.6
	a3	0.86	34.08	141.6	54.1	0.585	16.69	27.15	46.88	0.0094	23.1	9.68	16.55	0.3
	a4	1.62	44.69	132.3	76.9	0.667	4.12	12.86	30.12	0.0014	7.1	6.22	9.33	0.4
	a5	1.05	36.16	156.4	57.0	0.601	2.13	5.48	11.57	0.0003	3.4	3.48	5.79	0.5
30	JR-LAD11-2 (3 grains per aliquot). Precambrian Granite.													
	a1	0.71	33.25	110.9	55.4	0.560	1.75	11.05	89.39	0.0003	4.3	3.09	5.52	0.4
	a2	1.16	39.70	122.7	67.5	0.619	1.26	11.36	99.41	0.0007	3.9	5.25	8.48	0.4
	a3	1.97	46.96	154.0	78.6	0.676	1.35	7.38	114.80	0.0026	3.1	11.39	16.84	0.4
Lucero Uplift														
31	JR-CAR1 - Permian Sandstone.													
	a1*	8.30	75.36	256.7	124.9	0.799	1.18	1.56	6.08	0.0114	1.5	36.82	46.07	0.8
	a3	5.56	66.15	221.0	110.2	0.774	2.75	2.93	12.75	0.0077	3.4	14.03	18.12	0.3
	a4	4.07	58.71	214.0	95.8	0.750	2.61	1.62	7.07	0.0043	3.0	14.38	19.17	0.5
	a5	7.83	77.47	180.6	144.7	0.807	9.13	6.04	21.29	0.0121	10.6	13.95	17.29	0.6
32	JR-BQ-10 (3 grains per aliquot). Precambrian Granite.													
	a1	3.49	58.28	159.6	102.7	0.733	5.52	33.51	485.95	0.0230	13.4	13.90	18.96	0.2
	a2	2.15	49.93	129.1	89.7	0.694	5.27	28.81	529.76	0.0086	12.0	13.61	19.62	0.3
33	JR-BQ-11. Pennsylvanian Sandstone.													
	a1	1.48	43.44	126.3	75.2	0.670	3.96	2.85	37.52	0.0019	4.6	9.61	14.33	0.4
	a2	1.86	45.89	154.1	76.4	0.684	2.62	2.75	74.99	0.0026	3.3	15.36	22.45	1.0
	a3	1.19	40.67	112.1	71.5	0.650	4.74	3.92	40.46	0.0033	5.7	13.82	21.28	1.1
	a4	2.88	55.17	138.1	100.3	0.733	3.89	3.96	143.64	0.0018	4.8	11.29	15.40	0.3
	a5	1.15	39.87	117.8	68.7	0.614	6.94	160.89	158.62	0.0027	44.8	5.54	9.03	0.3
Joyita Hills														
34	JR-10-5 - Triassic Sandstone													
	a1	2.60	50.70	182.5	83.0	0.697	0.53	3.24	9.42	0.0016	1.3	11.72	16.82	0.3
	a2	2.55	50.26	182.4	82.1	0.697	3.38	16.06	62.38	0.0123	7.2	18.27	26.22	0.4
	a3	4.01	59.34	198.0	98.9	0.735	0.71	5.93	26.44	0.0026	2.1	11.62	15.80	0.8
	a4	2.31	50.67	140.9	88.9	0.696	0.78	5.34	20.34	0.0015	2.0	12.23	17.57	0.6
	a5	5.62	69.17	167.9	127.2	0.772	3.15	19.95	89.60	0.0054	7.8	10.89	14.10	0.2

*Anomalously old compared to other ages. Excluded from average sample age calculations.

Appendix 2: Apatite Fission Track Data Used in HeFTy Modeling

Sample 1 (84MP03)											
Length (µm)	Angle	Length (µm)	Angle	Length (µm)	Angle	Ns	Ni	Zeta	rhoD	Nd	Cl wt%
13.9	48.3	15.3	15.1	14	74.7	5	50	351 ± 40	1.27E+06	4600	Not Available
12.6	64.5	13.6	65.6	9.8	63.8	4	43				
12.1	72.1	12.1	12.1	14.4	62.9	5	70				
13.8	32.6	15	84.8	12.3	67.9	5	72				
12	55.9	12.1	37.6	13.4	5.6	3	49				
14.7	10.5	17.2	40.8	12.9	11.7	6	112				
13.6	41.4	12.3	20.4	14.2	4.6	5	100				
15.2	33.4	14	86.1	14	44.3	8	140				
16.8	71.8	14.4	16.4	16.7	87.1	13	57				
18.5	1.8	15.6	3.9	12.1	31.4	12	86				
10.2	28.8	13	50.9	12.9	40.1	3	38				
14.9	39.9	14.7	68.6	15.5	51.1	3	60				
16.1	45.7	14.8	22.9			8	113				
12.2	67.1	14.6	39.6			3	42				
11.7	63.9	5.7	60.5			4	60				
11.9	79.9	7.5	74.5			2	29				
11.7	33.9	15.8	81.8			4	80				
11.8	62.9	12.6	86.9			2	42				
15.5	47.1	12.7	75.9			4	70				
11.5	67.5	15.9	43			3	50				
12.4	63.4	13.9	42.9								
13.9	30.8	13.4	44.5								
11.5	68	11.7	58.4								
15.4	52.8	13.7	51.1								
17.2	9.5	15.4	31.5								
15.1	15.9	14.8	39.9								
14.7	4.7	13.8	74.8								
11.9	58.6	16.4	75.7								
15.2	24.8	16.6	80.8								
11.3	69.8	15.3	31.6								
12.4	88.6	12.6	85.3								
12.6	22.9	15.6	86.5								
14.6	51.2	7.5	49.3								
13.8	25.6	14.7	62.6								
8.1	53.9	12.3	18.9								
15.9	72.4	12.6	70.5								
15.4	50.5	12.7	77.7								
12.3	55.7	12.4	80.6								
14.3	75.8	15.1	2.3								
13.4	73.2	13.4	73								
8.4	88.3	17	72.1								
14.9	89.1	15.9	86.2								
8	48.7	14.9	26.2								

Sample 2 (84MP05)											
Length (µm)	Angle	Length (µm)	Angle	Length (µm)	Angle	Ns	Ni	Zeta	rhoD	Nd	Cl wt%
14.6	57	12.1	73.4	13.1	41	11	192	351 ± 40	1.31E+06	4600	Not available
13.5	1.7	12.6	70.4	14.2	84.3	2	32				
15.6	31.5	14.1	2.2	16.7	82.2	3	122				
10.5	45.5	6.8	47.2	5.6	49.9	6	214				
14.6	67.3	13.5	6.8	14.9	72.7	3	50				
11	20.9	5.6	89.1	13.8	56.6	2	76				
13.5	35	13.9	46	11.9	83.6	8	249				
16.1	1.3	14.2	34.9	15.3	56.6	3	118				
12.9	39.7	15.2	77.7	14.3	84.9	14	17				
14.9	51.7	14.8	59.1	12.4	48.9	9	77				
11.2	29	14.1	53.3			1	20				
12.6	59	9	47.8			3	135				
13.8	78	16.1	73.6			2	52				
14.4	15.5	10.9	45.2			6	67				
16.3	82.6	13.6	83.7			4	62				
14.4	79.5	12.5	4.5			8	234				
12.6	89.6	14	84.5			6	55				
15	76.5	13.7	23.4			5	85				
12.7	81.6	13.7	88.7			3	48				
15.2	25.6	13.4	57.5			2	44				
14.9	82.3	13.5	72.6								
5.6	82	14.2	33.9								
6.4	57.2	11.7	40.4								
13.2	39.1	15.3	71.2								
14.1	78.6	16.3	29.4								
15.6	76.3	4.6	50.4								
12.4	75.4	13	75.3								
12.6	65.1	15.1	30.7								
13.9	38.9	11.3	37.3								
12	51.4	6.7	36								
12	75	13.7	67.8								
14.1	68.5	12.9	79.9								
13.5	69.2	13.5	75.4								
13.9	87.7	15.4	20.2								
13.6	70.2	12.5	25.3								
13	58.3	14.6	76.2								
8.6	59.7	15.3	21.6								
12.4	73.9	15.1	69.3								
15.4	2.3	14.2	86.4								
11.2	69.5	8.4	54.5								
13.9	66.1	7.3	54.3								
13	82.3	15.3	9.7								
10.8	82.2	14.8	28.8								
12.5	76.8	15.3	42.2								

Sample 3 (84MP06)											
Length (µm)	Angle	Length (µm)	Angle	Length (µm)	Angle	Ns	Ni	Zeta	rhoD	Nd	Cl wt%
14.2	64	12.9	17.4	15.7	26.7	8	68	351 ± 40	1.33E+06	4600	Not available
11.7	33.8	15.4	75.8	14.2	28.5	7	47				
12.5	58.4	13.7	64.2	15	77.3	10	61				
15.7	61.7	14.6	52.8	15.7	30.1	6	42				
14.7	46.2	13.1	36.5	15.4	31.5	6	34				
13.4	31.6	13.3	82.1	14.1	60.5	6	38				
13.3	64.8	15.1	81.8	14.9	87.1	2	17				
13.4	81.7	12.8	83.9	15.1	60.9	9	76				
14.5	52.7	13.9	49.6	15	37.8	1	10				
17	89.3	14.1	60.1	16.6	49.6	5	53				
11.3	49	8.6	69.7	15.7	50.6	4	35				
16.5	45.8	12.8	54.8	13.9	88.5	6	62				
15.2	64.1	15.2	10.6			13	180				
13.3	37.9	14.6	35.4			5	69				
14.9	36.2	12.7	89.9			3	58				
14.4	4.7	16.1	65			7	106				
15.1	20.3	14.5	49.5			4	25				
17.9	55.9	8.5	50.9			2	39				
15.2	65.7	15.6	31.9			5	70				
14.7	75.6	14.5	77			3	49				
15.3	35	13.4	53								
14.6	88.9	15.6	27.2								
16.9	21.8	13	58.4								
15.2	75.1	13.3	80.4								
14.6	38.4	13.6	18.8								
16.5	41	14.1	47.9								
14.5	79.7	12.1	89.7								
15.3	54.9	14.9	57.8								
14.1	72.1	14.1	25.2								
15.2	82.9	13.9	48.5								
15.4	86.5	13.4	31.8								
14.8	87.7	16.4	80.2								
13.4	25.8	14.7	63.5								
16.2	34.5	13.3	15.3								
15.1	24.5	13.7	79.3								
14.8	3.9	11.5	87.9								
15.2	85.8	13.9	67								
15.4	58.4	14.3	41.9								
14.9	76.9	11.1	68.8								
14.2	61.6	15.4	85.1								
16.2	80.2	15.4	59.4								
15.5	49.6	16.7	24.4								
14.2	56.1	15.2	88.4								
13	60.6	9.8	88.9								

Sample 4 (84MP08)											
Length (µm)	Angle	Length (µm)	Angle	Length (µm)	Angle	Ns	Ni	Zeta	rhoD	Nd	Cl wt%
12.8	34.6	14.8	7.2	15	52.9	5	54	351 ± 40	1.36E+06	4600	Not available
14.1	51.7	14.2	88.2	12	72.2	6	43				
13.6	54.5	12.9	85.2	14.1	40.2	6	82				
14.7	38.3	15.4	55.3	14.4	78.4	4	43				
17.1	46.2	9.4	67.2	6.7	60.6	5	46				
13	72.2	15.1	30.2	14.7	64.8	1	7				
14.1	56.4	15.5	78.9	13.7	64.4	4	46				
14.1	66.7	15.7	73.1	16.8	51.2	5	32				
14.3	49.2	13.9	28.4	14.1	77.8	8	147				
16.1	27.8	18.9	45.4	12.9	65.6	8	48				
14.5	70.7	15.1	47.9	15.4	67.8	3	45				
13.5	88.9	15.5	64.1	14.3	73.5	5	64				
16.3	35.9	15.7	44.3			5	32				
14.5	70.2	14.3	31			7	63				
15.3	55.5	14.3	30.4			2	14				
17.6	41.2	14.3	30.9			3	28				
14.6	27.3	15.2	39.7			2	12				
13.3	81.4	14.6	35.4			5	27				
16.4	85.5	14.3	35.9			3	41				
15.6	37	14.3	81.1			5	77				
12.6	51.4	15.7	81.1								
13.8	58.2	14.6	87.2								
8	32.9	13.4	87.9								
15.2	48	14.8	66.2								
14.9	47.3	15.3	80.9								
14.9	61	14.4	32								
16.2	22.2	14.1	53.3								
17.2	27.3	14.1	28.4								
15.1	42.5	15	62.6								
14.4	72.6	15.2	28.7								
14.8	38.7	13.8	79.8								
12.5	74.7	14	88.3								
14.2	51.4	15.7	78.5								
14.9	53.6	15.6	18.5								
17.3	14.8	14.4	27								
14.6	0.8	13	67.6								
13.2	63	12.8	61.4								
14.6	24.2	14.6	88.6								
14.9	68.7	13.8	53.6								
17.1	46.7	15.2	19.5								
13.3	71.6	14.2	59.4								
14.7	39.3	13.9	73.2								
13.9	70.8	13.4	68.3								
15.5	86.6	14.8	21.3								

Sample 5 (84MP10)											
Length (µm)	Angle	Length (µm)	Angle	Length (µm)	Angle	Ns	Ni	Zeta	rhoD	Nd	Cl wt%
15.5	86.4	15.5	85.6	14.7	59.1	6	51	351 ± 40	1.40E+06	4600	Not available
14.4	62.7	17.5	66.3	14.8	32.4	5	63				
15.8	36.5	8.6	86.9	16.3	63	10	172				
13.8	54.8	16	90	15.3	88.1	3	25				
14.2	76.9	15	68.6	14.5	38.8	4	34				
15.9	24.1	14.6	42.8	14.9	87.9	1	25				
16.3	58.1	15.3	87.6	14.4	83.7	5	54				
15.2	35.7	15.4	58.5	12.7	32.7	3	33				
15.3	54.3	16.1	69.3	14.5	81.1	6	85				
15.3	9	16.6	27.4	9.4	56.9	3	23				
15	75.9	14.6	27.7	7.5	41	5	73				
16.5	15	16	11.1	13.6	41.4	2	27				
14.3	71.3	15.8	42	14.5	52.6	8	52				
14.2	58.9	14.6	68.2			4	44				
14.6	76.3	16	58.7			6	97				
15	80.3	13.8	65.1			7	110				
13.8	62.3	15.8	34.9			2	17				
15.3	83.8	15.7	28.2			12	152				
16.2	62	13.7	34.2			4	36				
14.6	15.3	16.9	18.3			2	23				
16.4	88.1	13.3	52.4								
16	30.7	15.6	30.9								
14.7	61.7	13.5	67.8								
14.3	32.9	15.5	35.8								
14.1	81.6	13.8	76.6								
14.2	57.9	14.5	69.3								
12.9	44.3	13.1	76.4								
13.2	50.5	8.7	78.7								
7	52.6	15.4	82								
13.8	73.6	14.5	49.2								
15.1	48.7	12.7	51.5								
14.5	54.2	14.2	63.2								
14.5	33.7	17.3	28.2								
14.8	33.9	13.5	58.4								
13.5	85.3	14.7	48.4								
14.6	72.9	15.8	54.3								
15.9	32.6	13.8	56.2								
15.6	37.3	15.1	80.3								
12.9	71.9	14.2	38.4								
14.2	76	15	56.6								
14.4	24.7	15.5	63.9								
14.7	50.5	14.1	74.9								
14.5	60.1	16.9	28.4								
6.7	77.6	15.8	38.4								

Sample 6 (84MP12)											
Length (µm)	Angle	Length (µm)	Angle	Length (µm)	Angle	Ns	Ni	Zeta	rhoD	Nd	Cl wt%
15.6	48.1	15.1	66.3	16.7	36.5	5	101	351 ± 40	1.44E+06	4600	Not available
13.9	35	13.1	88.1	15.4	16.2	3	78				
18.2	17.4	13.8	83.3	13.7	88.3	3	42				
16.5	51.5	12.3	78.7	14.8	79.4	9	159				
16.4	18.5	7.7	63.4	13.8	48	2	30				
15.9	21.6	15.3	43.7	16	17.5	3	50				
14.9	51.9	15	44.9	12.6	61	3	60				
9.9	87	14.1	82.8	15.6	84.3	2	21				
14.1	58.6	12.3	8.5	11.2	44.6	2	28				
14.4	37.8	14.6	12	14.5	62.1	1	39				
13.3	57	13.1	54.5	13.9	49.4	9	170				
14.6	42.6	12.6	54.2	14.6	48.3	1	48				
14	84.2	15.3	71.6			2	21				
15.1	52.1	13.6	21.3			4	68				
14.6	51.5	15.4	39.3			1	10				
15.6	71.4	15.6	47.4			2	17				
14.4	29.5	14.9	3.6			2	40				
13	65.2	13.1	70.7			6	105				
15.2	72.5	15.1	75.7			10	130				
14.9	68.7	13.9	47.4			4	39				
15.5	2.4	7.7	60.9								
11.5	4.7	13.7	89.2								
14.3	84.6	7.8	14.9								
15.1	53.4	14.9	57.6								
12.9	60.1	5.9	72.9								
15.1	49.4	14.8	45								
14.8	67.1	13.7	15.3								
14.8	58	15	75.2								
13.8	78.7	15.5	40.7								
13.1	66.5	14.6	85								
15.6	41	15.6	89.7								
14.9	83.9	14.7	69.5								
13.7	20.3	14.9	47.2								
14.5	49.1	15.2	83.5								
13	78.5	15.5	69.4								
16.7	16.1	15.5	48.3								
13.5	38.1	14.3	82.4								
14	86.6	13.9	87.7								
15.7	48.9	14.5	75.8								
11.6	82.3	14.2	73.8								
13.6	72.5	14.4	42.9								
15.7	34.8	15.7	62.5								
17.4	32.7	15.1	87.1								
13.3	77.4	15.1	83.4								

Sample 7 (88SG03)									
Length (μm)	Angle	Length (μm)	Angle	Ns	Ni	Zeta	rhoD	Nd	Cl wt%
10.7	23.3	11.3	65.5	3	120	351 ± 40	2.22E+06	4600	0.02 - 0.09
11.3	8.1	12.6	22.3	3	130				
13.3	46.1	17.1	21.8	4	89				
14	77.3	11.4	0.8	2	153				
14.4	66.2	15.5	39.1	2	91				
14.7	69.7	13.8	29.2	5	285				
13.9	87.7	14.4	17.5	4	216				
14.1	37.6	8.1	5.2	6	173				
12.8	25.9	17.1	33.2	2	56				
13.6	75.9	14.7	89.5	3	113				
14.5	66	13.2	80.5	4	117				
14.6	77.2	12.4	33.2	3	166				
15	25.2	15	36.2	3	106				
16.6	67.6	13.6	31.5	5	91				
15.1	1.3	14.2	71.5	3	101				
16.7	13.9	15.2	34.6	2	129				
16.3	13.5	14.8	8.9	2	86				
14.4	2.7	15.5	59.8	3	105				
13.6	49.6	13.8	67.3	5	183				
14.8	59.9	16.8	17.7	9	206				
13.5	77	11.8	11.7						
15.2	73.1	12.3	4.6						
10.3	88	12	28.6						
11.3	37.2	14	39.7						
9.4	8.6	9.9	8.7						
13.8	54.4	14.7	27.9						
12.1	79.4	13.4	76.5						
13.4	55.8	15	45.9						
8.5	16.5	15.9	78.2						
14.9	34.2	15.8	54.8						
16	47	14.6	16.6						
14.3	66.2	13.8	88.3						
15.5	88.5	11.1	63.3						
15	87	14.7	11.6						
14.7	59.5	13.9	77.4						
14.2	63.1	17.5	29.5						
15.4	35.9	15.9	70.8						
13.2	6.7	15.1	49.8						
12.5	3.5	16.8	46.4						
14.4	89.8	15.8	12.4						
14.9	25.5	15.9	13						
15	53.5	9.4	68.7						
16.1	13.1	14.5	61.6						
15.4	35.8								

Sample 8 (88SG07)											
Length (µm)	Angle	Length (µm)	Angle	Length (µm)	Angle	Ns	Ni	Zeta	rhoD	Nd	Cl wt%
15.5	66.9	16.4	86	15.4	23.7	1	5	351 ± 40	9.93E+05	4600	0.05 - 0.10
13.5	10.1	15.9	49.7	13.8	47.7	2	12				
16.4	43.7	15.9	82.3	13.1	55.3	2	20				
15.8	50.1	7.5	80.6	7.8	34.9	4	18				
14.9	30.7	16.2	18.4	14.5	49.6	1	3				
14.7	36.6	13.5	66.5	16	54.1	1	3				
13.3	22.6	15.6	81.6	16	29.9	2	13				
15.9	43.3	15.6	67.2	15.9	80.3	13	110				
14.3	0.3	15	64.6	15.3	78.5	14	70				
15.2	60.8	14.2	84.3	14.3	82.1	10	62				
15.5	87	16.2	64.3	13.6	5.8	3	8				
14.9	57	9.1	72.7	12.5	24.1	2	8				
11.9	24.1	16.6	22.8			7	36				
15.9	84.7	15.7	36			2	9				
13.7	55.2	11.1	45.2			1	4				
15	12.3	14.5	40.7			4	16				
14	79.4	16.1	28			1	7				
14.4	12.3	8	72.3			11	68				
12.1	15.8	15.5	44			3	11				
15.8	86.6	7.7	58.8			2	7				
15.2	58.6	14.4	65.7								
14.7	16	15.8	59.9								
15.7	7.6	18.1	64.6								
15.9	18.3	10.7	84.9								
14.6	68.9	15.6	22.9								
15.9	55.5	12	24.3								
15	80.4	14.5	72.8								
14	11.2	9.2	54.5								
10.8	87.9	9.8	43.1								
14.2	88	14.4	34.1								
16.1	30.7	12.8	60.8								
14.4	53.7	12.4	37.4								
15.6	61.9	12.2	86.9								
15.9	45.4	16	33.1								
14.8	14.5	14	82.2								
15.6	53.9	7.6	31.4								
6.1	45.5	12	58.1								
13.4	58	8.3	55.9								
15.1	37.5	15.4	52.8								
14.2	49.2	15.7	36.9								
15.2	63.7	16.1	6								
10.8	49.1	15.8	73.9								
10.2	17.3	15.9	39.5								
14.2	77.5	10	65.9								

Sample 9 (88SG09)									
Length (µm)	Angle	Length (µm)	Angle	Ns	Ni	Zeta	rhoD	Nd	Cl wt%
13.1	78.8	15.8	37.7	4	26	351 ± 40	9.75E+05	4600	0.03 - 0.20
13.2	67.1	15.7	84.8	6	56				
13.7	9	11.9	32.1	5	21				
14.7	8.3	15.1	81.6	2	8				
15	77.2	15.5	49.1	3	20				
19.8	21.4	15.6	70.2	12	177				
5.9	84	16.4	27.1	4	85				
14.7	67	3.9	77.1	3	12				
13.5	88.6	16.3	37.7	6	71				
15.6	35.2	16.8	19.9	10	55				
14.8	18.6	12.2	36	9	52				
16.7	26.9	15.4	67.2	3	41				
17.2	34.9	15	33.5	11	113				
14.9	27.2	12.5	12.3	3	13				
14.3	79.3	14.8	58.7	2	43				
13	71.8	16.2	7.5	11	67				
15.9	66	16.5	8.7	2	8				
15.7	40.5	10.4	70.2	2	26				
16.4	59.2	17.6	31.8	6	50				
13.7	57.1	16.8	15.8	2	17				
15.3	79.6	14.8	0.2						
15.3	44.6	10.5	60						
14.7	35.9	15.7	55.3						
11.8	76.8	17.1	62						
14.3	23	15	47.1						
15.6	3.4	15.9	63.2						
11.2	84.4	14.4	87.8						
15.7	65.8	12.9	71.4						
16.7	64.6	19.9	0.2						
14.6	66.9	13.8	83.8						
15.7	69.9	12.2	58.7						
10	4.7	13.6	70.1						
16.2	59.5	14.1	30.4						
16.1	63.9	13.7	19.2						
14	68.9	14.8	33						
14.6	59.9	15.7	79.3						
12	42.5	15.2	87.1						
13.1	7.7	16	11.2						
11.8	85.8	14.9	36.1						
15.7	36.4								
17.3	57.4								
15.2	57.5								
11.4	53.5								
13.5	25								

Sample 10 (88SG10)											
Length (µm)	Angle	Length (µm)	Angle	Length (µm)	Angle	Ns	Ni	Zeta	rhoD	Nd	Cl wt%
10.1	88.4	13.4	54.2	12.8	84.7	5	21	351 ± 40	9.65E+05	4600	0.03 - 0.22
14.3	68.7	14.6	47.7	14.9	56.5	3	21				
10.1	59.2	14.4	60.2	12.9	32.8	7	68				
10.2	65.4	12.7	42.9	13.5	47.5	2	10				
9.9	59	11.1	17.1	14.3	51.6	10	42				
14.9	20	15.4	33.1	13.3	72.4	9	28				
11.5	76.6	15.1	32.9	13.4	66.9	6	81				
15.3	45.1	13.2	47.8	11.7	41.3	7	24				
14.8	42.6	13.6	51.2	12.1	65.9	8	43				
14.2	19.2	16.5	69.2	14.4	45.2	4	20				
11.5	57	8.9	3.8	9	36.6	7	23				
8.9	69.2	12.3	41.7	10.8	86	1	15				
11.2	16.7	11	81.4			2	8				
10.9	56.1	13.4	10.9			11	56				
11.2	52.7	9	69.1			1	8				
12.5	25.6	12.8	55.4			30	84				
18.9	81.6	13.9	87.6			4	25				
15.4	82.1	12.1	25.7			2	12				
13.1	75.8	10.4	18.9			19	82				
13.5	30.3	9	45			25	57				
11.7	14.4	13.1	75.8								
12.9	52.9	11.2	49.4								
13.7	69.2	11.1	48.7								
16.5	30.4	14.3	58.7								
11	74.4	14.8	43.2								
3.2	16.8	11.1	66.3								
14.5	64.5	8.8	52.1								
9	82.4	8.2	26.9								
14.9	48.7	11.5	57.3								
14.7	40.8	13.6	45.6								
12.2	33.1	10.5	73.9								
9.6	68.4	13.1	44.1								
12	53.5	12.4	30								
12.8	75.4	13.2	77.2								
9.7	83.2	12.9	23.3								
11.4	48	7.3	17.3								
11.2	26.8	13	27.7								
11	51.2	10.1	73.2								
16	50.9	14.1	54.8								
12	80.3	13.3	47.9								
15.2	33.6	11.9	6.7								
13.8	67.2	13.9	33.1								
13.3	42.3	14.8	26.3								
13.7	37.8	11.6	30.6								

Sample 11 (88SG11)											
Length (µm)	Angle	Length (µm)	Angle	Length (µm)	Angle	Ns	Ni	Zeta	rhoD	Nd	Cl wt%
12.2	23.9	13.2	42.4	13	13.7	5	19	351 ± 40	9.55E+05	4600	0.03 - 0.20
15.1	31.8	13.2	80.7	13.5	39.9	16	106				
12.1	1.3	14.6	61.1	14	29.5	2	5				
14.8	53.6	13.5	50.7	15	39.6	15	147				
13.8	76.3	12	56.7	16.1	8.3	3	10				
12.1	63.7	13.4	61.4	12.8	72.9	9	50				
11.6	29.2	15.3	17.4	14.5	34.8	11	78				
12.3	35.1	12.3	83.3	13.6	21	16	86				
11.8	84	14.3	75.4	14.9	45.6	7	32				
11.2	69.8	12.2	47.7	13.7	1.5	11	70				
13	64.1	13.2	42.7	4.9	78.5	20	197				
14.3	23.2	15.9	44.3	12.7	79.6	22	78				
11.5	68.6	14.2	59.4	13.1	67.4	10	50				
13.8	29.4	13.3	11.7			14	78				
15.7	39.4	15.6	76.5			2	8				
12.1	63.9	10.8	64.2			15	78				
10.7	84.1	14.1	13.5			6	33				
14.5	83.9	15.2	32.8			19	92				
12.7	72.6	13.1	76.6			6	43				
11.2	34.1	9.3	68.5			11	67				
10.9	42.8	11.4	68.4								
15.7	63.7	14.3	62.2								
11.4	57.9	13.4	29.8								
14.9	32	11.9	29.9								
13	26.5	14.2	15.2								
13.4	40.5	14.9	89.8								
12.1	33	14.7	78.6								
11.8	89.3	12	27.3								
11.3	67.6	11	87.4								
12.1	78.9	11	15.3								
12.1	30	14.1	25.1								
13.2	35.1	10.8	56.5								
11.7	65.1	12.3	81.1								
14.6	59.6	6.8	75.2								
15.1	24.2	15.6	72								
13.5	7.8	11.8	59.1								
10	52.2	12.6	1.2								
13.6	22.6	6.6	70.4								
14.4	42.4	14.6	36.7								
10.4	80.1	14.9	11.4								
12.7	44.2	14.8	39.8								
12.9	67.6	11.7	54.5								
12.7	63.8	12.5	46.4								
15.9	34.4	10	70.7								

Sample 12 (88SG12)											
Length (µm)	Angle	Length (µm)	Angle	Length (µm)	Angle	Ns	Ni	Zeta	rhoD	Nd	Cl wt%
7.2	62.9	13.2	74.5	15	70.2	2	15	351 ± 40	9.71E+05	4600	0.02 - 0.09
15.1	21.3	9.5	43.6	14.5	43.5	10	141				
15.4	35.3	14.5	64	15.6	87.5	3	25				
13.8	63.1	16.1	84.6	14.5	31.5	4	62				
14.6	72.9	7.4	52.5	13.8	84	8	81				
15.4	34.2	15.1	60.8	13.3	75.2	5	46				
17.1	87.9	9.1	41.6	15	32.7	9	60				
14.1	75.9	16	83.1	9.8	72.8	7	50				
13.9	42.2	15	56	12.6	82.7	20	151				
10.7	21.7	15.2	86.2	8.7	45.9	3	36				
15.1	82.8	15.4	82	4.5	52.7	9	62				
15.9	3.1	16.2	49.5	9.3	30.5	6	73				
14.6	68.8	14.4	42.7	12.5	71.4	5	62				
11.1	49.6	13.9	82.6	14.9	67.9	40	192				
13.2	70.6	15.2	41.4	14.8	29.6	30	164				
11.5	56.3	15.8	13	8.6	39	4	37				
15	12.4	15.8	1.3	15.4	33.9	15	127				
14.6	40.9	10.4	68.3	14.8	60.2	7	50				
16.6	86.9	6.2	52.8	15.6	73.3	15	92				
16	59.7	15.3	87.8	16	42.2	9	108				
15.9	84.3	11.3	17.7	8.9	6						
13.9	62.5	9.1	55	11.3	60.6						
8.9	33.7	8.2	30.8	13.2	54.9						
14.6	70	14.6	55	9.5	29.4						
11	28.2	10.2	37.3	14.1	40.6						
15.2	66.5	15.2	46.5	15.1	52.8						
16.2	70.5	15.4	59.5	13.4	70.7						
15.4	85.6	11.6	11.5	14.2	47.8						
15.6	65.4	14.4	64.1	14.4	66						
11.6	9.5	14.7	68.1	9.9	70.1						
10.4	31.1	9.3	45.6	9.5	50.2						
12.3	80.7	16.3	31	9.8	37.3						
14.9	75	3.5	63.2	13.4	18.2						
14.5	59.9	14.5	85.5	14.7	41.3						
10.3	54.5	14.1	53.2	12.2	82.7						
5.5	81.2	13.9	55.7	7.8	58.8						
15.9	26.7	15.2	67.5	15.3	74.9						
15.5	86.4	14.4	22.9	16	23.5						
15.6	78.4	15.5	2.7	16.4	86.6						
10.2	22.1	14.6	77.2	12.6	50.8						
13.9	51.2	11.9	8.5								
13.3	52.2	14.1	61.2								
15	76.5	15.6	1.9								
14.2	77.1	14	88.2								

Sample 13 (88SG13)							
Length (μm)	Angle	Ns	Ni	Zeta	rhoD	Nd	Cl wt%
15.4	44.3	3	21	351 ± 40	9.61E+05	4600	0.00 - 0.31
15.3	24.3	7	91				
14.2	48.8	2	10				
16	66.1	4	24				
14.5	21.1	12	120				
16.2	32.1	12	101				
15.7	50.8	1	8				
12.8	50	6	47				
14.4	42.5	9	68				
14.5	55	11	104				
15	9	3	20				
16	57.5	13	127				
14.1	31.8	4	37				
15.1	57.4	7	99				
14.5	68.4	4	29				
15.1	76.9	6	62				
8.9	71.8	3	37				
16.7	62	5	51				
14.5	80.3	3	23				
13.1	81.5	2	17				
13.9	84.5						
15.9	64.9						
16.2	33.9						
13.2	79.5						
15.5	68.8						
10	79.9						
15.5	69.9						
14.7	68.7						
15.5	70.8						
13	41.3						
15.6	60						
13.8	83.7						
15.2	70.4						
15.1	20.8						
16.5	85.5						
15.6	44.5						
7.8	55.6						
14.8	54.6						
15.7	35.4						
13.3	74						

Sample 14 (88SG23)											
Length (µm)	Angle	Length (µm)	Angle	Length (µm)	Angle	Ns	Ni	Zeta	rhoD	Nd	Cl wt%
12	83.7	12.8	69.5	13.6	20.6	3	39	351 ± 40	2.22E+06	4600	Not available
10.6	23.4	12.4	77.7	11.4	57.6	5	68				
10.4	65.3	12.8	23.6	13	59	6	68				
11.9	74.1	17	37.2	12.6	41.2	3	40				
13	81	12.4	84.3	12.8	33.4	3	48				
11.8	82	12.9	89.5	12.5	83.8	4	39				
11.9	87.9	13.3	38.2	14.9	43.5	7	43				
15.5	48.2	14.9	38.4	9.4	29.1	2	22				
14.2	7.6	15	29.2	14.7	62.6	4	37				
14.9	87.2	14.5	33.6	12.1	46.5	5	60				
15	25.2	12.2	75.2	12.3	21.4	7	73				
13.2	74	13.7	69.7	14	46.4	7	108				
13.2	65.9	12.2	6.8			2	41				
16.4	34.7	12.9	64.5			7	90				
11.6	70.1	14.8	23.3			6	81				
13.4	87.2	13.7	75.2			3	39				
15.5	76.6	13	11.4			4	52				
16.5	2.6	11.8	65.3			2	16				
10.4	65.3	15.7	57			2	22				
13.2	77.5	11.7	53.5			5	52				
14.2	26.7	12.6	38.2								
12.1	88.6	12	47.5								
16.4	55.8	16.2	87.7								
14.7	25	13.7	54.6								
14.7	67.6	12.7	11.4								
13.9	28.1	12.5	71.4								
13.7	7.9	11.8	12.6								
12.6	60.8	12.6	78.2								
13.2	28.1	11.6	81.1								
13.6	38.5	12	65.2								
14.7	33.6	11.8	68.4								
14.9	45.2	13.8	57.7								
13.1	70.1	12.5	65.4								
13.5	42.9	12.1	80.9								
11.9	86.4	12.5	71.3								
14.6	50.7	14.4	23.3								
14.4	25.4	14.7	49.2								
13.1	31.1	14.8	58.9								
5	75.4	16	24.9								
14.5	35.5	13.8	78.8								
13.1	51	15.9	30.7								
11.6	43.3	17.1	67.2								
13.7	33.7	13	81.8								
11.7	86.8	11.6	51.8								

Sample 15 (88NAC02)											
Length (µm)	Angle	Length (µm)	Angle	Length (µm)	Angle	Ns	Ni	Zeta	rhoD	Nd	Cl wt%
14.2	10.4	14.6	81.8	14.2	45.7	6	95	351 ± 40	1.44E+06	4600	Not available
14.2	15.5	14.7	24.2	14.0	75.9	31	196				
8.2	41.7	13.3	59.3	13.8	74.5	11	78				
14.2	48.0	12.6	10.3	12.0	82.4	10	57				
14.2	72.6	15.6	67.8	14.3	26.6	40	204				
14.8	3.6	12.0	56.8	14.3	56.4	44	293				
10.8	53.0	15.5	65.9	13.3	79.9	15	108				
14.6	48.4	14.6	45.2	10.8	61.9	13	128				
10.4	79.2	15.0	17.1	13.7	40.2	35	187				
14.8	78.3	14.3	47.6	12.9	64.6	11	81				
15.2	66.6	12.4	52.0	12.9	60.9	24	127				
12.7	77.6	11.5	39.1	14.0	56.9	18	130				
14.7	55.5	12.6	9.6	14.7	47.6	14	115				
13.1	33.9	12.8	88.9	14.6	64.1	22	174				
14.0	1.3	13.6	81.4			9	78				
13.1	79.7	12.6	71.5			10	46				
14.3	56.2	13.8	75.0			19	103				
13.2	52.4	12.5	80.1			17	123				
13.4	87.2	14.5	12.3			13	64				
13.6	74.7	16.0	7.7			81	435				
13.4	49.2	13.4	56.4								
13.7	19.8	12.9	89.5								
13.5	82.6	16.3	59.2								
14.1	69.2	13.3	85.5								
11.9	78.8	15.1	17.2								
14.1	26.2	13.1	26.4								
16.2	31.5	12.3	71.5								
13.4	82.5	12.3	59.8								
15.0	46.9	13.2	46.2								
13.9	61.0	13.1	83.6								
14.5	87.3	13.8	34.7								
15.5	52.4	9.8	71.9								
15.1	80.8	14.1	82.0								
13.2	80.2	13.6	55.8								
10.7	82.8	14.7	46.9								
16.5	51.6	17.9	27.0								
12.8	44.6	8.6	40.4								
15.3	29.1	11.4	59.1								
14.0	86.1	13.9	43.5								
13.8	34.3	12.9	78.8								
15.5	31.4	13.4	36.6								
13.4	67.5	13.8	16.7								
13.2	72.3	14.1	30.3								
12.9	46.4	15.3	63.7								

Sample 16 (88NAC15)											
Length (μm)	Angle	Length (μm)	Angle	Length (μm)	Angle	Ns	Ni	Zeta	rhoD	Nd	Cl wt%
15	50.4	13.1	28.3	11.3	66.2	11	46	351 ± 40	1.48E+06	4600	0.13 - 0.39
10.7	72.8	15.1	78.9	12.6	36.2	65	207				
7.8	6.4	14.5	82.3	16.4	52.5	31	161				
14.9	26.8	11.8	53.6	15.5	2.7	10	51				
10	54.5	11	61.1	11.1	26.9	10	45				
14.1	71.2	16.7	40.7	13.9	23.8	38	129				
10.1	67.5	7.3	71.2	14.1	9.1	4	19				
10.2	81.1	13.8	40.7	15.3	30	63	294				
10.6	75.6	15.5	58.3	13.9	30.5	6	20				
11.2	31.2	13.5	67.9	12	70.5	3	11				
16.2	77.1	15	80.3	13.8	72.4	7	33				
12.8	79.8	15.2	77.2	14.3	56.5	6	23				
9.9	60.1	9.9	85.3	13.5	64.5	8	27				
16.1	37.3	10.2	75.7			8	34				
8.6	52.6	14	45.8			7	34				
8.7	69.4	10.5	57.2			11	70				
11	41.9	13.7	64.5			86	191				
13.9	47.5	11.8	76			25	135				
14.1	87.5	15.8	59.5			29	87				
10.8	81.1	12.1	65.4			5	17				
11.4	57.5	14.3	86.8								
11.9	0.5	14.6	87.6								
14.1	48	14	74.3								
8.2	31.9	14.9	49.9								
8	53.5	14.8	32.2								
13.7	82.2	14.9	46.7								
12.4	18.2	14.8	67.8								
12	63	16.1	32.1								
15	26.2	11.4	13.7								
13.5	76.4	10	63								
13.6	73.8	11.5	75								
14.8	13.4	10.7	79.7								
13.3	82.7	9.5	53								
14.3	52.5	10.6	71.1								
14.6	50.8	16	88.8								
7.9	57.1	13.4	86.7								
13.9	62	15.7	37.2								
12.3	78	10.4	40.2								
13.2	56	10.6	85.3								
11.2	52.6	11.6	12.5								
14.7	78.4	14.5	3.4								
13.2	47.9	13.9	60.2								
16.2	28.5	9.1	57.6								
9.3	6.5	16.4	48.2								

Sample 17 (88MAN03)											
Length (µm)	Angle	Length (µm)	Angle	Length (µm)	Angle	Ns	Ni	Zeta	rhoD	Nd	Cl wt%
14.6	73.5	8.3	39.7	12.2	73.9	5	16	351 ± 40	1.33E+06	4600	0.08 - 0.15
14.7	31.1	7.4	48.3	11.1	69.0	4	20				
14.8	57.7	16.3	19.7	14.6	27.8	9	83				
10.4	61.9	12.6	1.1	14.2	88.8	7	39				
16.9	42.1	14.2	48.6	14.0	51.5	4	22				
11.3	61.1	13.6	59.1	13.3	60.2	9	38				
10.3	53.8	14.4	61.5	15.2	64.9	5	35				
12.3	27.0	14.8	70.5	14.8	73.9	3	27				
14.6	53.4	12.7	49.6	15.0	80.6	9	36				
10.4	87.9	15.1	66.6	15.8	81.2	5	32				
14.0	71.9	13.9	63.0	14.6	34.6	6	35				
11.5	71.7	14.5	43.5	11.1	75.5	1	10				
14.7	41.8	11.6	52.9			10	53				
12.6	67.4	12.5	50.5			8	35				
13.2	36.9	12.7	73.4			4	26				
10.1	50.2	13.3	67.0			11	66				
10.4	12.0	14.5	61.3			5	35				
11.7	84.5	14.0	84.4			3	22				
13.8	75.0	7.6	77.7			12	78				
12.5	60.8	9.1	85.4			8	58				
14.0	86.3	12.5	83.4								
14.0	68.9	15.3	40.5								
13.5	45.9	12.8	79.4								
10.6	68.6	12.6	40.9								
14.0	67.4	14.9	49.9								
14.4	64.3	11.9	44.8								
11.5	40.0	10.8	78.0								
15.8	47.9	11.6	89.8								
13.9	32.7	13.7	62.4								
15.0	21.4	13.4	52.3								
15.2	56.9	13.2	68.4								
12.1	70.4	13.5	41.7								
9.1	83.4	12.6	23.1								
9.6	56.3	14.6	54.9								
13.1	71.1	12.7	37.2								
11.1	28.7	13.1	44.7								
9.9	60.4	13.7	57.5								
12.8	39.4	11.6	74.7								
14.3	72.3	15.3	22.5								
10.8	37.9	11.5	30.8								
13.4	39.8	10.9	63.3								
11.5	26.5	13.7	72.7								
12.9	51.7	13.5	50.6								
9.6	26.2	12.3	64.8								

Sample 18 (88MAN04)											
Length (µm)	Angle	Length (µm)	Angle	Length (µm)	Angle	Ns	Ni	Zeta	rhoD	Nd	Cl wt%
13.8	72.6	10.7	36.5	13.7	59.7	12	81	351 ± 40	1.33E+06	4600	0.09 - 0.14
9.5	50.7	12.5	64.2	14.8	50.0	22	160				
15.6	79.0	13.7	81.0	15.1	3.8	12	149				
15.8	63.2	8.2	37.2	12.8	69.5	2	11				
12.5	49.4	11.7	76.9	11.0	30.9	6	45				
16.3	49.2	10.5	75.8	10.8	30.3	8	79				
14.4	35.7	13.9	24.7	15.4	2.5	3	25				
14.8	51.9	9.4	31.3	11.9	48.9	9	90				
16.4	76.1	15.0	71.7	14.6	59.2	5	50				
10.7	49.0	15.2	88.1	15.0	55.7	6	65				
8.9	69.9	14.6	48.8	17.0	59.0	13	86				
13.1	53.9	13.6	33.5	12.3	80.4	5	29				
6.4	5.8	12.1	33.1			4	38				
10.8	11.0	10.6	67.0			11	65				
10.0	45.5	13.3	17.8			7	36				
13.7	31.5	8.9	54.0			6	33				
14.6	46.9	14.3	58.8			4	40				
9.7	71.5	11.5	22.2			8	72				
14.7	24.2	13.5	24.1			4	42				
15.9	63.4	12.4	53.5			3	30				
12.3	43.7	13.6	76.7								
13.1	32.8	11.2	31.6								
12.1	64.7	9.7	2.4								
8.9	71.8	11.8	46.3								
14.8	59.5	14.3	78.2								
10.7	64.6	15.8	81.4								
13.3	28.6	14.8	75.0								
13.7	60.4	13.1	74.9								
14.8	41.3	12.7	44.1								
6.7	47.9	15.3	55.5								
9.2	65.6	15.7	58.6								
11.6	5.4	10.0	71.7								
9.9	75.5	14.3	39.3								
16.1	49.5	13.8	75.2								
15.8	54.8	5.0	33.4								
11.2	36.9	13.6	86.8								
14.5	30.8	11.6	45.9								
12.1	74.0	13.7	62.4								
14.6	34.1	13.5	55.0								
11.9	76.6	13.5	54.7								
9.2	80.0	14.5	56.8								
11.8	29.8	16.3	60.4								
14.2	71.2	15.0	74.1								
13.3	29.5	13.7	62.4								

Sample 19 (88MAN13)									
Length (µm)	Angle	Length (µm)	Angle	Ns	Ni	Zeta	rhoD	Nd	Cl wt%
13.7	69.8	10.0	82.5	1	4	351 ± 40	1.37E+06	4600	0.20 - 0.86
14.6	83.9	14.5	58.8	7	40				
13.1	34.9	13.8	70.7	3	20				
12.9	79.9	14.8	36.5	5	37				
13.9	63.9	14.2	44.1	7	34				
13.9	72.9	15.9	79.2	3	9				
12.8	3.9	16.7	46.1	8	33				
7.4	39.3	14.6	35.9	9	43				
13.1	30.6	13.2	76.4	3	15				
13.0	34.5	13.1	63.4	10	39				
15.4	37.4	15.0	35.6	12	42				
12.9	45.6	13.1	53.6	11	45				
14.5	26.9	12.8	69.3	2	10				
13.3	55.9	13.2	69.5	9	38				
6.5	25.4	11.7	1.9	1	5				
7.9	62.4	13.2	28.2	11	77				
12.8	70.7	14.4	22.5	3	29				
10.9	88.6	14.3	76.1	7	34				
12.8	50.8	14.1	35.8	4	28				
13.1	80.5	7.8	82.2	1	4				
13.2	57.4	13.6	45.6						
14.1	63.8	14.3	55.5						
13.8	57.9	12.7	47.0						
7.6	5.1	12.5	7.9						
13.4	52.8	12.4	63.6						
14.4	34.3	14.0	51.9						
14.6	79.7	15.5	68.0						
13.6	61.0								
14.7	59.5								
10.7	40.8								
14.5	42.0								
12.3	66.4								
14.1	51.1								
15.1	54.1								
15.0	36.5								
13.4	36.4								
13.2	45.8								
10.1	11.9								
14.8	38.6								
12.1	72.7								
14.4	79.0								
12.3	53.6								
14.9	5.7								
13.7	59.9								

Sample 20 (90BR05)									
Length (µm)	Angle	Length (µm)	Angle	Ns	Ni	Zeta	rhoD	Nd	Cl wt%
14.7	30	16.6	65.2	35	300	4265 ± 300	2.80E+05	3756	Not available
15.6	83.7	14.7	77.9	8	77				
15.5	59.5	13.3	52.7	9	111				
15.1	63.9	14.7	62.7	27	236				
13.1	62.7	11	65.2	15	127				
13.8	42.4	13.8	35.4	1	17				
9.5	67.6	16.4	51.4	4	38				
15.6	45.8	15.5	27.2	4	30				
14.6	82.4			11	131				
15	45.3			16	140				
16.1	20.4			12	151				
13.5	78.7			8	75				
15.9	82.7			19	151				
9.5	34.8			42	350				
15.2	43.8			6	41				
11.7	36.6			2	31				
13.3	43			9	87				
15	78.7			15	150				
7.7	67.1			9	118				
15	64.4			20	180				
15.3	40.8								
15	71.7								
15	88.8								
14.3	55.4								
15.9	76.4								
14.1	85.7								
13.2	68								
16.8	76.7								
15.5	86.5								
13.2	53.8								
13.3	89.8								
14.7	53.4								
14.7	49								
13.9	64.1								
14.6	84.3								
16.6	1.8								
13.3	74								
14.3	54.4								
13.3	81.6								
16.7	14.9								
13.7	48.2								
15	35.2								
15.5	38.4								
14.2	46.8								

Sample 21 (90SB02)									
Length (µm)	Angle	Length (µm)	Angle	Ns	Ni	Zeta	rhoD	Nd	Cl wt%
14.4	70.9	15.3	64.8	3	54	4265 ± 300	1.83E+05	3900	Not available
12.9	57.9	15.6	52.3	4	66				
16.4	26.4	14	84.9	4	46				
15.4	69.9	15	19.3	3	55				
15.1	77.9	15.6	79.2	5	81				
15.1	35.3	16.1	59.1	6	83				
15.9	38.5	14.1	69.8	2	36				
14	61.6	16	66.9	8	131				
15.4	50.7	15.3	68	5	133				
15.1	55.6	16.9	25.1	23	369				
15.2	50.9	15.3	71.3	3	52				
14.3	51.4	14	87.2	7	106				
15.1	47.3	14	51.3	3	36				
7.8	55.6	14.7	75.1	2	35				
14.7	73.3	15.3	43.9	3	39				
14.2	25.8	16.1	67.4	4	68				
14.3	46	15.6	88.3	2	34				
7	18	15.2	12.6	7	97				
14.1	64.9	13.5	76.6	4	60				
15.7	47.1	15.4	44	3	67				
13.3	67.8	16	74.1						
15.3	48.1	15.9	9.5						
13.8	53.8	15.1	46.7						
9.7	56	16.9	55.4						
13.6	67.8	15.7	71.3						
15.4	61.8	14.2	38.4						
14	81.2	14.5	61.4						
16	20.5	13.2	77.8						
14.3	88.8	11.3	70.1						
12.6	59.4	16.2	33.3						
15.4	56.6	14.7	48						
16	70.2	14.4	48.2						
14.8	81	10.8	79.1						
14.3	61.3	13.4	68.1						
15.8	56.7	11.7	59.9						
16.1	62	13.9	59.2						
15.5	58.1	15.7	76.8						
8.9	51.2	14.8	48.5						
15.4	85.7	14.7	85						
13.3	85.5	15.5	81						
16.1	37.4	14.8	73.3						
15.4	40.8	6.1	72.4						
15.8	72.8	13.8	64.6						
14.6	74.5	15.6	27.7						

Sample 22 (90SA08)							
Length (µm)	Angle	Ns	Ni	Zeta	rhoD	Nd	Cl wt%
Not available	Not available	2	55	4265 ± 300	2.95E+05	3756	Not available
		1	11				
		0	11				
		1	8				
		1	14				
		0	25				
		2	35				
		1	36				
		1	33				
		2	62				
		0	11				
		1	25				
		1	28				
		2	67				
		1	31				
		2	35				
		2	56				
		1	50				
		2	34				
		2	93				

Sample 23 (81OR07)											
Length (μm)	Angle	Length (μm)	Angle	Length (μm)	Angle	Ns	Ni	Zeta	rhoD	Nd	Cl wt%
14.41	65.36	14.08	60.62	11.31	45.76	9	138	4265 ± 300	1.25E+05	3027	Not available
15.16	22.39	13.04	72.94	14.62	67.11	5	108				
13.41	69.34	14.45	42.04	15.55	50.35	6	110				
14.72	38.52	7.02	68.47	14.42	50.12	5	193				
15.6	72.22	15.84	28.4	11.77	50.7	2	77				
15.47	42.47	15.95	26.72	14.63	49.09	4	112				
8.02	78.73	14.58	68.93	14.88	54.92	2	77				
14.24	84.21	16.57	48.36	14.43	17.24	3	63				
13.5	43.07	17.24	50.39	13.87	28.36	3	79				
14.9	56.13	15.84	62.72	15.41	51.26	2	72				
15.43	61.09	9.11	74.16	15.45	47.73	3	77				
14	78.04	14.15	83.98	14.7	35.94	6	132				
15.82	61.02	8.31	87.54			4	124				
14.54	74.99	14.15	81.18			4	139				
14.63	62.26	13.38	68.85			3	104				
15.64	66.82	11.23	71.87			1	29				
12.97	77.06	10.51	29.12			5	93				
13.96	80.47	15.05	81.47								
14.85	60.16	14.09	51.47								
15.86	70.28	9.23	77.17								
15.24	29.81	16.07	51								
10.91	55.54	15.28	41.75								
14.86	63.42	13.5	75.89								
10.6	49.81	5.04	47.75								
15.25	64.31	14.73	63.94								
15.17	62.96	15.65	31.85								
15	48.79	14.82	68.7								
14.48	0.22	10.14	45.24								
14.98	67.83	15.17	83.35								
15.87	66.83	15.56	44.29								
14.17	63.1	6.52	66.22								
15.84	39.49	14.99	30.66								
15.15	46.3	16.2	71.66								
13.59	79.21	10.82	34.21								
14.29	46.5	15.68	46.62								
15.83	51.04	16.12	35.71								
14.48	73.08	13.52	52.43								
14.14	80.49	8.94	57.7								
16.28	57.64	14.86	36.97								
14.6	32.68	16.23	42.45								
15.63	22.86	16.16	76.42								
13.31	52.73	13.58	80.01								
15.25	43.35	11.78	62.53								
8.05	77.24	14.6	68.64								

Sample 24 (81OR08)											
Length (µm)	Angle	Length (µm)	Angle	Length (µm)	Angle	Ns	Ni	Zeta	rhoD	Nd	Cl wt%
14.07	70.25	14.71	68.27	15.68	39.68	9	164	4265 ± 300	1.26E+05	3027	Not available
15.75	59.02	8.94	2.11	14.54	36.52	5	78				
13.78	51.48	16.67	17.78	6.84	86.89	4	85				
14.57	71.2	12.07	55.03	14.79	28.68	21	333				
7.77	42.13	16.15	27.32	16.35	66.92	3	46				
15.62	45.71	15.72	36.71	16.17	79.21	7	138				
11.47	61.37	13.8	39.07	4.92	54.46	5	93				
14.11	65.56	12.99	89.12	16.25	28.18	5	85				
14.72	29.21	7.05	42.84	15.52	40.19	7	119				
15.9	17.31	11.99	89.08	15.3	20.32	6	129				
13.2	86.1	14.28	38.84	16.28	35.9	3	41				
15.54	83.38	13.05	35.33	15.47	45.17	5	131				
14.73	32.9	14.24	70.28			6	122				
14.42	24.56	14.51	30.29			8	126				
15	57.1	14.65	10.54			3	60				
15.21	76.62	14.44	80.16			7	208				
12.97	78.99	14.63	74.32			4	117				
15.36	36.7	16.56	25.44			5	144				
12.72	69.28	16.26	48.4								
15.08	67.53	14.94	20.55								
15.89	68.26	16.38	20.53								
15.31	46.05	15.98	57.89								
15.06	30.58	14.11	66.6								
12.01	11.93	15.67	49.49								
15.86	78.12	14.62	48.34								
16.04	60.3	14.09	69.84								
15.31	69.41	16.67	58.75								
15.62	84.46	12.51	61.38								
15.32	59.66	14.74	77.52								
14.03	56.79	15.65	13.86								
15.75	84.31	15.2	69.25								
15.32	54.07	14.64	33.83								
12.5	68.57	13.52	78.21								
15.55	52.54	14.57	87.85								
15.66	83.25	14.03	57.5								
15.76	64.2	15.66	79.74								
13.17	56.59	15.14	55.45								
14.92	52.82	15.89	29.22								
11.49	51.87	17.24	6.04								
14.1	60.32	15	73.4								
9.16	57.49	5.73	40.33								
17.11	21.81	13.63	24.07								
16.61	55.63	9.28	70.93								
16.2	57.19	14.55	6.17								

Sample 25 (81OR15)											
Length (μm)	Angle	Length (μm)	Angle	Length (μm)	Angle	Ns	Ni	Zeta	rhoD	Nd	Cl wt%
16.19	16.36	13.93	38.77	14.55	37.43	3	63	4265 ± 300	1.33E+05	3027	Not available
12.53	66.21	14.48	48.24	16.01	12.54	2	51				
14.49	60.83	13.81	64.73	14.66	46.31	4	83				
10.83	28.31	10.28	55.19	15.3	20.32	2	57				
11.96	60.84	15.6	45.23			6	158				
16.41	64.98	16.27	48.04			14	208				
14.74	51.68	12.85	24.54			2	67				
15.84	64.54	8.89	3.8			2	51				
14.47	89.86	14.96	31.81			3	33				
14.57	70.51	16.01	52.39			9	126				
15.95	44.12	12.67	70.28			6	137				
14.79	75.77	17.27	28.6			4	70				
15.68	54.55	16.22	67.56			6	154				
15.38	52.49	15.31	67.37			1	16				
15.13	37.13	14.79	72.66			2	49				
15.26	63.31	14.69	48.76			5	73				
15.67	30.14	14.54	48.07			6	129				
14.62	38.29	14.17	40.49			4	94				
16.65	48.99	13.69	57.97			6	142				
15.48	30.86	8.06	73.52			7	156				
16.42	62.53	14.59	58.38								
19.65	67.5	10.19	52.44								
13.34	42.48	16.08	24								
15.67	73	14.33	52.55								
12.12	40.91	14.74	77.52								
9.52	51.84	15.11	56.57								
14.04	74.22	14.13	71.5								
14.44	41.63	16.03	31.21								
8.35	59.19	15.91	23.23								
14.44	80.13	13.84	59.3								
14.79	46.96	14.07	50.56								
15.22	65.88	16.08	85.48								
11.81	84.64	15	42.31								
7.8	62.93	10.36	37.47								
14.94	63.48	14.49	33.71								
16.59	31.87	14.44	68.34								
14.67	71.3	16.45	50.45								
5.55	57.29	13.8	87.25								
14.95	45.9	17.19	32.04								
7.14	55.48	13.38	88.42								
15.37	61.35	12.86	81.7								
14.71	40.32	10.97	34.37								
15.71	47.42	15.73	32.28								
14.65	64.26	17.05	20.21								

Sample 26 (88LAD06)							
Length (µm)	Angle	Ns	Ni	Zeta	rhoD	Nd	Cl wt%
Not available	Not available	1	40	351 ± 40	1.40E+06	4000	0.02 - 0.13
		2	30				
		4	77				
		4	100				
		2	53				
		3	63				
		1	22				
		5	85				
		1	8				
		4	25				
		6	85				
		1	28				
		1	14				
		1	20				
		7	82				
		2	62				
		12	136				
		3	38				
		3	96				
		1	52				

Appendix 3: HeFTy Output Models

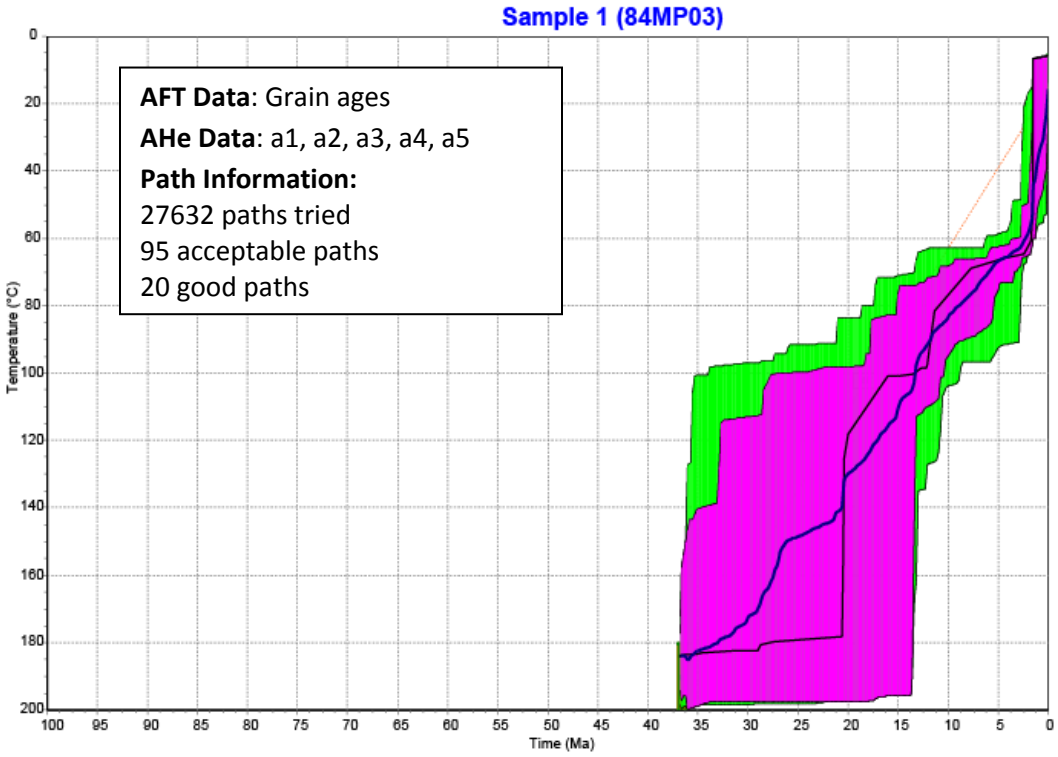

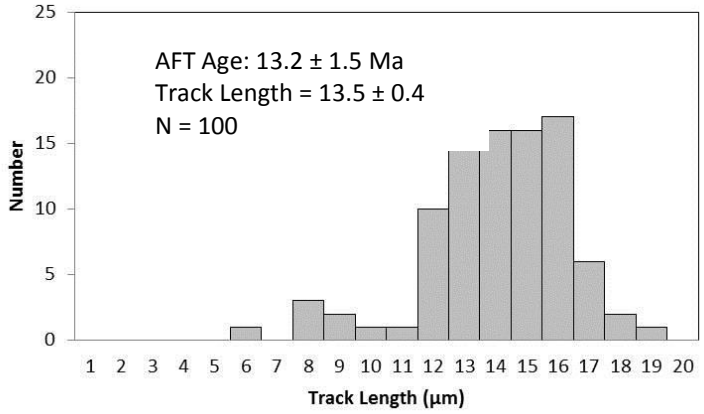

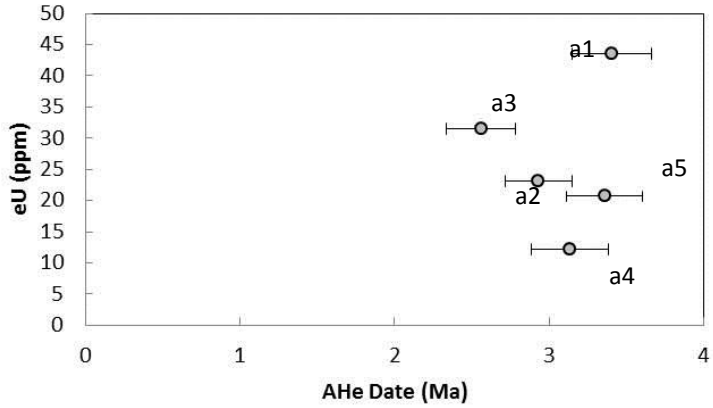

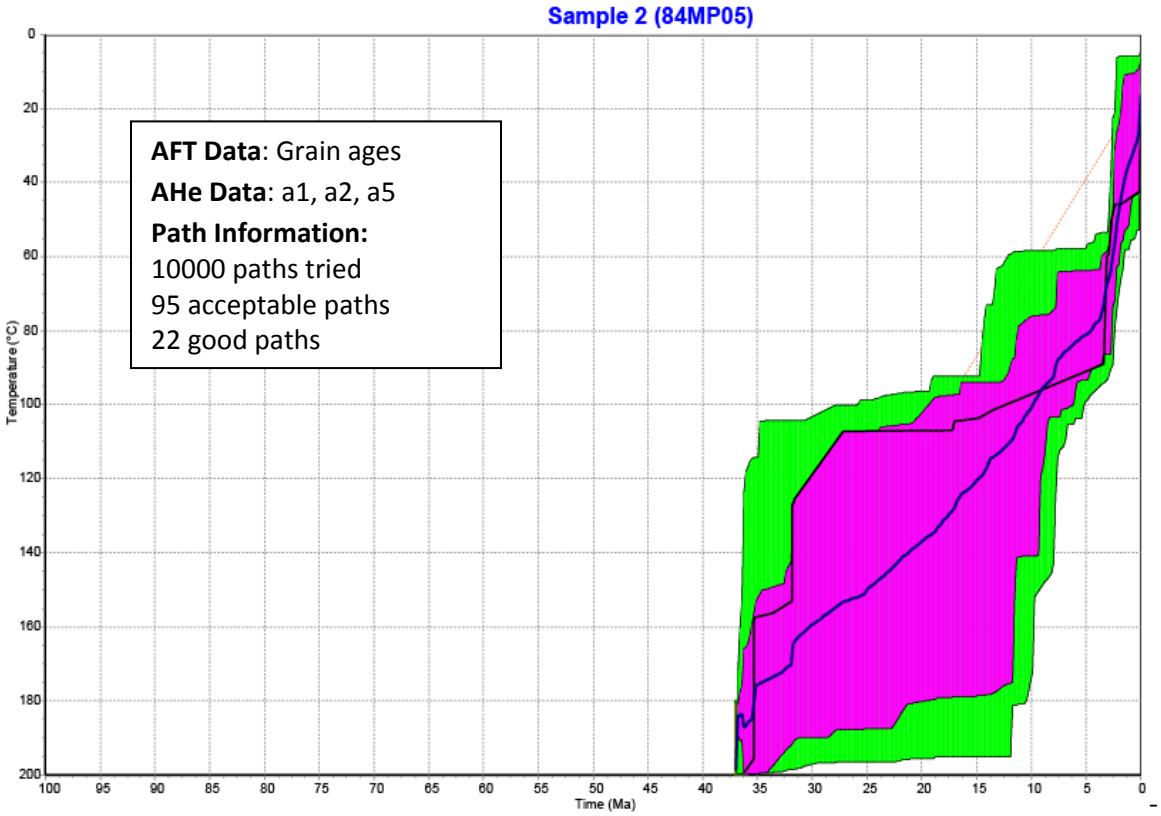
Sample 2 (84MP05)
AFT Data: Grain ages
AHe Data: a1, a2, a5
Path Information:
10000 paths tried
95 acceptable paths
22 good paths
Temperature (°C)
Time (Ma)

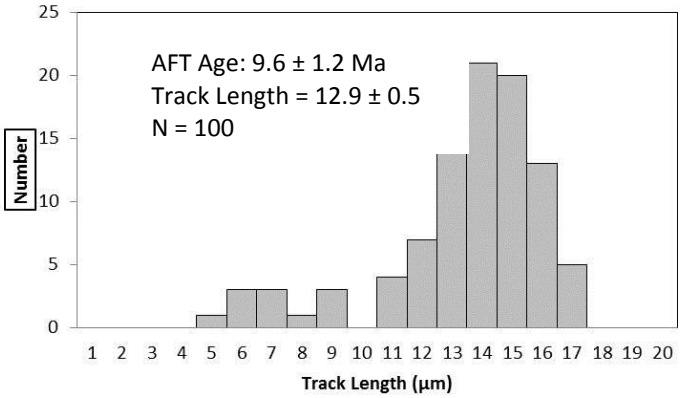
AFT Age: 9.6 ± 1.2 Ma
Track Length = 12.9 ± 0.5
N = 100
Number
Track Length (µm)

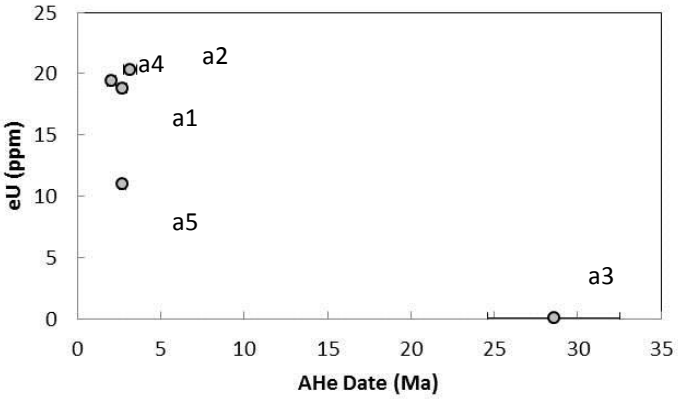
a4
a2
a1
a5
a3
eU (ppm)
AHe Date (Ma)

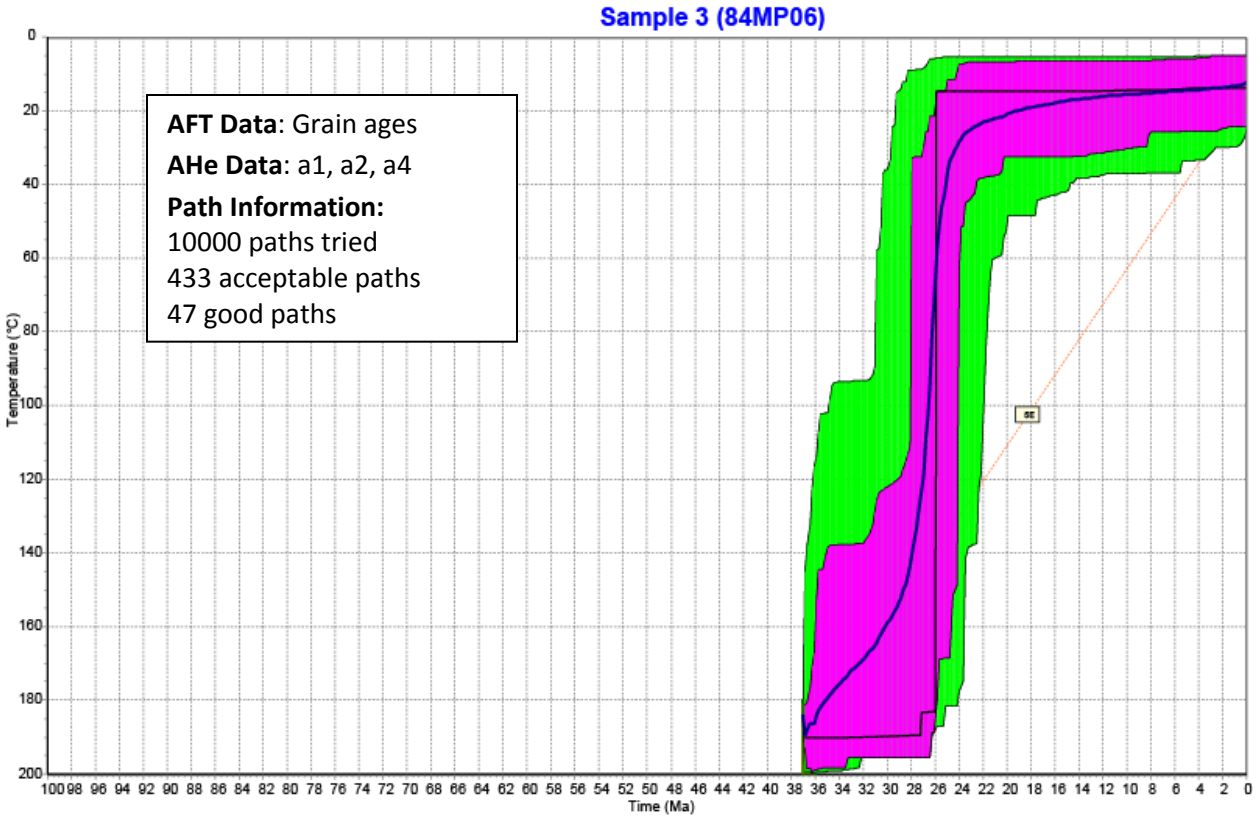
Sample 3 (84MP06)
AFT Data: Grain ages
AHe Data: a1, a2, a4
Path Information:
10000 paths tried
433 acceptable paths
47 good paths
Temperature (°C)
Time (Ma)

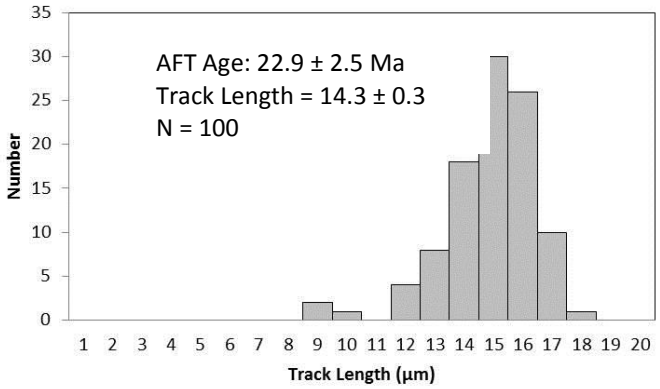
AFT Age: 22.9 ± 2.5 Ma
Track Length = 14.3 ± 0.3
N = 100
Number
Track Length (µm)

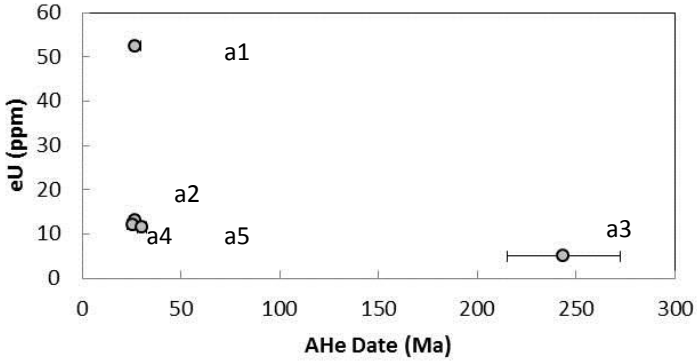
a1
a2
a3
a4
a5
eU (ppm)
AHe Date (Ma)

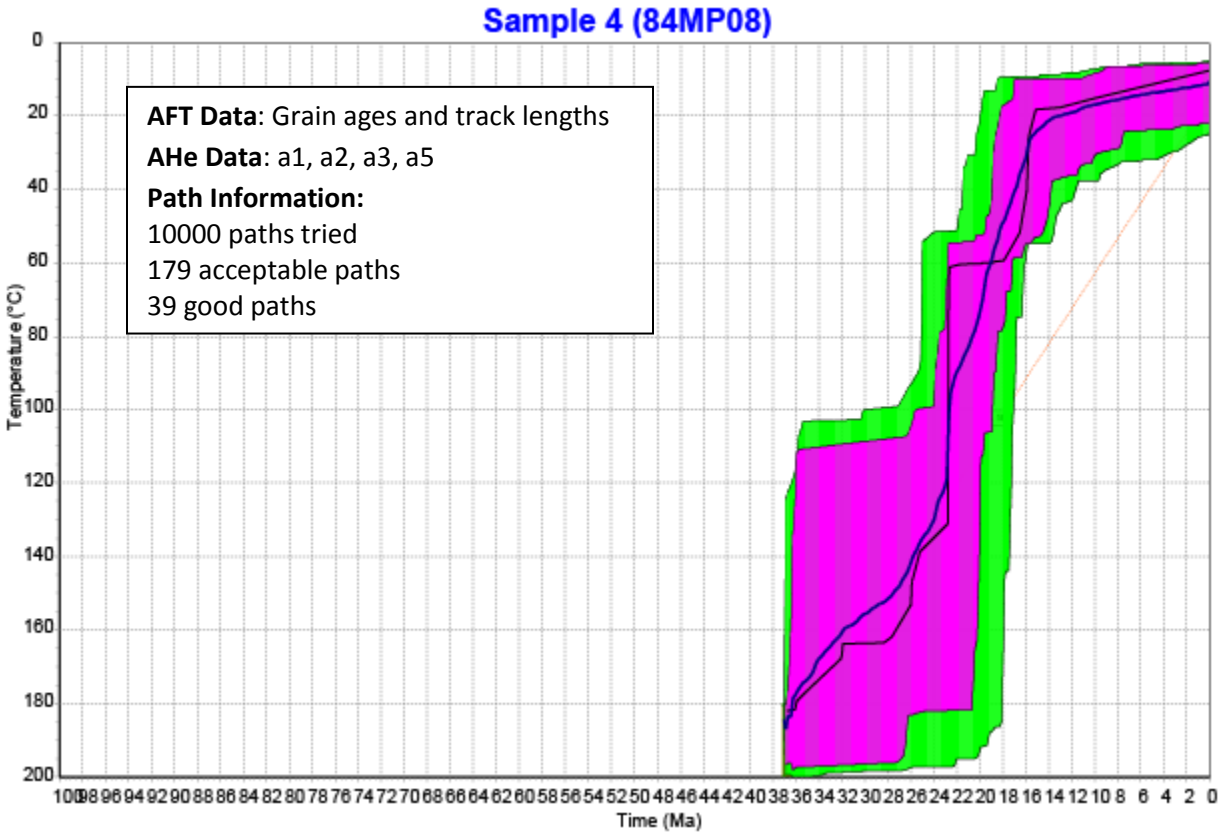
Sample 4 (84MP08)
AFT Data: Grain ages and track lengths
AHe Data: a1, a2, a3, a5
Path Information:
10000 paths tried
179 acceptable paths
39 good paths
Temperature (°C)
Time (Ma)

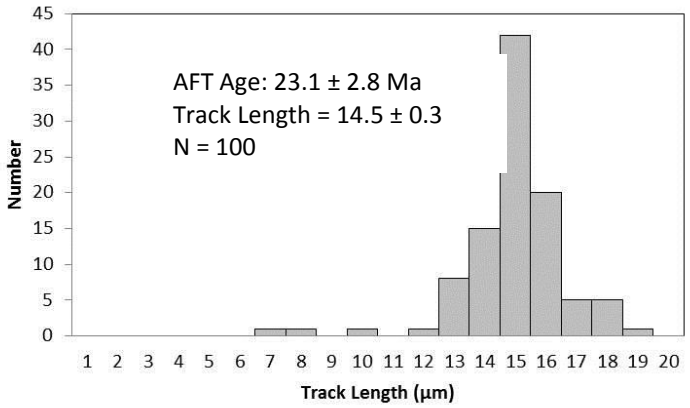
AFT Age: 23.1 ± 2.8 Ma
Track Length = 14.5 ± 0.3
N = 100
Number
Track Length (µm)

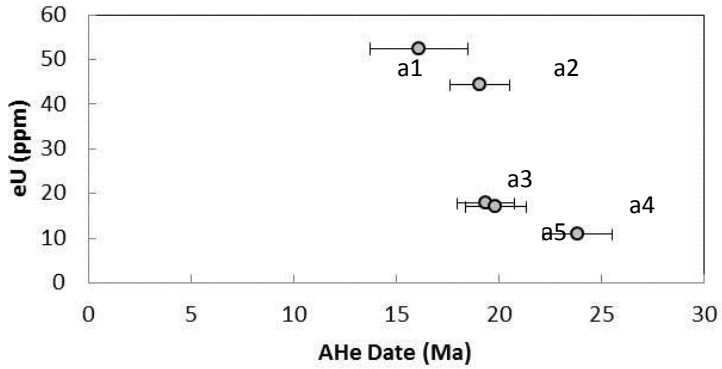
a1
a2
a3
a4
a5
eU (ppm)
AHe Date (Ma)

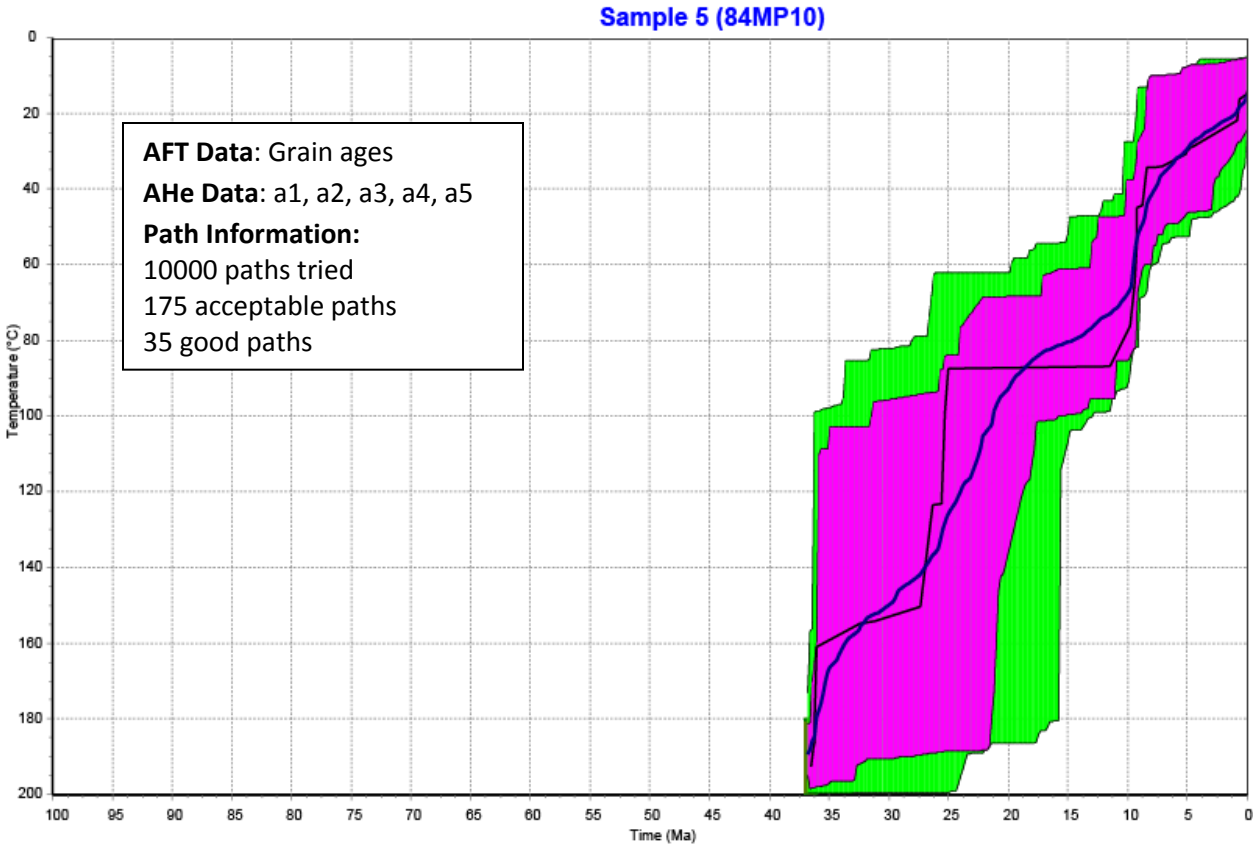
Sample 5 (84MP10)
AFT Data: Grain ages
AHe Data: a1, a2, a3, a4, a5
Path Information:
10000 paths tried
175 acceptable paths
35 good paths
Temperature (°C)
Time (Ma)

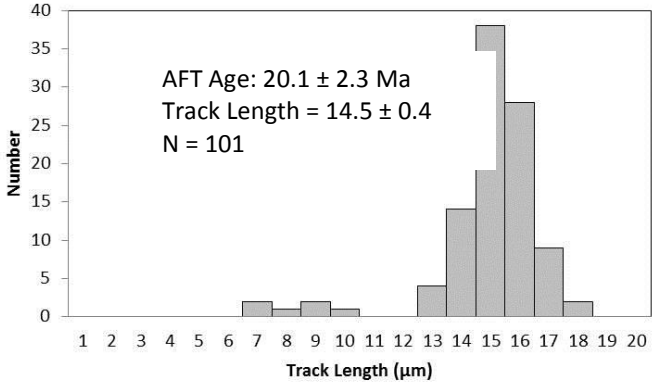
AFT Age: 20.1 ± 2.3 Ma
Track Length = 14.5 ± 0.4
N = 101
Number
Track Length (µm)

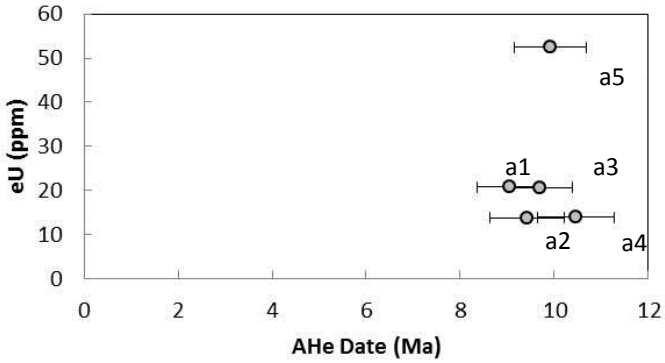
a5
a1
a3
a2
a4
eU (ppm)
AHe Date (Ma)

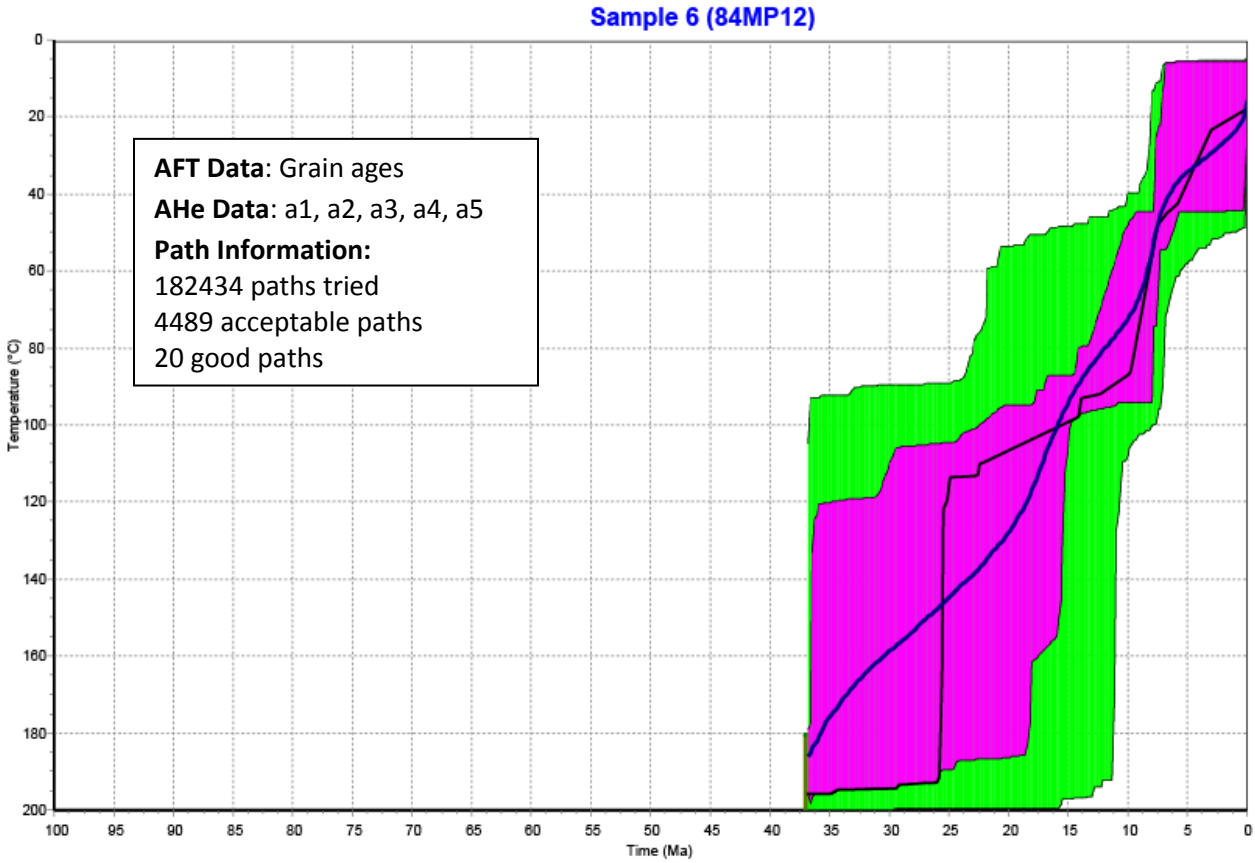
Sample 6 (84MP12)
AFT Data: Grain ages
AHe Data: a1, a2, a3, a4, a5
Path Information:
182434 paths tried
4489 acceptable paths
20 good paths
Temperature (°C)
Time (Ma)

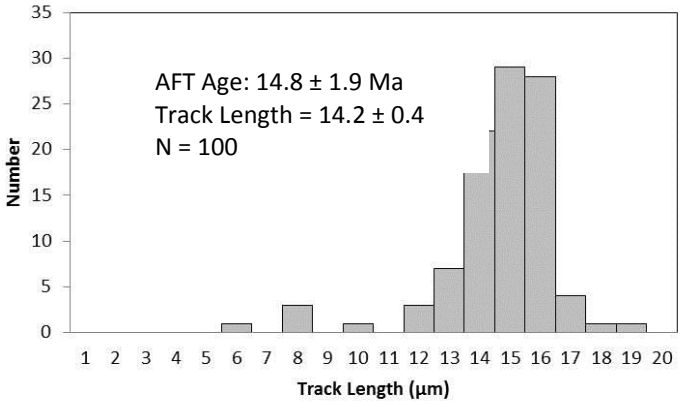
AFT Age: 14.8 ± 1.9 Ma
Track Length = 14.2 ± 0.4
N = 100
Number
Track Length (µm)

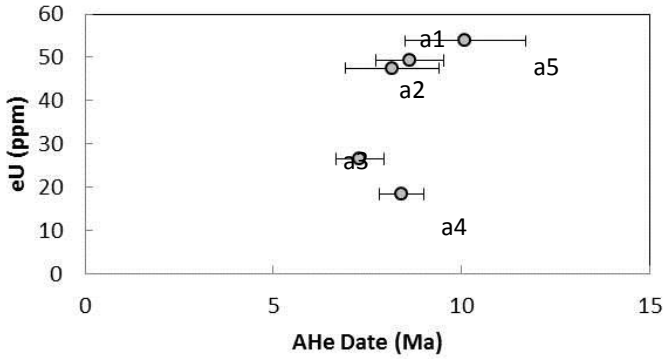
a1
a5
a2
a3
a4
eU (ppm)
AHe Date (Ma)

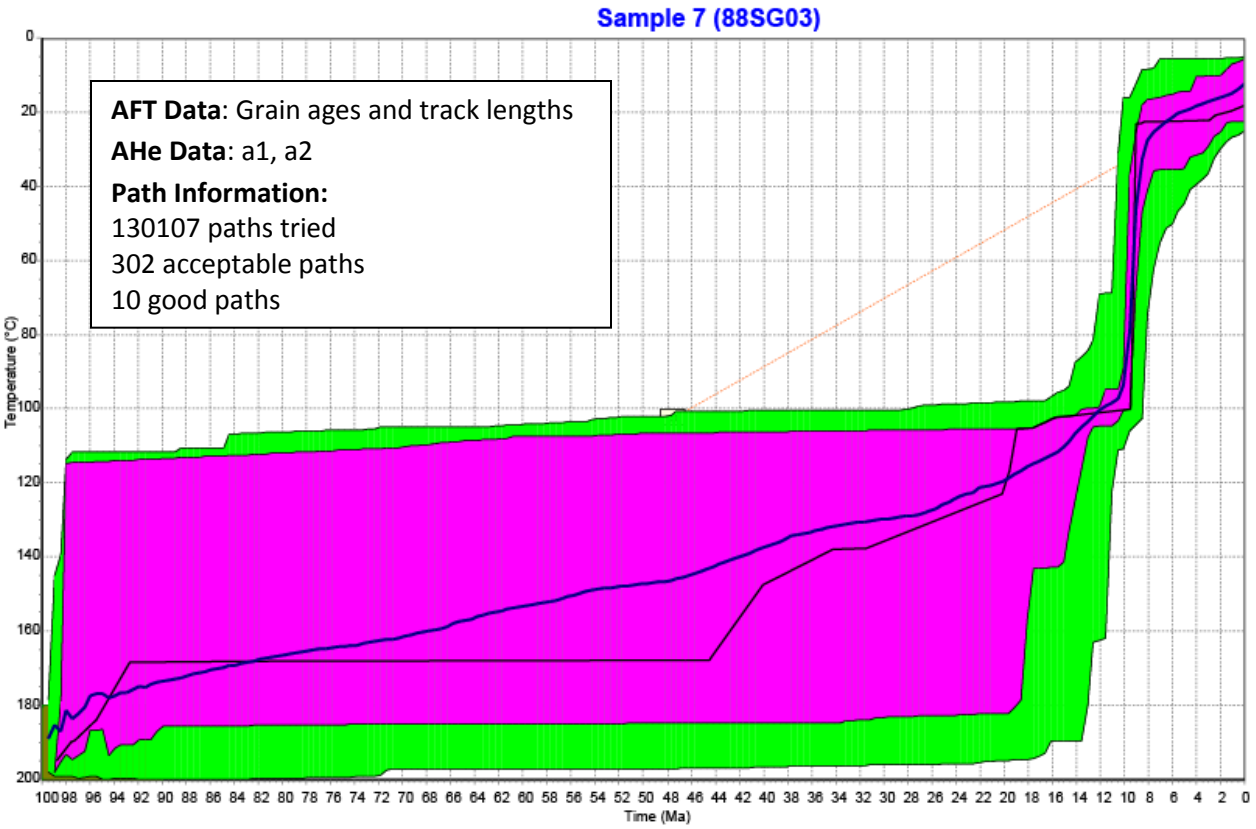
Sample 7 (88SG03)
AFT Data: Grain ages and track lengths
AHe Data: a1, a2
Path Information:
130107 paths tried
302 acceptable paths
10 good paths
Temperature (°C)
Time (Ma)

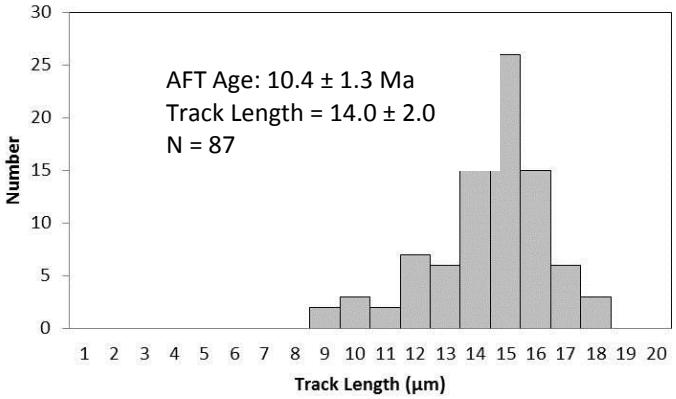
AFT Age: 10.4 ± 1.3 Ma
Track Length = 14.0 ± 2.0
N = 87
Number
Track Length (µm)

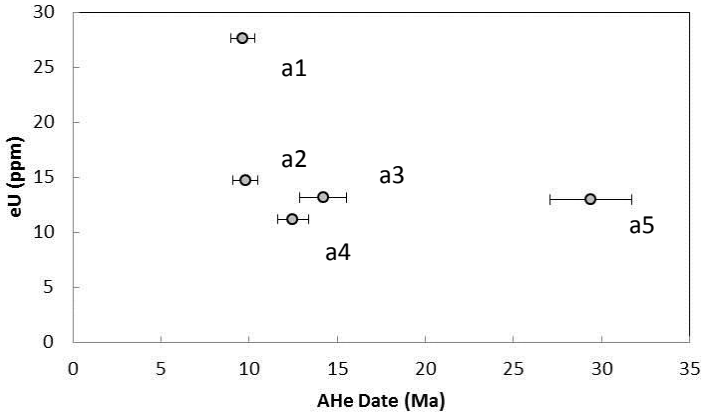
a1
a2
a3
a4
a5
eU (ppm)
AHe Date (Ma)

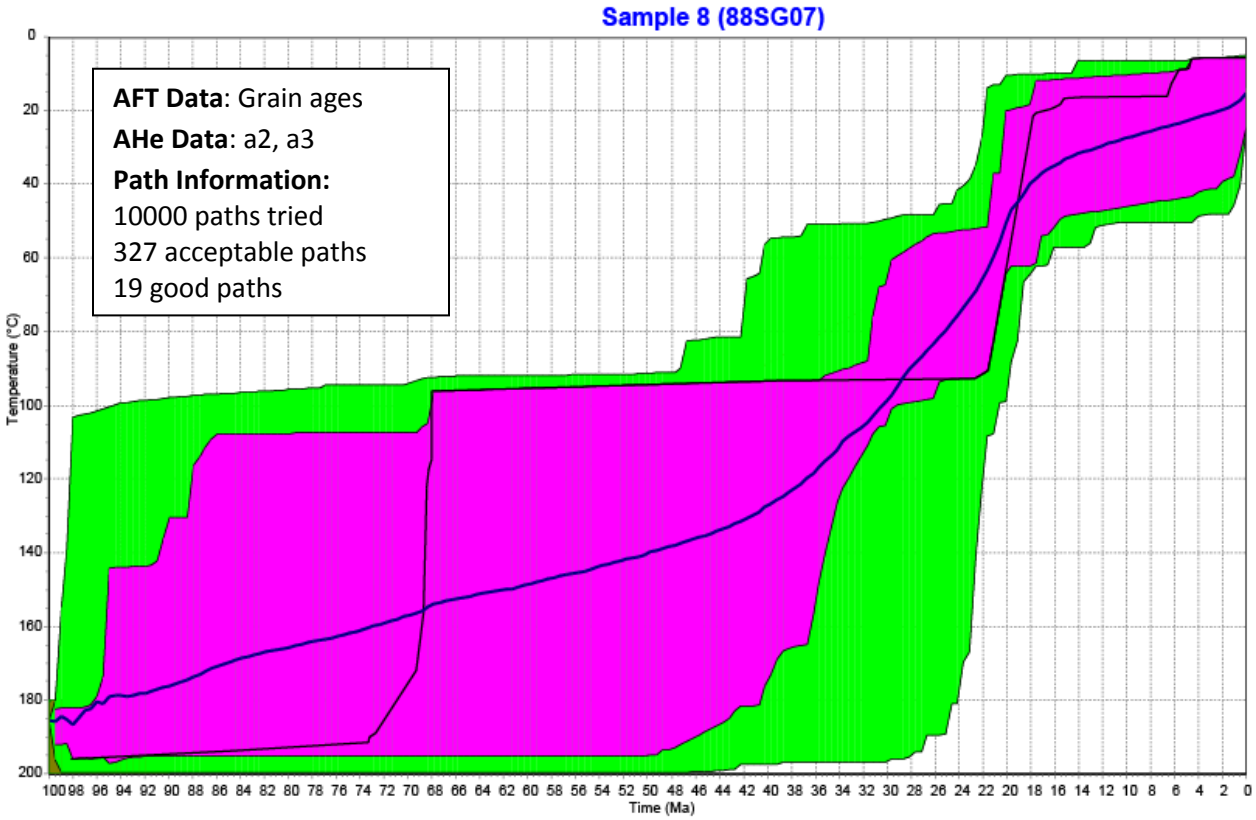
Sample 8 (88SG07)
AFT Data: Grain ages
AHe Data: a2, a3
Path Information:
10000 paths tried
327 acceptable paths
19 good paths
Temperature (°C)
Time (Ma)

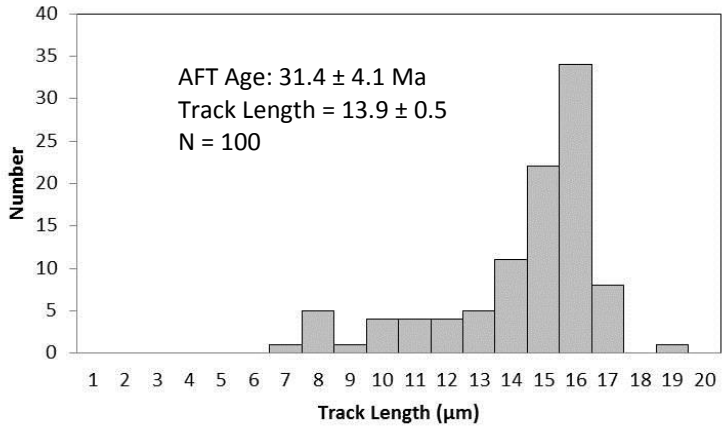
AFT Age: 31.4 ± 4.1 Ma
Track Length = 13.9 ± 0.5
N = 100
Number
Track Length (µm)

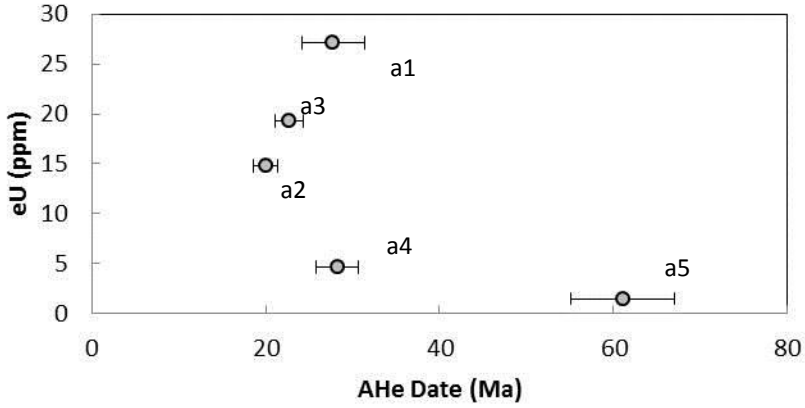
a1
a3
a2
a4
a5
eU (ppm)
AHe Date (Ma)

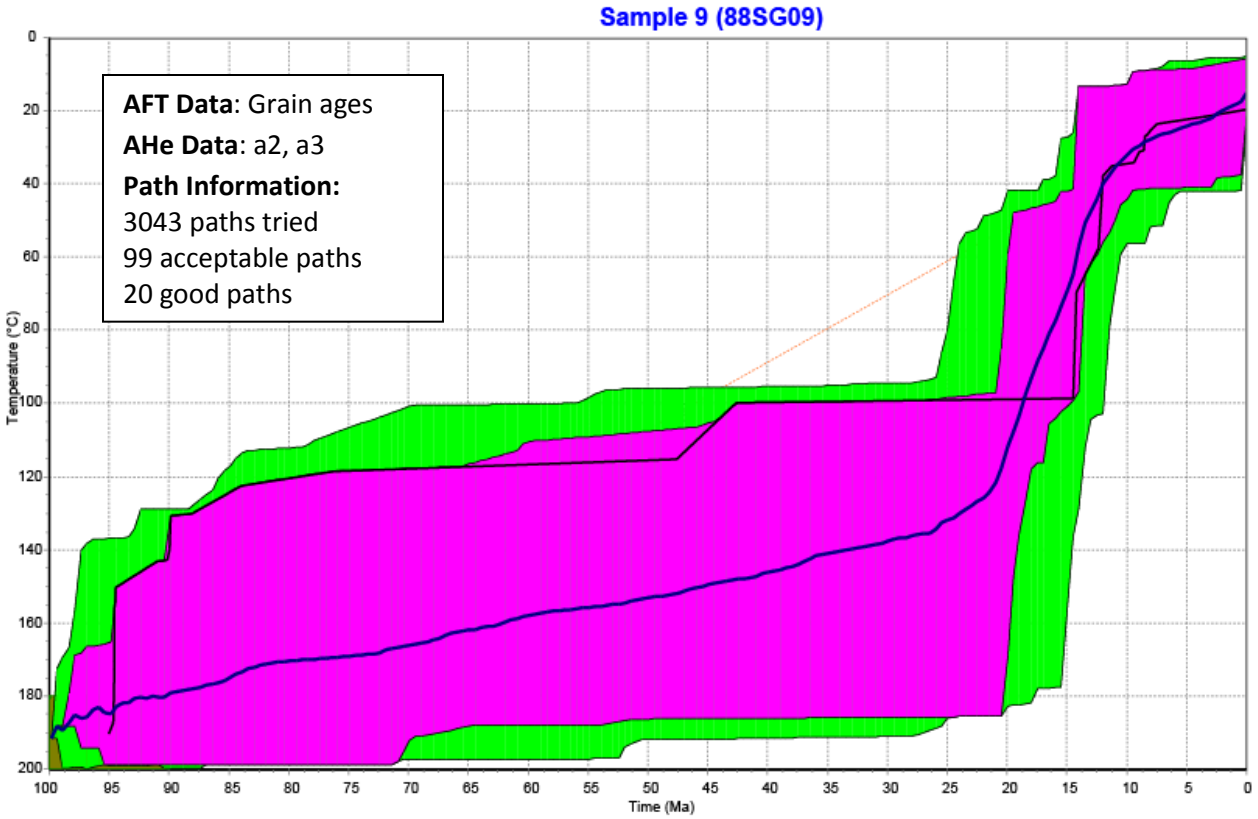
Sample 9 (88SG09)
AFT Data: Grain ages
AHe Data: a2, a3
Path Information:
3043 paths tried
99 acceptable paths
20 good paths
Temperature (°C)
Time (Ma)

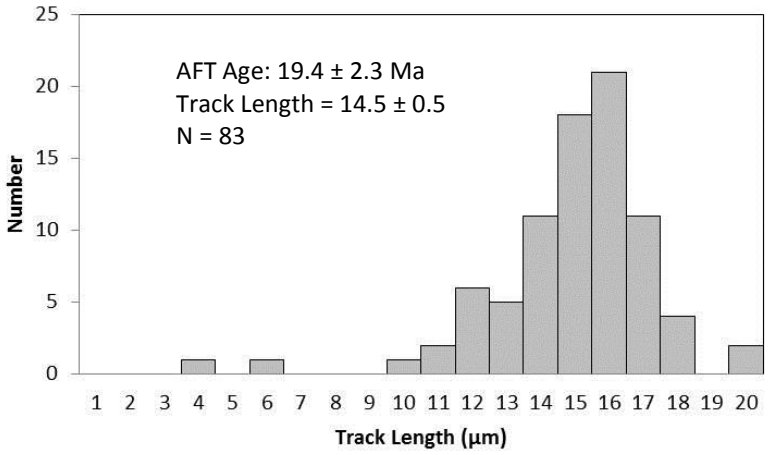
AFT Age: 19.4 ± 2.3 Ma
Track Length = 14.5 ± 0.5
N = 83
Number
Track Length (µm)

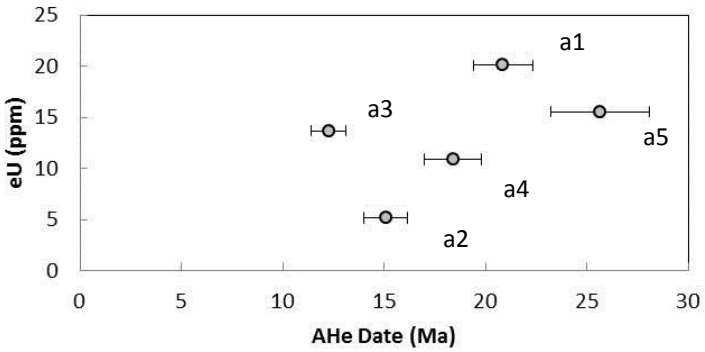
a1
a3
a5
a4
a2
eU (ppm)
AHe Date (Ma)

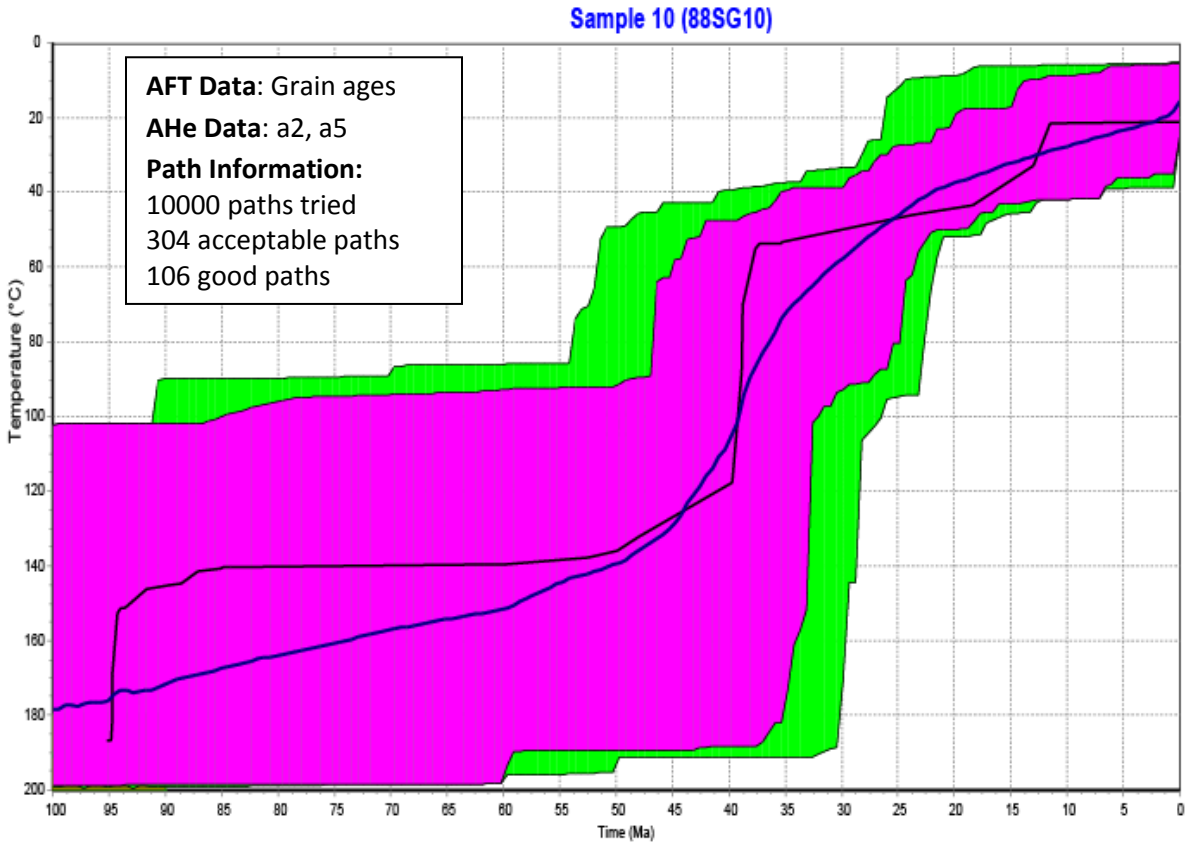
Sample 10 (88SG10)
AFT Data: Grain ages
AHe Data: a2, a5
Path Information:
10000 paths tried
304 acceptable paths
106 good paths
Temperature (°C)
Time (Ma)

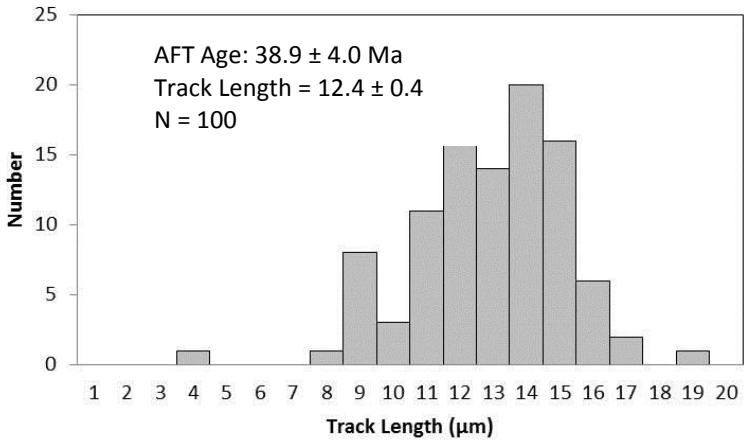
AFT Age: 38.9 ± 4.0 Ma
Track Length = 12.4 ± 0.4
N = 100
Number
Track Length (µm)

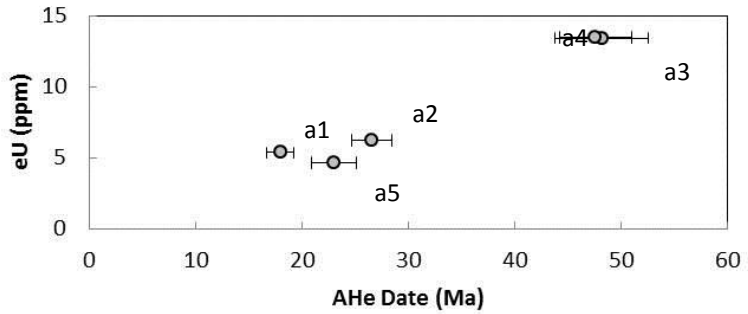
a1
a2
a3
a4
a5
eU (ppm)
AHe Date (Ma)

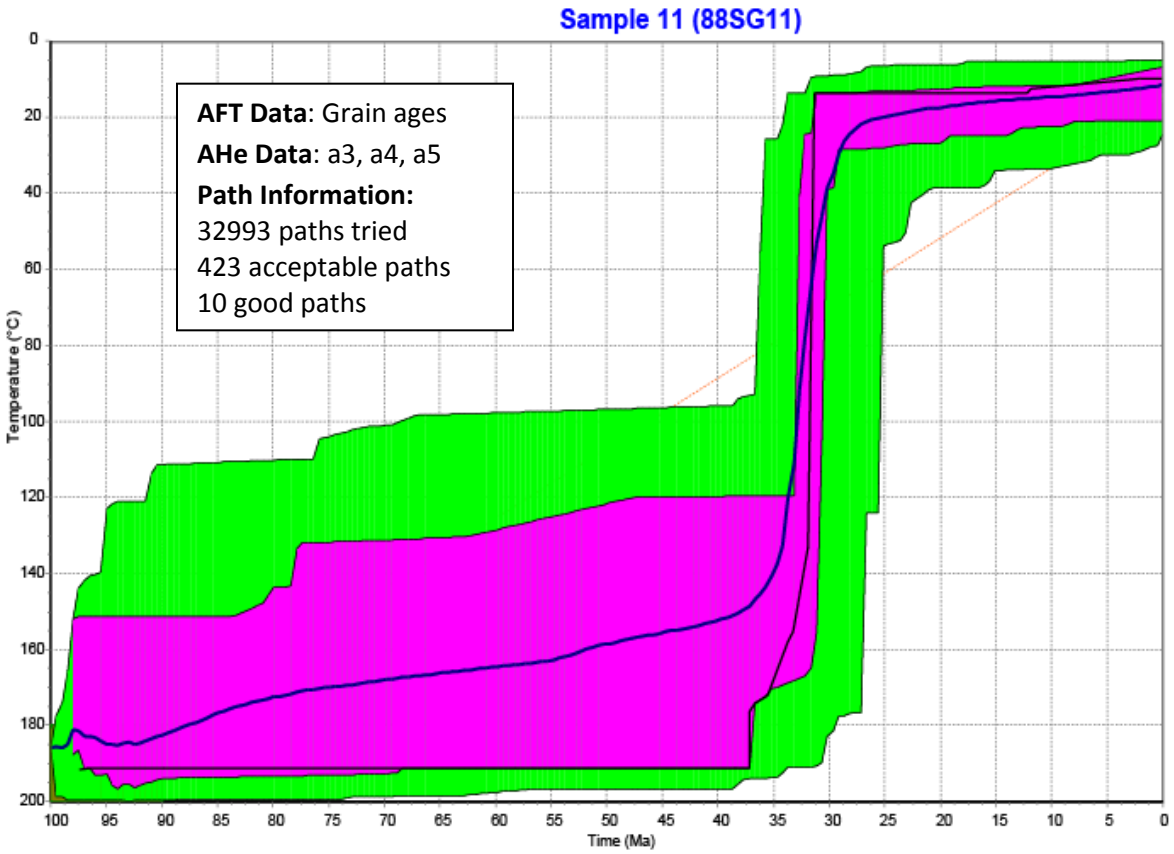
Sample 11 (88SG11)
AFT Data: Grain ages
AHe Data: a3, a4, a5
Path Information:
32993 paths tried
423 acceptable paths
10 good paths
Temperature (°C)
Time (Ma)

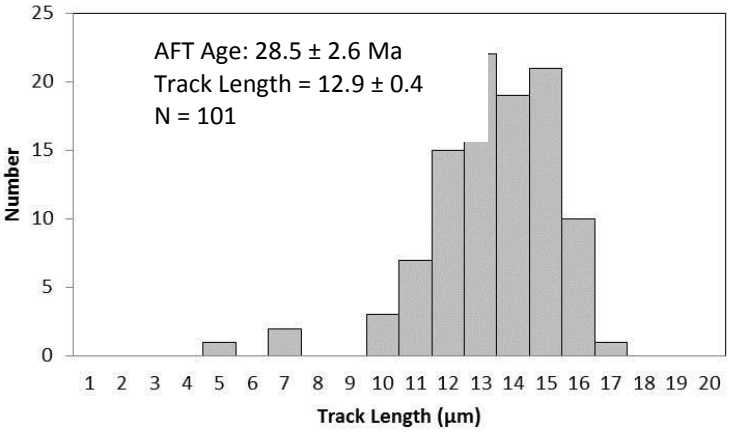
AFT Age: 28.5 ± 2.6 Ma
Track Length = 12.9 ± 0.4
N = 101
Number
Track Length (µm)

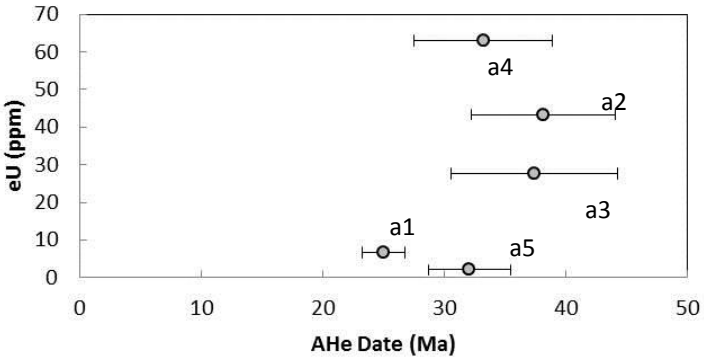
a4
a2
a3
a1
a5
eU (ppm)
AHe Date (Ma)

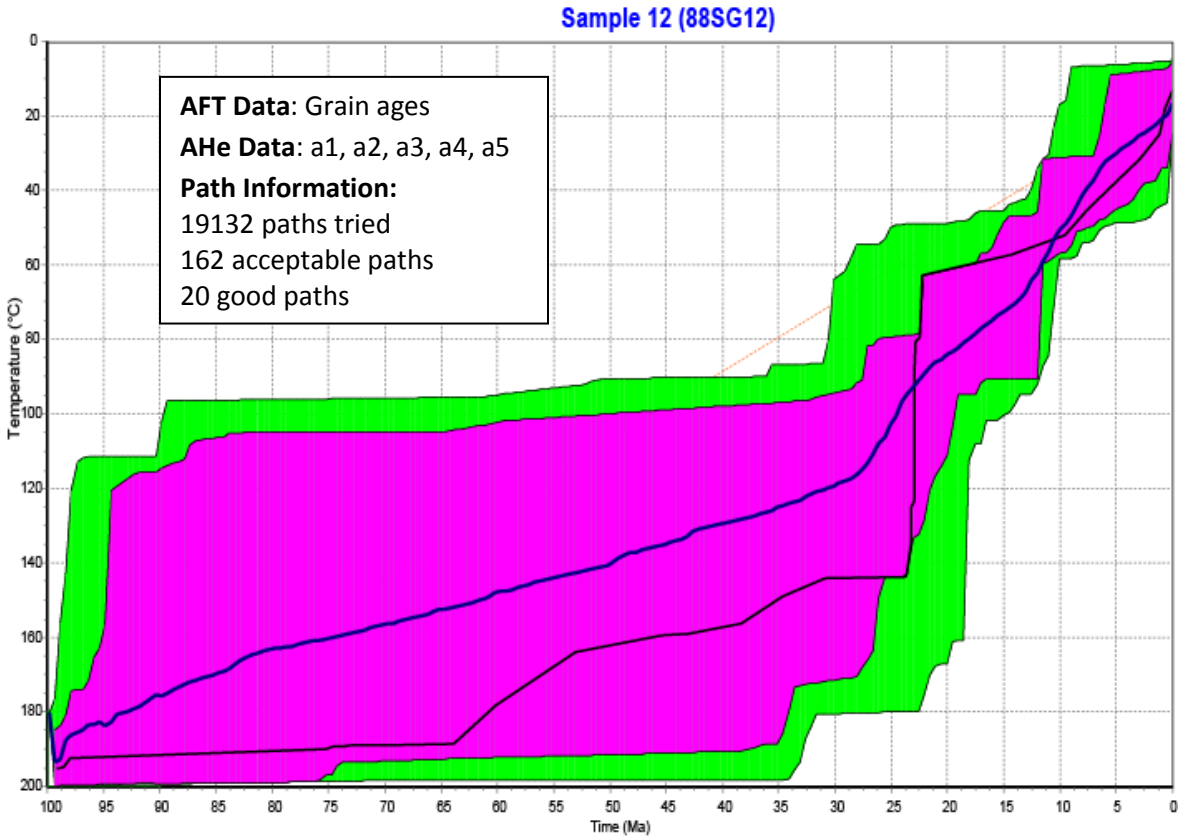
Sample 12 (88SG12)
AFT Data: Grain ages
AHe Data: a1, a2, a3, a4, a5
Path Information:
19132 paths tried
162 acceptable paths
20 good paths
Temperature (°C)
Time (Ma)

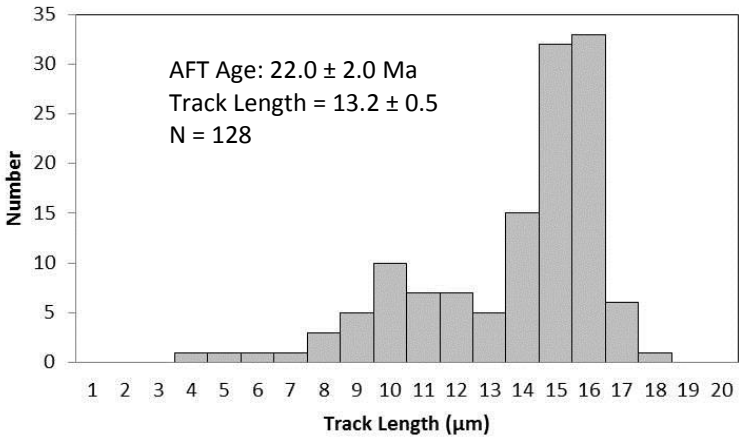
AFT Age: 22.0 ± 2.0 Ma
Track Length = 13.2 ± 0.5
N = 128
Number
Track Length (µm)

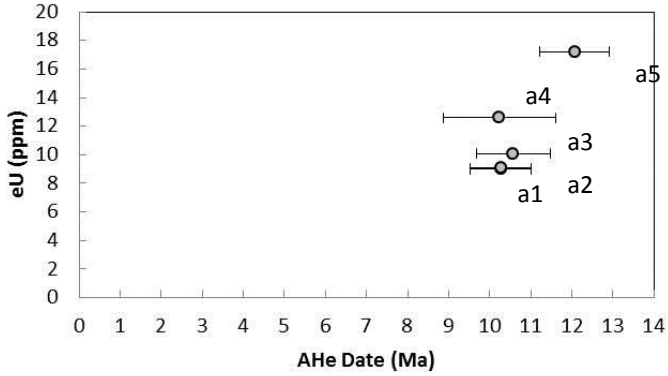
a5
a4
a3
a2
a1
eU (ppm)
AHe Date (Ma)

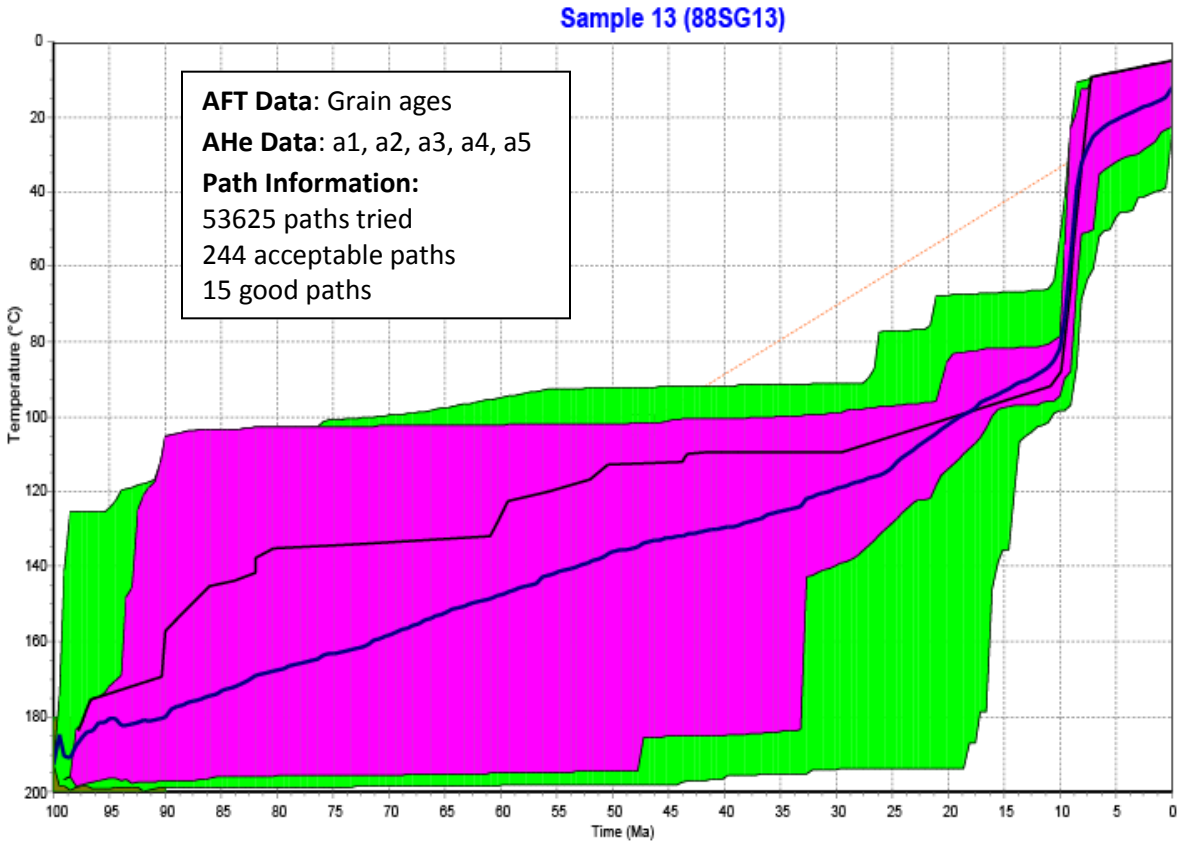
Sample 13 (88SG13)
AFT Data: Grain ages
AHe Data: a1, a2, a3, a4, a5
Path Information:
53625 paths tried
244 acceptable paths
15 good paths
Temperature (°C)
Time (Ma)

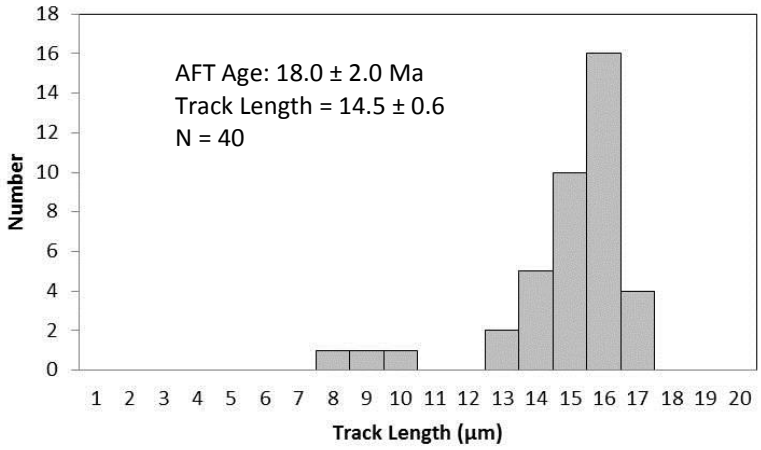
AFT Age: 18.0 ± 2.0 Ma
Track Length = 14.5 ± 0.6
N = 40
Number
Track Length (µm)

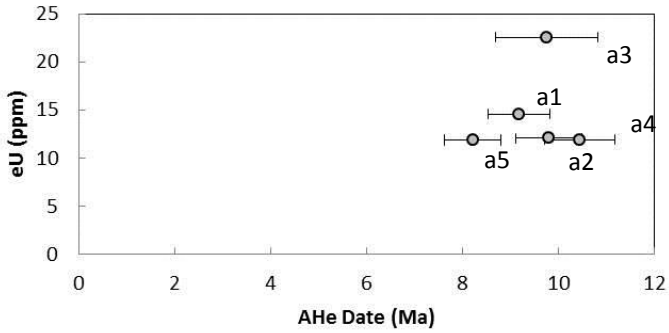
a3
a1
a4
a5
a2
eU (ppm)
AHe Date (Ma)

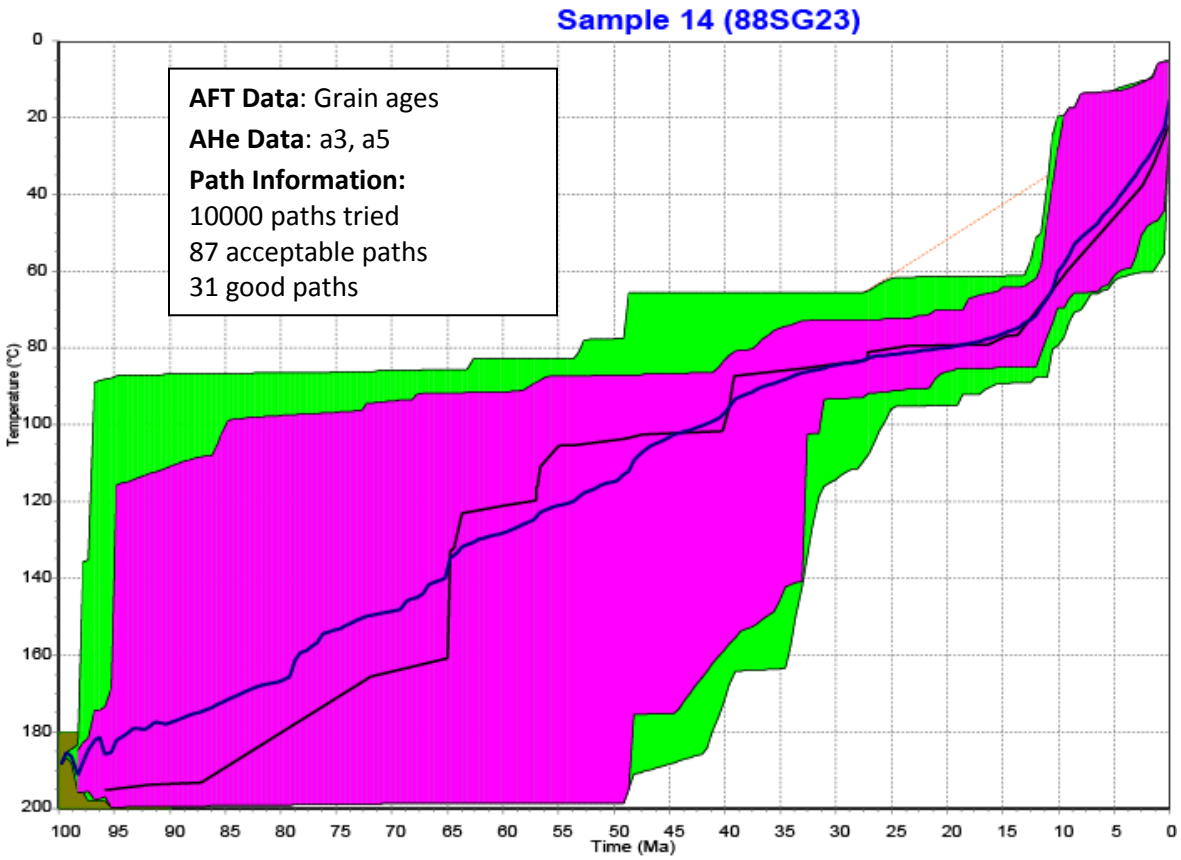
Sample 14 (88SG23)
AFT Data: Grain ages
AHe Data: a3, a5
Path Information:
10000 paths tried
87 acceptable paths
31 good paths
Temperature (°C)
Time (Ma)

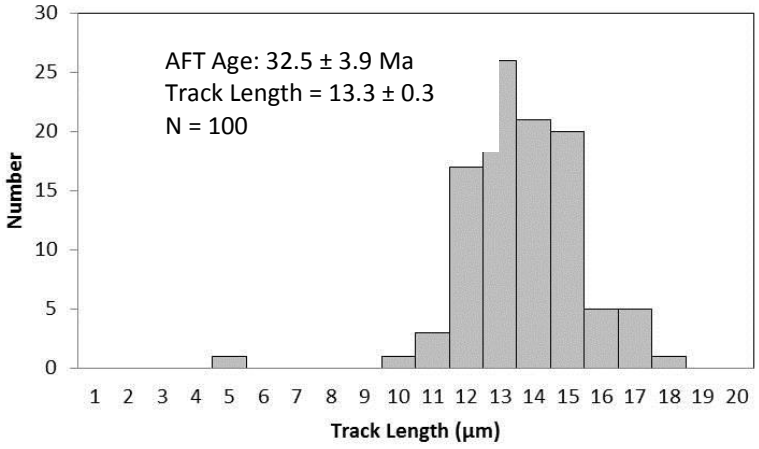
AFT Age: 32.5 ± 3.9 Ma
Track Length = 13.3 ± 0.3
N = 100
Number
Track Length (µm)

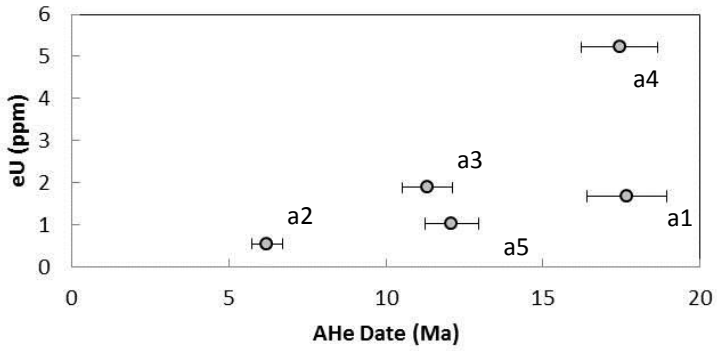
a1
a2
a3
a4
a5
eU (ppm)
AHe Date (Ma)

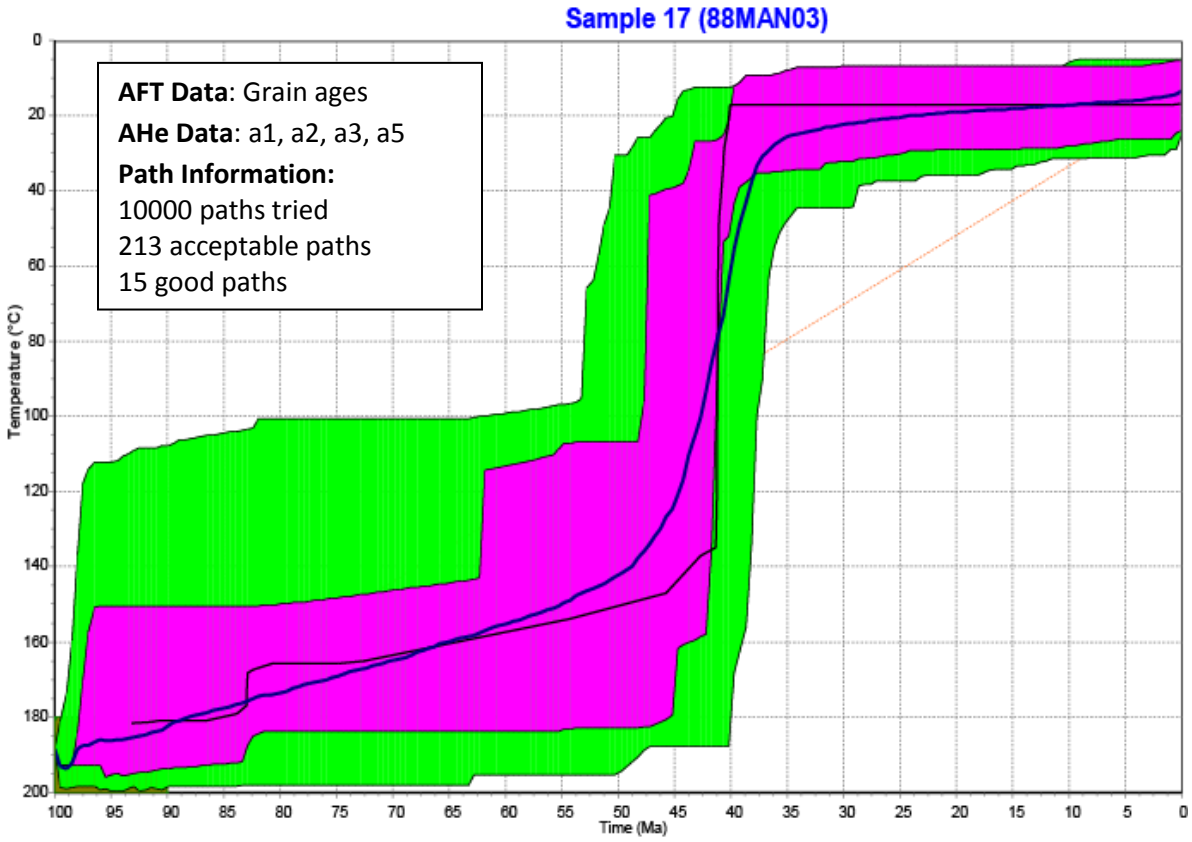
Sample 17 (88MAN03)
AFT Data: Grain ages
AHe Data: a1, a2, a3, a5
Path Information:
10000 paths tried
213 acceptable paths
15 good paths
Temperature (°C)
Time (Ma)

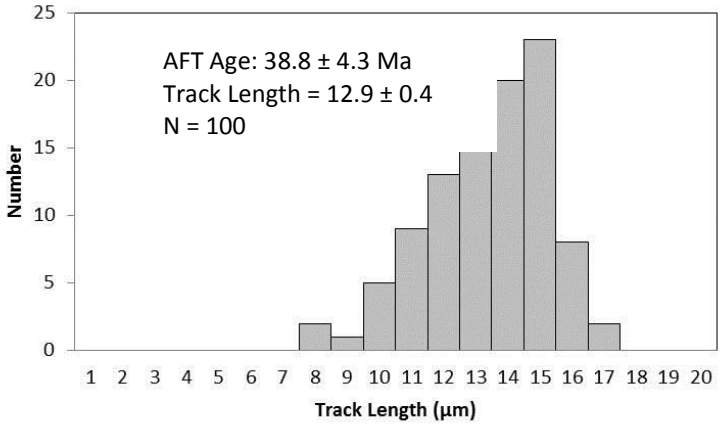
AFT Age: 38.8 ± 4.3 Ma
Track Length = 12.9 ± 0.4
N = 100
Number
Track Length (µm)

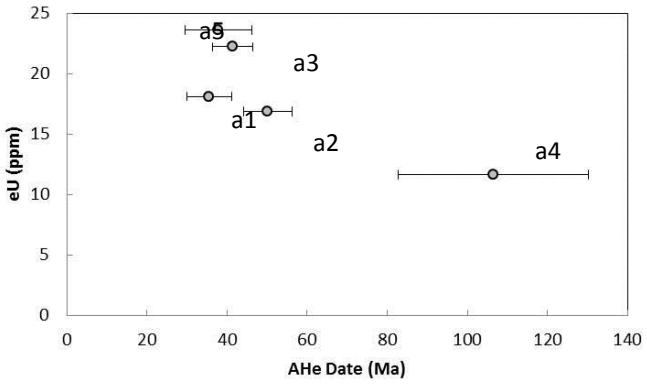
a5
a3
a1
a2
a4
eU (ppm)
AHe Date (Ma)

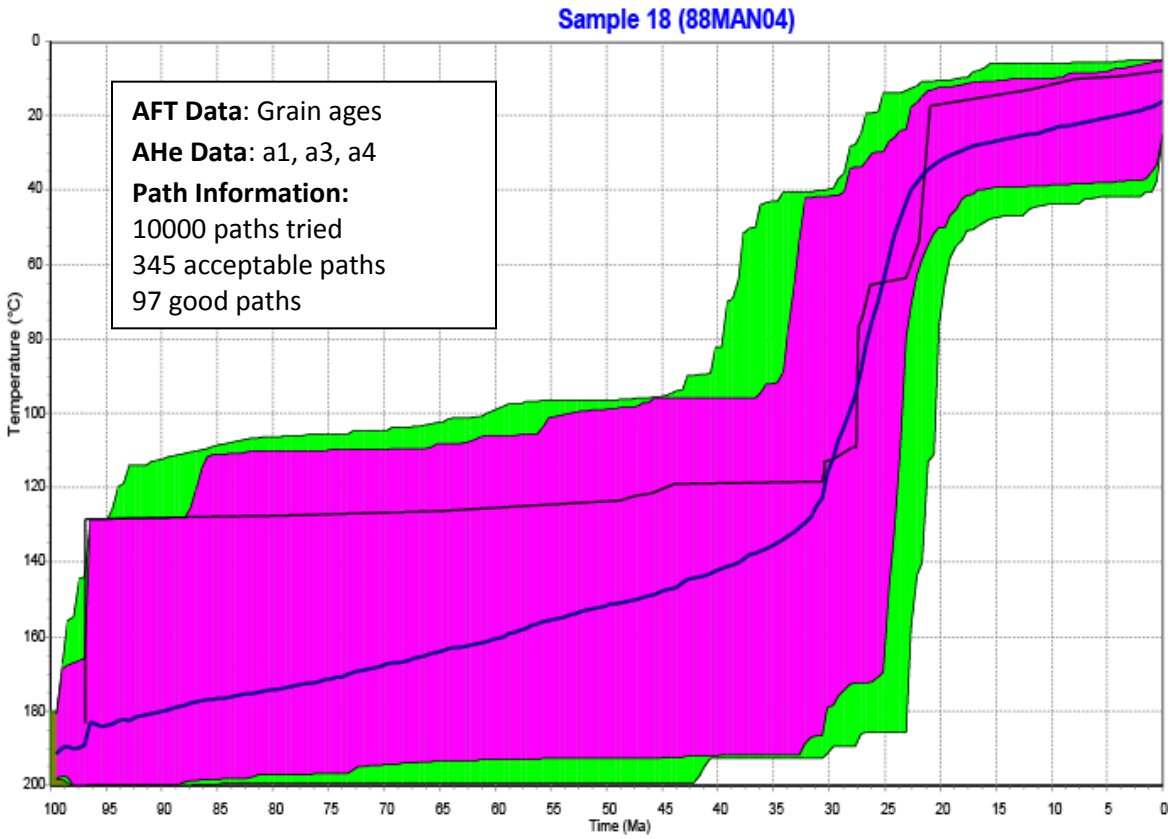
Sample 18 (88MAN04)
AFT Data: Grain ages
AHe Data: a1, a3, a4
Path Information:
10000 paths tried
345 acceptable paths
97 good paths
Temperature (°C)
Time (Ma)

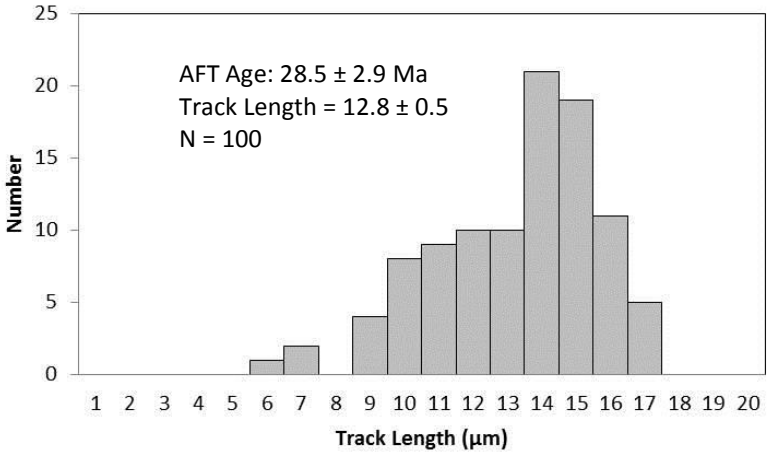
AFT Age: 28.5 ± 2.9 Ma
Track Length = 12.8 ± 0.5
N = 100
Number
Track Length (µm)

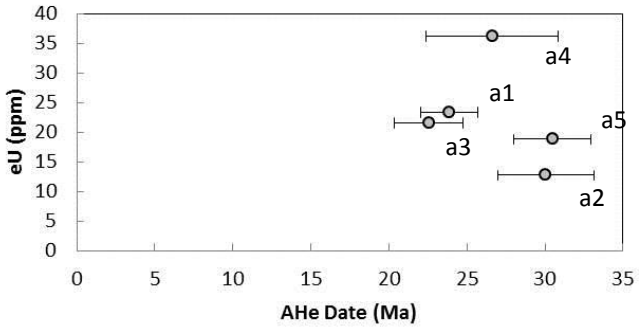
a4
a1
a5
a3
a2
eU (ppm)
AHe Date (Ma)

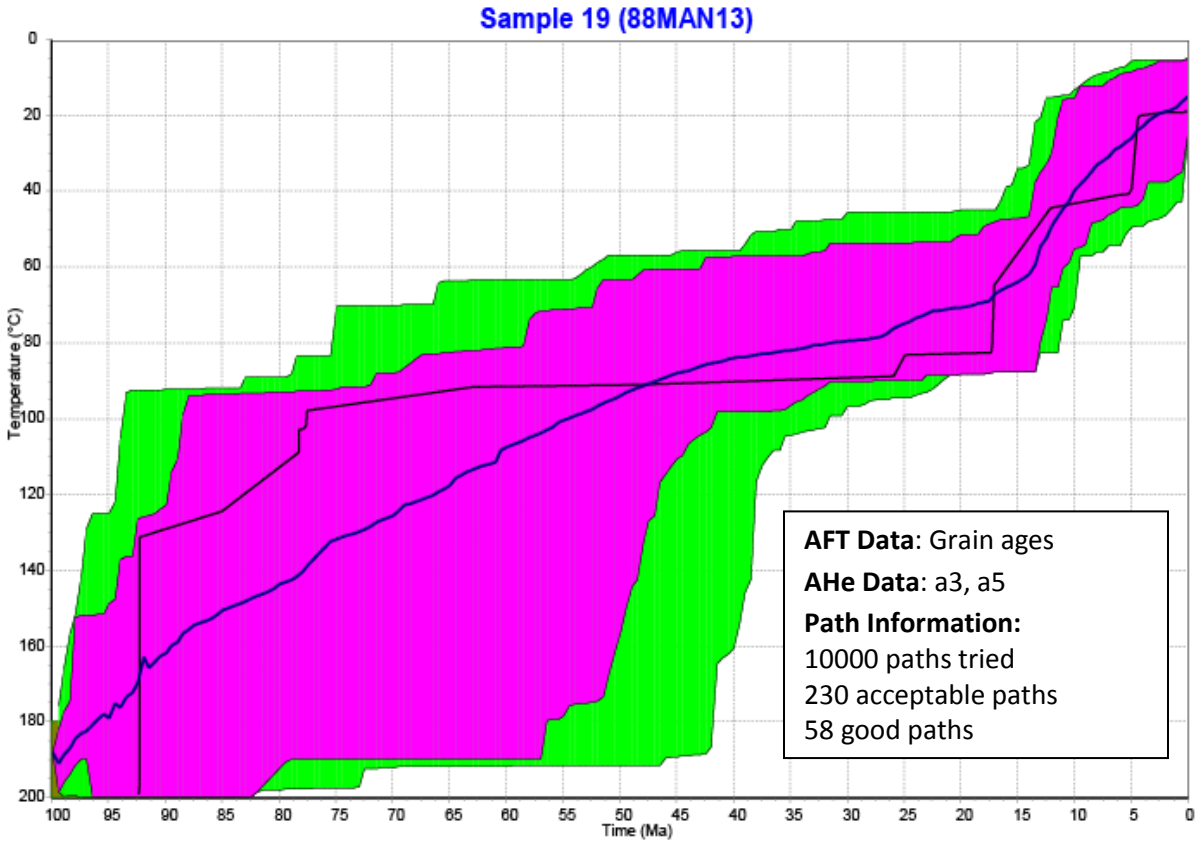
Sample 19 (88MAN13)
Temperature (°C)
Time (Ma)
AFT Data: Grain ages
AHe Data: a3, a5
Path Information:
10000 paths tried
230 acceptable paths
58 good paths

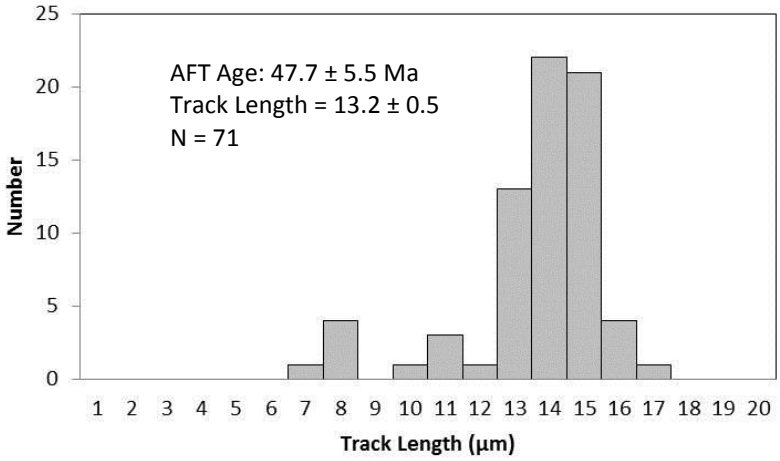
AFT Age: 47.7 ± 5.5 Ma
Track Length = 13.2 ± 0.5
N = 71
Number
Track Length (µm)

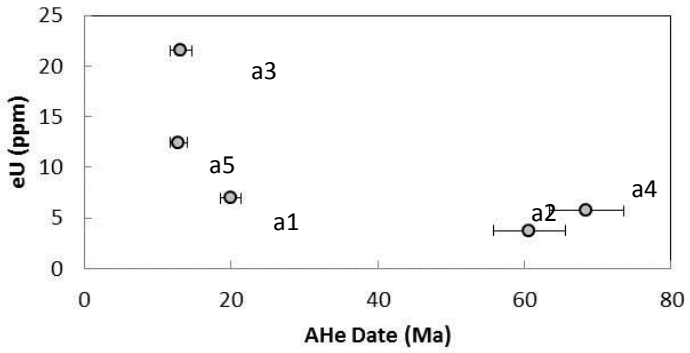
eU (ppm)
AHe Date (Ma)
a1
a2
a3
a4
a5

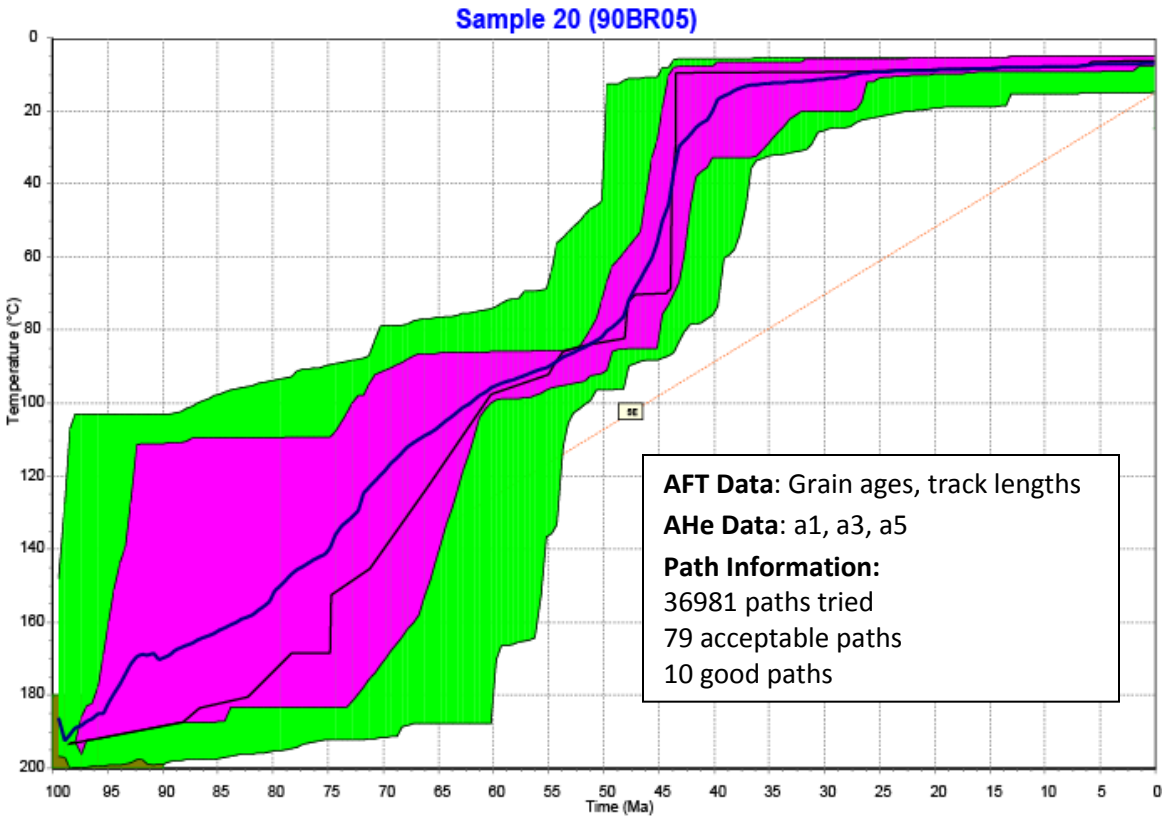
Sample 20 (90BR05)
Temperature (°C)
Time (Ma)
AFT Data: Grain ages, track lengths
AHe Data: a1, a3, a5
Path Information:
36981 paths tried
79 acceptable paths
10 good paths

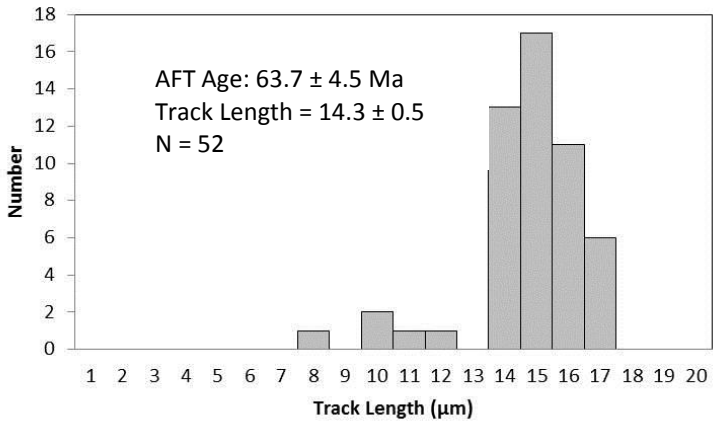
AFT Age: 63.7 ± 4.5 Ma
Track Length = 14.3 ± 0.5
N = 52
Number
Track Length (µm)

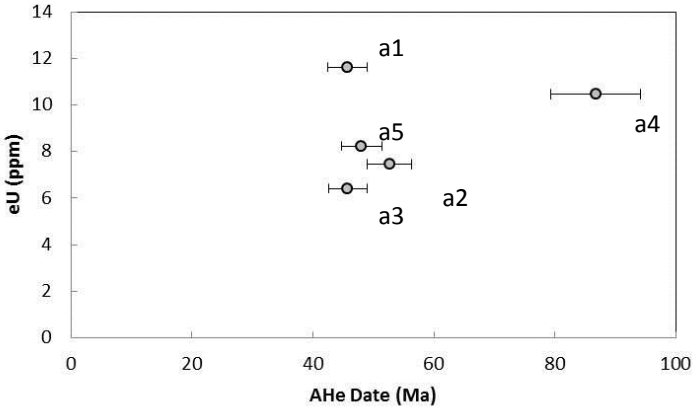
a1
a4
a5
a2
a3
eU (ppm)
AHe Date (Ma)

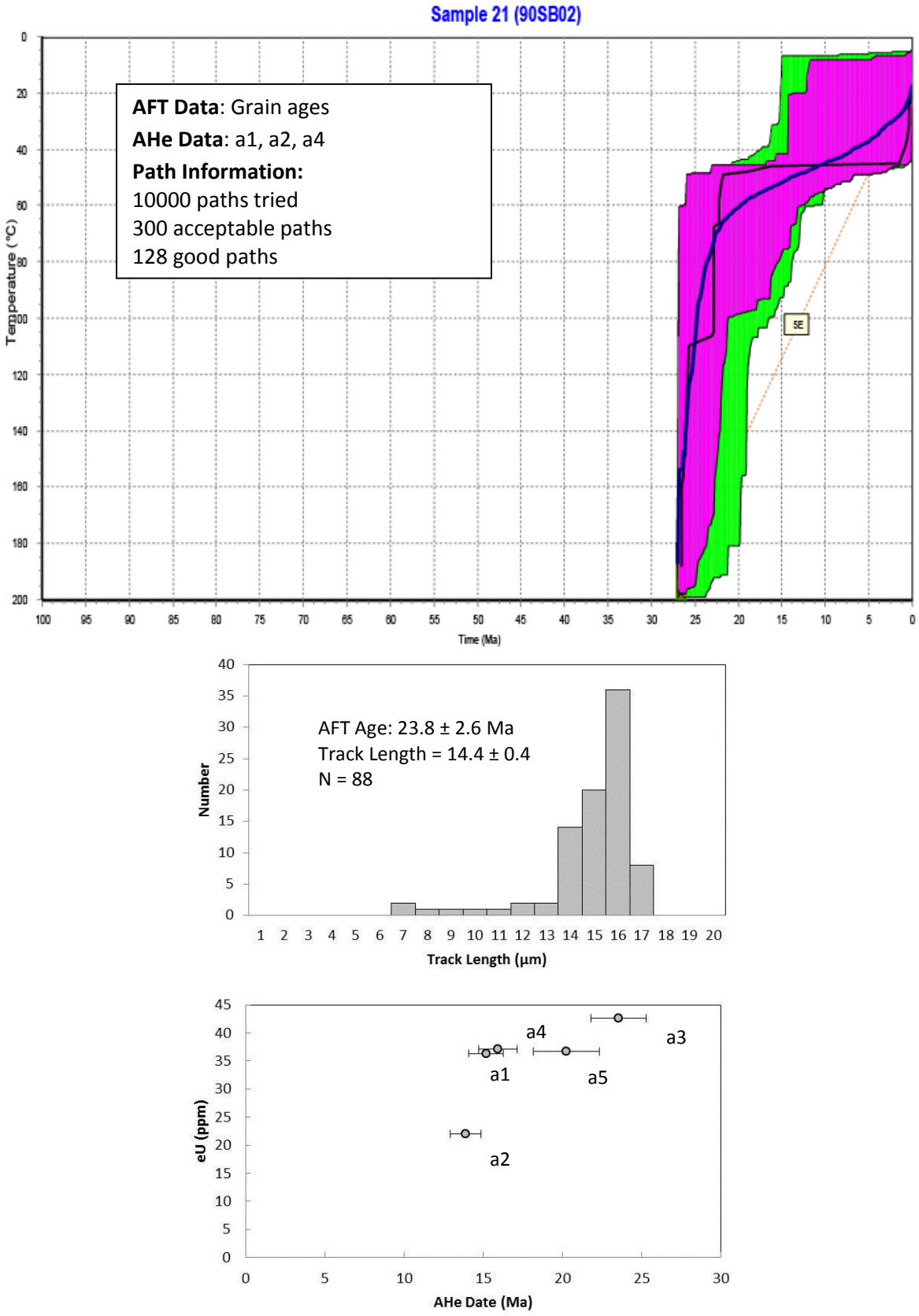
Sample 21 (90SB02)
AFT Data: Grain ages
AHe Data: a1, a2, a4
Path Information:
10000 paths tried
300 acceptable paths
128 good paths
Temperature (°C)
Time (Ma)
AFT Age: 23.8 ± 2.6 Ma
Track Length = 14.4 ± 0.4
N = 88
Number
Track Length (µm)
a1
a2
a3
a4
a5
eU (ppm)
AHe Date (Ma)

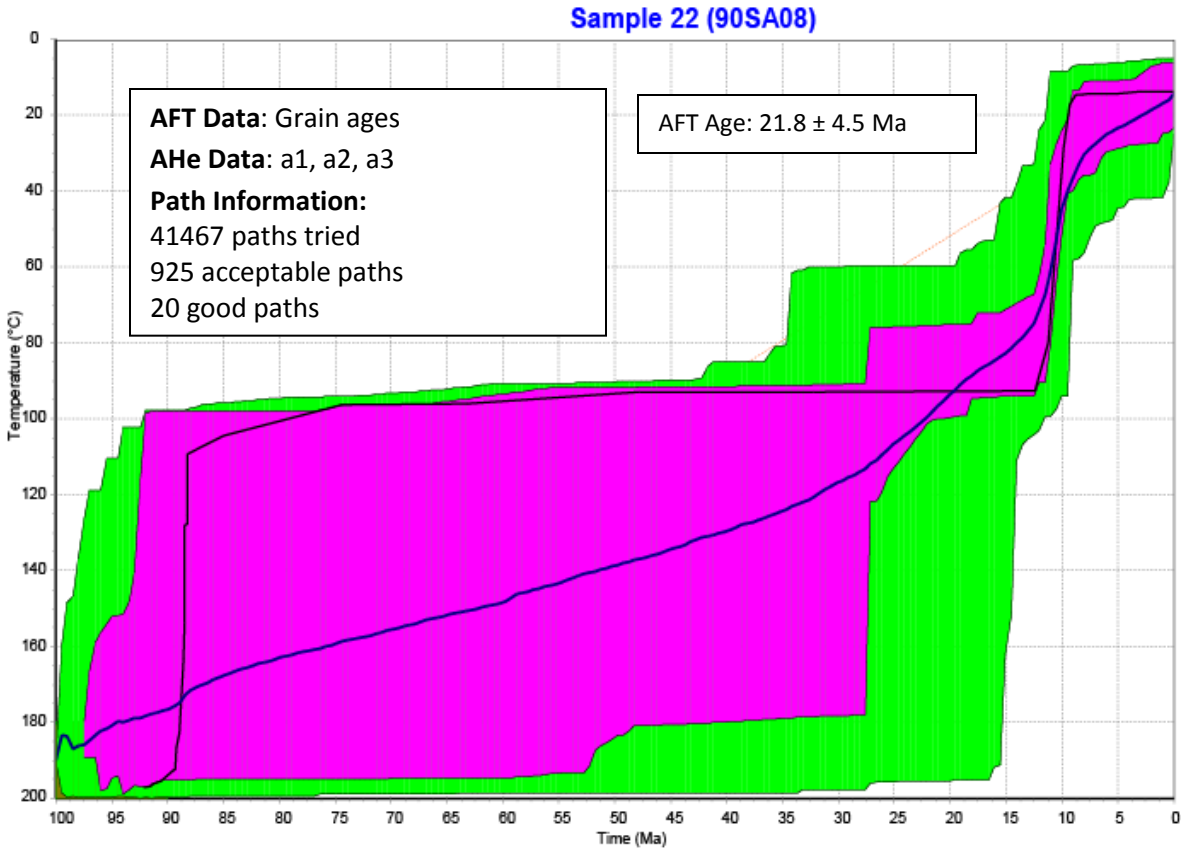
Sample 22 (90SA08)
AFT Data: Grain ages
AHe Data: a1, a2, a3
Path Information:
41467 paths tried
925 acceptable paths
20 good paths
AFT Age: 21.8 ± 4.5 Ma
Temperature (°C)
Time (Ma)

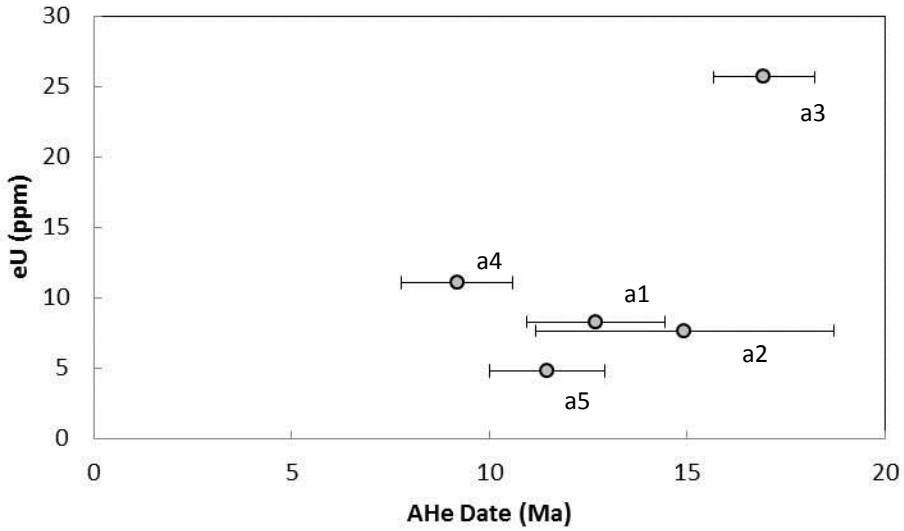
eU (ppm)
AHe Date (Ma)
a3
a4
a1
a2
a5

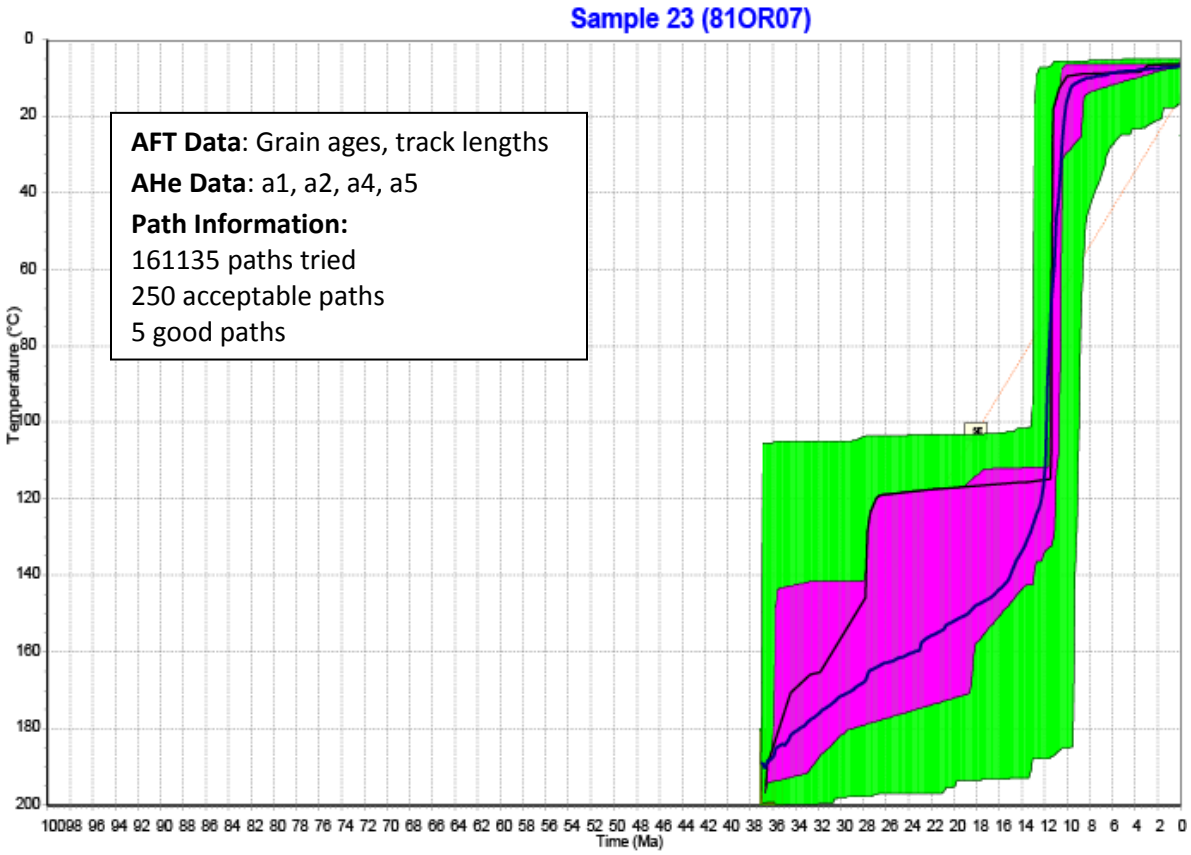
Sample 23 (81OR07)
AFT Data: Grain ages, track lengths
AHe Data: a1, a2, a4, a5
Path Information:
161135 paths tried
250 acceptable paths
5 good paths
Temperature (°C)
Time (Ma)

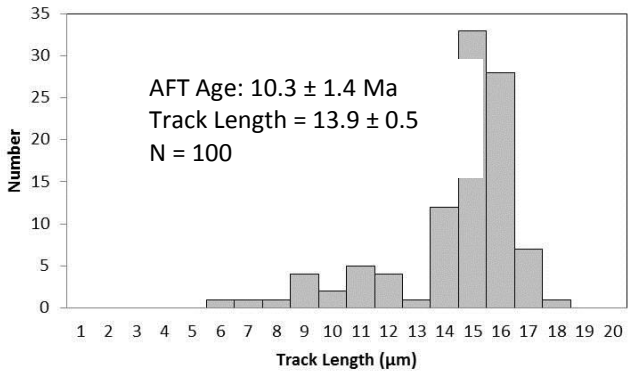
AFT Age: 10.3 ± 1.4 Ma
Track Length = 13.9 ± 0.5
N = 100
Number
Track Length (µm)

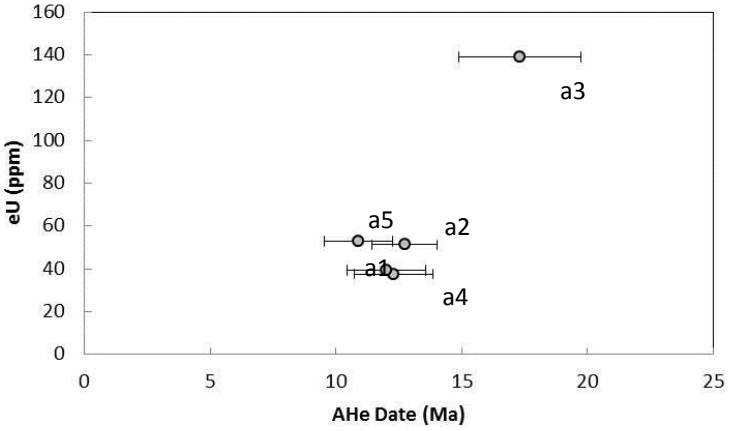
a3
a5
a2
a1
a4
eU (ppm)
AHe Date (Ma)

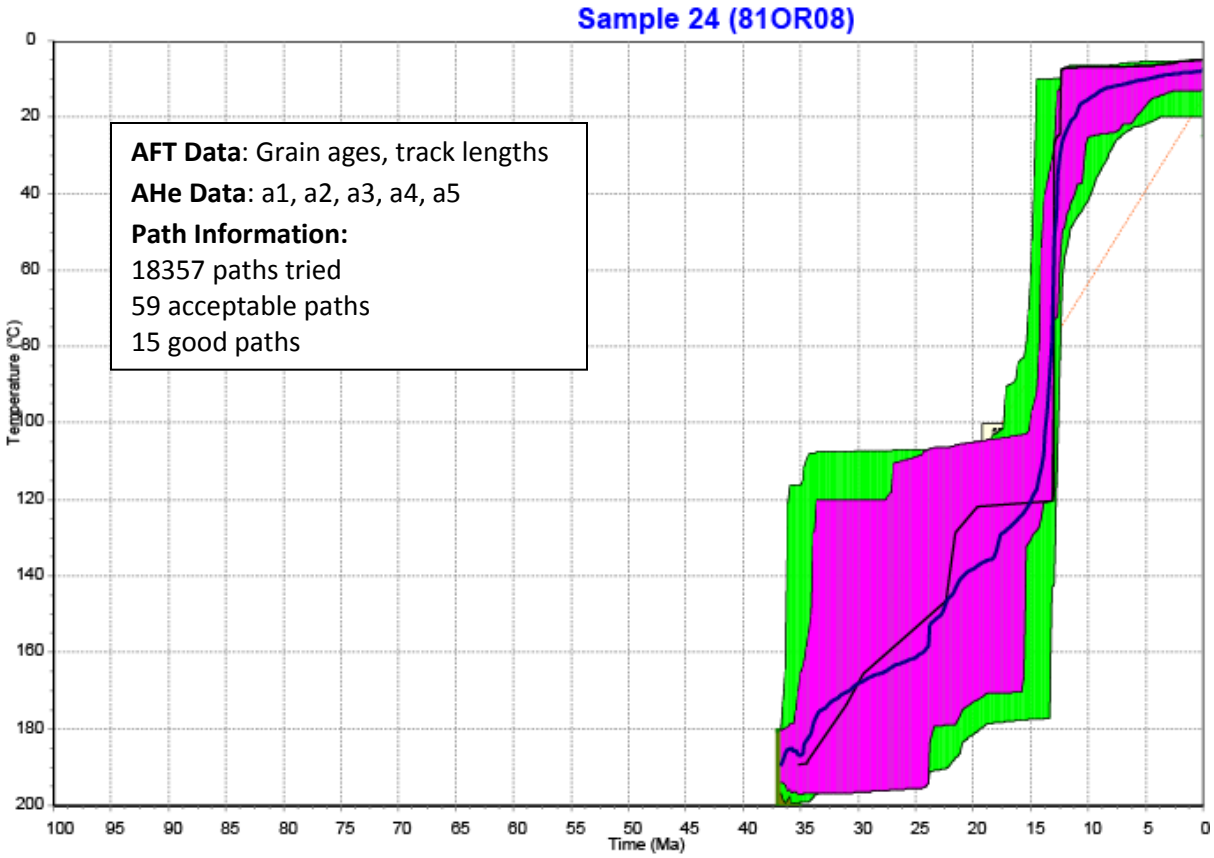
Sample 24 (81OR08)
AFT Data: Grain ages, track lengths
AHe Data: a1, a2, a3, a4, a5
Path Information:
18357 paths tried
59 acceptable paths
15 good paths
Temperature (°C)
Time (Ma)

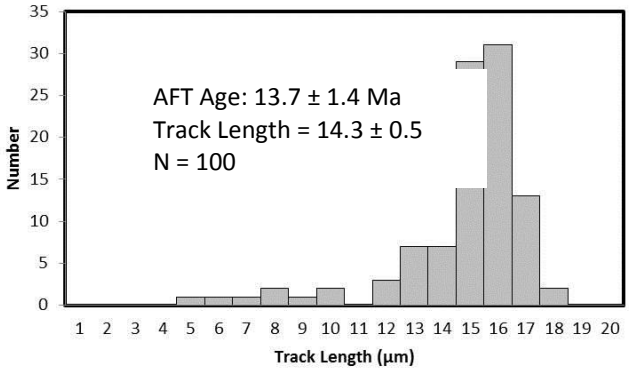
AFT Age: 13.7 ± 1.4 Ma
Track Length = 14.3 ± 0.5
N = 100
Number
Track Length (µm)

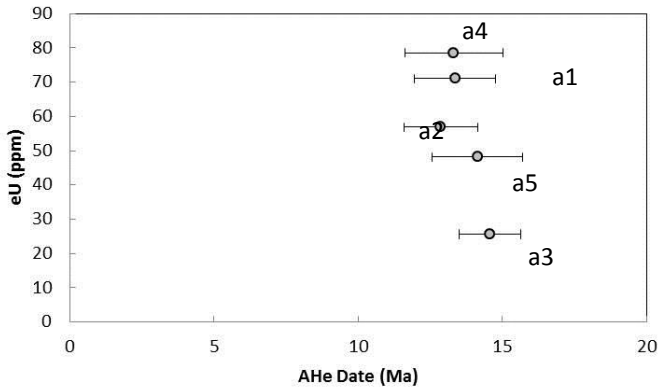
a4
a1
a2
a5
a3
eU (ppm)
AHe Date (Ma)

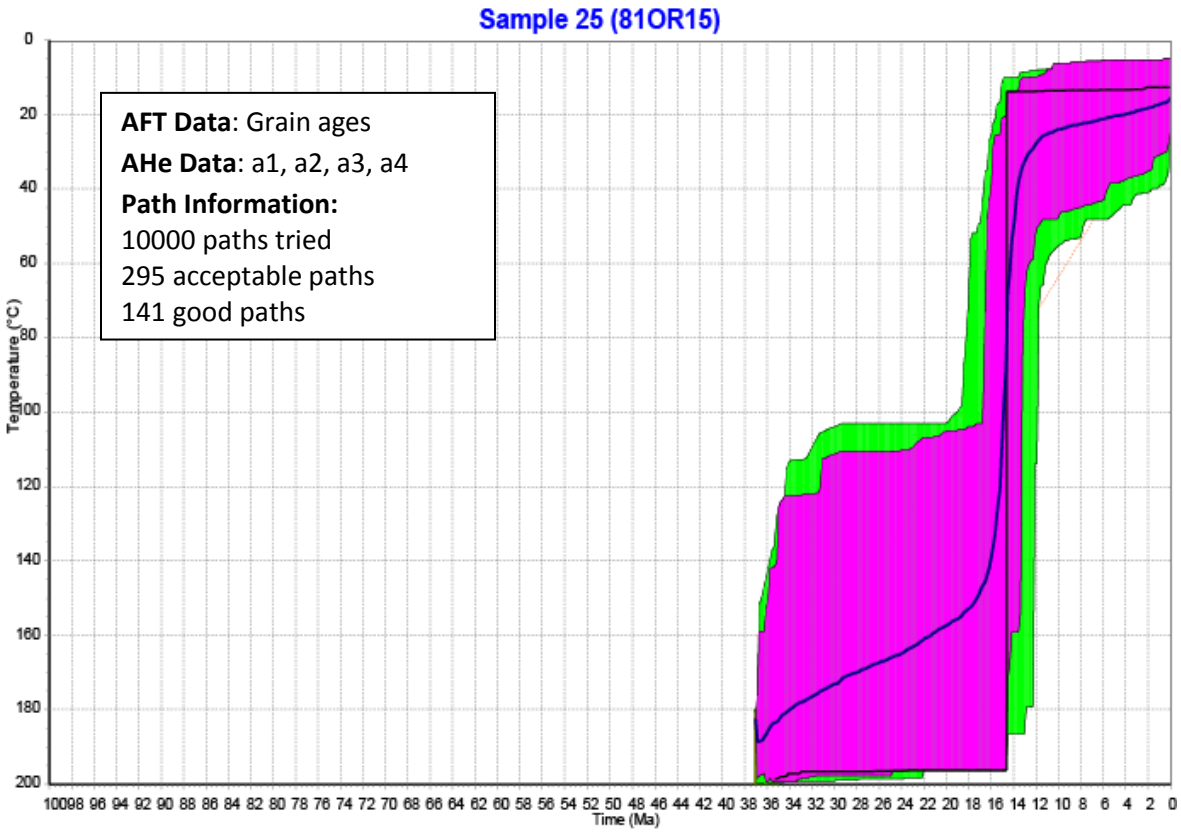
Sample 25 (81OR15)
AFT Data: Grain ages
AHe Data: a1, a2, a3, a4
Path Information:
10000 paths tried
295 acceptable paths
141 good paths
Temperature (°C)
Time (Ma)

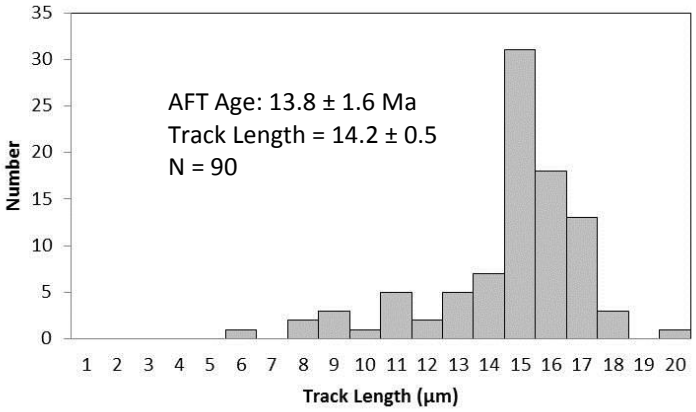
AFT Age: 13.8 ± 1.6 Ma
Track Length = 14.2 ± 0.5
N = 90
Number
Track Length (µm)

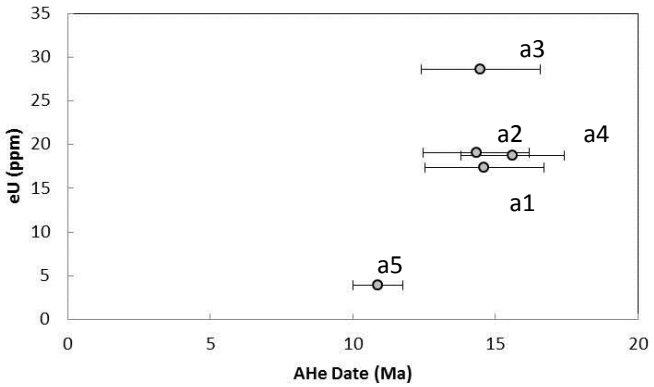
a3
a2
a4
a1
a5
eU (ppm)
AHe Date (Ma)

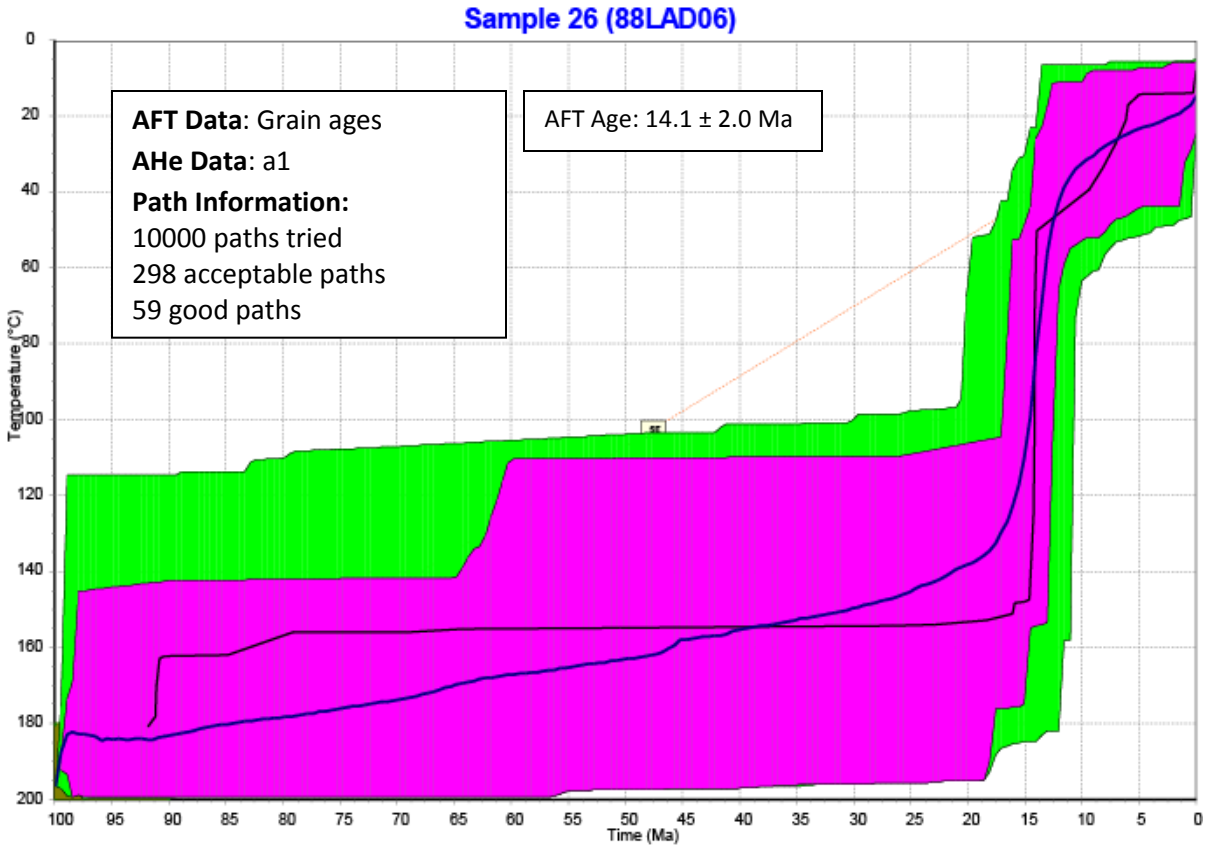
Sample 26 (88LAD06)
AFT Data: Grain ages
AHe Data: a1
Path Information:
10000 paths tried
298 acceptable paths
59 good paths
AFT Age: 14.1 ± 2.0 Ma
Temperature (°C)
Time (Ma)

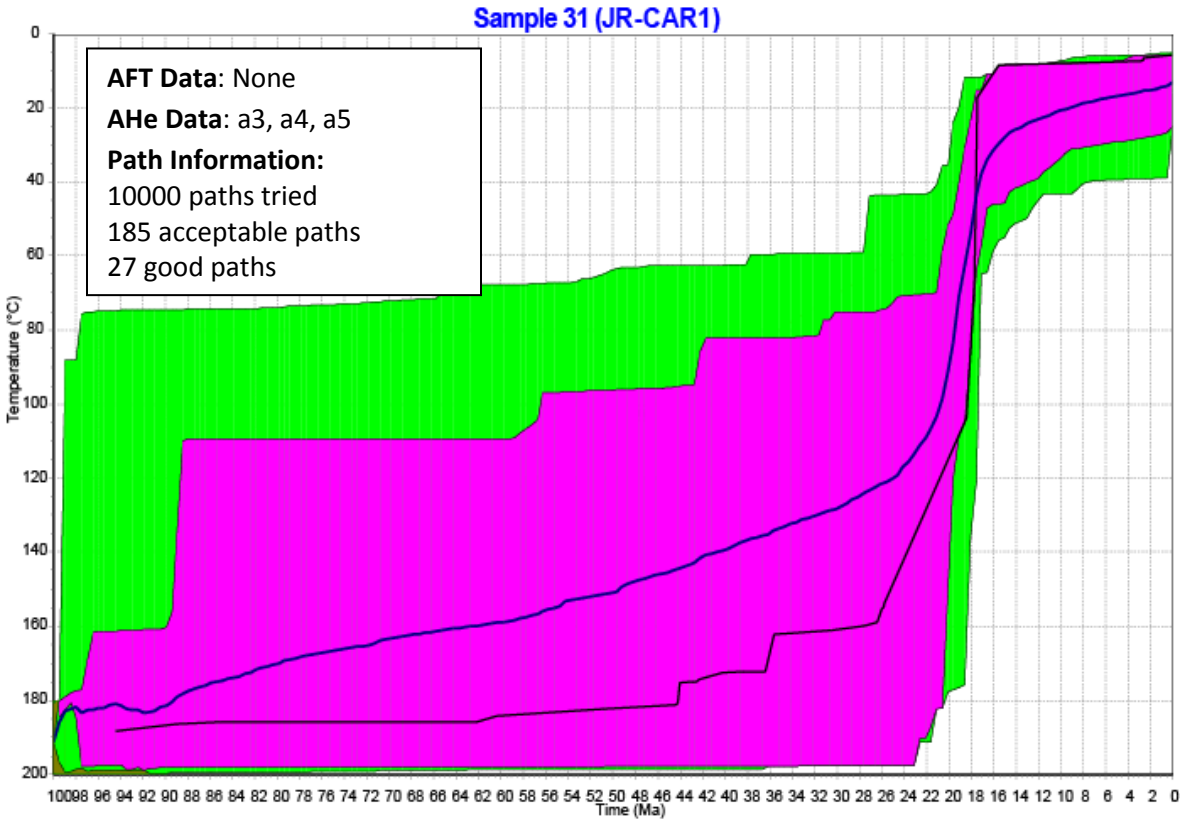
Sample 31 (JR-CAR1)
AFT Data: None
AHe Data: a3, a4, a5
Path Information:
10000 paths tried
185 acceptable paths
27 good paths
Temperature (°C)
Time (Ma)

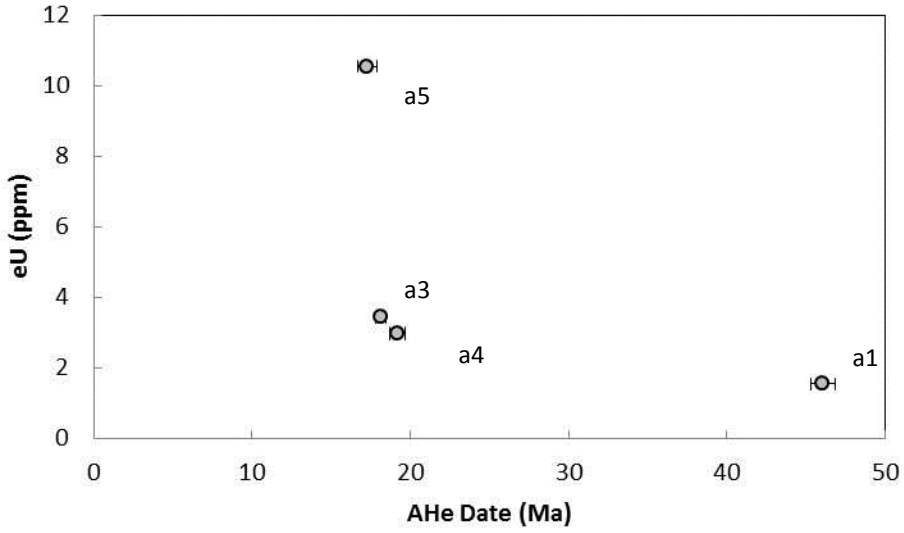
eU (ppm)
AHe Date (Ma)
a5
a3
a4
a1

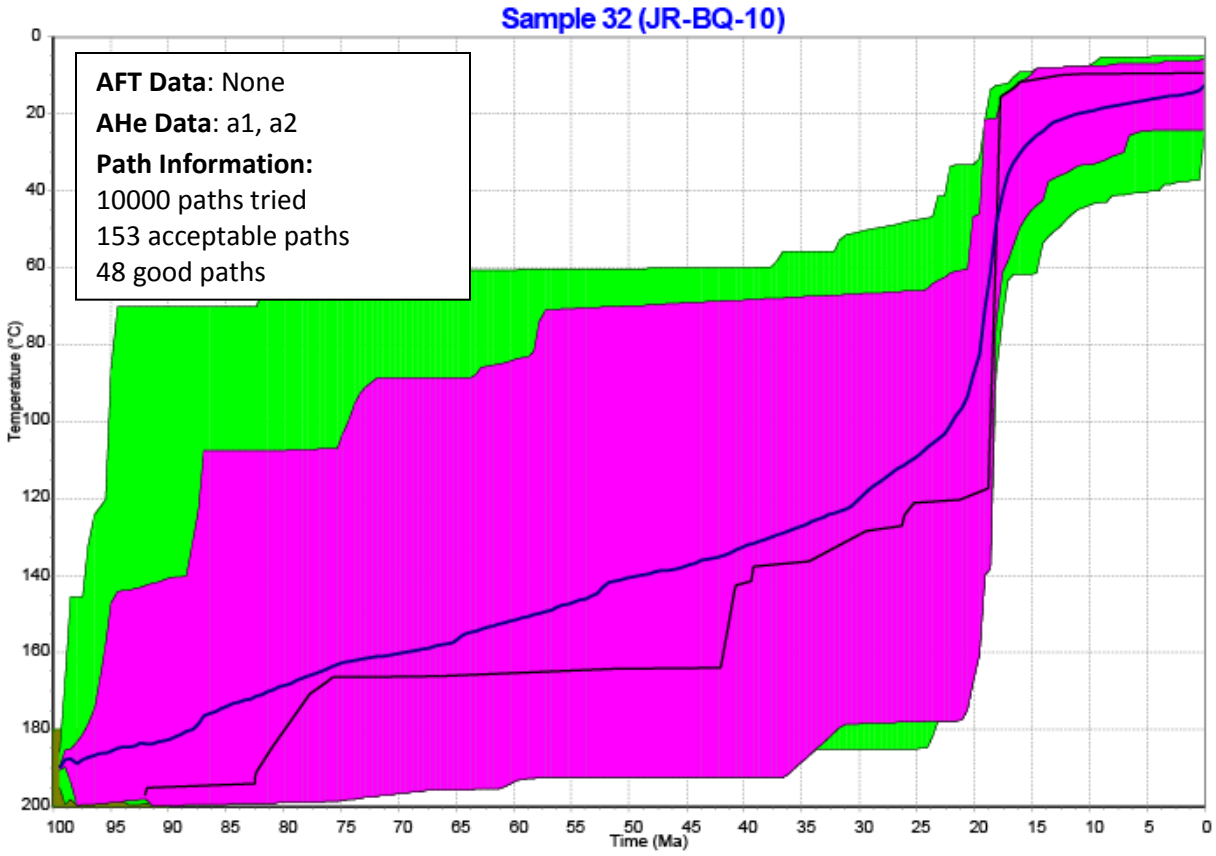
Sample 32 (JR-BQ-10)
AFT Data: None
AHe Data: a1, a2
Path Information:
10000 paths tried
153 acceptable paths
48 good paths
Temperature (°C)
Time (Ma)

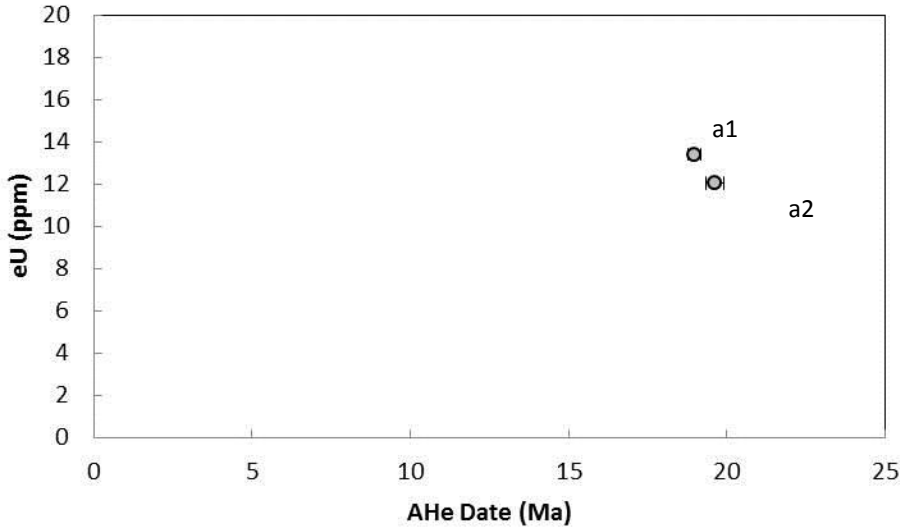
eU (ppm)
AHe Date (Ma)
a1
a2

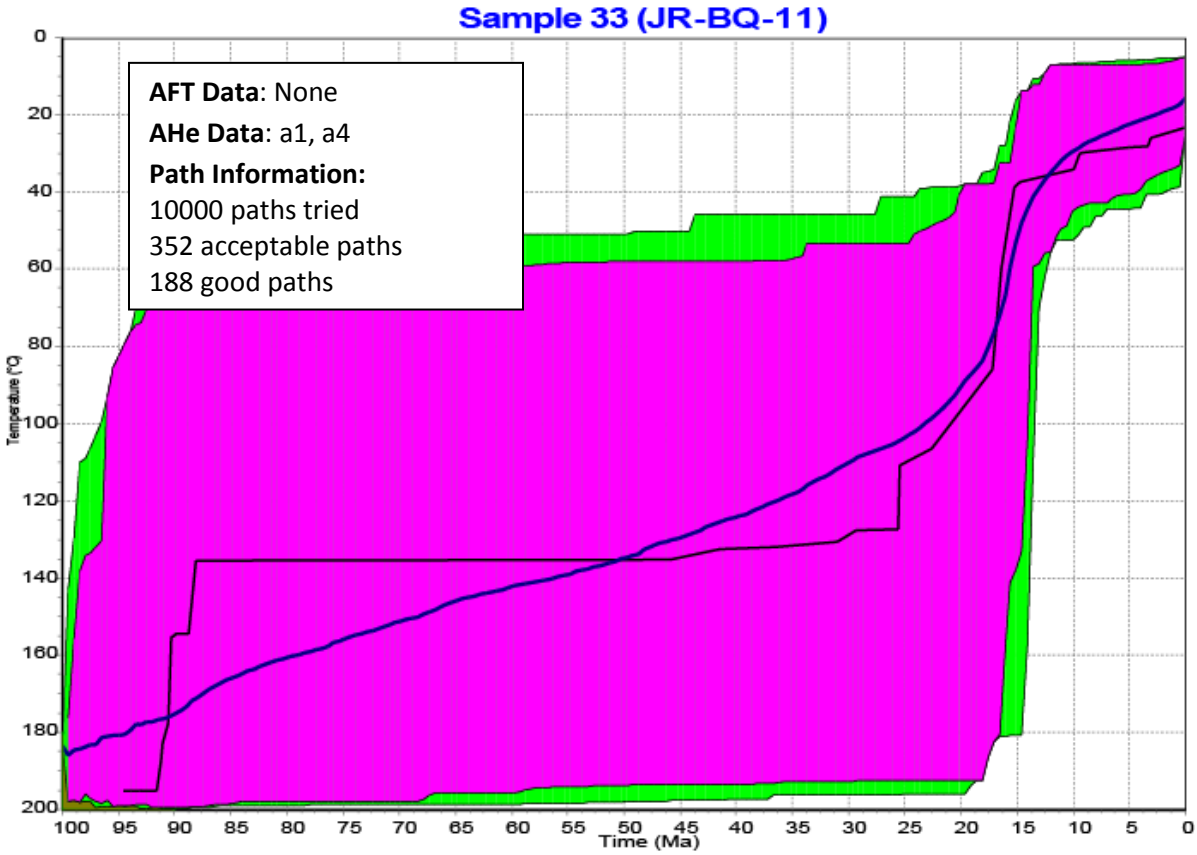
Sample 33 (JR-BQ-11)
AFT Data: None
AHe Data: a1, a4
Path Information:
10000 paths tried
352 acceptable paths
188 good paths
Temperature (°C)
Time (Ma)

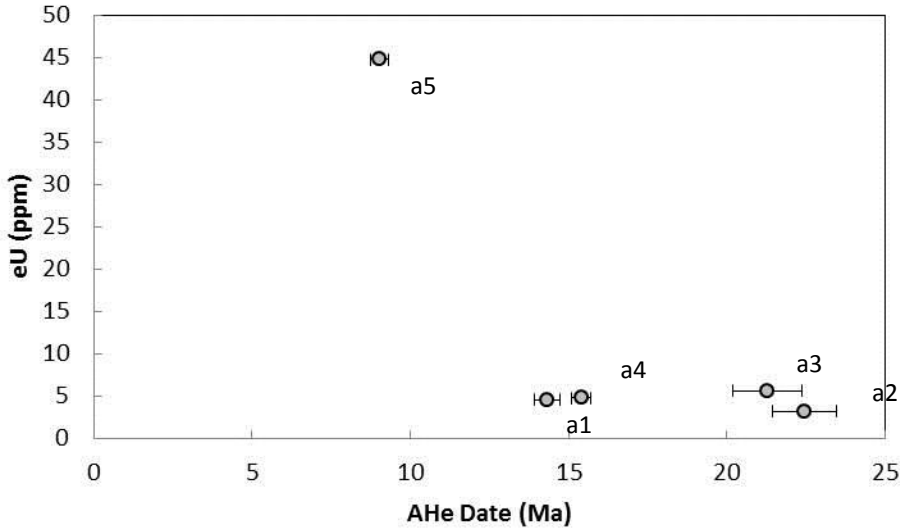
eU (ppm)
AHe Date (Ma)
a5
a4
a3
a2
a1